ABSTRACT

Title of Dissertation: EL NIÑO SOUTHERN OSCILLATION AND RELATED PRECIPITATION IN RECENT ATMOSPHERIC REANALYSES AND CMIP5 MODEL SIMULATIONS

Ni Dai, Doctor of Philosophy, 2018

Dissertation directed by: Research Scientist Phillip A. Arkin, Earth System Science Interdisciplinary Center

Professor Sumant Nigam, Department of Atmospheric and Oceanic Science

The El Niño-Southern Oscillation (ENSO), originating in the tropical Pacific, is the most significant mode of interannual variability of the ocean-atmosphere system. ENSO can modulate global climate through teleconnections with significant socioeconomic consequences, especially in the Tropics and along the western coastline of the Americas. It is thus important for the general circulation models (GCMs) of the oceans and atmosphere to simulate ENSO and its regional hydroclimate impacts with some fidelity. Although our understanding of the ENSO structure and dynamics has improved in the past few decades, its modeling remains challenging. Analysis of climate simulations produced by the Coupled Model Intercomparison Project Phase 5 (CMIP5) GCMs and long-term global precipitation datasets as well as recent high-resolution atmospheric reanalyses provides insights on

improving the ENSO simulation as well as the recent and projected ENSO-related changes under global warming.

A classification of CMIP5 models into two groups is developed on the basis of pattern correlation of the precipitation climatology and the ENSO-related precipitation anomalies with their counterparts in the 20th Century Reanalysis (20CR) and a statistically reconstructed precipitation dataset (REC). ENSO-related diabatic heating, atmospheric circulations, and air-sea interaction in the two model groups are then assessed using the state-of-the-art high-resolution atmospheric reanalysis, ERA-Interim, whose representation of tropical diabatic heating is considered optimal. The better performing model group simulates the ENSO-related features well, while the underperforming group exhibits severe biases, including deficient equatorial precipitation in both climatology and ENSO precipitation anomalies. This group also simulates a more westward-located and less robust ENSO precipitation/diabatic heating anomaly center together with weaker associated Walker and Hadley circulations and air-sea interaction compared to the better performing group.

Regarding multidecadal and centennial change in ENSO variability during the 20th and 21st centuries, ENSO-related SST anomalies strengthened in the later part of the last century, while the changes in ENSO-related precipitation were diverse and included both zonal shift and intensification. The underperforming group of models exhibits a robust increase and zonal shift of ENSO-related precipitation, SST and diabatic heating in the 21st century. The other group shows an increase in ENSO precipitation in the central-eastern equatorial Pacific, with related intensification of diabatic heating anomalies in the mid-to-upper troposphere.

EL NIÑO SOUTHERN OSCILLATION AND RELATED PRECIPITATION IN RECENT ATMOSPHERIC REANALYSES AND CMIP5 MODEL SIMULATIONS

by

NI DAI

Dissertation submitted to the Faculty of the Graduate School of the
University of Maryland, College Park, in partial fulfillment
of the requirements for the degree of
Doctor of Philosophy
2018

Advisory Committee:
Professor Sumant Nigam, Chair/Co-Advisor
Research Scientist Phillip A. Arkin, Co-Chair/Advisor
Professor James Carton
Professor Eugenia Kalnay
Associate Professor Sujay Kaushal

Dedication

To my beloved Mom and Dad,

who have always been my source of inspiration and encourage me to go on every adventure,

especially this one.

Acknowledgements

First and foremost I owe my deepest gratitude to my advisor, Dr. Phillip Arkin, for his mentorship, support, encouragement and patience throughout my graduate studies. I have always considered myself extremely lucky to have an advisor who responded to my questions and queries so promptly, who never failed to offer wise advice, and who shared the excitement of over six years of research discovery with me. His unwavering enthusiasm and optimism for research kept me constantly engaged with this work. I also couldn't be more thankful to him for believing in me and giving me enough freedom to explore every interesting topic, for providing me with great scientific input and forethought, for helping me improve my English writing and presenting skills, and finally, for encouraging me to do better and supporting me when things got difficult. Without him, I would not be where I am in my scientific career today and I immensely thank him for all he has done.

I also express my warmest gratitude to my academic advisor Prof. Sumant Nigam for his high-quality guidance, encouragement and patience. I am fortunate indeed to have had the opportunity to collaborate with him. His guidance on atmospheric dynamics and thermodynamics has been essential during this work. His constructive critique has also shaped my critical thinking in science. This work would hardly have been completed without him. Furthermore, thanks to him, my enthusiasm for climate science has been strengthened more than ever.

I would like to express my sincere gratitude to Prof. James Carton, Prof. Eugenia Kalnay, and Prof. Sujay Kaushal for agreeing to take the time and sit on this committee, and for providing insightful comments on my dissertation. I thank Prof.

Rachel Pinker and Prof. Ning Zeng for accepting my dissertation committee invitation as well as their guidance and help in the past.

I would then like to thank Dr. Thomas Smith for providing the Reconstructed Precipitation dataset and his indispensable advice regarding my research. I truly appreciate Dr. Alfredo Ruiz-Barradas for helping me with GrADS and providing the HadISST dataset. I also thank Dr. Li Ren for providing her regridded CMIP5 precipitation outputs. I could not thank enough to CICS-MD for financially supporting me throughout my graduate studies.

I would like to thank my friends, fellow students, and stuff members from University of Maryland for their continuous support and help. They have all contributed in their own unique way to my experience, which has encouraged my growth both as a scientist and as a person. In particular, I am grateful to all my past and current officemates for their support and friendship, and for making the workplace a fun place to be.

Finally, I thank my family for their unfailing faith, endless support and unconditional love throughout my life. Words cannot describe my thanks to my parent, Yan Zhang and Bing Dai, for always being the rock in my life and helping me to sustain. Mom, thank you for being a selfless, hardworking, and loving parent. Thank you for always being there for me during the good and the bad. Dad, thanks for letting me explore my passions and you have always been an outstanding inspiration to me. Without both of you, none of this would have been possible.

Table of Contents

List of Tables

List of Figures

Chapter 1: Introduction

1.1 Background and Importance of Problems

1.1.1 El Niño – Southern Oscillation

The El Niño-Southern Oscillation (ENSO) is the most significant mode of interannual ocean-atmosphere coupled phenomena in the global climate system (e.g. Philander 1990; McPhaden et al. 2006). ENSO originates in the tropical Pacific region and has two phases, usually referred to as El Niño and La Niña. During an El Niño event, equatorial trade winds weaken, as does the Walker Circulation (Bjerknes 1969), a direct thermodynamic circulation in the longitude-height plane over the equatorial Pacific Ocean. Sea surface temperature (SST) in the central-eastern tropical Pacific becomes anomalously higher and the subsurface thermocline across the equatorial Pacific flattens as a result of less upwelling cold water in the eastern Pacific as well as more eastward warm water migrating from the west Pacific warm pool. Surface wind convergence and convective precipitation also maximize over the central Pacific during the El Niño phase, instead of over the west Pacific warm pool in normal conditions (Wang et al. 2004; McPhaden et al. 2006; Lindzen and Nigam 1987). The La Niña phase is in most respects the opposite of El Niño, and is associated with a stronger Walker Circulation and anomalously lower SST over the central-eastern Pacific, along with less rainfall over the central Pacific and more over the Maritime Continent.

The oscillations between these two ENSO phases involve great changes of SST/precipitation amplitude and distribution in the tropical Pacific Ocean. In

addition, ENSO can modulate the weather and climate in other parts of the world, even those that are far from the tropical Pacific, via Rossby wave propagation and energy transport (Hoskins and Karoly 1981; Horel and Wallace 1981; Trenberth et al. 1998). Some of these severe ENSO-related heavy rainfall, droughts, wildfires, and off-shore warming can have damaging socioeconomic impacts on the societies in the entire tropics and the western coastline of the Americas (Philander 1985; Ropelewski and Halpert 1987; Hsiang et al. 2011). The strong 2015/16 El Niño event alone affected more than 60 million people around the world, according to a World Health Organization report (WHO 2016), with particularly significant impacts in the Pacific islands, Central America, and central to southern Africa where the level of vulnerability to extreme weather/climate events is high and the economy depends on agriculture, fisheries and livestock. Therefore, accurate ENSO modeling and forecasts are crucial to enable these highly-impacted regions and the United Nations to plan preparedness and future budgets in order to lower socioeconomic losses from extreme ENSO events as much as possible.

During the past four decades, theoretical understanding, observation and modeling of ENSO have become among the most active fields in climate research. In the later 1960s, Bjerknes (1966 and 1969) discovered the positive feedback between the weakened strength of the easterly winds and increased amplitude of the SST anomalies over the eastern and central equatorial Pacific, thus linking the two phenomena, El Niño (fluctuation in SST of the eastern-central equatorial Pacific) and the Southern Oscillation (change of air pressure of the overlying atmosphere). Since then, ENSO research has continued to develop and expand. From the 1970s to the

early 1980s, more ENSO observations (e.g. Wyrtki 1975; Rasmussen et al. 1982) and modeling (e.g. Zebiak 1982) improved understanding of the El Niño and La Niña events during the 1940s to 1970s and their global impacts (Hoskins et al. 1981). Later, the strong 1982-83 El Niño, which evolved very differently from the previous events, brought more attention to ENSO research and inspired the ten-year Tropical Ocean-Global Atmosphere (TOGA) project (McPhaden et al. 1998) to support research into tropical oceanic and atmospheric seasonal-to-interannual variability. TOGA enabled the establishment of an advanced ocean observing system called Tropical Atmosphere Ocean (TAO) Array using moored buoys in the tropical Pacific to monitor real-time surface winds, SST and deep ocean data. During the TOGA era, understanding and modeling of ENSO quickly advanced. Some notable studies include: an intermediate dynamic coupled ocean-atmosphere model (Zebiak and Cane 1987) that successfully reproduces ENSO-like oscillations; empirical ENSO indexes (e.g. Southern Oscillation Index (SOI), Ropelewski et al. 1987); delayed oscillator theory (Suarez et al. 1988) that uses propagation and reflection of oceanic Kelvin and Rossby waves to explain the mechanism of the ENSO cycle; and several statistical models (Barnston et al. 1992) and hybrid models (Barnett et al. 1993) to predict tropical Pacific SST and wind stress. From the 1990s to 2010s, modern coupled general circulation models (CGCMs) that incorporate physical processes in the atmosphere, ocean, cryosphere and land surface have been used for ENSO simulation, together with advanced satellite data and data assimilation techniques. Such technological advancements enabled improved seasonal climate predictions of actual

ENSO events (e.g. Ji et al. 1994; Stockdale et al. 2011), and projection of potential ENSO-related changes in a warming world (IPCC 2013).

1.1.2 Precipitation Observation and Data

Precipitation is a key component in the water cycle, which replenishes water to the earth. It has long been one of the most important and useful meteorological/climatic quantities to observe. Precipitation not only influences people's daily activity patterns, but too little or too much precipitation can also lead to disastrous droughts or floods. Moreover, the global precipitation field is strongly influenced by ENSO on an interannual time scale (Dai et al. 1997), and thus can be used to represent the intensity and atmospheric influences of ENSO events (Cai et al. 2014).

The modern precipitation observation network can be traced back to the over 150 rain gauge stations in England and Wales recorded by the meteorologist George James Symons in 1860 (Symons 1866). Nowadays, more advanced techniques are being used to monitor global precipitation. The most widely used among them are rain gauges, weather radars, and satellites. The rain gauges measure rainfall at certain points on the ground surface, and weather radars and satellites are remote sensors that observe or estimate precipitation from either a side view or above. Most of the current precipitation datasets heavily depend on these monitoring techniques. Based on the types of platforms, precipitation data can be divided into three categories: gauge datasets, satellite-only datasets and merged satellite-gauge products.

The homogeneity of long-term observed global precipitation, unlike other weather parameters such as temperature, suffers from the following limitations: 1) precipitation itself is more spatially variable and temporally discontinuous than temperature, therefore, greater observation density is required; 2) observations of precipitation over the ocean and high latitudes are very scarce and uncertain before the satellite era (1979 to present); 3) precipitation rain gauges on land during the earlier periods are spatially sparse and the quality of these observations are susceptible to wind eddies, vegetation growth, and the types of gauges.

Since 1979, a number of satellites have permitted the estimation of precipitation over many ocean areas. Due to the fact that most of the satellites with global coverage only view the same region twice per day, global precipitation datasets usually incorporate products from multiple satellites in order to reduce the sampling errors. For example, CICS High-resolution Optimally Interpolated Microwave Precipitation from Satellites (CHOMPS, Joseph et al. 2009) employs all available passive microwave satellite estimates to improve global daily precipitation. Many global precipitation datasets are also constructed using both satellite derived/observed precipitation and the rain gauge data over land, such as CPC Merged Analysis of Precipitation (CMAP, Xie and Arkin 1997), Global Precipitation Climatology Project (GPCP, Adler et al. 2003) and Tropical Rainfall Measuring Mission (TRMM, Kummerow et al. 1998) precipitation.

For precipitation data before the satellite era, the lack of observations over the ocean can be resolved either by reconstructing precipitation based on statistical techniques or through a reanalysis approach. Smith et al. (2009 & 2012) used GPCP

as base data and reconstructed precipitation for the period of 1900-2008 from the leading Empirical Orthogonal Function (EOF) modes that were adjusted by a Canonical Correlation Analysis (CCA) with SST and sea level pressure (SLP) and the Global Historical Climatology Network (GHCN, Peterson et al. 1997) gauge data. The reanalysis approach is more similar to operational weather/climate forecasts. Atmospheric reanalyses are produced by assimilating historical records (e.g. SLP and sea surface temperature) via a fixed data assimilation scheme and model system. For instance, the 20th Century Reanalysis Version 2 (Compo et al. 2011) is an atmospheric reanalysis dataset that covers the period of 1871-2012. It was generated using an NCEP atmosphere–land model with an Ensemble Kalman Filter data assimilation system (Whitaker and Hamill 2002), which assimilates only SLP and surface pressure observations.

It is exciting that these long-term global datasets have become available, as well as other recent state-of-the-art satellite-era atmospheric reanalyses (for more information, see Section 2.1.2). However, limitations for these datasets do exist. For the reconstructed precipitation, usually only limited leading empirical orthogonal function (EOF) modes of observed precipitation are used and many natural small-scale variations are filtered out. In addition, the weights of these EOF modes are determined by land gauge data, which may not be adequate to represent the precipitation variability over the ocean (Smith et al. 2012). The precipitation reanalysis data, on the other hand, are produced from dynamical models. However, these datasets are sensitive to the scheme choices of data assimilation and the model physical parameterizations. For example, it is challenging to represent cloud

processes in the models due to their nonlinearity and the spatial discontinuity of precipitation (Gao & Li 2008). The reanalysis data can also be influenced by the changes in the sources of assimilated observations for different time periods, which can lead to artificial variability (Bengtsson et al. 2004). Therefore, it is crucial to intercompare these reanalysis datasets in precipitation and the related atmospheric features including diabatic heating and atmospheric circulations (Chan and Nigam 2009) and validate them with other observations (e.g. TRMM), before using these reanalyses to study the atmospheric part of climate variations, such as ENSO, the Pacific Decadal Oscillation (PDO), and the global warming trend.

1.1.3 CMIP5 Models and Model Biases

CGCMs can be great tools for scientists both to study and predict ENSO and the related precipitation anomalies. The Coupled Model Intercomparison Project phase 5 **(**CMIP5; Taylor et al. 2012) brings together most of the state-of-the-art CGCMs to simulate past and project future climate changes in support of the Intergovernmental Panel on Climate Change (IPCC) Fifth Assessment Report (AR5) (IPCC 2013). Previous research suggests that the models used in CMIP5 have the capacity to simulate basic ENSO characteristics such as amplitude, evolution, timescale, seasonal phase locking, air-sea feedbacks and teleconnections (e.g. Bellenger et al. 2014; Kim et al. 2014; Ham et al. 2015; Guilyardi et al. 2012) more realistically than their precursors. However, there still exist systematic errors in these simulations. For instance, ENSO-related SST anomalies and the related precipitation anomalies are more westward extended and meridionally narrower than observed

anomalies, and surface easterly winds are stronger than observed (Zhang et al. 2013; Ham et al., 2015; Dai and Arkin 2017). The lifecycles of the ENSO-like air-sea interaction in the models appear to be shorter and less variable (Brown J.N. 2014) than in observations. Most of the CMIP5 models underestimate the observed Bjerknes feedback (Bellenger et al. 2014) and about half of the models lack the ability to realistically simulate two different types of El Niño: a conventional eastern-Pacific type and a central-Pacific type that has occurred more often in recent decades (Kug et al. 2009). In addition, model biases in thermocline, SST, sea level pressure (SLP) and the Hadley and Walker cells all play a role in aggravating the ENSO-related biases in the CGCMs (Kirtman et al. 2002; Zhang et al. 2013; Ham et al. 2014).

Besides the ENSO-related biases mentioned above, biases also exist in the simulations of precipitation and SST climatology in the CMIP5 models. The CMIP5 models tend to exhibit much cooler cold tongue-like features (an equatorial SST minimum that extends from the western coast of the Americas into the central Pacific; Wyrtki 1981) in their SST, which could arise from unrealistic Bjerknes feedback in the models (Bjerknes 1969; Li et al. 2013). Precipitation, as one of the most difficult parameters to simulate in CGCMs (Räisänen 2007), is derived from heating, water vapor and cloud budget equations in the CGCMs., along with appropriate parameterization schemes. One of the most well known biases of the precipitation climatology in CGCMs is the double Intertropical Convergence Zones (ITCZs) with overestimated precipitation both north and south of the equator in the eastern Pacific (Zhang 2001; Lin 2007; Bellucci et al. 2010). Other precipitation biases in the models include the “dry equator” over the Pacific Ocean (Zhang et al. 2013; Grose et al.

2014) and overly zonal South Pacific Convergence Zone (SPCZ), a band of precipitation located over the western and central South Pacific (Trenberth 1976; Vincent 1994). Such model biases of SST and precipitation in mean states can contribute to the biases of ENSO and related precipitation variations (Watanabe et al. 2010; Guilyardi et al. 2012; Ham and Kug 2014).

In addition, although previous studies have shown that the CMIP5 models have improved intermodel consistency regarding many of these aforementioned model biases compared to their CMIP3 precursors (e.g. Bellenger et al. 2014; Ham and Kug 2015; Kim and Yu 2012), the intermodel diversity of ENSO and the related precipitation is still very large in the CMIP5 models (e.g. Capotondi et al. 2015; Dai and Arkin 2017). Research is needed to 1) assess the capability of individual models in simulating ENSO and the related precipitation variations, 2) investigate the dynamic and thermodynamic causes of the intermodel diversity with regard to ENSO and its related precipitation, and 3) understand the connections between the biases in the mean states and the ENSO-related biases in the models.

1.1.4 Projected Changes of ENSO in CMIP5 Models

The earth's warming signal arising from anthropogenic forcings may alter ENSO and the related precipitation (Cane 2005; Vecchi and Wittenberg 2010; Collins et al. 2010; Li et al. 2013; Cai et al. 2014). ENSO under global warming should continue to dominate year-to-year climate variability (Cai et al. 2015), and changes in the ENSO phenomenon may be among the largest changes in climate under global warming (Guilyardi et al. 2012). Numerous studies have implied that the Walker

Circulation will weaken in response to greenhouse warming (Collins et al. 2010; IPCC, 2013; Cai et al. 2015), which would accelerate warming in the eastern Pacific and create a more favorable environment for more extreme El Niño and La Niña events (Cai et al. 2014 & 2015). The asymmetry between El Niño and La Niña (strong El Niño exhibits a warm maximum SST anomaly center in the eastern equatorial Pacific, while an extreme La Niña features an anomaly center in the central equatorial Pacific; Larkin and Harrison 2002) is likely to shrink in a warming world (Ham 2017). More intense central equatorial Pacific type El Niños may occur instead of the canonical eastern Pacific type (Kim and Yu 2012). The projected ENSO-related precipitation is likely to intensify and shift eastward due to increasing atmospheric moisture and changes in SST anomalies associated with El Niño (Power et al. 2013; Chung et al. 2014; Huang 2016).

However, uncertainties exist for these projected changes of ENSO in the models. First of all, the IPCC Fifth Assessment (IPCC 2013) and other studies (e.g. Cai et al. 2015) conclude that there is low confidence in projected changes of ENSO amplitude due to large intermodel diversity. Second, it is unclear what impact the diverse model biases mentioned in Section 1.1.3 may have on the ENSO response to global warming, which further adds uncertainties to the CMIP5 multi-model averaged projection of ENSO-like features. Therefore, it will be valuable to separate the models into groups for reduced intermodel diversity to further understand the potential ENSO changes. Third, in contrast to the model projections, the observed Walker Circulation strengthened during the last three decades (L'Heureux et al. 2013). Potential contributing factors to this phenomenon could be the negative phase

of Pacific Decadal Oscillation (PDO) and the decadal variation of ENSO. PDO has a similar pattern to ENSO in character, but is most intense in the North Pacific region and varies on a 20 to 30 year time scale, much longer than that of ENSO. Verdon et al. (2006) examined the relation between PDO and ENSO using proxy climate records during the past 400 years and found that the positive (negative) phase PDO is associated with increased frequency of El Niño (La Niña) events. The amplitudes of ENSO can also vary on decadal and longer time scales (e.g. Wang and Ropelewski 1995; Allan et al. 1996; Kestin et al. 1998). It is unclear what causes these long-period variations. Possible explanations include intrinsic variability of the tropical climate system (e.g. An et al. 2000) and extra-tropical interdecadal to multi-decadal forcings from the North Pacific and the Atlantic basins (e.g. Deser and Blackmon 1995; Dong et al. 2006; Kravtsov 2012; Kang et al. 2014). Both of these multi-decadal modes of variability are less studied than the canonical ENSO, and it is less likely that the CMIP5 models are able to capture them correctly and to simulate their influences on the canonical ENSO variability. This further necessitates an improvement of ENSO modeling in the CGCMs.

1.2 Motivation and Objectives

It is indeed very challenging to address all these aforementioned problems in the CMIP5 models and the recent reanalyses/observations. The current simulations and forecasts of ENSO and the related precipitation are still limited by imperfect model parameterizations, insufficient observations (subsurface data in particular), data assimilation methods and computing power (Chen et al. 2008). Despite these

limitations, the CMIP5 models combined with the recent observations and reanalyses provide great opportunities to study the inter-model diversity of ENSO simulations, to evaluate and diagnose model biases, and to improve our understanding of ENSO variability in the past and future. Such research is necessary and important to improve the CGCMs simulating and forecasting skills, to generate more advanced reanalysis products and to better understand and prepare for climate changes.

This dissertation focuses on three studies in which the CMIP5 models are compared with different reanalyses: the ENSO-related precipitation mean states, the ENSO-related atmospheric dynamical and thermodynamical structure and air-sea interaction, and the multi-decadal change of ENSO-related precipitation during the 20^{th} and 21^{st} centuries.

1.2.1 ENSO-related Precipitation Mean States

Evaluating precipitation climatology and ENSO-related precipitation in the CMIP5 models can provide valuable information about the model capability and intermodel diversity of ENSO simulations, since it is difficult to simulate precipitation well in the GCMs and precipitation can be a good indicator for ENSO events (Cai et al 2014). It is also beneficial to evaluate the models with more observational datasets, especially those covering a long time period (Räisänen 2007), in order to reduce the biases of the ENSO-related precipitation mean state and the associated precipitation climatologies in the CMIP5 models. Longer-term datasets contain more samples of ENSO events and tend to produce more reliable typical ENSO mean states for both observations and model outputs. In the past several years,

global precipitation datasets that cover the entire 20th century have become available, including the 20th Century reanalysis from NOAA (20CR, Compo et al. 2011) and the statistically Reconstructed Precipitation (REC, Smith et al. 2009 & 2012). This study (Dai and Arkin 2017) aims to:

- Compare precipitation climatology and ENSO-related precipitation between 20CR and REC, and validate these two precipitation datasets against other advanced precipitation reanalyses and observations during the satellite era;
- Compare spatial similarities and dissimilarities of precipitation climatology and ENSO-related precipitation between the CMIP5 models and these newly developed datasets (20CR and REC) during the 20th century, and identify the climatological and ENSO-related precipitation features that need to be improved;
- Investigate the impact of model biases in precipitation climatology on the ENSO-related precipitation biases;
- Study the connections between the biases of the ENSO-related precipitation and the ENSO-related SST variability in the models;
- Develop a method to separate the models into two groups: a better performing group in simulating ENSO-related precipitation and an underperforming one.

1.2.2 ENSO-related Atmospheric Dynamical and Thermodynamical Structure and Air-sea Interaction

ENSO itself is a natural thermodynamic phenomenon, and thus improved understanding can contribute tremendously to validating the quality of climate

models. In the atmosphere, large-scale diabatic heating is the major driving force of the atmospheric circulation. Over the tropical Pacific, diabatic heating is generated primarily from the phase changes of water substance (Tao et al. 1993), meaning that the tropical diabatic heating approximately corresponds to the surface precipitation rate. The diabatic heating combined with the atmospheric circulation, therefore, can provide a three-dimensional (3D) dissection of the precipitation mean states and ENSO-related precipitation studied in Section 1.2.1. Since diabatic heating cannot be directly observed, residual diagnoses of diabatic heating from the thermodynamic budget in modern atmospheric reanalyses can serve as excellent observational references. ERA-Interim (Berrisford et al. 2011), MERRA-2 (Gelaro et al. 2017) and CFSR (Saha et. al. 2010) are three state-of-the-art atmospheric reanalyses with fine spatial resolution and temporal coverage of the satellite era (1979-present). Assessing the diabatic heating and atmospheric circulations in the CMIP5 models against those of the reanalyses can help understand the biases of ENSO-related precipitation anomalies in Section 1.2.1. In addition, it is important to intercompare and validate the three atmospheric reanalyses with independent observations (e.g. TRMM convective and stratiform heating, Tao et al. 2006) in order to determine the most reliable reanalysis in representing diabatic heating, atmospheric circulations and precipitation. The detailed goals for this study are to:

- Compare the horizontal climatology and vertical profiles of diabatic heating in ERA-Interim, MERRA-2, and CFSR with the latent heating component from the TRMM convective and stratiform heating to determine the best reanalysis for depiction of diabatic heating.

- Compare the 3D diabatic heating and atmospheric circulation climatology of the CMIP5 models with those of the reanalyses to further explain the model biases of precipitation climatology in Section 1.2.1;
- Examine the deviations of the CMIP5 models from the reanalyses in ENSO diabatic heating, upper and lower tropospheric stream function and velocity potential, Walker circulation, local Hadley circulation, and air-sea interaction, in order to fully investigate the atmospheric part of the ENSO-related biases in the models;
- Understand how the better performing CMIP5 group differs from the underperforming one, from the perspective of ENSO.

1.2.3 Multi-decadal and Centennial Changes of ENSO-related Precipitation During the 20th and 21st Centuries

Due to previously unavailable century-long global precipitation datasets, the multi-decadal variability of ENSO-related precipitation during the 20th century has not been comprehensively studied. CMIP5 models together with those recent-developed long-term reanalysis precipitation datasets (20CR and REC) can form a relatively statistically meaningful basis with which to investigate the ENSO-related precipitation multi-decadal changes during the whole 20th century. The projected changes of ENSO-related precipitation in the 21st century in the CMIP5 models are less studied than the other ENSO-related features. Also, most of these studies use a less optimal approach by using the multi-model mean to study ENSO-related changes. As mentioned in Section 1.1.3 and 1.1.4, one of the most robust changes of ENSO SST under global warming in the CMIP5 models is over the eastern Pacific

region where the cold tongue exists. If the cold tongue in one model has strong cold biases, the amplitude change of its ENSO and the related precipitation could be exaggerated. Therefore, it is important to consider intermodel diversity by grouping the models based on severity of the biases in climatology and ENSO.

The objectives of this study include:

- Use a method to separate ENSO variability cleanly from variations related to the longer-term phenomena, e.g. PDO and global warming;
- Identify and compare the multi-decadal changes of ENSO-related precipitation patterns in the 20th century in 20CR, REC and the CMIP5 models, and determine whether these changes are statistically significant;
- Study the multi-decadal changes of ENSO-related precipitation in the 21st century under different greenhouse gas emission scenarios, based on different groups of the CMIP5 models in simulating ENSO dynamics and thermodynamics.
- Investigate the contribution of dynamical and thermodynamical components to the differences of ENSO-related precipitation between the 20th and 21st centuries in different CMIP5 groups.

1.3 Organization of This Dissertation

The dissertation begins by introducing the details of the datasets and methodology used in this study in Chapter 2. Chapter 3 presents the results of the ENSO-related precipitation mean states and explains the relation between the biases of precipitation climatology and of ENSO-related precipitation in two different

CMIP5 groups. Chapter 4 intercompares the 3D structure of diabatic heating and atmospheric circulation climatology in the reanalyses and the CMIP5 groups, and investigates how the ENSO-related biases in diabatic heating, atmospheric circulation and air-sea interaction are related to the ENSO-related precipitation biases within each group. Chapter 5 presents the multi-decadal and centennial change of ENSO-related precipitation during the 20th and the 21st centuries. A summary and suggestions for the direction of future research are provided in Chapter 6.

Chapter 2: Datasets

This chapter describes the reanalysis datasets, satellite observations and CMIP5 models used in this dissertation. The reanalysis dataset subsection includes two parts: recent long-term precipitation/SST reanalyses covering the whole 20th century and the most advanced atmospheric reanalyses of the Satellite Era (1979 - present).

2.1 Reanalysis Datasets

2.1.1 Long-term Reanalysis Datasets

a. NOAA/CICS Reconstructed Precipitation (REC)

Reconstructed precipitation is a long-term reanalysis dataset of precipitation rate anomalies that was developed by NOAA/CICS-MD (Smith et al. 2009 & 2012). The version used in this study is archived on a 2.5° by 2.5° global grid from January 1901 to December 2008 in units of mm/month. The monthly precipitation anomaly field of REC uses the precipitation climatology from the Global Precipitation Climatology Project (GPCP V2, Adler et al. 2003; Huffman et al. 2009) as base data, and was reconstructed using a first-guess annual anomaly field and monthly anomaly increments (monthly anomaly minus annual anomaly). The first-guess annual field was based on the 10 leading EOF modes of annual GPCP anomalies. Data fit to those EOFs includes CCA-based estimates over oceans and Global Precipitation Climatology Center (GPCC, Rudolf et al. 2005) rain gauge estimates over land. This CCA-based annual anomaly (Smith et al. 2009) used the relation between annual combined sea level pressure (Allan et al. 2006) and sea surface temperature (Smith et

al. 2008) and annual precipitation anomalies. The monthly increments were created from the 40 leading EOF modes of monthly GPCP, which were weighted by the monthly GPCC anomalies, and were later added to the first-guess annual field to create the monthly REC dataset. In this study, the units of the REC are converted to mm/day and the period of January 1901 to December 2005 is used. Since this dataset has fewer observations at high latitudes, the domain of 75°S to 75°N is used for REC and all the other long-term reanalysis datasets.

b. 20th Century Reanalysis Version 2 (20CR)

The 20th Century Reanalysis Version 2 (Compo et al. 2011) monthly-averaged precipitation rate is employed as a quasi-observational dataset to compare with REC and the CMIP5 models over the 20th century timespan. The 20CR was produced by utilizing a short term forecast from an ensemble of 56 members of an NCEP atmosphere–land model and assimilating only surface and sea level pressure data from marine observations (International Comprehensive Ocean-Atmosphere Data Set, ICOADS, Worley et al. 2005), land stations (Yin et al. 2008) and the International Best Track Archive for Climate Stewardship (IBTrACS, Knapp et al. 2010) every six hours with an Ensemble Kalman Filter data assimilation system (Whitaker and Hamill 2002). Global SST and sea ice data from the Hadley Centre Sea Ice and SST dataset 1.1 (HadISST 1.1 – see Section 2.1.1d, Rayner et al. 2003) are used as boundary conditions for 20CR. Solar, volcanic, and carbon dioxide forcings are prescribed. The precipitation rate is the average of ensemble mean and ensemble spread of the 3-hour first guess precipitation rate on a global Gaussian T62

grid from January 1871 to December 2012. More details can be found on the 20CR website (https://www.esrl.noaa.gov/psd/data/gridded/data.20thC_Rean V2.html). The 20CR precipitation rate used in this study is the monthly mean and is interpolated to 2.5° by 2.5° to be comparable to REC, with units of mm/day and covering the period from 1901 to 2005.

c. NOAA Extended Reconstructed Sea Surface Temperature Version 3b (ERSST v3b)

The NOAA Extended Reconstructed Sea Surface Temperature Version 3 (ERSST v3, Smith et al. 2008) is a monthly long-term SST reanalysis for January 1854 to present. This dataset is based on the most widely used collection of surface marine observations, the ICOADS SST anomaly data, and is reconstructed using improved statistical methods and historical bias adjustment (Smith et al. 2003 & 2008). ERSST v3 also includes bias-adjusted Advanced Very High Resolution Radiometer (AVHRR) satellite SST data for 1985 onwards. However, the addition of this data causes a small residual cold bias in ERSST v3 (in the order of 0.01°C), so even though this bias does not strongly impact the long-term trend, the newer version, ERSST v3b, does not include this satellite SST data. Both ERSST v3 & v3b are archived as anomalies in 2° by 2° global grids. More details can be found on the ERSST v3&v3b website (https://www.ncdc.noaa.gov/data-access/marineocean-data/extended-reconstructed-sea-surface-temperature-ersst-v3b). ERSST v3b is used in this study. This dataset has been converted to same spatial resolution as the precipitation reanalyses (2.5° by 2.5°) with a unit of °C and same period (1901 - 2005).

d. Hadley Centre Global Sea Ice and Sea Surface Temperature 1.1 (HadISST 1.1)

The Hadley Centre Global Sea Ice and Sea Surface Temperature 1.1 (Rayner et al. 2003) is a SST reanalysis from U.K. Hadley Center, consisting of monthly global SST and sea ice coverage fields from January 1870 to present. HadISST 1.1 is based on in-situ observations and satellite-derived estimates. The in-situ observations are individual ships' observations from the Met Office Marine Data Bank and the Global Telecommunication System (from 1982 onwards), and the monthly median SST data from ICOADS for 1871 to 1995. For 1982 onwards, adjusted AVHRR satellite SST data and Special Sensor Microwave Imager (SSMI) satellite sea ice data are also included. HadISST is primarily used as boundary conditions for atmospheric models and the HadISST 1.1 version is used for the 20CR V2 (see Section 2.1.1.b above). Additional information can be found on the HadISST website (http://www.metoffice.gov.uk/hadobs/hadisst/). The original spatial resolution for HadISST 1.1 is 1° by 1° on a global grid, and this has also been interpolated to 2.5° by 2.5°. The time period used here is from 1901 to 2005.

2.1.2 Satellite-era Reanalysis Datasets

a. ERA-Interim

The ERA-Interim reanalysis (Berrisford et al. 2011) is a state-of-the-art global atmospheric reanalysis produced by the European Centre for Medium-Range Weather Forecasts (ECMWF). It serves to replace its predecessor ERA-40 and is expected to be continued until the end of 2018. This dataset is archived on a high spatial resolution (0.75° by 0.75°) global grid and 37 pressure levels from January 1979 to

present. The ERA-Interim model forecast fields are generated by an operational Integrated Forecast System (IFS CY31r2) with T255 spectral resolution, N128 Gaussian grid and 60 vertical levels up to 0.1 hPa. This system uses a 12-hourly 4-dimensional variational assimilation (4D-Var) that enables improved analyses by assimilating the model forecast fields, multiple satellite products (e.g. European Remote Sensing Satellite, European Organization for the Exploitation of Meteorological Satellites, Global Ozone Monitoring Experiment, Gravity Recovery and Climate Experiment, Constellation Observing System for Meteorology, Ionosphere and Climate), along with observations and boundary forcing fields acquired for the ERA-40 (1979 to 2001) and from ECMWF operations (2002 onwards). The satellite radiance biases are automatically corrected via a variational bias correction scheme. Additional information can be found on the ERA-Interim website (http://www.ecmwf.int/en/research/climate-reanalysis/ERA-Interim).

b. Modern-Era Retrospective Analysis for Research and Applications, Version 2 (MERRA-2)

MERRA-2 (Gelaro et al. 2017) is a National Aeronautics and Space Administration (NASA) atmospheric reanalysis spanning the period from 1980 to the present. It is a follow-on project to the original MERRA reanalysis (Rienecker et al. 2011). Numerous improvements to the data assimilation, model, and observing system are incorporated to generate MERRA-2. MERRA-2 is obtained from a new version of the Goddard Earth Observing System Data Assimilation System Version 5 (GEOS-5, Suarez et al. 2015) produced by the NASA GSFC Global Modeling and Assimilation Office (GMAO) and Global Statistical Interpolation (GSI) assimilation

system. Beyond assimilating modern operational sounder radiance observations, MERRA-2 also uses new observations and estimates from the Moderate Resolution Imaging Spectrometer (MODIS), AVHRR, GPS Radio Occultation, Ozone Monitoring Instrument (OMI), and Microwave Limb Sounder (MLS) instruments. The key advances of MERRA-2 include incorporation of an aerosol model and the assimilation of space-based observations of aerosols, improved water vapor assimilation, and land surface forcing by observed precipitation. MERRA-2 has a spatial resolution of 0.675° by 0.5°, with 42 pressure levels and 3-hourly intervals. More details can be found on the MERRA-2 website (https://gmao.gsfc.nasa.gov/reanalysis/MERRA-2/).

c. Climate Forecast System Reanalysis (CFSR)

The National Centers for Environmental Prediction (NCEP) Climate Forecast System Reanalysis (CFSR, Saha et al. 2010) covers the period of January 1979 to March 2011. It was the first atmospheric reanalysis system in which the guess fields (the 6-hourly forecast) are from a global coupled atmosphere-ocean-land surface-sea ice system. CFSR uses high atmosphere horizontal resolution (T382, ~38 km) and 64 vertical levels up to 0.26 hPa. This system assimilates satellite-based radiances rather than the retrieved temperature and humidity variables and is forced by observed estimates of carbon dioxide concentrations, aerosols, and solar variations. For its precipitation reanalysis, the CFSR also uses NOAA's Climate Prediction Center (CPC) pentad merged analysis of precipitation (CMAP, Xie and Arkin 1997) and the CPC unified global daily gauge analysis (Xie et al. 2010). The CFSR data are

archived at a global gridded resolution of 0.5° by 0.5°. From 2011 into the future, the CFSR is extended by an operational, real time NCEP coupled forecast system model version 2 (CFSv2) product. Additional information can be found on the CFSR website (http://cfs.ncep.noaa.gov/cfsr/).

2.2 TRMM Observations and Estimates

The Tropical Rainfall Measuring Mission (TRMM, Kummerow et al. 1998) was a cooperative mission between NASA and the Japan Aerospace Exploration Agency (JAXA) for monitoring and studying tropical and subtropical precipitation and the related latent energy. The TRMM observatory was launched in November 1997 and the mission ended in April 2015, with a 350-km (increased to 400km in August 2001) orbit inclined 35° to the Earth's equatorial plane. The Global Precipitation Measurement (GPM, Hou et al. 2014) mission was launched in 2014 as the successor to TRMM.

a. TRMM Precipitation 3B43 Version 7

The TRMM precipitation product 3B43 (Huffman et al. 2007) was designed to provide the best monthly precipitation estimate and is useful for validating tropical precipitation in climate models and reanalyses. Five instruments were used in the TRMM mission: Precipitation Radar (PR), TRMM Microwave Imager (TMI), Visible Infrared Scanner (VIRS), Clouds & Earths Radiant Energy System (CERES) and Lightning Imaging Sensor (LSI). Among them, PR and TMI are the primary precipitation monitoring instruments aboard the TRMM satellite. The TRMM 3B43 monthly precipitation rate is produced from the 3B43 algorithm that combines

multiple precipitation estimates from TMI, Advanced Microwave Scanning Radiometer for Earth Observing Systems (AMSR-E), SSMI, Special Sensor Microwave Imager/Sounder (SSMIS), Advanced Microwave Sounding Unit (AMSU), Microwave Humidity Sounder (MHS), microwave-adjusted merged geo-infrared (IR), and GPCC gauge data. The TRMM 3B43 precipitation has been produced since January 1998 and will be continued to early 2018. It is archived on a 0.25° by 0.25° spatial resolution from 50°S to 50°N. More information can be found on the TRMM 3B43 website (https://mirador.gsfc.nasa.gov/collections/TRMM_3B43__007.shtml).

b. TRMM 3H31 Combined Convective and Stratiform Heating

The TRMM 3H31 monthly combined convective and stratiform heating (TRMM CSH, Tao et al. 2010) was generated from an updated version of the convective-stratiform heating algorithm in Tao et al. 2006. The CSH algorithm calculates latent heating using surface convective and stratiform rain rates from PR and models as input. The cloud model data generated by a cloud resolving model (CRM) is also a necessary input for this algorithm. The TRMM 3H31 monthly heating data has a spatial resolution of 0.5° by 0.5° with a time period from December 1997 to March 2015. More details can be found on the TRMM 3H31 website (https://mirador.gsfc.nasa.gov/collections/TRMM_3H31__007.shtml).

2.3 CMIP5 Models

30 CMIP5 models (Taylor et al. 2012) are used in this study. Details of these models can be found in Table 2.1. The model outputs are from three experiments: 'historical', 'RCP4.5' and 'RCP8.5'. The historical simulation is carried out from 1850 to 2005 with the same pre-industrial initial conditions for every model. All forcings are included in the historical simulation, including changes of atmospheric composition due to anthropogenic and volcanic influences, solar radiation, aerosol emissions and land use change. The projections of the 21st century are derived from the two experiments 'RCP4.5' (Clarke et al. 2007) and 'RCP8.5' (Riahi et al. 2007). RCP, or Representative Concentration Pathway, represents time-dependent projections of atmospheric greenhouse gas concentrations (not emissions) adopted by the Intergovernmental Panel on Climate Change (IPCC) Fifth Assessment Report (IPCC, 2013). RCP4.5 is one of the stabilization scenarios (radiation forcing stabilized to 4.5 W/m^2 before 2100) with the equivalent CO_2 of 650 parts per million (ppm) and temperature rising 2.4°C on average. RCP 8.5 is the business-as-usual scenario (radiative forcing rising to 8.5 W/m^2 in 2100) with CO_2 of 1313 ppm and temperature anomaly reaching 4.9°C (Moss et al. 2010) by the end of the 21st century. Although each model has a different spatial resolution, all data have been interpolated to 2.5° by 2.5° global grids and 17 vertical levels.

Table 2.1 List of the 30 CMIP5 models. The numbers of ensemble members shown here are for the historical simulation of the 20th century. The total ensemble member number that is available for all historical simulation, RCP4.5 and RCP 8.5 scenarios is about 50.

Institute ID	**CMIP5 Model Name**	**No. of Ensemble Member**	**Resolution (degree)**
CCCma	CanESM2	5	2.81*2.81
CMCC	CMCC-CM, CMCC-CMS	1, 1	0.75*0.75, 1.88*1.88
CNRM-CERFACS	CNRM-CM5	10	1.41*1.41
CSIRO-BOM	ACCESS1.0, ACCESS1.3	1, 1	1.88*1.25, 1.88*1.25
CSIRO-QCCCE	CSIRO-Mk3-6-0	10	1.88*1.88
INM	INM-CM4	1	2.00*1.50
IPSL	IPSL-CM5A-LR, IPSL-CM5A-MR, IPSL-CM5B-LR	6, 2, 1	3.75*1.88, 2.50*1.25, 3.75*1.88
MIROC	MIROC5	5	1.41*1.41
MOHC	HadCM3	10	3.75*2.50
MPI-M	MPI-ESM-LR, MPI-ESM-P	2, 3	1.88*1.88, 1.88*1.88,
MRI	MRI-CGCM3	3	1.13*1.13
NASA-GISS	GISS-E2-H, GISS-E2-H-CC, GISS-E2-R, GISS-E2-R-CC	4, 1, 5, 1	2.50*2.00, 2.50*2.00, 2.50*2.00, 2.50*2.00
NCAR	CCSM4	5	1.25* 0.94
NCC	NorESM1-M, NorESM1-ME	3,1	2.50*1.88, 2.50*1.88
NIMR/KMA	HadGEM2-AO	1	1.25*1.88
NOAA-GFDL	GFDL-CM3, GFDL-ESM2G, GFDL-ESM2M	5, 1, 1	2.50*2.00, 2.50*2.00, 2.50*2.00
NSF-DOE-NCAR	CESM1-BGC, CESM1-CAM5, CESM1-FASTCHEM	1, 3, 3	1.25*0.94, 1.25*0.94, 1.25*0.94

Chapter 3: Twentieth Century ENSO-related Precipitation Mean States in Twentieth Century Reanalysis, Reconstructed Precipitation and CMIP5 Models

3.1 Introduction

As stated in Chapter 1, the El Niño-Southern Oscillation (ENSO) phenomenon is one of the better-observed and understood climate phenomena (e.g. Clarke 2008). Although sea surface temperature (SST) anomalies have been historically used to classify the intensity of El Niño or La Niña, atmospheric parameters such as precipitation anomalies can also be employed to define ENSO events (Lengaigne and Vecchi 2010; Cai. et al. 2014) and to show both local and remote impacts of ENSO. In addition, as one of the most difficult parameters to simulate in global climate models (Räisänen 2007), precipitation responds nonlinearly to ENSO SST changes (e.g. Power et al. 2013). Therefore, both simulations of the precipitation mean states and the ENSO-like precipitation features can shed more light on climate model performance.

The Coupled Model Intercomparison Project Phase 5 (CMIP5; Taylor et al. 2012) incorporates most of the state-of-the-art coupled general circulation models (CGCMs). This project provides excellent opportunities to study inter-model diversity of ENSO and the related precipitation. Previous studies have shown that CMIP5 models simulate ENSO and its teleconnections more realistically than their precursors (e.g. Bellenger el at. 2014; Kim et al. 2014; Ham et al. 2015). However, there still exist biases of ENSO-related precipitation in the models. One of the major biases is that the positive precipitation anomaly center is located more westward than the observed one, which is consistent with the westward extended ENSO SST anomalies

and ENSO zonal winds (Zhang and Sun 2014; Ham et al., 2015). Also, the meridional width of the positive precipitation anomalies is usually narrower in the models than in the observations. Such a bias could be related to the narrow sea surface temperature anomalies (SSTA) (Zhang and Jin, 2012) that additionally lead to systematic errors in the lifecycles and variations of ENSO-related precipitation in the models (Brown, J.N. 2014). Previous studies suggest that the model biases in subsurface thermocline, SST, sea level pressure (SLP) and the resulting Hadley and Walker cells all play a role in the biases of the location and amplitude of ENSO and the related precipitation in the global circulation models (GCMs; Kirtman et al. 2002; Zhang and Jin 2012; Ham et al. 2014).

The mean state biases of precipitation in the CMIP5 models might also contribute to the ENSO-related precipitation biases (Watanabe et al. 2010; Brown, J.N. 2013; Ham et al. 2014). One of the most well-known biases of the precipitation climatology in the GCMs is the Double Intertropical Convergence Zones (DITCZ), that is, an underestimation of simulated precipitation over the equator but an overestimation both north and south of the equator in the eastern Pacific during most of the year (Mechoso et al. 1995; Zhang 2001; Lin 2007; Bellucci et al. 2010; Brownet al., 2013). Previous studies suggest that the causes of the DITCZ bias usually include: i) model biases in the large-scale circulations, such as a too strong and westward extended equatorial cold tongue in the eastern Pacific, together with strong easterlies that can generate unrealistic convergence over the north and south edges of the cold tongue (Mechoso et al. 1995; Wittenberg et al. 2006; Lin 2007); ii) model biases of the regional scale circulations, for example, the underestimated cross-

equatorial winds over the southeastern Pacific and the associated less upwelling in this region (Mechoso et al. 1995; de Szoeke and Xie 2008) ; iii) biases of the variables in the convective processes such as SST gradient (e.g. Lindzen and Nigam 1987), surface heat fluxes, or thresholds for deep convection (Bellucci et al., 2010); iv) parameterization biases and oversensitivity in ocean-atmosphere feedbacks and cloud schemes (Chikira 2010; Hirota 2013). In CMIP5, more models show the DITCZ problem than their CMIP3 precursors (Gros et al. 2014). Hwang et al (2013) point out that the CMIP5 models with more energy flux into the Southern Hemisphere atmosphere tend to have stronger DITCZ bias. Another well-known bias in the models is the drier equator across the Pacific Ocean that is usually caused by an overly narrow and strong cold tongue combined with excessively strong trade winds (Zhang et al. 2013; Grose et al. 2014). The South Pacific Convergence Zone (SPCZ) is another feature that is difficult for models to simulate well. Similar to the ITCZ, the SPCZ is a band of precipitation formed by low-level wind convergence, located over the western-to-central South Pacific (e.g. Trenberth 1976; Vincent 1994). The SPCZ biases in the GCMs are relatively less studied. In the CMIP5 models, the SPCZ tends to be overly zonal without significant improvement from the precursor models in CMIP3 (Brown J. R. 2013; Gros et al. 2014). Brown J. R. (2013) points out that the SPCZ orientation bias in the CMIP5 models might be related to the absence of ocean heat flux-adjustment. Additionally, the DITCZ, the dry equator, and the SPCZ biases in the model precipitation mean states, in addition to influencing ENSO-related precipitation, but can also be affected by the changes in the air-sea interaction during ENSO (Watanabe et al. 2010; Sun et al., 2014).

To reduce these biases of ENSO-related precipitation mean state and associated precipitation climatology in current GCMs, it is very important to validate the models with observed datasets, especially those covering a long-term period (Räisänen 2007). Long-term datasets contain more ENSO events than the shorter-term ones that only cover the past few decades. Since each ENSO event is different from the others, a larger sample of ENSO events tends to produce more reliable typical ENSO mean states for both observations and model outputs. Particularly in recent decades, the central Pacific variety of El Niño tends to occur more frequently (Kug et al., 2009) than the canonical eastern Pacific type; however the ability of CMIP5 models to simulate the two types of El Niño varies widely (Yeh et al., 2014). Comparing the models with long-term observations instead of short-term ones would minimize sampling biases in the characterization of typical ENSO mean states.

Over the last few years, better global precipitation datasets that cover the entire 20th century have become available, including the 20th Century Reanalysis from NOAA (Compo et al. 2011) and Reconstructed Precipitation (Smith et al. 2012) as introduced in Chapter 2. It is very useful to compare the CMIP5 models with these datasets along with SST reanalyses (ERSST v3b and HadISST 1.1, see Chapter 2) for the past century to further improve understanding of the precipitation climatology and ENSO-related precipitation in these models. In this paper, the 30 CMIP5 models introduced in Chapter 2 will be compared to 20CR and REC with respect to the precipitation climatology and ENSO-related precipitation mean states. We will identify the features that need to be improved in the models and show the spatial influences of the precipitation climatology on the ENSO-related precipitation in the

observations and the CMIP5 models in order to explain some of the spatial dissimilarities.

This chapter is organized as follows. Section 3.2 introduces methods used in this study. An overview of precipitation climatologies in recent precipitation reanalyses and observations will be presented in Section 3.3 to evaluate 20CR and REC in comparison with the other reanalyses/observations during the satellite era. The CMIP5 models will be compared with 20CR and REC, in terms of the annually and seasonally (e.g. December-January-February and June-July-August) averaged precipitation climatology over the 20th century in Section 3.4, and the performance of each CMIP5 model will be assessed, with particular attention to identifying the crucial biases in the models. In Section 3.5, an Empirical Orthogonal Function analysis of annually and seasonally averaged ENSO precipitation anomalies will be used to provide a general idea of the mean ENSO-related precipitation patterns in the 20th century, as well as to evaluate the performance of CMIP5 models in simulating ENSO precipitation anomaly patterns. In Section 3.6, composites of ENSO-related precipitation anomalies will exhibit spatial dissimilarities between the CMIP5 models and REC/20CR, and to analyze the differences between the better and worse performing models in simulating the amplitude and the seasonality of El Niño/La Niña-like precipitation. Potential connections from the model biases of precipitation climatology and ENSO-related SST variability to ENSO-related precipitation biases will be discussed in Section 3.7. Section 3.8 will summarize the major findings of the chapter.

3.2 Methodology

Empirical Orthogonal Function (EOF, Lorenz 1956) analysis and ENSO composites are used to extract ENSO-related precipitation signals from the observations and the CMIP5 models. EOF analysis is a widely used statistical tool in climate science. This method can extract from a large dataset an optimal set of orthogonal patterns (e.g. space and time) that capture the largest variances in the original data. In this study, the EOF analysis computes the modes of eigenvalues and eigenvectors from the original spatially weighted anomaly covariance matrix of the annually or seasonally averaged precipitation fields, with the background trend and other low frequencies being removed by a 15-year high pass filter. The eigenvalues measure the percentage of the total variance explained by each EOF mode. Without the mean seasonal cycle and the long-term trend, the first few EOF modes can be expected to exhibit the majority of the ENSO signals (e.g. Xie and Arkin, 1997; Dai 2000). Although the EOF method does have limitations (e.g. physical normal modes are not generally orthogonal; Simmons et al. 1983), it is computationally efficient and sufficient to identify the mean ENSO-related structures in the observations and the CMIP5 models.

The method of ENSO composites permits the separation of the El Niño and La Niña-related precipitation, unlike the combined ENSO signals derived using the EOF methods. To calculate the ENSO precipitation composites, we use an ENSO time series from the first EOF mode of SST anomalies during 1901-2005 rather than the conventional ENSO indexes (e.g. Niño 3.4 index) since the CMIP5 models may not exhibit maximal air-sea interaction over the same spatial regions used for these

indexes. An El Niño/La Niña precipitation composite is defined by averaging precipitation anomalies during the El Niño (top quartile of the ENSO time series) or La Niña years (bottom quartile of the ENSO time series).

The ENSO-related precipitation index created by Curtis and Adler (2000) is also utilized in this study to quantitatively compare the ENSO-related precipitation composite results. This index is generated by using a 10° latitude × 50° longitude block constrained to move within two gridded boxes separately, a Maritime Continent (MC, 10°N-10°S, 90-150 °E) box and a central-eastern Pacific (P, 10°N-10°S, 160-100 °W) one. The El Niño-related precipitation index (EI) is defined by the maximum of the block average of the P box minus the minimum of the block average in the MC box. The La Niña-related precipitation index (LI) is created from the maximum of the averaged block in the MC box minus the minimum of the averaged block in the P box. ENSO-related precipitation index is defined by EI minus LI.

Before applying these methods, all data have been interpolated to a 2.5° × 2.5° grid. The period used in this study is 1901-2005, and anomalies are calculated relative to this entire period.

3.3 Precipitation Climatology During Satellite Era

This section compares the annual-averaged precipitation climatology during the period of 1998-2005 among the precipitation products from the most recent atmospheric reanalyses (20CR, ERA-Interim, MERRA-2 and CFSR), REC and TRMM 3B43 satellite-retrieved precipitation. Fig. 3.1 exhibits the annually averaged precipitation climatology of these six datasets over the domain 48.75°S-48.75°N (Fig. 3.1a) and the differences between TRMM and the other five datasets (Fig. 3.1b). REC

resembles TRMM the most, with a pattern correlation coefficient r of 0.96. This high correlation is to be expected because REC uses the TRMM dataset as a base climatology. The ERA-Interim outperforms the other reanalyses (r~0.92), followed by CFSR (r~0.91). 20CR (r~0.87) and MERRA-2 (r~0.77) are the two reanalyses least resembling TRMM.

Generally, REC and TRMM show less rainfall over the Tropics than the four reanalyses (Fig. 3.1a&b). The region in which the six datasets disagree most is the western tropical Pacific where the ITCZ and the SPCZ meet. Usually the largest rainfall and maximum convection (Rouge et al. 2013) occur in this region. Compared with TRMM, each of the five reconstructed/reanalysis datasets exhibits its own characteristics in the precipitation pattern over this region: 1) REC shows the weakest precipitation among all the datasets; 2) the ITCZ and the SPCZ maximum centers in 20CR are located more eastward (~165°E) than in the other datasets (~150°E); 3) ERA-Interim has slightly stronger rainfall maxima than are found in TRMM; 4) MERRA-2 has the most robust maximum center of the SPCZ; and 5) CFSR exhibits a drier equator over the western-central Pacific and its ITCZ maximum center is separated from the SPCZ one.

Considering the ITCZ over the central and eastern Pacific: ERA-Interim and CFSR show stronger ITCZ-related precipitation (>1-3mm/day, see Fig. 3.1b) than TRMM, while the ITCZs of REC, 20CR and MERRA-2 are weaker. There is diversity of precipitation patterns between TRMM and the other five datasets over other regions, including the tropical Indian Ocean, the tropical Atlantic Ocean, Central Africa and northern South America. Some of the negative departures can be

as much as -3 mm/day and positive differences can be larger than 4mm/day (Fig. 3.1b). In particular, the four reanalyses tend to show greater precipitation than TRMM over Central America and the Southeast Asian monsoon region.

Overall, the annually averaged precipitation pattern of REC during 1998-2005 is more similar to those of the reanalyses with finer resolution (ERA-Interim, MERRA-2 and CFSR) and TRMM (mean spatial correlation coefficient r~0.90) than to the coarser resolution 20CR (r~0.85). The precipitation differences among the six datasets over the majority of the tropical region are larger than 0.5 mm/day (Fig. 3.1b). The uncertainty of the precipitation pattern increases as the precipitation amount increases.

3.4 Precipitation Climatology During the 20th Century

In this and the following sections, we use REC and 20CR during 1901-2005 as observations and compare them to the CMIP5 models. The annually averaged precipitation climatologies of REC, 20CR and the mean of the 30 CMIP5 models are exhibited in Fig. 3.2, together with the difference maps among them. The spatial correlation coefficient between the annually averaged climatology of REC and 20CR is 0.87. Seasonally averaged results between REC and 20CR are also highly correlated, with coefficients of 0.84 (MAM), 0.87 (JJA), 0.89 (SON) and 0.89 (DJF).

Despite the high spatial correlations, there are some pronounced spatial differences between REC and 20CR, especially over the tropical western-central Pacific where REC can be as much as 3-4 mm/day less than in 20CR. Based on the analysis of the previous section, these large precipitation differences are the result of

the drier ITCZ/SPCZ centers in REC and the more eastward located ITCZ/SPCZ centers in 20CR. Moreover, these differences are also seasonally consistent. Fig. 3.3 shows the seasonal cycle of the zonally-averaged (150°E - 90°W) meridional distribution of precipitation over the tropical Pacific. The rainfall both north and south of the equator in 20CR is heavier than REC throughout the 12 months. In general, REC is drier than 20CR over the global ocean by an ocean-averaged 0.50mm/day (annual), 0.60mm/day (JJA) and 0.46mm/day (DJF). The ocean regions where REC is more robust than 20CR are the southern edge of the Pacific ITCZ, the western part of the Indo-Pacific warm pool, the eastern Atlantic ITCZ region, the southern edge of the SPCZ, the northern Pacific subtropics, and the storm tracks in both the Northern and the Southern Hemispheres. Over land, REC exhibits more rainfall over tropical South America, Northern Australia, Central Africa, the Mediterranean region and Eastern Europe, while 20CR has more over North America, the middle part of South America as well as the Indian monsoon region.

The 30 CMIP5 models have spatial pattern correlation coefficients with the two observation datasets that range from 0.59 to 0.87 (Table 3.1) in the annually and seasonally averaged climatology. The mean of these correlation coefficients is 0.76. The annually averaged coefficients are the highest (~0.79), and DJF (~0.77) and SON (~0.78) exhibit higher correlations than JJA (~0.75) and MAM (~0.72). The annually averaged precipitation climatology of the multi-model mean (Fig. 3.2) exhibits the largest disagreements with the observations over the tropical Pacific and Atlantic Ocean, where the models tend to have the DITCZ, the dry Pacific equator, and an overly zonal SPCZ that is connected with the southern part of the DITCZ. The

CMIP5 seasonal climatologies over the topical Pacific (Fig. 3.4) also confirm that the northern Pacific ITCZs and the averaged precipitation over the southern tropical Pacific are consistently stronger in most of the models throughout the seasons than in the observations, in combination with overly dry equators. The seasonal precipitation climatology maps of the CMIP5 models (not shown) indicate that, instead of showing the DITCZ during MAM, when it is actually present in observations (Zhang 2001), most of the models have the DITCZ pattern in other seasons, especially DJF. In terms of the southern branch of the DITCZ over the eastern Pacific, the largest bias of the models from the observations is found in MAM, and in some models, this southern branch becomes so strong that its northern counterpart even disappears (e.g. MIROC5 and CCSM4). The bias of the northern branch of the DITCZ in models is largest in SON. Fig. 3.4 and Table 3.1 indicate that models exhibiting the most severe DITCZ problems (e.g. GISS-E2-H and GISS-E2-H-CC) and the ones with wide and seasonally consistent dry equators (e.g. CSIRO-Mk3-6-0 and MPI-ESM-P) are among those models that have lowest correlations with both observations. Contrarily, the models showing the smallest biases of the DITCZ or the dry equators, for example, model CESM1-BGC and CCSM4, tend to correlate better with the observations.

Besides the DITCZ, SPCZ and dry equator problem, Fig. 3.2 shows that the CMIP5 models also often exhibit overestimated precipitation over the tropical Atlantic and Indian Ocean, the Maritime Continent, the northern Pacific subtropical high region, central and southern Africa and Australia, as well as underestimated rainfall over the northern extra-tropical storm track region, central America and

tropical South America and the central United States. Previous studies suggest that the theories for the GCM-based overestimated precipitation over the tropical Atlantic and Indian Ocean are similar to those of the Pacific DITCZ. For example, the simulation of large-scale circulations tends to be biased over these regions leading to unrealistic magnitude and location of regional convection and precipitation. Poor parameterizations and over-sensitivity of atmosphere-ocean coupling and feedbacks further aggravate the biases of circulations (e.g. Bollasina et al. 2011).

3.5 Mean States of ENSO-related Precipitation

This section presents the annually and seasonally averaged ENSO-related precipitation anomaly mean states and the precipitation climatology for the period of 1901-2005 in both the observations and the CMIP5 models. The ENSO-related precipitation anomalies and their time series in this section refer to the spatial pattern and the time series of the first EOF mode calculated from 15-year high-pass filtered annually or seasonally averaged precipitation anomalies.

3.5.1 Annually-averaged Precipitation Anomaly EOF Results

a. REC and 20CR

Fig. 3.5a exhibits the ENSO-related precipitation of the 20CR and the REC annually averaged precipitation anomalies. The annually averaged precipitation climatologies are also shown in Fig. 3.5a as contours to facilitate comparison with the ENSO-related precipitation anomalies. The time series of the first EOF modes of the observations are highly correlated (r~0.90) with the annually averaged Niño 3.4 index

(downloaded from https://www.esrl.noaa.gov/psd/gcos_wgsp/Timeseries/Data/nino34.long.data), which confirms that the first EOF mode captures the majority of the signals of the annually averaged ENSO-related precipitation mean states in these two datasets. The spatial patterns of 20CR and REC strongly resemble each other with a pattern correlation coefficient of 0.89. As with ENSO-related precipitation anomaly patterns found in previous studies (Ropelewski and Halpert 1987; Xie and Arkin 1997; Dai et al. 2000), positive anomalies in these two datasets are shown over the eastern and central tropical Pacific Ocean as a result of the SPCZ and the ITCZ moving toward the equator and merging together during El Niño (Vincent et al. 2011; Widlansky et al. 2012). The maximum positive anomalies in both the REC and 20CR are located around 180°E. Negative precipitation anomalies exhibit a horseshoe pattern with a maximum center over the Maritime Continent and spreading out poleward and eastward in both hemispheres from there. Despite the fact that these patterns resemble each other in these large-scale features, differences in spatial detail exist. In the western Pacific region, REC has a larger maximum positive anomaly center over 180°E and a larger negative center over the Maritime Continent, as well as more robust ENSO-related rainfall over the Indian Ocean at 10°S, the northeastern Atlantic Ocean, and Eastern Europe/West Asia. Over the eastern Pacific, REC exhibits dry anomalies over the off-equator regions in both Northern and Southern Hemispheres, while the 20CR precipitation is less symmetric about the equator, with larger negative anomalies over the northern ITCZ region and more positive ones over its counterpart in the Southern Hemisphere. In addition to the spatial differences, the variance

explained by the first EOF mode of the annually averaged REC anomalies is 88.93% of the total variance, which is four times larger than the 20CR one (22.04%). One explanation for this difference is that the annual first guess field of the REC was generated using a limited number (~10) of the EOF modes of the annually averaged GPCP (Smith et al. 2012), filtering out the remainder of the total variance. Thus, the variance explained by the ENSO-related mode appears to be larger in the REC, especially in this annually averaged result. On average, REC includes around 70% of the total explained variance of 20CR.

In the second EOF mode (Fig. 3.5b), the time series of both observations show significantly larger positive anomalies in years 1973, 1983, and 1998. Those years are all the concluding years of strong El Niño episodes (1972-73, 1982-83 and 1997-98; Wolter et al. 1998). This suggests that the second EOF mode is related to the decaying El Niño phase of ENSO. The spatial fields of the second mode in both observations exhibit positive anomalies over the tropical central-eastern Pacific Ocean, the eastern part of the Indian Ocean, and the Maritime Continent. Negative anomalies exist over the tropical western-central Pacific in both hemispheres. There are also spatial differences between the two observations. For instance, positive precipitation anomalies in 20CR are larger over the tropical central Pacific Ocean, the northern and tropical Atlantic Ocean, the eastern Indian Ocean, and Eastern Europe. 20CR also has drier anomalies over the tropical northwestern Pacific. Over the eastern Pacific, the negative (positive) anomalies in 20CR over the northern (southern) off-equatorial region, similar to those in the first mode, are larger than those in REC. This may suggest some background difference between the dynamical

20CR model and the statistical REC model in the precipitation anomalies over the tropical eastern Pacific.

b. CMIP5 Models

The spatial correlation coefficients of the first EOF modes between the 30 CMIP5 models and the observations are shown in Table 3.2. The average of these correlation coefficients is about 0.58. The CMIP5 models that are highly/poorly pattern-correlated with the observations in their precipitation climatology (Table 3.1) also have similar performances in Table 3.2. Therefore, based on Table 3.1 & 3.2, we build two CMIP5 groups. Group 1 is the CMIP5 group with the 11 best models in simulating precipitation climatology and ENSO-related precipitation mean states, including the models CanESM2, CCSM4, CESM1-BGC, CESM1-CAM5, CESM1-FASTCHEM, CMCC-CM, CMCC-CMS, CNRM-CM5, GFDL-ESM2M, GISS-E2-R and NorESM1-ME. Group 2 contains the 11 worst performing models: CSIRO-Mk3-6-0, GFDL-ESM2G, GISS-E2-H, GISS-E2-H-CC, HadCM3, inmcm4, IPSL-CM5A-LR, IPSL-CM5A-MR, MPI-ESM-LR, MPI-ESM-P and MRI-CGCM3.

Fig. 3.6 exhibit the CMIP5 group 1 and group 2 first and second EOF spatial results of annual-averaged precipitation anomalies. Both groups have ENSO-like anomaly patterns over the tropical Pacific Ocean in their first EOF mode (colors of Fig. 3.6, upper panel), with group 1 much more similar to the observations ($r\sim0.7$) than group 2 ($r\sim 0.43$). Other ENSO-related precipitation features are also captured by both groups, such as the positive anomalies over the northeast Pacific through northern Atlantic Ocean due to the southward shift of the storm track during El Niño,

as well as the positive ones over the western Indian Ocean and negative anomalies over the eastern tropical Indian Ocean and northern South America. However, the detailed spatial patterns of the two CMIP5 groups differ quite substantially from each other and from many aspects of the observations. The positive anomaly centers over the equatorial Pacific in both groups appear to be larger in both magnitude and area than those in the observations, despite part of the ENSO precipitation signal being filtered out by averaging the model ensemble members. The positive anomaly maximum center in group 1 is located around 180°E, similar to those in the observations, while the one in the group 2 is located 30° more westward (~150°E). The positive anomalies over the central Pacific Ocean, the negative anomalies over the tropics, and the storm tracks over the extratropics all appear very zonal in both groups, showing more "Hadley-like" patterns than the "Walker-like" ones in the observations (Nigam et al. 2000).

In each of the CMIP5 groups, the precipitation climatology is strongly related to the details of the ENSO-related precipitation anomalies. As Fig. 3.6 shows, group 2 has more severe DITCZ and SPCZ biases than group 1, along with a dry equator across the Pacific basin. This dry equator in group 2 separates the ITCZ and the SPCZ and the merging region of the two rainfall bands is located more westward than in both group 1 and the observations. In association with these precipitation climatology biases, group 2 exhibits much more obvious ENSO-related biases of excessive precipitation over the southern off-equator in the eastern Pacific, precipitation deficiency over the Pacific equator and the westward-extended maximum anomaly center in its first EOF spatial pattern, compared with group 1. In general, the

precipitation climatology (contours in Fig. 3.6, upper panel) confines the shape of the ENSO-related precipitation pattern (colors in Fig. 3.6, upper panel) more in the models than in the observations (Fig. 3.5a), which indicates that the precipitation background in the models might have large impact on its ENSO-related precipitation spatial patterns (e.g. Ham and Kug 2011, 2014).

In the second EOF mode (Fig. 3.6, lower panel), both groups exhibit positive anomalies over the central-eastern Pacific and the Maritime Continent that are similar to the observations. The spatial pattern of group 1 is especially similar to the one of 20CR (r~0.71), while the group 2 pattern is more zonal and "Hadley-like" (Nigam et al. 2000) with the positive anomalies over the central-eastern Pacific extending too far west and merging with those over the Maritime Continent.

Overall, both of the CMIP5 groups, especially group 1, demonstrate that the models have the capability to simulate similar mean state features of the ENSO-like precipitation anomalies as in REC and 20CR, although detailed patterns are different.

3.5.2 Seasonally-averaged Precipitation Anomaly EOF Results

a. REC and 20CR

Spatial patterns of seasonally averaged ENSO-related precipitation are intercompared among the CMIP5 models and the observations in this section. Two solstice seasons, DJF and JJA, are chosen to represent the seasons with the most (DJF) and least (JJA) robust ENSO features, as the peak phase of ENSO generally occurs in boreal winter (e.g. Rasmusson and Carpenter 1982; Trenberth 1997). The first EOF spatial patterns of DJF-averaged precipitation anomalies in REC and 20CR

(Fig. 3.7b) are more similar to each other (pattern correlation coefficient r equals to 0.89) than the JJA-averaged ones (Fig. 3.7a, r~0.87). There are numerous pattern differences in the JJA-averaged ENSO-related precipitation results between the two observation datasets (Fig. 3.7a). For example, the maximum positive anomaly center in REC remains located at 180° in JJA, while in 20CR it shifts to the east of 180° by about 15°. The ENSO-related precipitation over the Indian monsoon region in 20CR is more robust than in REC and connects with the positive precipitation anomalies over the tropical western Pacific, which might be due to the fact that the boreal summer Indian monsoon is much stronger in 20CR than in REC (see the contour of 6 mm/day in Fig. 3.7a). Another major difference is that the positive anomalies over the equatorial central Pacific in 20CR are separate from the SPCZ-related ones over the southeastern Pacific, unlike the connected anomalies in the REC. In addition, 20CR exhibits larger positive anomalies than REC in the north of the ITCZ in the eastern Pacific.

The DJF-averaged ENSO-related precipitation results (Fig. 3.7b) show very robust positive anomaly centers over the tropical Pacific in REC and 20CR. 20CR exhibits more ENSO-related precipitation beyond the southeastern edge of the positive anomaly maximum center than in REC. This difference might be related to the fact that both the ITCZ and the SPCZ (contour of 6 mm/day in Fig. 3.7b) over the central-eastern Pacific in 20CR are more toward the equator than in REC, and when they merge together during the DJF El Niño events (Meehl 1987; Vincent 1994), larger positive anomalies accumulate over the tropical southeastern Pacific. The drier anomalies over the north of the eastern Pacific ITCZ in 20CR than in REC can also

be found in the DJF results, suggesting that these differences are associated with fundamental disagreements between the two datasets.

The time series of the first EOF modes of the two observations correlate better with each other in DJF (r~0.86) than JJA (r~0.78). In DJF, REC exhibits larger variance in the second half of the 20th century, while 20CR dose not show such changes in its first EOF time series but does in its second EOF mode (not shown). Our preliminary study suggests that this difference may reside in the power (period of 1-15 year) of the time series of the first two EOF modes combined. The wavelet power spectrums of these time series (not shown) exhibit power increases in the second half of the last century in both observations. However, this power of the 1-15 year period in the REC is about 4 times larger than the 20CR one. Therefore, the increasing variability of the 20CR EOF time series may not be large enough to be shown in its first EOF mode, but in the second EOF mode instead.

b. CMIP5 Models

The spatial patterns of the first JJA-averaged EOF mode in the two CMIP5 groups (Fig. 3.8, upper panel) are more similar to those of 20CR than REC, with the positive anomaly center over the equatorial Pacific being separated from the southeastern extra-tropical one by negative anomalies. Over the western Pacific, as in 20CR, the maximum positive anomaly center in the CMIP5 models also connects with the positive anomalies associated with the Indian Monsoon. The differences between the two groups are the same as in the annually averaged results: the JJA maximum positive anomaly center of group 1 is located at 180°E, while that of group

2 is at 150°E; group 2 exhibits the DITCZ- and dry equator-like biases in the JJA-averaged ENSO-like precipitation, even though these biases are less severe than in the annually averaged figures (Fig. 3.6, upper panel).

The first EOF spatial patterns of the DJF-averaged CMIP5 precipitation anomalies, as Table 3.2 shows, are generally better correlated (multi-model ensemble mean of pattern correlation coefficients r~0.58) with the observations than are the JJA-averaged patterns (r~0.51). As in the observations, the maximum anomaly centers in DJF (Fig. 3.8, lower panel) are stronger than in JJA and in the annually averaged results. The models also capture features such as the storm-track-related extratropical positive anomalies in the Northern Hemisphere. However, the positive anomaly patterns in the tropical Pacific in the models are meridionally narrower and more westward extended than those in the observations. In CMIP5 group 1, the positive anomalies reach the western boundaries of the Pacific basin and separate the actual negative anomaly center over the Maritime Continent into two centers, one over the Philippines and the other east of Australia. The negative anomalies also extend zonally along the northern and southern boundaries of the positive anomalies over the tropical Pacific, forming a "Hadley-like" pattern rather than the "Walker-like" ones in the observations. For group 2, the biases such as the locations of the maximum anomaly centers and the deficiency of equatorial ENSO-like precipitation continue to be exhibited in the DJF results. Both groups have excessive ENSO-like precipitation over the southern off-equator in the central-eastern Pacific.

3.6 El Niño and La Niña Composites

El Niño/La Niña composites are used in this section to examine separately the details of El Niño- and La Niña-related precipitation. The spatial patterns of the ENSO (El Niño minus La Niña) composite precipitation anomalies in the observations and the models correlate very well (correlation coefficients r ~ 0.9) with their own first EOF mode spatial patterns for all the annual, JJA, and DJF results.

A typical magnitude for the El Niño-related precipitation maximum positive anomaly center in the REC over the tropical Pacific Ocean is about 2 - 3 mm/day, as Fig. 3.9 shows, and the maximum negative anomaly center over the Maritime Continent is about -2 to -1 mm/day. Fig. 3.9 also shows the differences of 20CR from REC in the annually, JJA-, and DJF-averaged El Niño precipitation composite results. In the annually averaged result, 20CR is drier east of the Maritime Continent and is wetter in the central-eastern equatorial Pacific by 0.25 - 1mm/day, due to its slightly more eastward-located maximum anomaly center. 20CR also has more El Niño-related precipitation over the Maritime Continent. The La Niña composites and comparison results (not shown) are in the opposite sense, with slight differences. In JJA, the maximum positive anomaly center in REC over the tropical Pacific slightly shrinks, while the negative anomaly center over the Maritime Continent expands. 20CR exhibits more (less) ITCZ-related precipitation in the eastern Pacific and more (less) rainfall over Southeast Asia in its JJA El Niño (La Niña) results. In DJF, 20CR has more (less) precipitation over the central Pacific Ocean and less (more) over the western Pacific during El Niño (La Niña) events, which indicates that 20CR has stronger DJF El Niño- (La Niña-) related precipitation (droughts) than REC.

In order to show the most common biases among the 30 CMIP5 models from the observations regarding the El Niño precipitation composite results, the numbers of the models that agreed on the same sign (positive or negative) of the El Niño-related precipitation biases from the observations are shown for each grid in Fig. 3.10. The La Niña-related results (not shown) are almost opposite to the El Niño ones. Compared with both of REC and 20CR, most of the 30 models have positive biases (less robust El Niño-like droughts) in the observed "horse-shoe"-like dry anomaly region over the western-central Pacific, but larger negative anomalies (less robust El Niño-like precipitation) in the observed SPCZ-related positive anomaly region over the southern Pacific. These biases could be related to the more westward-located positive precipitation anomaly centers in the models than in the observations. In addition to these biases, the models exhibit larger El Niño-like precipitation in the western Indian Ocean, eastern North America and the Southern Hemisphere storm tracks regions, less rainfall at the northern edge of the positive anomaly center in the central-eastern Pacific, East Asia, the west of Australia, and southern South America. The model underestimation of the drought anomalies in the western Pacific and precipitation anomalies in the SPCZ region and in the west of Australia, as well as the overestimation of the precipitation anomalies in the western Indian Ocean are all seasonally consistent.

Both CMIP5 groups show the same biases as above in their own model agreement maps (Fig. 3.10b), although the areas of the biases are generally smaller in group 1 than group 2. Group 2 particularly exhibits a seasonally consistent negative bias in the equatorial Pacific. Note that the DITCZ-like model bias in the eastern

Pacific is more obvious when comparing with REC (Fig. 3.10b, left panel) than 20CR (Fig. 3.10b, right panel). This indicates that this DITCZ-like bias may be sensitive to the number of reference datasets.

To further quantitatively compare the El Niño- and La Niña-related precipitation signals in the observations and the models, the El Niño and La Niña precipitation indexes introduced by Curtis and Adler (2000) are used on the El Niño- and La Niña-related precipitation composite results. The monthly-averaged El Niño and La Niña precipitation indexes (Fig. 3.11a) show that the majority of CMIP5 models have weaker El Niño- and La Niña-related precipitation signals than the two observations. This may be due to the fact that the models' maximum positive (negative) anomaly centers in the El Niño- (La Niña-) like patterns are located more westward than in the observations, and therefore can be out of the Pacific box defined by Curtis and Adler (2000). Meanwhile, the negative (positive) El Niño- (La Niña-) related anomalies over the Maritime Continent are generally too weak in the models. As a result, the El Niño and La Niña precipitation index (see their definition in Section 2) values in most of the CMIP5 models are smaller compared with the observational ones, especially the group 2 models that have more severe dry equator bias. Those more biased models also exhibit less seasonal variability of the ENSO-like precipitation, despite the fact that most of them show larger El Niño or La Niña precipitation indexes in DJF, similar to the observations. Fig. 3.11b further indicates that the magnitudes and seasonal variability of both the El Niño and La Niña precipitation indexes in group 2 are much smaller than those of group 1 and the observations. Group 1 has the mean value (2.8 mm/day for El Niño) and the seasonal

variability (range between maximum and minimum of 2.3 mm/day for El Niño,) that are similar to the two observations in both El Niño and La Niña phases, while group 2 has a much smaller mean value (1.1 mm/day for El Niño) and seasonal range (range of 0.6 mm/day for El Niño). The differences between El Niño and La Niña phases (known as the ENSO nonlinearity) are also smaller in group 2 than group 1.

Additionally, Fig. 3.11c shows the normalized El Niño and La Niña precipitation indexes by removing the influence of the corresponding El Niño- and La Niña-related SST. The normalized indexes are calculated using the El Niño/La Niña precipitation indexes divided by the El Niño- (La Niña-) related SST variance, which is defined as the standard deviation of the positive (negative) values of the SST's first EOF time series. The seasonal variability of the normalized El Niño precipitation indexes is identical to the original one (Fig. 3.11b) for both group 1 and 2. The normalized La Niña-related seasonal variability is also very similar to the original one; however, the mean values of group 1 are clearly smaller than those from the observations after the normalization, especially in DJF. Therefore, it is possible that the ENSO-related SST variability exerts larger influence on the DJF La Niña-related precipitation extremes than the El Niño ones.

3.7 Discussion

The aforementioned results indicate that the ENSO-related precipitation anomaly biases in the CMIP5 models are related to the precipitation climatology biases. In this section, detailed connections between these two kinds of biases are further discussed. Fig. 3.12 shows the CMIP5 models' agreement maps of the same

sign (either positive or negative) shared by the model biases of the annual-averaged precipitation climatology and the biases of the annual-averaged El Niño-related precipitation from REC (Fig.3.12, left panel) and 20CR (Fig.3.12, right panel). The Maritime Continent and the western Indian Ocean (Fig. 3.12 a&b) are the two areas where the connections between the positive precipitation climatology bias and the positive El Niño-related precipitation bias are highly consistent among the 30 CMIP5 models compared to both observations. Additionally, the connection between the negative model bias of the SPCZ and the related negative bias of the El Niño-related precipitation in the central-southern Pacific is highly agreed among the 30 models.

The group 2 models show high agreement (Fig. 3.12b, lower panel) on the relation between the dry equator bias and the bias of the El Niño-related negative precipitation anomalies in the equatorial Pacific, indicating that the deficiency of the group 2 equatorial ENSO-like precipitation is strongly related to the dry equator in its precipitation mean state. The influence of the DITCZ bias on the DITCZ-like precipitation anomalies is consistent among the models when compared to REC, but such effect is not as clear in the agreement map with 20CR. This difference further emphasizes the importance of comparing the CMIP5 models with more observational datasets in order to identify detailed biases in the models.

Due to the strong connection between ENSO-related SST and precipitation (e.g. Trenberth et al. 1998), it is possible that these ENSO-related precipitation anomaly biases are also associated with the ENSO-related SST variability. Singular value decomposition (SVD) analysis (Bretherton et al. 1992) is used for both observations and the CMIP5 models to search for coupled patterns of ENSO-related

precipitation and SST that are co-varying in time. Fig. 3.13 exhibits the first SVD mode (the ENSO mode) with homogeneous correlation (temporal correlations between the normalized SST field and the SST time series of the first SVD mode) maps for SST and heterogeneous correlation ones (temporal correlations between the normalized precipitation field and the SST time series of the first SVD mode) for precipitation. In the observational SVD results (Fig. 3.13a), the SST reanalysis ERSST v3b (HadISST) is paired with REC (20CR). The SST time series of the first SVD mode is highly correlated with the precipitation time series in both REC (r~0.93) and 20CR (r~0.98). In addition, the homogeneously correlated ERSST field strongly resembles that of the HadISST. For the heterogeneous precipitation correlation results, however, the correlations between the normalized REC field and the ERSST first SVD time series are generally much higher at most grid points than the 20CR and HadISST correlated ones. This can be explained by the fact that the annual first guess field of REC is reconstructed based on the leading covariances of ERSST. The same reasoning explains the larger variance associated with the first SVD mode of the REC and the ERSST (79.57%) compared to 20CR and HadISST (46.13%).

For the CMIP5 SVD results (Fig. 3.13b), both CMIP5 groups exhibit the ability to simulate ENSO-like SST and precipitation correlated structures. However, the group 2 models have patterns less similar to those in the observations than the group 1 ones. For example, the group 2 positive SST correlation pattern in the Pacific is more westward extended and meridionally narrower, and everywhere else the correlations are smaller than in group 1. Both groups show a cold tongue-like feature

(the region in the tropical Pacific where SSTs are less than 26°C) in the eastern equatorial Pacific that is more prominent than the observations, with this bias in group 2 more prominent than in group 1.

Corresponding to the meridionally narrow and westward-extended ENSO-like SST patterns in the models, especially in group 2, the positive ENSO-like precipitation patterns in the tropical Pacific in the models are also narrower and more westward-extended than the observations. In addition, both groups exhibit relatively high correlation ($r>0.5$) between the ENSO-related SST variability and the excessive ENSO-related precipitation at the southern off-equator in the eastern Pacific, suggesting that this bias is more related to the ENSO variability rather than the bias in the precipitation climatology. In the group 2 models, the low correlation in the central-eastern equatorial Pacific between the precipitation anomalies and the ENSO-related SST variability indicate that the negative bias of equatorial ENSO-related precipitation in these models is more associated with the dry equator bias in the precipitation mean state than the variability of ENSO-related SST. Our preliminary research indicates that the group 2 models tend to simulate a much more robust cold tongue-like feature that extends from the eastern to the central Pacific and is less sensitive to seasonal and interannual changes in their SST climatology (not shown) compared to the models in group 1. This cold tongue bias in these models could lead to a severe dry equator bias in the precipitation climatology (Zhang et al. 2013; Grose et al. 2014), which then worsens the equatorial deficiency of the ENSO-related precipitation.

3.8 Summary

In this chapter, the two long-term precipitation datasets, REC and 20CR, are used as the observations to provide guidance for the CMIP5 models' simulations of the precipitation climatology and the ENSO-related precipitation. We have intercompared the spatial patterns of the precipitation climatology, the precipitation EOF results, and the ENSO precipitation composites among 20CR, REC and the 30 CMIP5 models during the 20th century. The following results have been found:

- REC resembles the TRMM precipitation and the three reanalyses with high resolution (ERA-Interim, MERRA-2 and CFSR) better than 20CR in the spatial pattern of the annually-averaged precipitation climatology for the period of 1998-2005. The differences of the precipitation rate among these six datasets are larger than 0.5 mm/day over the majority of the tropical region, especially the maximum centers of the ITCZ and the SPCZ where the rainfall is heaviest.
- REC is drier than 20CR by an average of 0.5 mm/day over the ocean. The 30 CMIP5 models all have relatively good spatial correlation with the two observations, but biases such as the dry equator, the DITCZ in the eastern tropical Pacific, and an overly zonal SPCZ are more obvious in some models than the others. Overall, the DITCZ bias in the models is most severe in DJF, which is also related to the strong and eastward-extended SPCZ. The dry equator bias is more seasonally consistent.
- The spatial fields of the ENSO-related precipitation in REC and 20CR resemble each other. Although the 30 CMIP5 models have statistically

meaningful spatial correlations with REC and 20CR in their ENSO-like precipitation results, the models exhibit some common biases. For example, the ENSO-like precipitation features over the tropical Pacific Ocean in the models extend too far west and are meridionally narrower than in the observations, exhibiting a more "Hadley-like" than "Walker-like" pattern. Also, most models tend to simulate more robust dry anomalies in the observed "horseshoe"-like negative anomaly region in the western Pacific, but more ENSO-related rainfall in the central to eastern Pacific, especially in the SPCZ region.

- Two groups of the CMIP5 models are defined based on their higher (lower) spatial correlations with the observations in the precipitation climatology and the ENSO-related precipitation. The better performing group (group 1) simulates spatial patterns, the mean magnitude and the seasonal variability of ENSO-related precipitation, as well as the SST and precipitation correlation structures produced from the SVD analysis, that are more realistic than the underperforming group (group 2). The group 2 models are the ones with the most severe dry equator biases in their precipitation climatology. They tend to show more obvious biases of deficiency in their equatorial ENSO-related precipitation.
- The ENSO-related precipitation bias of the deficiency at the equatorial Pacific is strongly related to the underestimated precipitation climatology in this region. The ENSO-related SST variability also exerts influences on the ENSO-related precipitation. For example, the ENSO-related SST variability

may affect the DJF La Niña-related precipitation extremes more than the El Niño ones. The meridional width and zonal length of the ENSO-related positive precipitation anomaly pattern over the tropical Pacific correspond with those of the ENSO positive SST anomaly pattern. The ENSO-related precipitation bias of the DITCZ-like anomalies in the eastern Pacific in the models is also more related to the variability of ENSO-related SST than the DITCZ bias itself. The bias of the equatorial deficiency of the ENSO-related precipitation, on the other hand, is less sensitive to the ENSO variability.

Table 3.1 Spatial correlation coefficients between the precipitation climatology of the 30 CMIP5 models and of the observations (1901-2005, area weighted). Models with higher (lower) correlations are marked in red (blue).

	Annual		MAM		JJA		SON		DJF	
Corr. Coefficient	**REC**	**20CR**	**REC**	**20CR**	**REC**	**20CR**	**REC**	**20CR**	**REC**	**20CR**
CESM1-CAM5	0.87	0.87	0.81	0.79	0.86	0.85	0.87	0.87	0.85	0.85
CCSM4	0.88	0.88	0.79	0.79	0.85	0.85	0.87	0.87	0.87	0.86
CanESM2	0.84	0.87	0.78	0.81	0.84	0.84	0.83	0.85	0.84	0.86
CESM1-BGC	0.87	0.87	0.77	0.78	0.84	0.85	0.86	0.86	0.87	0.85
CESM1-FASTCHEM	0.86	0.86	0.78	0.77	0.84	0.84	0.85	0.85	0.86	0.84
ACCESS1-0	0.86	0.85	0.80	0.79	0.81	0.81	0.83	0.82	0.85	0.82
ACCESS1-3	0.87	0.84	0.81	0.78	0.83	0.79	0.82	0.80	0.84	0.81
CNRM-CM5	0.81	0.82	0.74	0.76	0.80	0.81	0.82	0.84	0.80	0.81
CMCC-CMS	0.82	0.83	0.73	0.77	0.79	0.78	0.80	0.82	0.81	0.82
CMCC-CM	0.81	0.83	0.72	0.75	0.78	0.77	0.80	0.82	0.81	0.81
GFDL-ESM2M	0.80	0.80	0.71	0.72	0.78	0.77	0.79	0.80	0.80	0.78
HadGEM2-AO	0.80	0.79	0.71	0.70	0.79	0.75	0.78	0.76	0.79	0.76
GFDL-CM3	0.79	0.80	0.66	0.69	0.78	0.77	0.79	0.79	0.78	0.79
NorESM1-ME	0.79	0.79	0.71	0.71	0.73	0.74	0.79	0.78	0.76	0.74
GISS-E2-R	0.77	0.77	0.74	0.73	0.70	0.72	0.78	0.78	0.76	0.75
GFDL-ESM2G	0.77	0.75	0.70	0.68	0.77	0.75	0.78	0.78	0.78	0.75
HadCM3	0.77	0.73	0.72	0.68	0.74	0.70	0.79	0.75	0.78	0.74
NorESM1-M	0.79	0.79	0.70	0.70	0.73	0.75	0.79	0.78	0.76	0.74
MIROC5	0.79	0.76	0.76	0.76	0.75	0.73	0.79	0.77	0.74	0.73
GISS-E2-R-CC	0.77	0.77	0.73	0.73	0.70	0.71	0.78	0.78	0.76	0.75
CSIRO-Mk3-6-0	0.74	0.75	0.67	0.69	0.71	0.72	0.76	0.77	0.73	0.73
inmcm4	0.75	0.76	0.73	0.74	0.68	0.69	0.70	0.71	0.77	0.78
IPSL-CM5A-LR	0.74	0.74	0.66	0.68	0.73	0.71	0.76	0.76	0.74	0.72
IPSL-CM5A-MR	0.74	0.74	0.66	0.69	0.72	0.69	0.75	0.75	0.73	0.73
MRI-CGCM3	0.73	0.74	0.65	0.64	0.73	0.70	0.74	0.74	0.69	0.68
GISS-E2-H-CC	0.73	0.72	0.69	0.69	0.64	0.66	0.74	0.73	0.71	0.69
MPI-ESM-LR	0.71	0.71	0.62	0.67	0.69	0.69	0.76	0.76	0.69	0.69
GISS-E2-H	0.73	0.72	0.68	0.69	0.64	0.65	0.73	0.72	0.71	0.70
IPSL-CM5B-LR	0.71	0.73	0.59	0.61	0.68	0.67	0.72	0.73	0.71	0.69
MPI-ESM-P	0.71	0.71	0.62	0.67	0.69	0.68	0.76	0.75	0.68	0.68

Table 3.2 Spatial correlation coefficients between the first EOF mode spatial fields of precipitation anomalies of the 30 CMIP5 models and of the observations (1901-2005, area weighted). Group 1 (2) models are marked in red (blue).

	Annual		JJA		DJF	
Corr. Coefficient	**REC**	**20CR**	**REC**	**20CR**	**REC**	**20CR**
CESM1-CAM5	0.72	0.69	0.69	0.75	0.66	0.65
GFDL-ESM2M	0.77	0.76	0.63	0.61	0.75	0.69
CMCC-CMS	0.80	0.78	0.70	0.61	0.76	0.79
CNRM-CM5	0.59	0.50	0.70	0.66	0.82	0.82
CESM1-FASTCHEM	0.75	0.74	0.64	0.74	0.68	0.66
CESM1-BGC	0.75	0.72	0.66	0.72	0.68	0.68
NorESM1-ME	0.76	0.75	0.56	0.68	0.73	0.72
NorESM1-M	0.71	0.72	0.54	0.67	0.77	0.74
MIROC5	0.75	0.74	0.60	0.60	0.67	0.64
IPSL-CM5B-LR	0.77	0.71	0.56	0.45	0.77	0.73
CCSM4	0.73	0.72	0.62	0.74	0.69	0.68
GISS-E2-R-CC	0.69	0.74	0.52	0.58	0.71	0.69
CanESM2	0.53	0.55	0.59	0.63	0.65	0.61
GISS-E2-R	0.67	0.73	0.48	0.56	0.73	0.71
CMCC-CM	0.63	0.72	0.52	0.46	0.74	0.78
GISS-E2-H-CC	0.49	0.51	0.51	0.58	0.54	0.51
GFDL-CM3	0.42	0.44	0.38	0.47	0.61	0.57
ACCESS1-0	0.42	0.49	0.43	0.42	0.63	0.58
ACCESS1-3	0.57	0.53	0.43	0.36	0.55	0.52
GISS-E2-H	0.48	0.48	0.44	0.46	0.49	0.47
MRI-CGCM3	0.58	0.46	0.52	0.42	0.51	0.43
MPI-ESM-LR	0.49	0.41	0.44	0.47	0.32	0.30
HadCM3	0.43	0.46	0.31	0.22	0.59	0.56
IPSL-CM5A-MR	0.38	0.40	0.40	0.39	0.45	0.47
inmcm4	0.43	0.42	0.37	0.34	0.40	0.38
MPI-ESM-P	0.47	0.40	0.40	0.49	0.34	0.31
HadGEM2-AO	0.47	0.49	0.19	0.11	0.59	0.55
GFDL-ESM2G	0.38	0.34	0.42	0.45	0.30	0.28
IPSL-CM5A-LR	0.36	0.35	0.36	0.35	0.36	0.38
CSIRO-Mk3-6-0	0.35	0.30	0.34	0.37	0.28	0.24

(a). Annual-averaged Precipitation Climatology

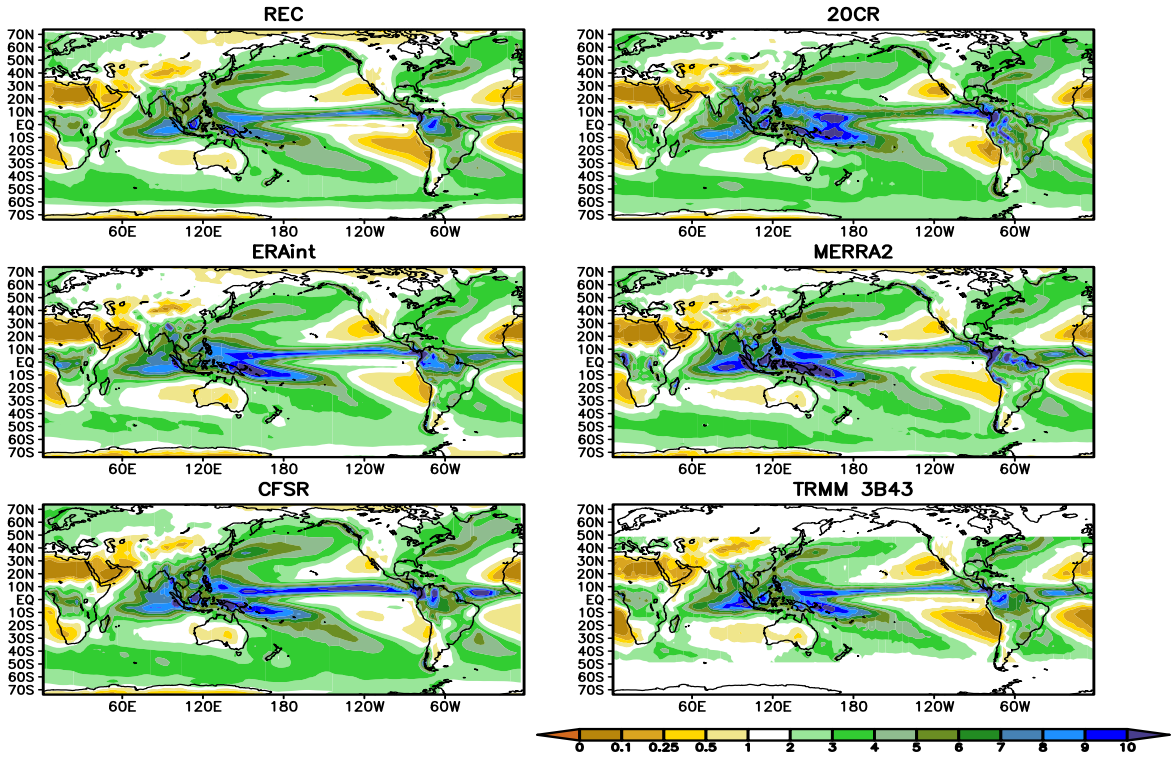

(b) Precipitation Climatology Differences

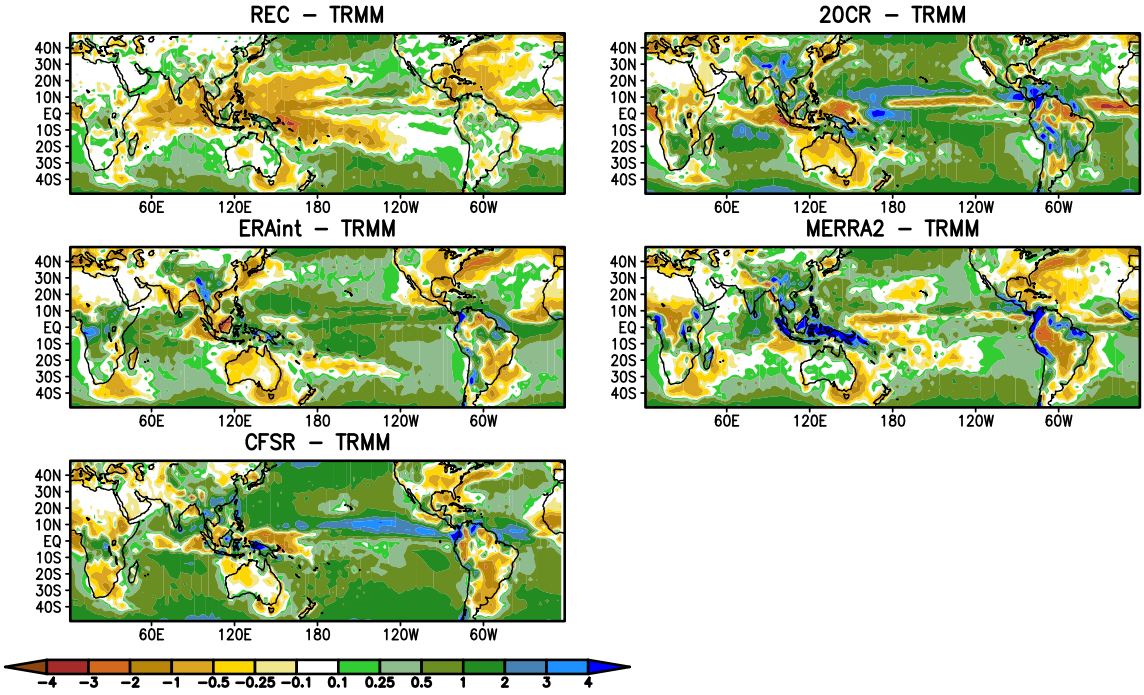

Figure 3.1 (a) Annually averaged precipitation climatology of REC, 20CR, ERA-Interim, MERRA-2, CFSR and TRMM 3B43 (mm/day, 1998-2005), and **(b)** the difference maps between TRMM 3B43 and the five other datasets.

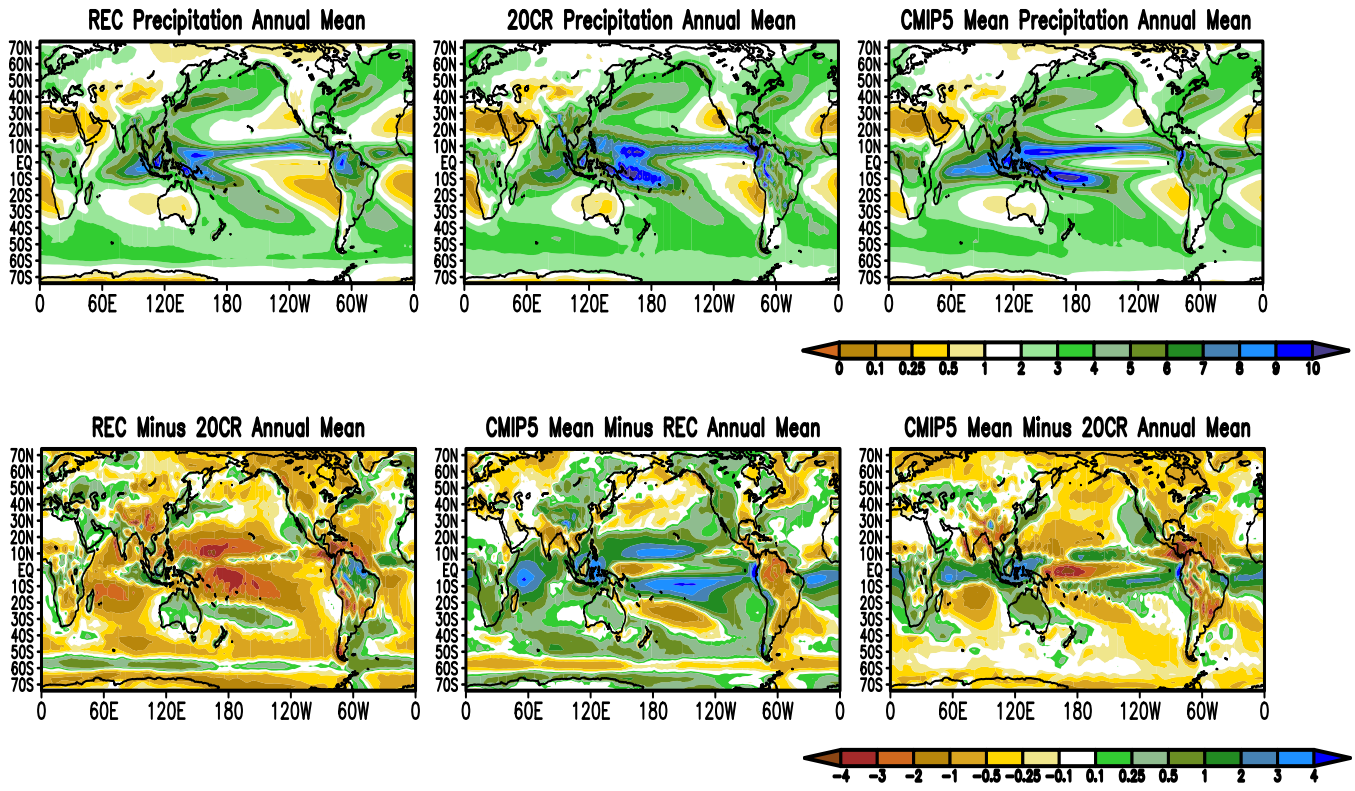

Figure 3.2 Annually averaged precipitation climatology of REC, 20CR and the mean of the 30 CMIP5 models (mm/day, 1901- 2005) and the difference maps among them (REC minus 20CR, the mean of the 30 CMIP5 models minus REC and the mean of the 30 CMIP5 models minus 20CR)

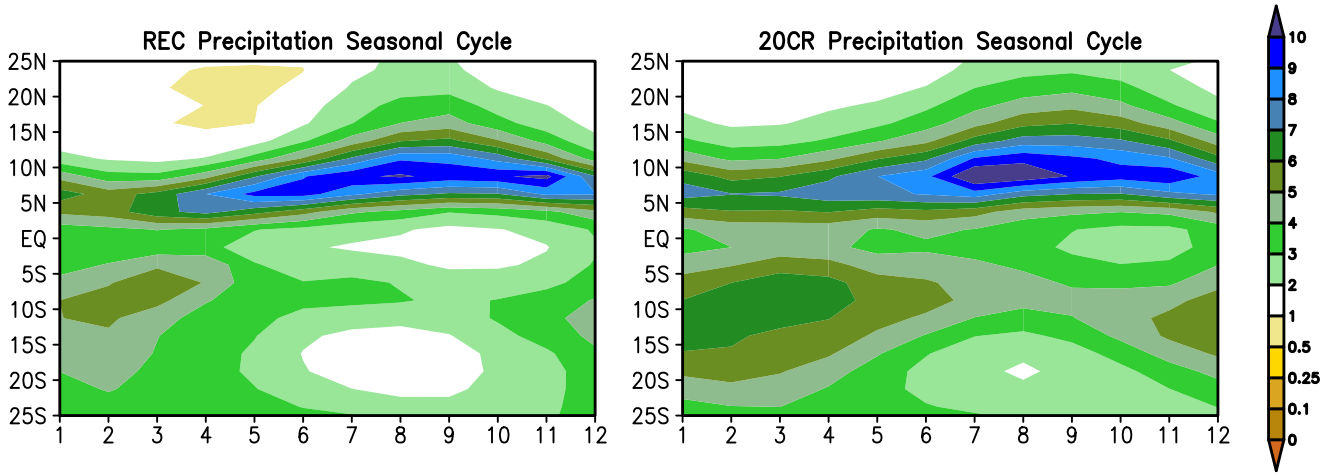

Figure 3.3 Seasonal cycle of the meridional distribution of the precipitation climatology in the tropical Pacific Ocean (zonal average of 150°E-90°W) in REC and 20CR (mm/day, 1901-2005)

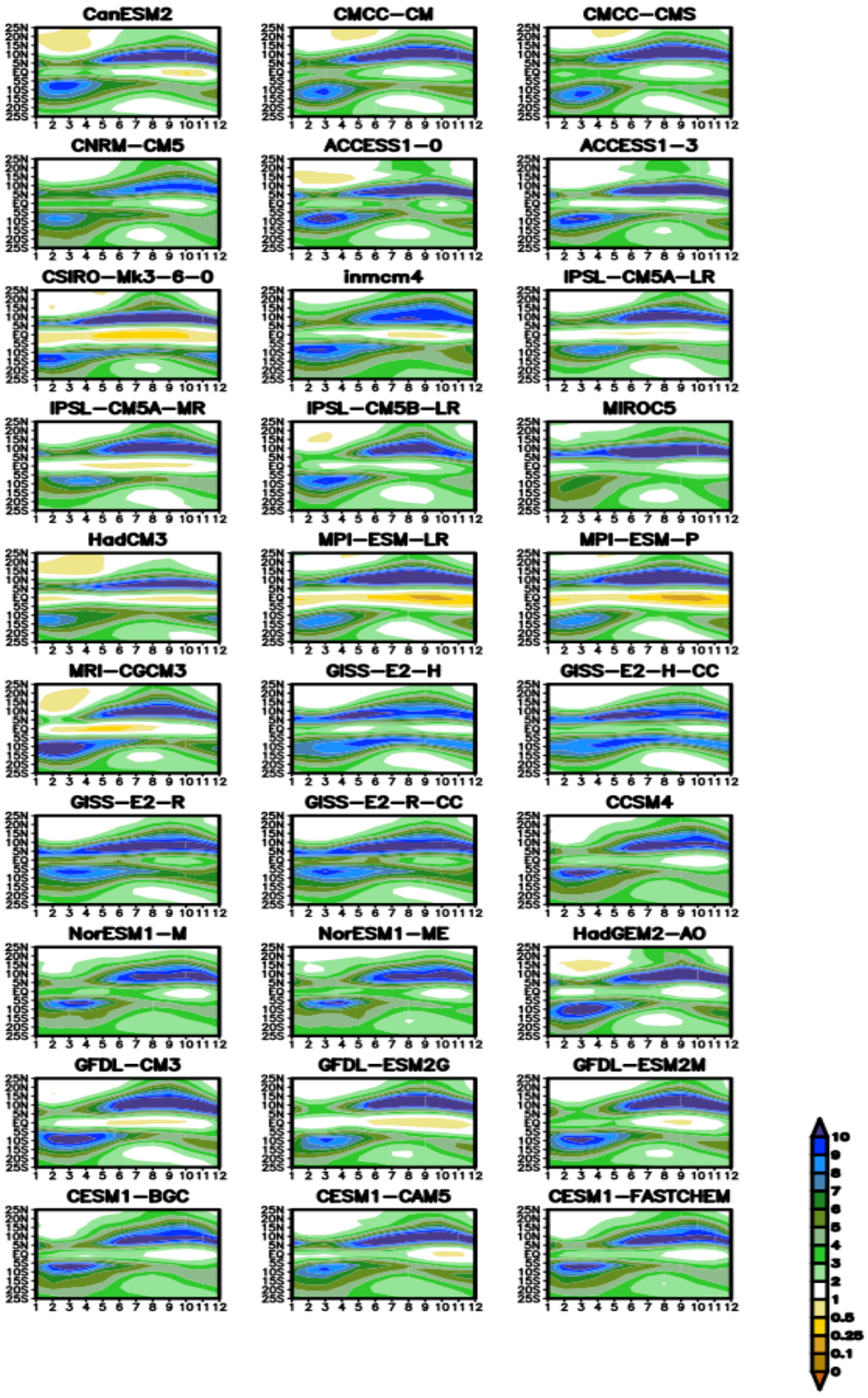

Figure 3.4 Seasonal cycle of the meridional distribution of the precipitation climatology in the tropical Pacific Ocean (zonal average of 150°E-90°W) in the 30 CMIP5 models (mm/day, 1901-2005)

(a) First EOF mode

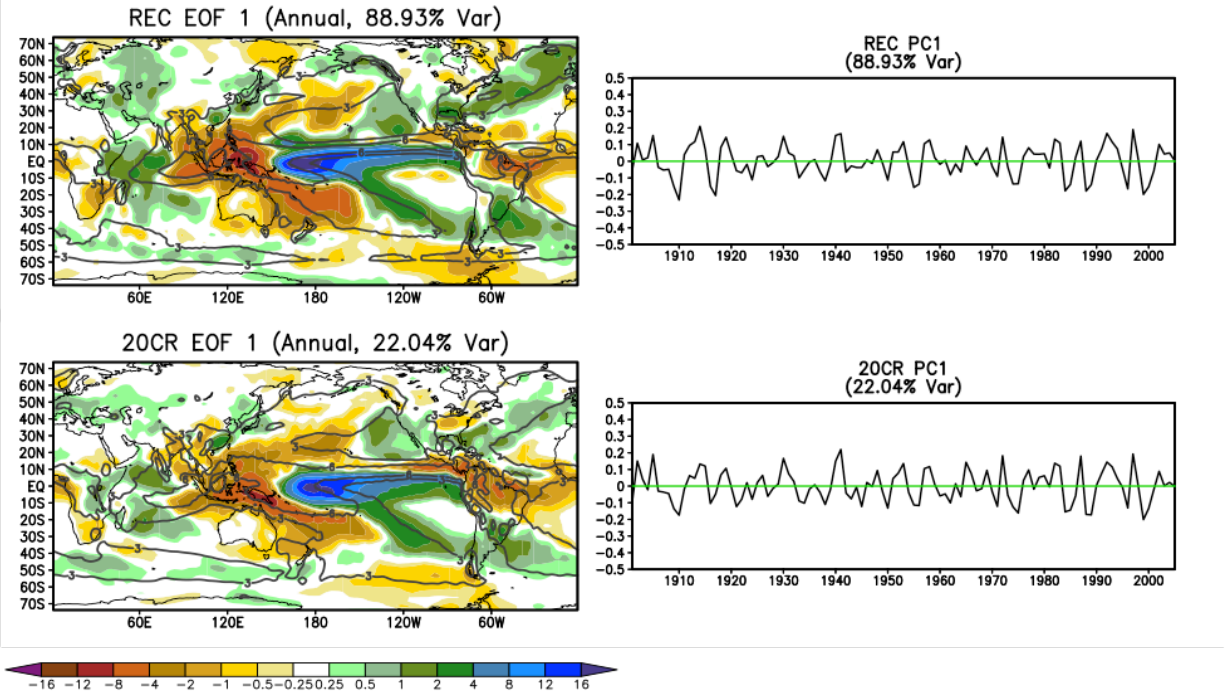

(b) Second EOF mode

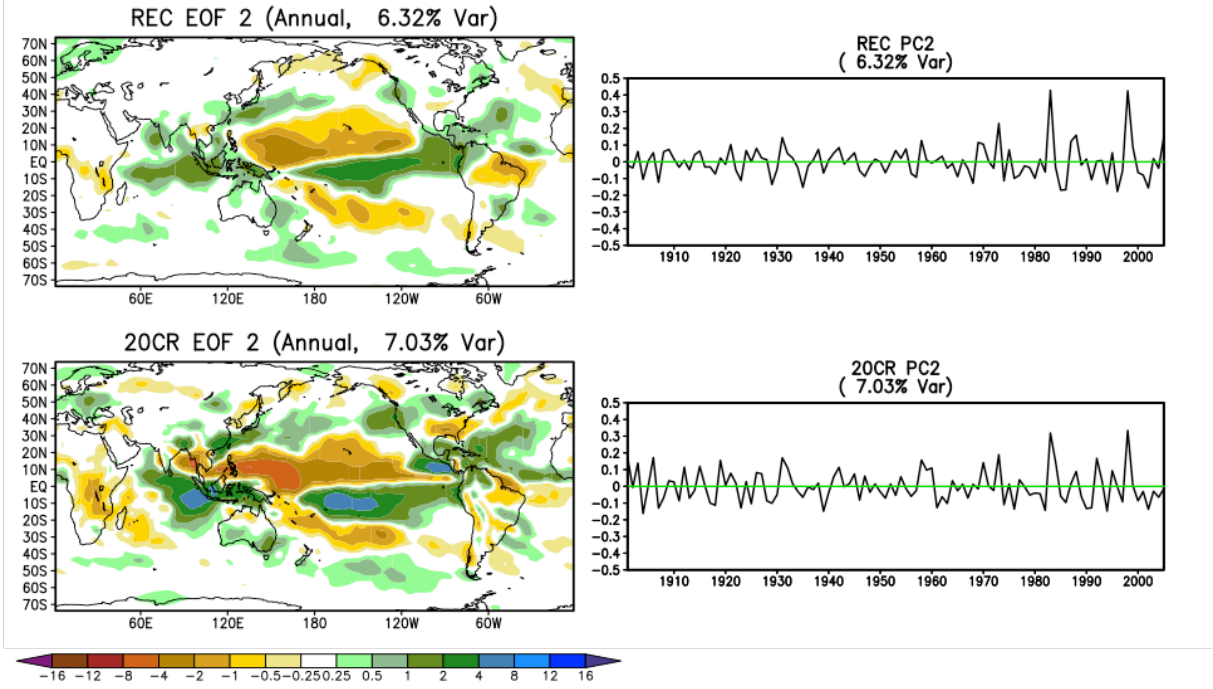

Figure 3.5 The **(a)** first and **(b)** second EOF modes of the annually averaged precipitation anomalies in REC and 20CR (mm/day, 1901-2005) (colors stand for the precipitation anomalies; the annually averaged precipitation climatology of 3 and 6 mm/day are plotted in contours)

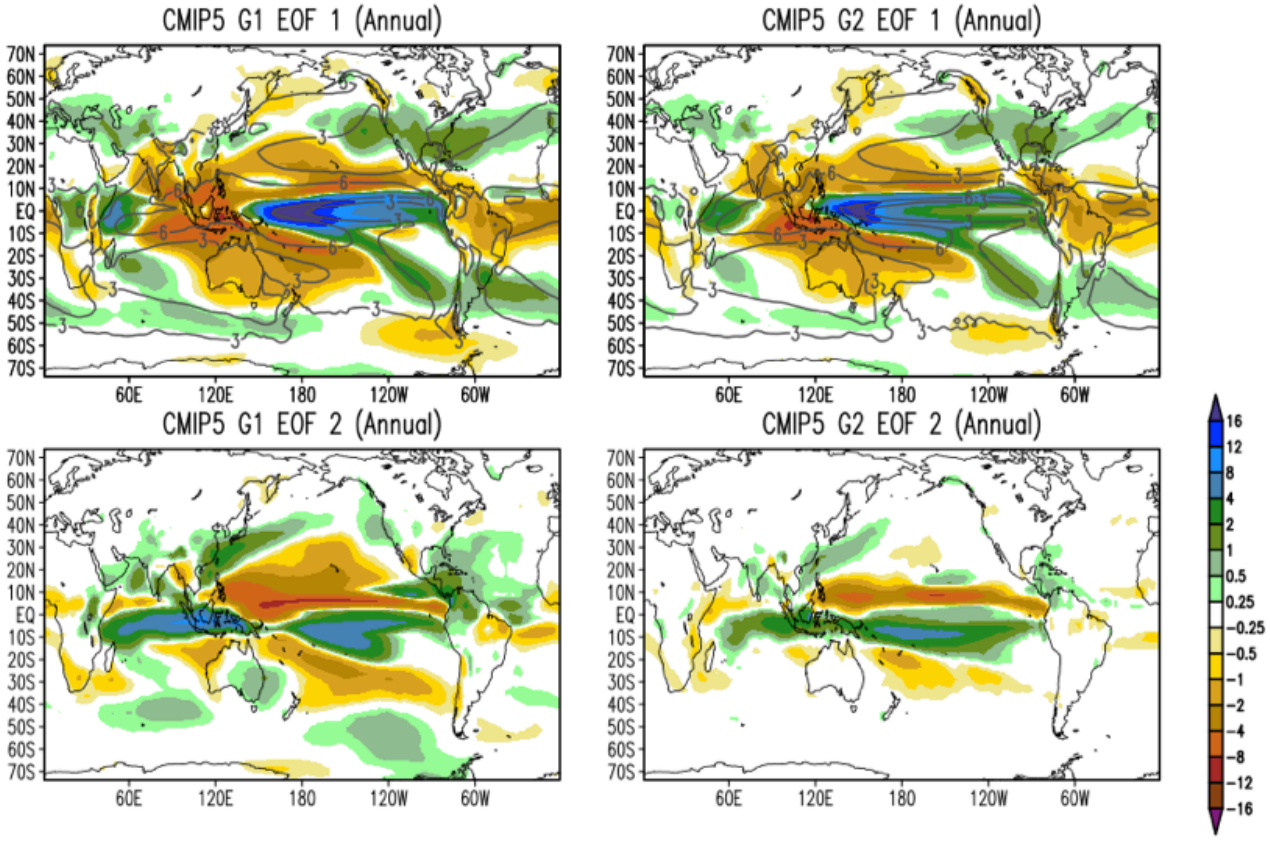

Figure 3.6 Spatial results of the first **(upper panel)** and second EOF modes **(lower panel)** of the CMIP5 group 1 and 2 precipitations anomalies (mm/day, 1901-2005). The colors represent the precipitation anomalies. The contours are the annually averaged precipitation climatology for the values of 3 and 6 mm/day. For each group, the EOF spatial pattern or the precipitation climatology is calculated for each ensemble member within a model first, and then an average of the model is computed. A weighted mean (based on the ensemble numbers) of the 11 models within each group is shown this figure.

(a) JJA-averaged precipitation anomalies EOF results

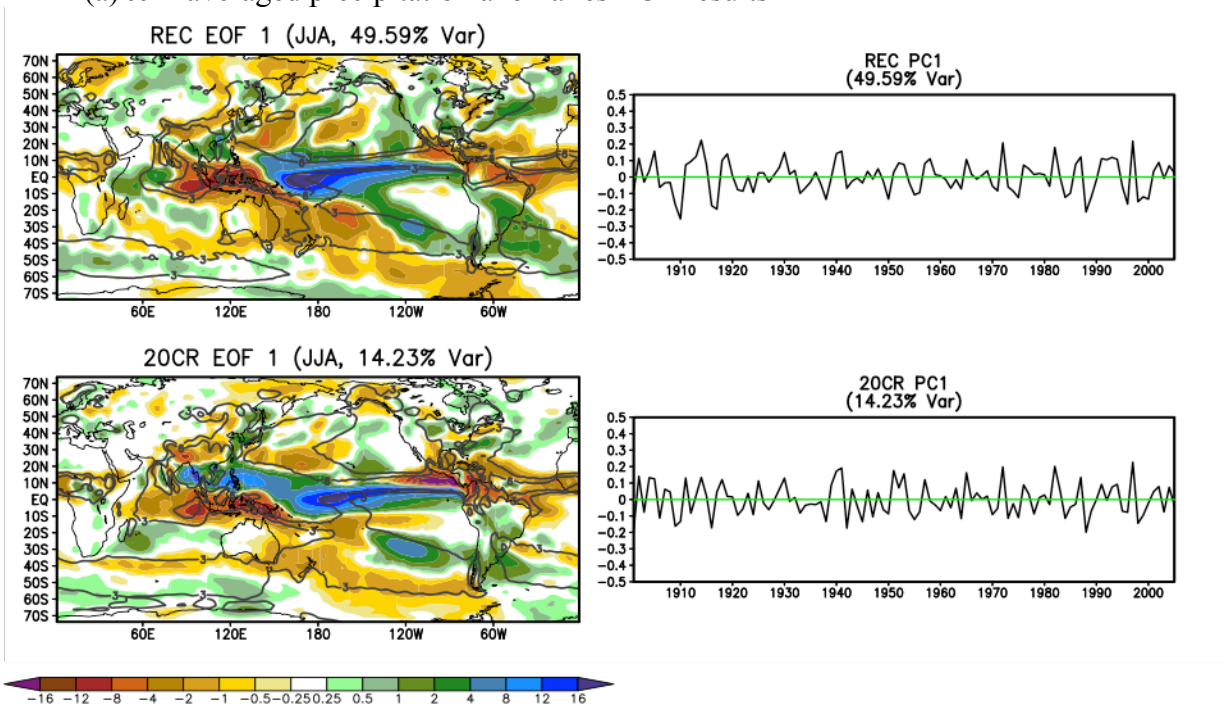

(b) DJF-averaged precipitation anomalies EOF results

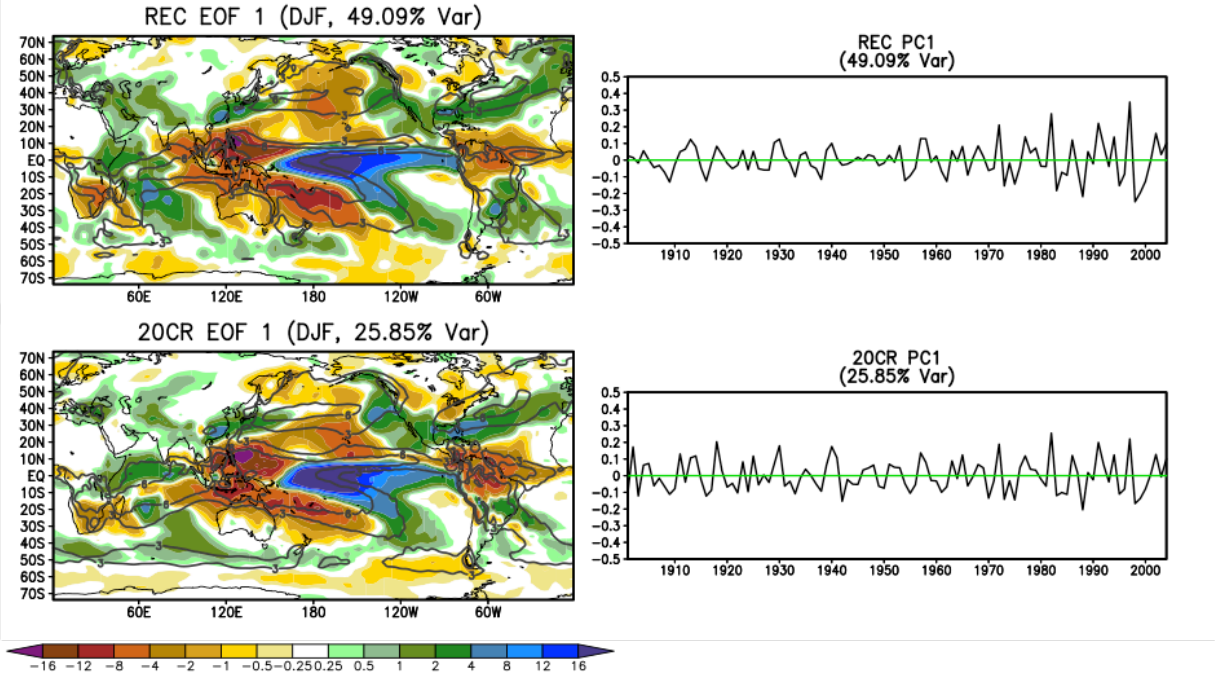

Figure 3.7 The first EOF spatial fields and time series of the **(a)** JJA-averaged and **(b)** DJF-averaged precipitation anomalies in REC and 20CR (mm/day, 1901-2005). Colors stand for the seasonally averaged precipitation anomalies, and contours are the JJA-/DJF-averaged precipitation climatology of 3 and 6 mm/day.

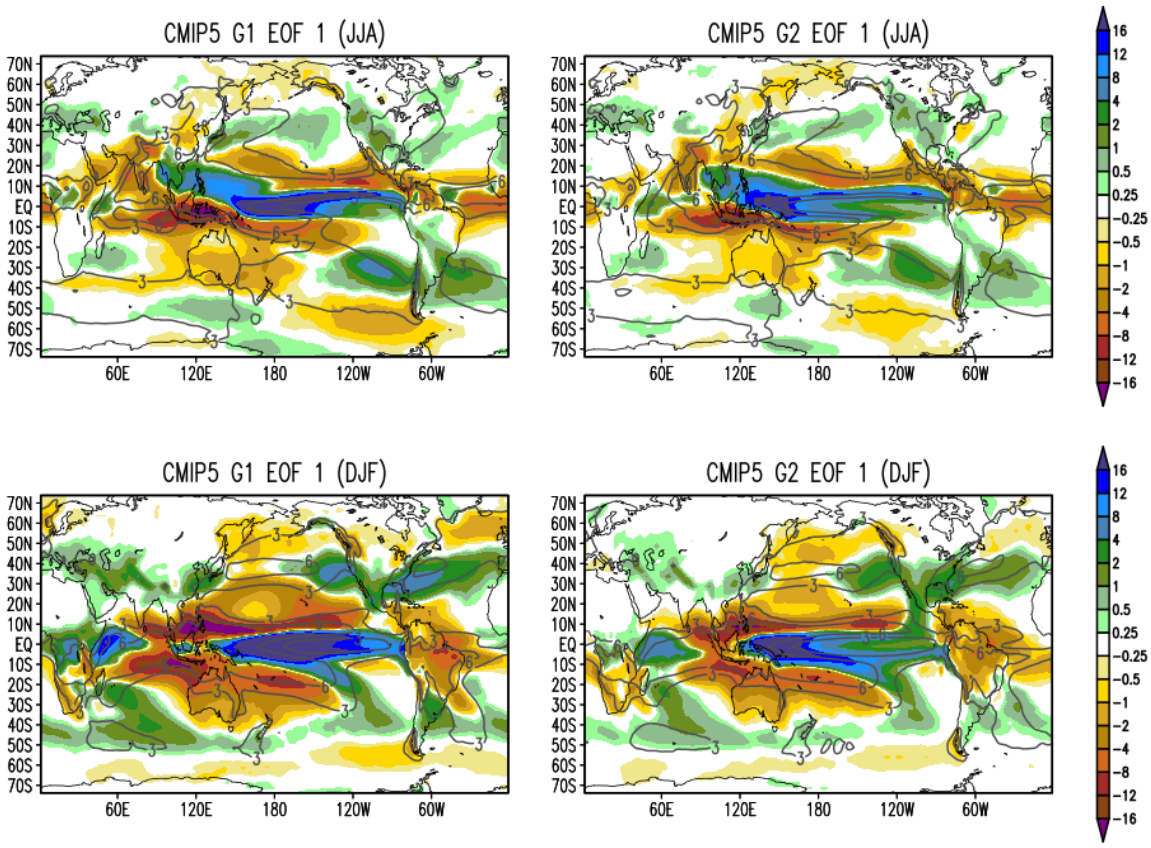

Figure 3.8 The first EOF spatial fields of the JJA-averaged (**upper panel**) and DJF-averaged (**lower panel**) precipitation anomalies of the CMIP5 group 1 and 2 models (mm/day, 1901-2005). Colors stand for the seasonally averaged precipitation anomalies, and contours are the JJA-/DJF-averaged precipitation climatology of 3 and 6 mm/day. For each group, the EOF spatial pattern or the precipitation climatology is calculated for each ensemble member within a model first, and then an average of the model is computed. A weighted mean (based on the ensemble numbers) of the 11 models within each group is shown this figure.

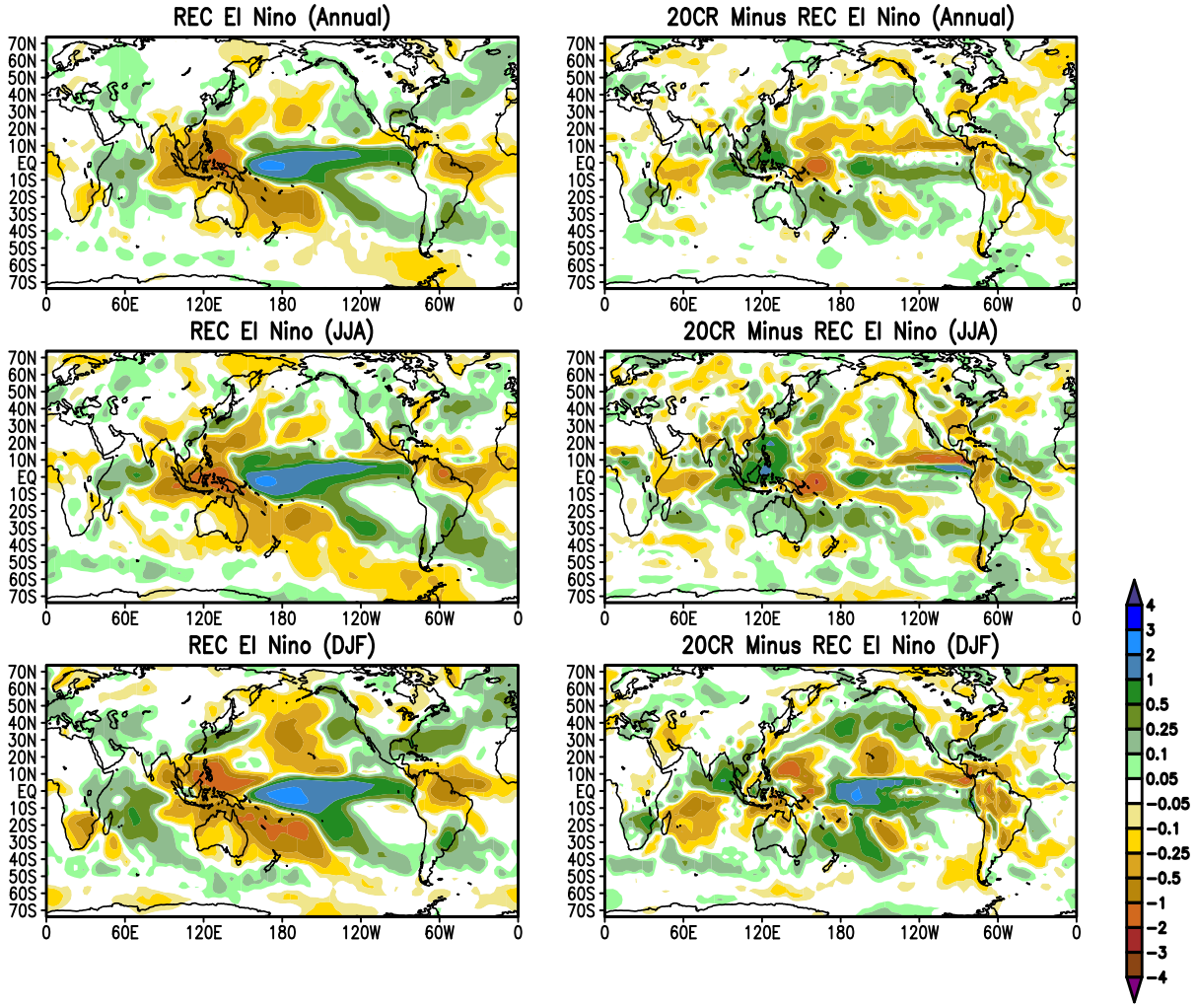

Figure 3.9 Annually- (**upper panel**), JJA- (**middle panel**) and DJF- (**lower panel**) averaged El Niño-related precipitation composites maps of REC (left column) and the difference maps between REC and 20CR (right column) (mm/day, 1901-2005)

(a) Agreement among the 30 CMIP5

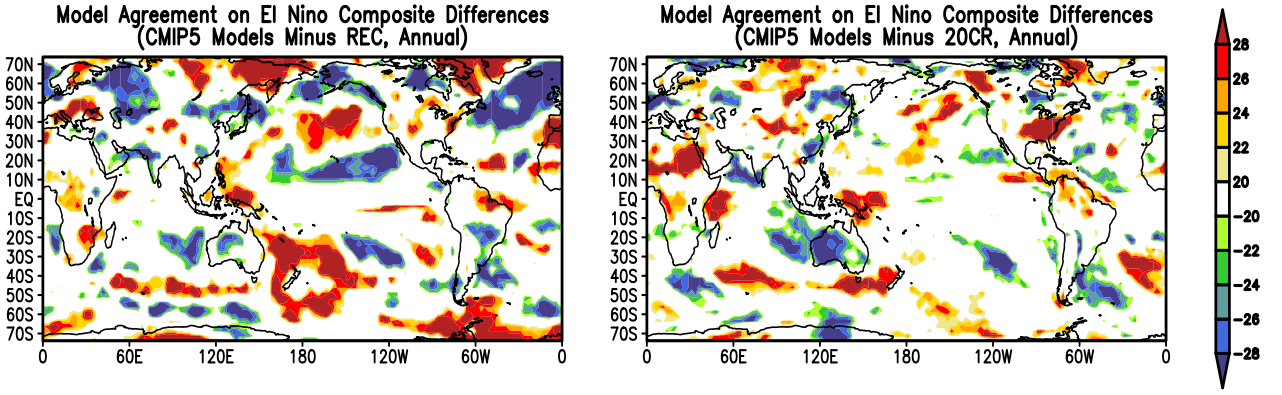

(b) Agreement among the 2 CMIP5 groups

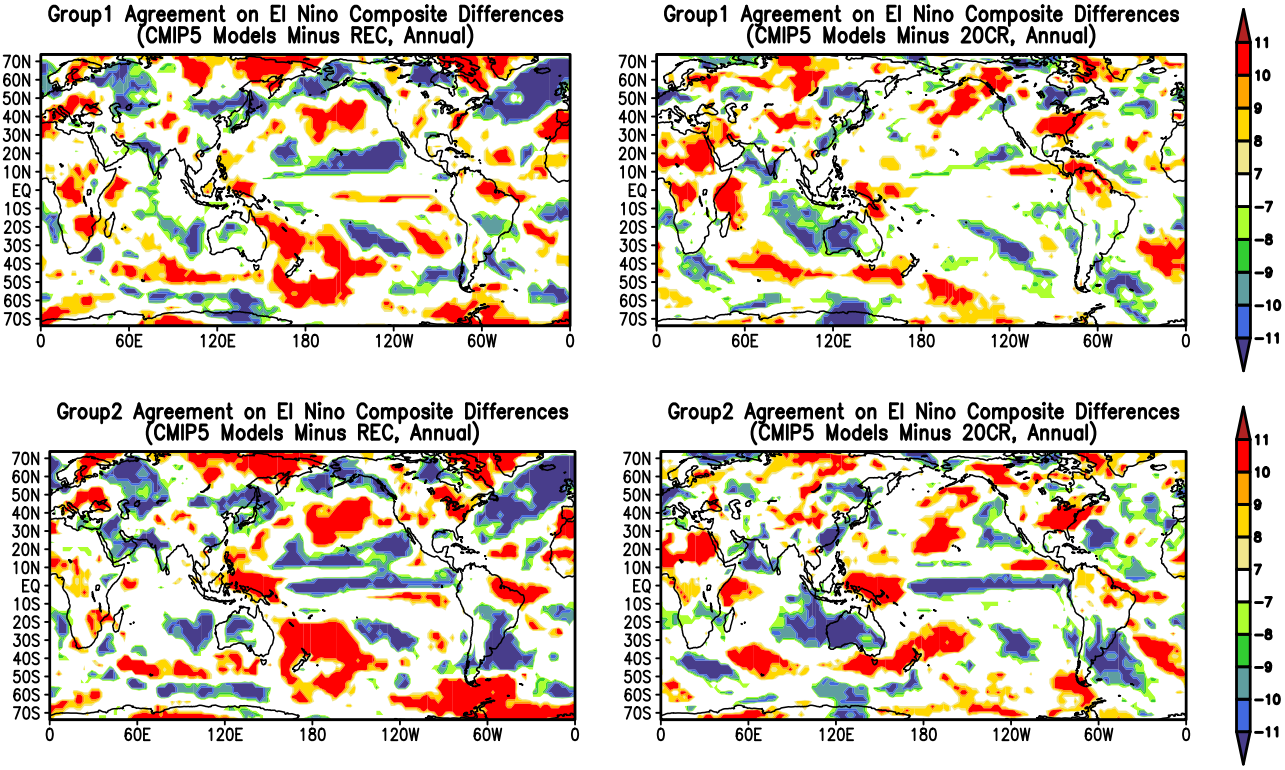

Figure 3.10 (a) Agreement among the 30 CMIP5 models on the same sign (positive or negative) of the bias of the annually averaged El Niño-related precipitation composites from 20CR and REC. **(b)** Same as (a), but within CMIP5 group 1 (upper panel) and group 2 (lower panel). Each group has 11 members. Red (blue) color or positive (negative) value at each grid point represents the number of models that have positive (negative) El Niño-related precipitation anomaly biases from the two observations.

(a) El Niño and La Niña precipitation indexes

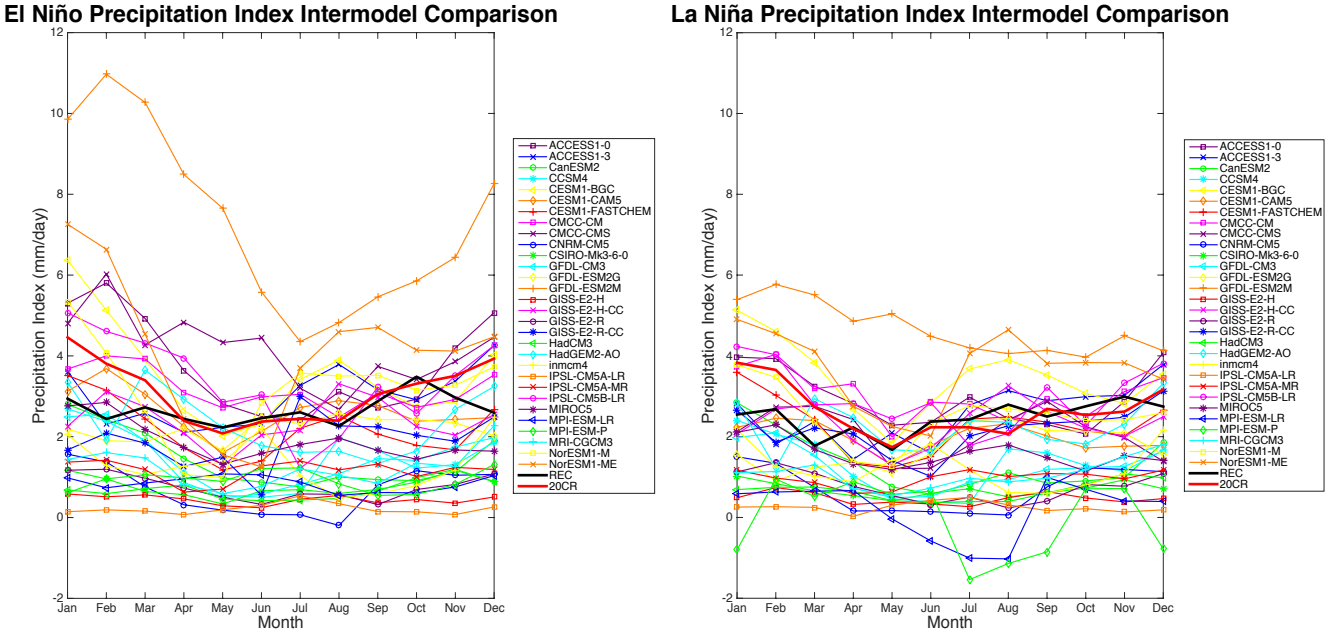

(b) El Niño and La Niña precipitation indexes

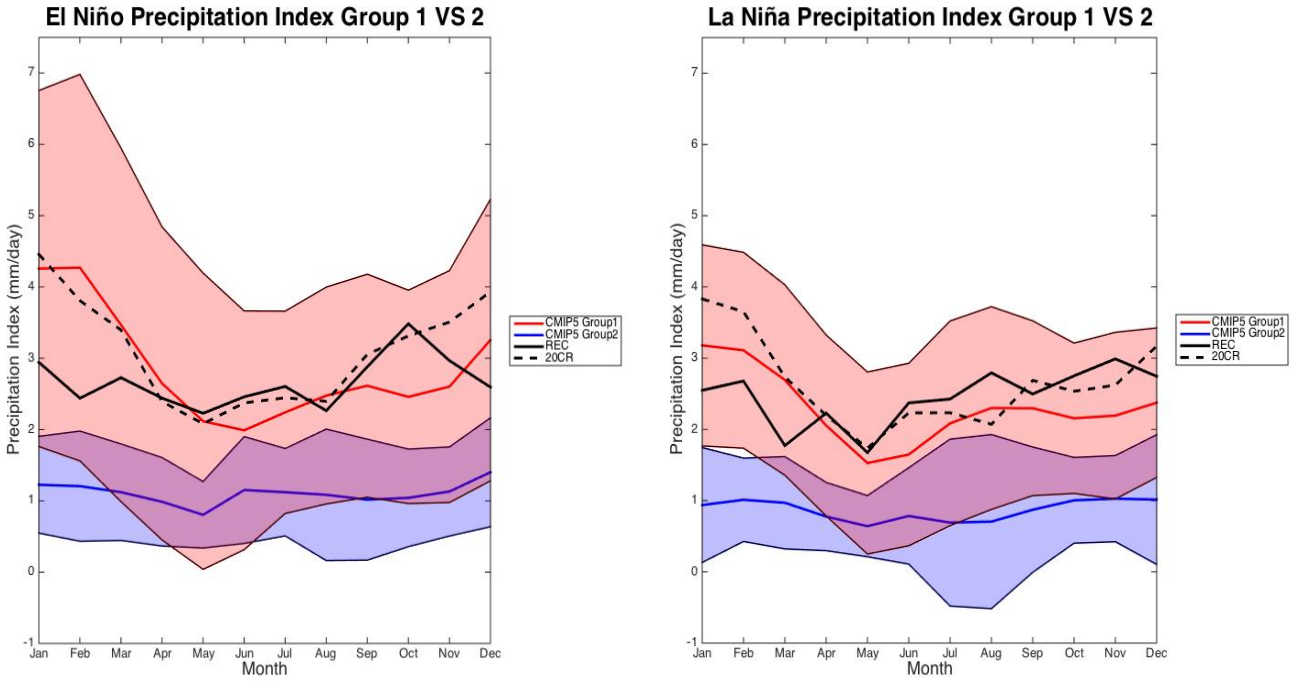

(c) Normalized El Niño and La Niña precipitation indexes

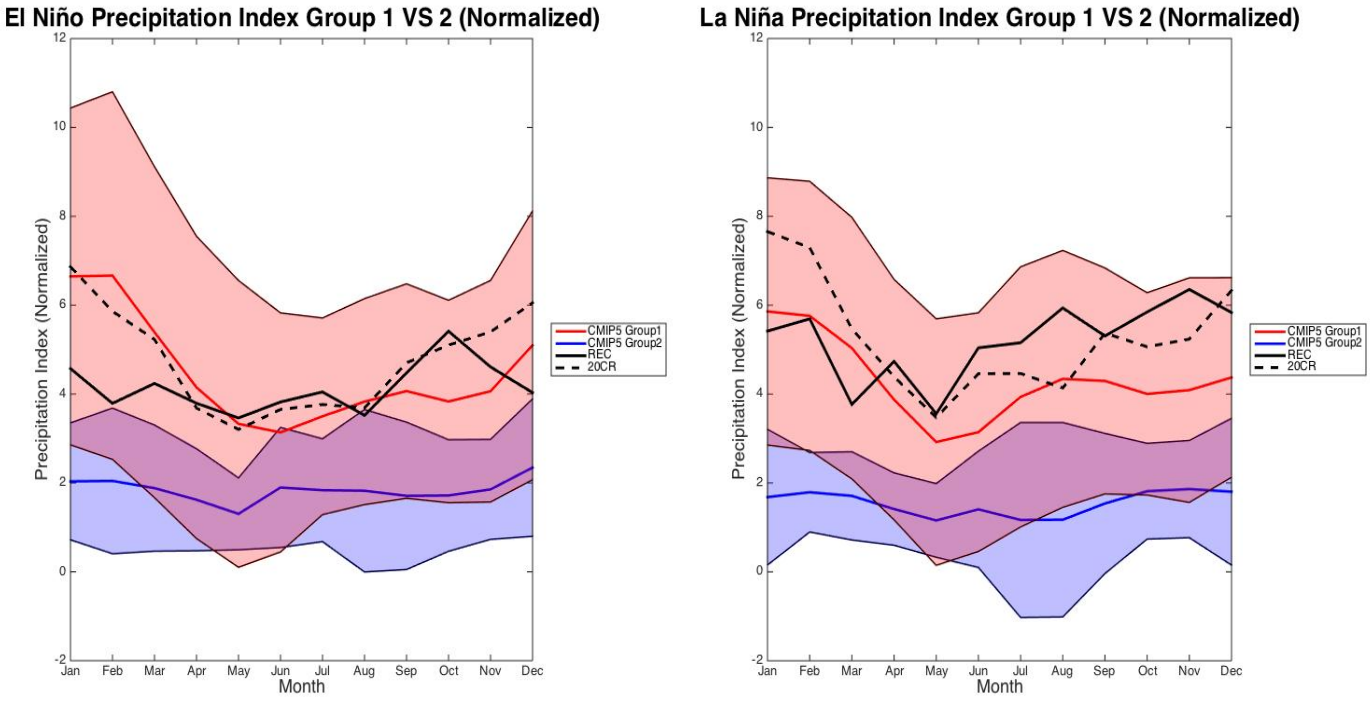

Figure 3.11 (a) monthly-averaged El Niño and La Niña precipitation indexes among 20CR, REC and the 30 CMIP5 models (mm/day, 1901-2005); **(b)** monthly-averaged El Niño and La Niña precipitation indexes of the 20CR, the REC and the two CMIP5 groups (color shades stand for the standard deviation; color lines stand for the means of each group); **(c)** normalized results of the middle panel using standard deviation of first EOF time series of the monthly-averaged SST in each dataset.

(a) Agreement among the 30 CMIP5 models on same sign

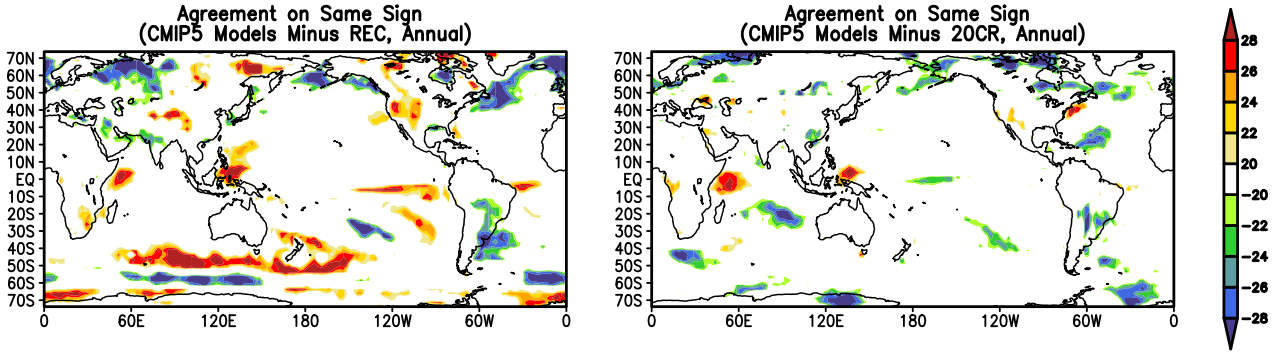

(b). Agreement among each CMIP5 group

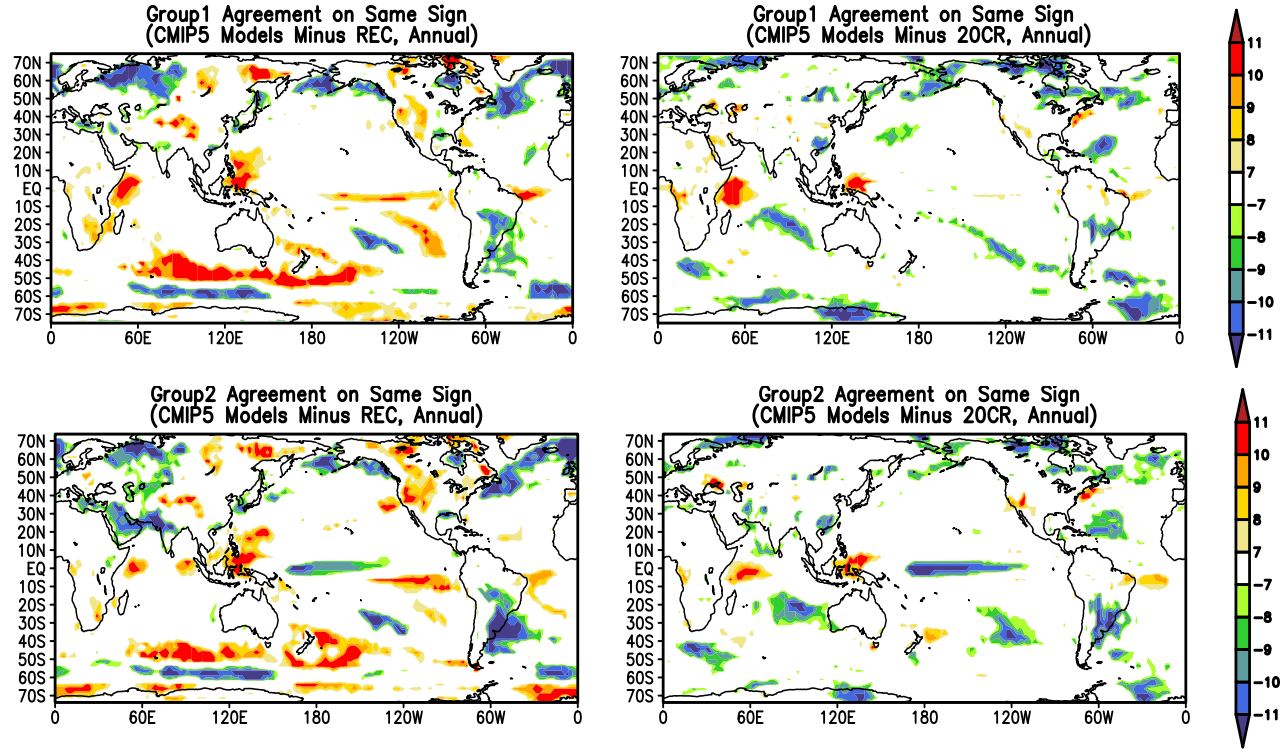

Figure 3.12 (a) Agreement among the 30 CMIP5 models on same sign (positive or negative) shared by the annual-averaged precipitation climatology biases and the annual-averaged ENSO-related precipitation composites biases from 20CR and REC. **(b)** Same as (a), but within CMIP5 group 1 (upper panel) and group 2 (lower panel). Each group has 11 members. Red (blue) color or positive (negative) value at each grid point represents the number of models that have positive (negative) biases of both precipitation climatology and ENSO-related precipitation anomalies when compared with the observations.

(a) Observations

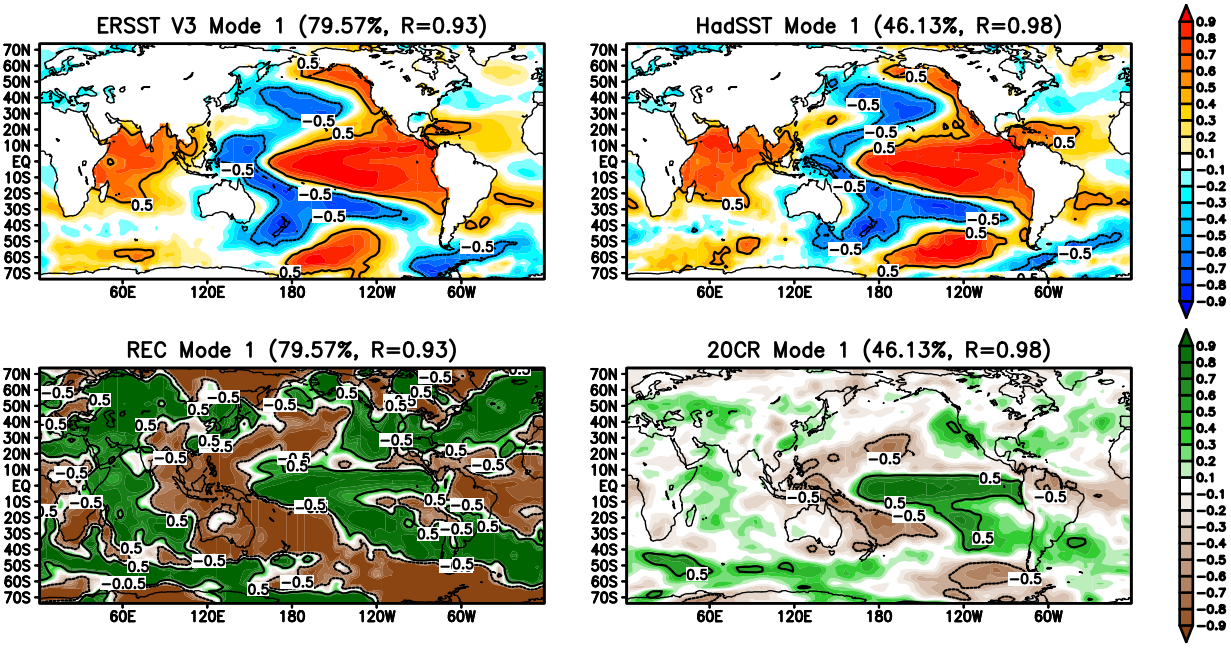

(b) 2 CMIP5 Groups

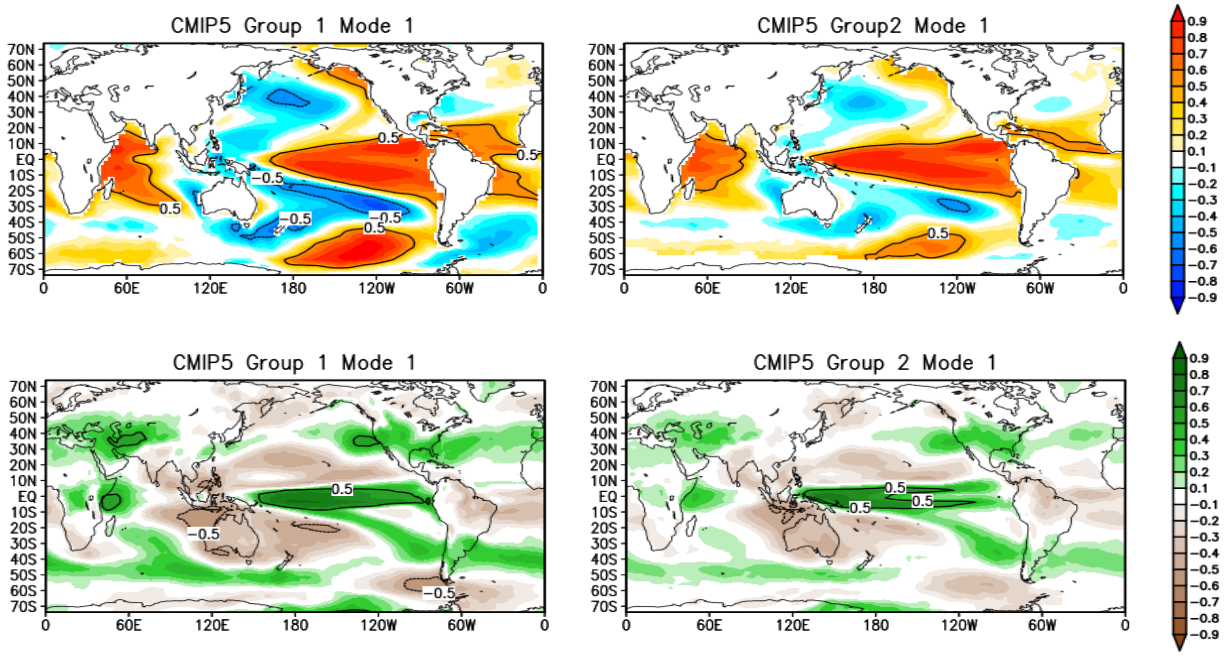

Figure 3.13 Annual-averaged first SVD mode of **(a)** the observations and **(b)** the 2 CMIP5 groups. Upper panel: homogenous temporal correlation between the normalized SST field and the SST time series of the first SVD mode; lower panel: heterogenous temporal correlation between the normalized precipitation field and the SST time series of the first SVD mode. The percentage stands for the total variance explained by the first SVD mode. R represents the temporal correlation coefficient between the SVD time series of the SST and of the precipitation.

Chapter 4: Intercomparison of the ENSO Diabatic Heating Distribution and related Atmospheric Circulations among ERA-Interim, MERRA-2, and CFSR Reanalyses, and CMIP5 Model Simulations

4.1 Introduction

Surface precipitation climatology and ENSO-related precipitation anomalies in two long-term precipitation datasets and the 30 CMIP5 model simulations were documented in the previous chapter. Precipitation distribution, whose representation is challenging for coupled general circulation models (CGCMs), can provide insights for improving ENSO in the CMIP5 model simulations. In this chapter, we expand and investigate more deeply the ENSO structure in recent atmospheric reanalyses and CMIP5 simulations, focusing on the three-dimensional (3D) structure of atmospheric diabatic heating and related rotational and divergent circulations.

Diabatic heating is an important energy source for atmospheric circulations. It is the sum of radiative heating, sensible heating, and latent heating from phase changes of water substance. The atmospheric general circulation is driven by the horizontal and vertical gradients of diabatic heating, generating zonal and meridional heat transport and vertical motions (e.g. convective processes). Diabatic heating is influenced by the surface temperature, wind, and moisture distributions as well as by upper-level cloud microphysics, cloud distribution, and upper tropospheric circulation (Fueglistaler et al. 2009). Diabatic heating is thus intimately related to both atmospheric circulation and the water cycle.

In the tropics, the major component of diabatic heating is latent heating (Tao et al. 1993) released by convective (60%) and stratiform (40%) precipitation

(Schumacher et al. 2003). The large-scale zonal circulation in the Tropics is impacted by the latent heating released in both convective and stratiform precipitation processes (Hartmann et al. 1984; Schumacher et al. 2004). As diabatic heating is strongly related to precipitation, the 3D diabatic heating and related atmospheric circulation structure is analyzed to obtain insights into the causes of deficient ENSO simulation by some of the CMIP5 models.

Diabatic heating, however, cannot be directly observed/measured. Observation-based estimates of diabatic heating are thus used, with two methods commonly used for estimation: The first, a physical method, uses observations of temperature, humidity, and rainfall and models of radiative transfer, cloud structure, and surface sensible heat flux to estimate each heating component. The second, a thermodynamic method, diagnoses total diabatic heating as a residual of the thermodynamic equation using temperature and wind data (Yanai et al. 1973; Hoskins et al. 1989; Nigam et al. 1994 & 2000).

In CGCMs, diabatic heating strongly depends on the model parameterization schemes. Especially in the tropics, individual convective cells and many cloud features and processes have horizontal scales smaller than the model's grid (1°-2°×1°-2° in CMIP5 models). These sub-grid processes are included in the models from representation of their overall statistical effects on the grid-scale dynamics and thermodynamics; such representations are referred to as physical parameterizations (e.g. cumulus parameterization). Given the relatively coarse resolution of the GCMs and the imperfectly understood cloud-precipitation microphysics, it is challenging to develop suitable parameterization schemes for the diabatic heating-related physical

processes. The IPCC AR5 report (IPCC 2013) commented that although the CMIP5 models have improved simulation of cumulus convection compared to their precursors (CMIP3 models) from the perspective of ENSO and the Madden-Julian Oscillation (MJO, an eastward-moving, intraseasonal atmospheric disturbance over the tropical Indian and Pacific Ocean), the models still face difficulties in realistically simulating many aspects of the cloud microphysics. The stratiform precipitation processes, moreover, remain less well represented than the convective process in these models (Jiang et al. 2012). The biases in these cloud parameter schemes and moist processes can lead to unrealistic diabatic heating profiles, which further cause systematic biases in the atmospheric circulation and precipitation patterns (Hartmann et al. 1984; Raymond et al. 1990; Hirota et al. 2011). It is well known that the CGCMs tend to simulate too much (little) convective (stratiform) precipitation over the tropics. For example, most of the CMIP3 models produced ~95% of total precipitation from the convective processes in the lower latitudes (Dai 2006). A similar bias is found in the CMIP5 models, at least in the context of the South Asian Monsoon precipitation (Sabeerali et al. 2014). The associated vertical profiles of diabatic heating over these regions also tend to be bottom-heavy (maximum in the lower troposphere) in the models (e.g. Nigam et al. 2000).

Comparison of the CGCM diabatic heating profiles with observation-based estimates allows identification of the prominent heating-bias areas and facilitates the development of hypotheses for improvements in the convective and stratiform precipitation schemes in the CMIP5 models. Residual diagnoses of diabatic heating from the thermodynamic budget in modern atmospheric reanalyses can serve as

excellent and independent observational references. The reanalysis heating estimates are constrained by the observed dynamic and thermodynamic variables, and have the advantage of global and long-term coverage based on the use of both in-situ and satellite observations. The residually diagnosed diabatic heating is not without some limitations: 1) it depends on the model's convection parameterization schemes and data analysis procedure; 2) it depends strongly on vertical velocity – a variable not assimilated during reanalysis, and thus not observationally constrained, making it susceptible to errors, especially at low resolution. Therefore, residual diagnoses of diabatic heating from reanalyses need to be intercompared among themselves and with the in-situ observations and satellite observation-derived estimates.

Previous studies (Nigam et al. 2000; Chan and Nigam 2009; Hagos et al. 2010; Li et al. 2013) have cross-compared residual diagnosis of diabatic heating from several reanalyses and observations in the aspects of horizontal distributions, amplitudes, and vertical structures. Their results suggest that the reanalyses tend to agree better in the extra-tropics than the tropics, and better over land than the ocean. In the Pacific Ocean basin, diabatic heating over the Maritime Continent region is more biased than over the eastern Pacific in January (Chan and Nigam 2009). There are three types of diabatic heating vertical profiles (Schmacher et al. 2007; Zhang et al. 2009): the bottom heavy (shallow convective process, peak at 700 hPa), the middle heavy (deep convective process, peak at 400 hPa), and the top heavy one (stratiform process, heating peak at 400 hPa and cooling peak at 700 hPa). Hagos et al. 2010 found that that these three profiles can be represented by two leading rotated EOF modes, a deep mode with heating peak in upper troposphere and a shallow mode in

which heating accumulates in low level troposphere. Their results also showed that diabatic heating analyses from four reanalyses and four TRMM heating products concur in the deep modes of normalized heating, while the shallow heating modes among the datasets tends to be more diverse. In addition, Chan and Nigam (2009) pointed out that TRMM convective-stratiform heating (CSH) latent heating (an older version, Tao et al. 2006) is weaker than heating diagnosed from the ERA-40 and NCEP reanalyses by a factor of 2.

In this study, we use diabatic heating diagnosed from ERA-Interim, MERRA-2 and CFSR (detailed description is given in Chapter 2), the three most recent atmospheric reanalyses with high spatial resolution and temporal coverage of the whole satellite era (1980-2016), as references in comparing with the CMIP5 model simulations. As these three reanalyses have finer horizontal and vertical resolution than those in the aforementioned studies, intercomparisons against them may be more revealing of both agreements and biases in several regions, including the planetary boundary layer and the tropopause. The implication/reflection of potential heating biases on atmospheric circulation are noted, as one identifies an optimal reanalysis-based diabatic heating from comparisons with an updated version of the TRMM CSH latent heating (Tao et al. 2010); the identified heating will be used in assessment of the CMIP5 diabatic distributions. The ENSO-related diabatic heating and circulations in the reanalyses will be used to characterize the ENSO-related biases in the models and to advance understanding of how these biases relate to the ENSO precipitation biases documented in the previous chapter.

The residual diagnosis of diabatic heating is introduced in Section 4.2. Section 4.3 intercompares the horizontal and vertical distribution of climatological diabatic heating in the three atmospheric reanalyses and the CMIP5 climate simulations. The regionally averaged vertical heating profiles are intercompared in Section 4.4. ENSO-related diabatic heating and atmospheric circulation are presented and analyzed in Section 4.5. Discussion and summary follow in Section 4.6.

4.2 Residual Diagnosis of Diabatic Heating

The 3D diabatic heating is diagnosed as a residual in the thermodynamic equation (e.g. Nigam 1994; Nigam et al. 2000):

$$Q = \frac{\Delta T}{\Delta t} + \bar{\boldsymbol{v}} \cdot \boldsymbol{\nabla}\bar{T} + \left(\frac{p}{p_0}\right)^{\left(\frac{R}{C_p}\right)} \bar{\omega}\frac{\partial \bar{\theta}}{\partial p} + \left(\frac{p}{p_0}\right)^{\left(\frac{R}{C_p}\right)} \left[\boldsymbol{\nabla} \cdot \overline{\boldsymbol{v}'\theta'} + \frac{\partial \overline{\omega'\theta'}}{\partial p}\right]$$

Q is the monthly diabatic heating rate (K/day), $\boldsymbol{v}$ is the horizontal wind vector, and ω is the pressure vertical velocity. $\theta = T\left(\frac{p_0}{p}\right)^{\left(\frac{R}{C_p}\right)}$ is the potential temperature with T being the temperature. p is the pressure and $p_0$is the surface pressure (usually 1000hPa). C_p is the specific heat capacity of dry air and R is the specific gas constant of dry air. The overbar represents the monthly mean and the prime denotes the deviation of the 6-hourly analysis from the monthly average. The last two terms of the equation, the transient components, represent the average of sub-monthly fluctuations. The transient terms are usually more significant in the extratropics and higher latitudes. In this study, Q is calculated using central finite differencing in both horizontal and vertical directions.

The three reanalyses and the CMIP5 models are all diagnosed at their native horizontal and vertical resolutions. We use the ERA-Interim as a basis for comparison with other reanalyses and models. This is because among the three reanalyses, MERRA-2 is relatively recent and thus not extensively compared with the other reanalyses in the context of diabatic heating, while CFSR is the only atmospheric reanalysis produced by a coupled atmosphere–ocean–land surface–sea ice data assimilation system. To facilitate data comparison, both the latent heating of TRMM CSH and the diabatic heating of CFSR and MERRA-2 are converted to same resolution as the ERA-Interim diabatic heating (0.75° × 0.75° and 37 pressure levels) when we calculate their departures from ERA-Interim. The CMIP5 model diabatic heating fields are regridded to a 2.5°× 2.5° global horizontal resolution and 17 pressure levels. The ERA-Interim fields are converted to the same resolution as the model simulations to which they are compared. Only the tropical region (latitude range of 23.5°S - 23.5°N) is analyzed in the CMIP5 case as a transient term (vertical heat flux) needed in residual estimation of diabatic heating could not be computed from the archived fields (due to the lack of archival of the 6-hourly vertical velocity). The period of January 1998 to March 2015 is used for comparing the TRMM CSH latent heating and the ERA-interim diabatic heating, while the January 1980 to December 2016 period is analyzed in the reanalysis intercomparison. The CMIP5 model assessment period is a bit shorter (January 1980 - December 2005) due to the simulation period.

In this chapter, 10 models are selected from the 30 CMIP5 models mentioned in Chapter 2. The criteria for choosing the 10 models are similar to those used in the

previous chapter: model performance in precipitation climatology and ENSO-related precipitation. The CMIP5 model choice in this chapter is based on 20CR and REC, as well as the ERA-Interim, the MERRA-2, the CFSR, the TRMM and the GPCP precipitation. Precipitation assessment and model popularity (e.g. number of citations) informed the choice of 10 models in this study. These models are lumped into two groups, the better performing group (NCAR.CCSM4, CNRM-CERFACS.CNRM-CM5, CCCma.CanESM2, MIROC.MIROC5 and NOAA-GFDL.GFDL-ESM2M) and the under performing group (IPSL.IPSL-CM5A-LR, INM.INM-CM4, CSIRO-QCCCE.CSIRO-Mk3.6.0, MRI.MRI-CGCM3 and MPI-M.MPI-ESM-LR).

4.3 Diabatic Heating Climatology Intercomparison

In this section, the zonal average and horizontal distribution of the vertically averaged diabatic heating are presented first, followed by the vertical structure of heating and the associated zonally- and meridionally-averaged atmospheric circulations, as well as the regional vertical heating profiles.

4.3.1 Horizontal Distribution – ERA-Interim Diabatic Heating Versus TRMM CSH Latent Heating

The ERA-Interim diabatic heating is first compared/validated with another heating reference – the TRMM CSH latent heating, a satellite-retrieved heating product derived from the combination of TRMM precipitation and cloud outputs from a cloud resolving model (Tao et al. 2010). The TRMM-CSH heating has been found

by Tao et al. (2016) to closely resemble multiple diagnostically calculated diabatic heating fields from sounding networks during two TRMM field campaigns. Although diabatic heating and latent heating are not identical, comparing them over the tropical oceans is reasonable because the diabatic heating in these regions is dominated by the latent heating component (Tao et al. 1993), i.e., the net effect of radiative cooling and heating in the tropics, especially in the near-equatorial region (e.g. 10°S-10°N) is generally small enough that it can be neglected (Wright and Fueglistaler 2013).

The vertically-averaged time-mean diabatic heating in ERA-Interim and the TRMM CSH latent heating (Fig. 4.1) and their differences are shown in the tropics for January and July. These are the central months of the solstice seasons of DJF and JJA, and exhibit the most robust heating within the seasons. The vertically-averaged diabatic heating from ERA-Interim (Fig. 4.1a&b) exhibits both heating and cooling, while the total vertically-averaged TRMM CSH latent heating (Fig. 4.1c&d) is all positive. In the difference figures (Fig. 4.1e&f), only the heating part of the ERA-Interim diabatic heating (i.e., the sum of latent, sensible, and radiative heating) is used to compare with the TRMM CSH latent heating. The smallest differences (< +/- 0.5K/day) between these two products are found in the heavy rainfall region over the oceans, for example, the SPCZ in January, the ITCZ in the central-eastern Pacific in July, and the merging region of the ITCZ and the SPCZ in the western Pacific and the center of the ITCZ branch in the Indian Ocean in both January and July. ERA-Interim exhibits slightly larger heating (0.25 - 0.5K/day) than the TRMM CSH latent heating in those regions where rainfall is the heaviest, particularly the center of the SPCZ in January and the maximum of the ITCZ in the eastern Pacific and the western Pacific

in July. In those regions where the tropical precipitation is relatively less robust, however, ERA-Interim shows less heating than the TRMM CSH latent heating, especially in the January ITCZ in the central-eastern Pacific, the SPCZ in July, as well as the edges of ITCZ bands in the tropical Indian Ocean and the Atlantic Ocean in the two solstice months.

4.3.2 Zonal Average

The zonal average of the vertically averaged tropical diabatic heating of the reanalyses and the two CMIP5 models is shown in Fig. 4.2. On average, the reanalyses and the two CMIP5 groups show peak heating over the latitudes of the ITCZ maximum (3°-10°N) and the SPCZ (3°-12°S), with a local minimum over the equator. All datasets exhibit larger peak heating over the SPCZ (ITCZ) latitudes in January (July) than in July (January). These changes in the heating seasonality correspond to the fact that the SPCZ reaches its maximum in DJF (Vincent 1994) while the ITCZ convection process is strongest in JJA (Karoly 2015). The five datasets differ the most over the equator, with standard deviation of 0.31 in January and 0.20 in July (Table 4.1). The standard deviation of heating in the ITCZ appears to be larger than in the SPCZ in both January and July. Overall, the heating profiles differ more in boreal winter than summer.

Among the reanalyses, the curves of ERA-Interim and MERRA-2 are closer to each other than to that of the CFSR, especially over the latitudes from the equator to the SPCZ. In January, the MERRA-2 heating is smaller than in ERA-Interim from the equator to 20°N (the range that contains the ITCZ) by as much as 0.3 K/day;

while in July, the MERRA-2 heating is smaller in the Southern Hemisphere (5°-20°S, the SPCZ latitudes). The diabatic heating of CFSR is smaller by up to 0.4K/day than in both the ERA-Interim and MERRA-2 between the SPCZ and the ITCZ latitudes (10°S-7°N in January; 5°S-10°N in July).

The two CMIP5 groups exhibit larger (smaller) heating values over the SPCZ (ITCZ) latitudes than the reanalyses in January. In both January and July, the latitudes of peak heating over the ITCZ and SPCZ of group 1 are in the same as the reanalyses; however, the heating maxima in group 2 are found at latitudes that are farther away from the equator than group 1 and the reanalyses. Over the equator, the models have much smaller heating values than ERA-Interim and MERRA-2 in both January and July, although group 1 has smaller averaged heating departure from either ERA-Interim or MERRA-2 than are exhibited in CFSR. The equatorial cooling bias is most severe in group 2 and as with the more widely separated ITCZ and SPCZ heating, these features in group 2 are all consistent with its tropical precipitation climatology as discussed in Chapter 3. The models of group 2 are the ones with the most severe dry equatorial bias throughout all seasons, as the precipitation seasonal cycle figure (Fig. 3.4 in Chapter 3) shows. The dry equators in the group 2 models are wider than in group 1, and the ITCZs/SPCZs tend to be oriented more north/south, as is the related vertically-averaged diabatic heating.

4.3.3 Horizontal Distribution – ERA-Interim Versus Other Datasets

The horizontal distributions of the diabatic heating climatologies of the reanalyses and the CMIP5 models are intercompared for January (Fig. 4.3) and July

(Fig. 4.4). In general, the disagreements of heating patterns among these datasets are larger over the tropics where rainfall is the heaviest and the least uniform among different precipitation datasets (e.g. Fig. 3.1 in Chapter 3). The heating patterns also tend to be diverse over regions with strong fine scale orographic gradients (e.g. the Andes in South America). Compared with the previous generation of reanalyses (e.g. ERA15, ERA40 and NCEP, Fig. 2 & 3 of Chan and Nigam 2009), the three recent reanalyses exhibit much smaller heating differences among themselves, especially in the extratropics. This encouraging result demonstrates the improvement of recent reanalysis datasets that have been generated with better observing systems, models and data assimilation techniques.

The January diabatic heating horizontal distributions (Fig. 4.3) show that larger diabatic heating is found in ERA-Interim over the near-equatorial oceans than in MERRA-2 and CFSR. Compared with ERA-Interim, MERRA-2 exhibits more cooling departures in the Northern Hemisphere, such as over the northern edge of the ITCZ in the western Pacific and in the ITCZs over the central to eastern Pacific and the Atlantic Ocean. CFSR heating is weaker over the entire equator than in ERA-Interim. This corresponds to the lighter precipitation present in CFSR over the equator in the same month (not shown). Over land, ERA-Interim has more heating in the African Monsoon region than the other datasets. The heating/cooling exhibited by the South American monsoon tends to be quite diverse among the reanalyses. In MERRA-2, stronger heating is found along the Andes and over the South Pacific islands than in the other datasets. Similar features can be found in the departure of MERRA-2 annual-averaged precipitation climatology from the TRMM precipitation

(Fig. 3.1 in Chapter 3). Our preliminary research suggests that MERRA-2 has excessive vertical velocity over the same regions in January (not shown) and that the larger heating and precipitation over these regions may be related to these strong vertical velocities.

Compared to ERA-Interim, both the CMIP5 groups exhibit DITCZ-like heating/cooling biases in the eastern Pacific and the Atlantic Ocean. These heating/cooling departures in the eastern Pacific are more obvious in CMIP5 group 1 than in group 2, while those over the tropical Atlantic Ocean are larger in group 2. Across the tropical western-central Pacific, CMIP5 group 2 shows much smaller heating (minimum of heating departures can reach negative 2-3 K/day) than ERA-Interim over the entire equatorial and the near-equatorial regions (10°S-10°N). Group 1 exhibits less heating bias over this region than group 2. Both groups show stronger heating over the Maritime Continent, with more heating in group 2 than group 1. In the ITCZ over the Indian Ocean, group 1 (group 2) has weaker (stronger) heating than ERA-Interim. The heating from the African monsoon in both CMIP5 groups is weaker than in ERA-Interim.

In July (Fig. 4.4), the heating differences are intense and/or extensive in the Indian summer monsoon region and over the tropical western-central Pacific, where rainfall is the heaviest in this month. MERRA-2 exhibits less heating than ERA-Interim in the SPCZ. CFSR continues to exhibit more cooling over the equator in the western-central Pacific. For the CMIP5 groups regarding the Indo-Pacific region, group 1 shows less heating in the heating maxima regions (i.e. over the ITCZ and the equator in the western Pacific, as well as over the Bay of Bengal). In group 2, similar

biases of robust cooling over the equator across the entire Pacific as in January are found in the July heating difference result, together with the heating bias at the northern/southern edge of the ITCZ/SPCZ. The two CMIP5 groups also exhibit stronger heating over the Maritime Continent than ERA-Interim as in January. For the Atlantic ITCZ in July, the two groups both have stronger heating than ERA-Interim. Over land, ERA-Interim still has more heating in the African monsoon region than the other datasets, similar to the January results. ERA-Interim also exhibits larger heating than the other datasets over the Amazon in South America.

In summary, diabatic heating comparisons in both January and July show that MERRA-2 and CFSR diabatic heating are smaller than in ERA-Interim in those regions where ERA-Interim already exhibits smaller heating than the TRMM CSH latent heating (Fig. 4.1), e.g. the Pacific and Atlantic ITCZ in January and the southeastern edge of SPCZ in July. These differences indicate that the diabatic heating and precipitation in ERA-Interim could be more realistic than in both MERRA-2 and CFSR, at least in the tropics.

4.3.4 Hadley Circulation

The zonally-averaged diabatic heating vertical structures in ERA-Interim and the deviances of the other four datasets from ERA-Interim are shown in Fig. 4.5, along with the zonally-averaged Hadley circulations displayed in both wind vectors and mass stream function. The zonally-averaged mass stream function $\psi = 2\pi R cos\phi \int_0^{p_s} [\bar{v}] \frac{dp}{g}$ is a commonly used index to measure the overturning strength of the Hadley circulation (e.g. Oort et al. 1996; Quan et al. 2004). Here, R represents the

planetary radius and g is the gravitational acceleration. The mass stream function is integrated from the top of the atmosphere to the surface. The square bracket represents the zonal mean. Following Oort et al. (1996), the zonally averaged meridional wind vector $[\bar{v}]$ used in this study is corrected by removing the mass-weighted vertical mean value $[\hat{\bar{v}}] = \int_0^{p_s}[\bar{v}]\frac{dp}{p_s}$ from the original v. This is to ensure the zonally-averaged vertical mass balance in each dataset. The positive (negative) values stand for clockwise (counterclockwise) circulations.

Compared with ERA-Interim, the aforementioned seasonal variation of the heating departures (weaker heating in the Northern/Southern Hemisphere in January/July) in MERRA-2 from ERA-Interim and the seemingly seasonally-consistent cooler equator in CFSR can both be explained by their seasonal variability of the Hadley-cell-related diabatic heating and circulation climatology. In January (July), the deep heating center in ERA-Interim is found over the latitudes between 15°S - 5°N (equator - 20°N), while the cooling center is in the Northern (Southern) Hemisphere between 10°- 30°N (10°- 30°S). The northern ITCZ cooling departures of MERRA-2 from ERA-Interim in January in Fig. 4.2 & 4.3 are shown as continuous vertical cooling departures from near surface to 150 mb in Fig. 4.5b. These cooling departures are related to weaker ascending motion at the northern edge (between 5°N to 10°N) of the deep heating center in ERA-Interim, although the MERRA-2 Hadley circulation is stronger than that of ERA-Interim (Table 4.2) in this month. In July, the SPCZ-related cooling departures (15°S to 10°S) of MERRA-2 from ERA-Interim are related to the stronger descending motion of the Hadley cell in MERRA-2. In CFSR, the seasonal Hadley circulation varies quite differently from the

other two reanalyses. In January, the Hadley cell in CFSR is the weakest and is located most southward among the reanalyses; conversely, its July Hadley cell is the strongest and the most northward. Accordingly, the large cooling departures over the equator in CFSR from ERA-Interim in January are a result of both weaker total heating over this latitude and a more southward location of the heating center of CFSR (Fig. 4.5e and Table 4.2). In July, although both the cooling and heating in CFSR are much stronger than in ERA-Interim and MERRA-2, its northward-located Hadley cell and the cooling center lead to more cooling over the equator than in ERA-Interim.

For the CMIP5 models in January, both groups show weaker heating over the 0°-10°N latitudes, especially in group 2. Over the deep heating latitudes, the CMIP5 models have stronger heating than the reanalyses, mostly at lower levels (900-700hPa). These heating/cooling biases in the models and the associated strong Hadley cells correspond with the DITCZ bias in the January precipitation climatology (not shown). In July, group 1 has fewer biases from ERA-Interim than MERRA-2 and CFSR, while group 2 exhibits strong cooling bias above the equator, together with a strong Hadley cell. The center of the group 2 Hadley cell is also located more northward than in the other datasets.

4.3.5 Pacific Walker Circulation

Hartmann et al. (1984) pointed out that the strength and vertical structure of the Walker circulation depend on the vertical structure of diabatic heating. In this section, we diagnose the meridionally-averaged equatorial diabatic heating (averaged

from 5°S to 5°N) over in the tropical Pacific region and the Pacific Walker circulation (PWC) climatology (as in divergent circulation and mass stream function), in order to see how these two features show up in the reanalyses and the models. The mass stream function used here was defined in Yu el al. 2010 as $\psi = 2\pi R \int_0^{p_s} u_{div} \frac{dp}{g}$. u_{div} is the divergent component of the zonal wind u. The mass stream function for the PWC in this study is averaged for the meridional band between 5°S and 5°N. In Fig. 4.6, October and April are the two months chosen since the gradient of sea surface temperature between the western and eastern Pacific is largest in October and smallest in April. This is due to the fact that the cold tongue in the eastern Pacific is the coldest during October and the warmest during April (Dijkstra 2006; Chen et al. 2008). The associated PWC, therefore, tends to be most robust during October and weakest in April.

In October, ERA-Interim exhibits a complete and strong Walker circulation over the equatorial Pacific with the ascending branch and the diabatic heating accumulating over the Maritime Continent. The sinking motion and the cooling center are above the central-eastern Pacific. The maximum cooling center is located between 900 to 800 hPa, with heating existing below 900 hPa. This low-level inversion of heating/cooling is associated with a type of low-level stratiform cloud that can be found in the subsidence region above the well-developed eastern Pacific cold tongue (e.g. Norris and Leovy 1994; Mansbach and Norris 2007). The center of the ERA-Interim mass stream function is found around 165°W (see Table 4.3) at 450hPa. In April, the center of the ERA-Interim PWC is found to be 4.5° - 15° more eastward than in October (Table 4.3), and heating dominates the entire equatorial Pacific

region, as the eastern Pacific SST warms up and the low-level stratus clouds disappear. In both October and April, MERRA-2 exhibits a stronger but narrower and westward-located heating center as well as a stronger inversion of low-level cooling/heating in the eastern Pacific than in ERA-Interim. The related PWC of MERRA-2 is wider and weaker, with its maximum center shifted more westward (~7°- 16°). In CFSR, the deep heating is weaker and is located more westward than in ERA-Interim in both months, but not as far as in MERRA-2. As is the case with the CFSR Hadley circulation, the CFSR PWC is also the most seasonally variable among the reanalysis PWCs. In October when the PWC tends to be the most robust, CFSR exhibits a weaker PWC than ERA-Interim and MERRA-2, along with weaker diabatic heating (cooling) over the western (eastern) Pacific. In April when the PWC is supposed to be the weakest, CFSR shows the most robust PWC among the reanalyses. Although the CFSR deep heating over the western to central Pacific in this month is weak in absolute terms, the cooling and the downward flow over the eastern Pacific are much stronger than in the other reanalyses. Given the fact that CFSR has more cooling over the equator than ERA-Interim and MERRA-2 in January and July as well, this equatorial cooling in CFSR appears to represent a seasonally consistent difference from the other two reanalyses.

Both CMIP5 groups exhibit weaker and more westward-located heating than all the reanalyses in October and April. In October, group 1 has the least robust deep heating and cooling among all the datasets, along with the weakest PWC. Although the PWC in group 1 is in a similar longitude range as ERA-Interim and CFSR, its maximum center is located around 10° more eastward. The maximum center of the

PWC in group 2 is 2.5° farther eastward. These biases above are even worse in April. The maximum centers of the PWCs in the models are located 10° - 20° more eastward than in the reanalyses. The weak heating centers in the CMIP5 models correspond with weak and wide PWCs. The PWC in group 2 is the broadest and even has two maximum centers.

4.4 Regional Heating Profiles

The regional vertical heating profiles are intercompared among the TRMM CSH latent heating and the diabatic heating of the three reanalyses and CMIP5 group 1 for the period of 1998-2005 (Fig. 4.7). These heating vertical profiles, to a certain extent, reveal the convective-stratiform mix of precipitation, given the rather different characteristic heating profiles associated with the two precipitation processes (Fig. 3 in Houze 1997). Four regions with different types of precipitation are chosen to study the vertical heating profile differences: Indian summer monsoon (80° - 90°E, 20° - 25°N); Maritime Continent or the Malaysian-Australian monsoon (130° - 155°E, 10°S - 0°); South America monsoon (55° - 40°W, 20°S - 0°); and winter storm tracks in the northern Pacific (145° - 175°E, 32.5° - 35°N). Among these four regions, the first two are characterized by deep convection intensified by the seasonal merger of the ascending branches of Hadley cells and the PWC in the western Pacific. The South American monsoon is characterized by the strong continental convection that is mostly triggered by orographic lift and surface heating. The Pacific winter storm tracks, on the other hand, are synoptic systems that produce extensive amount of

stratiform cloud/precipitation (Weaver, 2003). The Indian summer monsoon region is shown by the box drawn in Fig. 4.4, while the other three are marked on Fig. 4.3.

TRMM CSH latent heating serves as a reference here rather than to validate the reanalyses. The older version of this TRMM CSH latent heating used in Chan and Nigam (2009) is shown to be smaller than the ERA40 and NCEP diabatic heating in the entire troposphere, even as much as twice smaller in the mid to lower troposphere. In this study, although the updated TRMM CSH latent heating exhibits larger diabatic heating than the reanalyses in the middle troposphere in two convective precipitation regions (Fig. 4.7a&c), the total CSH latent heating is comparable to the reanalysis diabatic heating, as the small latent heating in upper and lower troposphere can potentially cancel out the larger mid-tropospheric counterpart. This shows an improvement of this newer version of the TRMM CSH latent heating.

a. Indian Summer Monsoon

The Indian summer monsoon vertical heating profiles (Fig. 4.7a) exhibit the archetypical bow shape f convective heating (Houze 1997), with a heating peak in the middle to upper troposphere. Between 500-400 hPa, the TRMM CSH latent heating is about double (~9 K/day) compared to the diabatic heating of the reanalyses and the CMIP5 models (4-5 K/day). The TRMM CSH latent heating also shows a secondary heating peak at 700hPa more obviously than the other datasets. This heating peak, as well as those in the other convective regions (Fig. 4.7b&c), was not found in Fig. 4.9 of Chan and Nigam (2009) and could be a result of the more diverse heating profiles used for generating the TRMM CSH (Tao et al. 2010). Among the reanalyses, the

heating profiles of ERA-Interim and CFSR are very close to each other, while MERRA-2 exhibits larger heating (up to 1.5K/day, which is about 37.5% larger than in ERA-Interim) from 800 to 200 hPa. The heating values of CMIP5 group 1 are generally close to but slightly smaller than those of ERA-Interim and CFSR. ERA-Interim and the CMIP5 group 1 models show peak heating at 500 hPa, while the others peak at 400 hPa.

b. Maritime Continent/Malaysian-Australian Monsoon

The convection over the Maritime Continent is very intense in January because, as with the Indian monsoon in Boreal summer, the ascending motion associated with both the Hadley cell and the Pacific Walker cell are located in this region. The heating vertical profiles over the Maritime Continent are similar to those in the Indian summer monsoon region, except that the heating profiles of the reanalyses in this region vary more than in the Indian monsoon region. The profile of the MERRA-2 diabatic heating (maximum heating about 2K/day or about 50% larger than in ERA-Interim) is comparable to the TRMM CSH latent heating profile. ERA-Interim, CFSR and the CMIP5 group 1 continue to show very similar vertical profiles, with the heating maxima in the similar range as in the Indian monsoon region (around 3-4 K/day at 500-400 hPa).

c. South American Monsoon

The diabatic heating vertical profiles over the South American monsoon region of ERA-Interim, MERRA-2, CFSR and CMIP5 group 1 agree remarkably well

with each other. Since the convection in this region is not as strong as in the other monsoon regions, both the deep heating and the lower level shallow heating in these regions (~2-3 K/day) are smaller in these datasets. The heating maxima are also lower, at levels about 550-500 hPa. The TRMM CSH latent heating, however, continues to show a profile that is very similar to those of the other two monsoon regions, with the heating maximum being 6.5K/day at around 400 hPa.

d. Northern Pacific Winter Stormtrack

The northern Pacific winter stormtrack, unlike the other regions, has a large amount of stratiform precipitation. The latent heating of this type of precipitation is shown as a reverse S-shaped profile in the TRMM CSH latent heating in Fig. 4.7d. This is because of cooling due to melting of ice particles in the lower troposphere below the bow-shaped positive heating profile in the middle to upper cloud layers. The diabatic heating of the reanalyses in Fig. 4.7d exhibits a reverse profile from the TRMM latent heating and they agrees very well in the upper troposphere but become more diverse at the lower levels.

4.5 ENSO-related Diabatic Heating and Atmospheric Circulations

The ENSO time series used in this section for the reanalyses is the first EOF time series of the detrended DJF-averaged HadISST 1.1 (domain of 75°S-75°N). Fig. 4.8 shows that this time series resembles the detrended DJF-averaged Niño 3.4 index with a correlation coefficient of 0.96, and well captures the strong El Niño events during the boreal winters of 1982, 1997 and 2015. The ENSO covariant diabatic

heating and atmospheric circulation fields are then generated from regression with this time series. The regression analysis used in this study projects the ENSO time series onto the time series of the diabatic heating anomaly or atmospheric circulation (e.g. wind and mass stream function anomalies) fields to determine the optimal (in the sense of maximal explained variance/linear correlation) linear relationship between the two time series at each grid point.

For every CMIP5 model used in this study, the SST first EOF time series is calculated for each ensemble member of each model and is regressed onto the member's diabatic heating/atmospheric circulation anomaly field. The model group results shown in this section are weighted averages of all the members in the selected group based on the number of the members of each ensemble.

4.5.1 ENSO-related Diabatic Heating Horizontal Distribution

The vertically-averaged ENSO covariant diabatic heating anomaly field is shown in Fig. 4.9. In ERA-Interim, the ENSO-related diabatic-heating pattern is similar to the DJF-averaged ENSO-related precipitation results (Fig. 4.7b in Chapter 3). Strong heating anomalies that reflect robust precipitation can be found in the central and eastern Pacific. The maximum heating anomaly center in ERA-Interim is located just east of 180° in the southern off-equatorial region. The cooling anomalies that are related to rainfall reduction are found over the western Pacific/Maritime Continent and the SPCZ region. Compared with ERA-Interim, MERRA-2 has a westward shift of the heating anomaly center as well as more robust cooling anomalies in the Maritime Continent and the SPCZ. Similar to MERRA-2, CFSR

exhibits a westward shift of its heating anomalies from ERA-Interim. In addition, CFSR shows weaker heating anomalies than are found in both ERA-Interim and MERRA-2 over the equator across the central to eastern Pacific.

In CMIP5 group 1, the heating anomalies in the tropical Pacific are more westward-extended than in the reanalyses, as in the ENSO-related precipitation results in Chapter 3 (Fig. 3.8). In closer inspection, unlike in ERA-Interim, the maximum center in CMIP5 group 1 is located west of 180° to the south of equator and extend to the east. CMIP5 group2 shows an even more westward located maximum heating anomaly center (~150°E). The ITCZ-related heating anomalies (> 0.1 K/day) in group 2 are found to be less zonally extensive than their SPCZ-related counterparts, with a span only from the Maritime Continent to 160°W. The heating anomalies in group 2 over the equator across the central to eastern Pacific are all smaller than 0.1K/day (others datasets exhibit greater than 0.2K/day). This bias is similar to the group 2 bias of ENSO-related rainfall reduction over the equatorial Pacific that was demonstrated to be strongly related to the dry-equator bias in the corresponding precipitation climatology (Chapter 3). As for the models' cooling anomalies, group 1 exhibits an ENSO-related cooling anomaly pattern in the tropical Indo-Pacific similar to that in ERA-Interim, except that the cooling anomalies over the equator across the Maritime Continent are much weaker (<0.1K/day) and separate the cooling anomalies to the north of the equator from those to the south. Although the equatorial cooling anomalies in group 2 are shifted to the west of the Maritime Continent, they are more robust than in group 1 and connect the northern and southern off-equatorial cooling anomalies as shown in the reanalyses. This difference

between the two groups suggests that the group 1 or 2 models are not necessarily "good" or "bad" models in simulating every feature of ENSO.

4.5.2 ENSO-related Stream Function and Velocity Potential at 800 and 200 hPa

The ENSO-related horizontal wind fields at upper (200hPa) and lower (850hPa) levels are examined in this section to understand how the atmospheric circulation differences are related to the aforementioned ENSO-related diabatic heating biases. The horizontal wind fields are partitioned into nondivergent (represented by stream function) and irrotational (represented by velocity potential) components.

The ENSO-related velocity potential anomalies at 850hPa (shown as colors in Fig. 4.10 left column) in the reanalyses are characterized by an east-west dipole near the equator with a positive anomaly center east of the dateline (~110-150°E) and a negative one in the west (160°W-120°W). At 200hPa (Fig. 4.10 right column), the anomaly centers show a reverse dipole pattern: the divergence center is located over the central equatorial Pacific (~180°-140°W); and the convergence center is found north of the Maritime Continent. The areas of convergence (divergence) at 850hPa are clearly associated with the areas of divergence (convergence) at 200hPa and by continuity this indicates anomalous upward (downward) motion through the majority of the troposphere.

The ENSO-related stream function anomalies at 850hPa (shown as lines in Fig. 4.10 left column) in the reanalyses show an anticyclonic circulation over the central Pacific in the Southern Hemisphere, with its center (~140°W) close to the zero

stream function line at the equator. The easterly anomaly flow near the equator over the central Pacific is very zonal; whose representation is the lower branch of the Walker circulation anomalies. At 200hPa, the stream function anomalies over the central Pacific region are characterized by the twin tropical gyres on each side of the equator and the zonal equatorial flows (upper branch of the Walker circulation anomalies) in between. In the Indo-Pacific region, the stream function anomalies at 850hPa show a small clockwise gyre north of the Maritime Continent and a relatively larger counterclockwise one in the west of Australia. The anomaly flow between them is in the southeast/northwest direction, same as the case in 200hPa.

At 850hPa and 200hPa, the anomalies of velocity potential and stream function in ERA-Interim, MERRA-2, and CFSR are very similar. The convergence (divergence) anomaly center at 850hPa (200hPa) in ERA-Interim is the weakest and is located farthest eastward among the three reanalyses, consistent with the weakest and the most eastward-located diabatic heating anomaly center of ERA-Interim. For the CMIP5 models, both the ENSO-related convergence/divergence anomaly centers and the horizontal circulations are generally much weaker than in the reanalyses. Although the velocity potential and the stream function anomalies in group 1 are more similar to the reanalyses than those in group 2, group 1 exhibits two stronger and more equatorially-symmetrical gyres in the north and south of the equator in the Indian Ocean/Maritime Continent region that are closer to each other (meaning that the flow in-between is faster), compared with the reanalyses. The flow between these two gyres is also very zonal without much curvature, as is the zonal flow at 200hPa above the same region. Considering that the divergence/convergence in group 1 is

much weaker than in the reanalyses, one can speculate that these zonal horizontal flows might dominate above the equatorial Indian Ocean/Maritime Continent region and the linked descending motion may be relatively less robust than in the other datasets, thus the weaker cooling anomalies in the same region (Fig. 4.9d).

The group 2 models exhibit the weakest velocity potential and stream function anomalies among all the datasets. At 850hPa (200hPa), these models have weak convergence (divergence) anomalies west of the dateline. However, their 200hPa equatorial zonal flow between the two central Pacific gyres (upper branch of the Walker circulation anomalies in the other datasets) is located much more eastward (~135°W) than in the reanalyses and group 1, and therefore are extremely far away from the convergence/divergence center and the related convection in the western Pacific. This horizontal inconsistency between the already-weak rotational and divergent flow of group 2 indicates that the linked vertical motion could be less robust in group 2 and as is its PWC anomalies.

4.5.3 Pacific Walker Circulation

The ENSO-related diabatic heating cross section along the equatorial Pacific (averaged from 5°S to 5°N) is shown in Fig. 4.11. In ERA-interim, the deep heating extends from 160°E to 80°W. The heating center (>1.2K/day) inclines from the lower-level convergence center (~900-700hPa) over 160°W-125°W towards an upper divergence center around 180°-140°W. The ENSO-related cooling in ERA-interim is found over the western Pacific (west of 160°E). MERRA2 exhibits a stronger upper heating center located more towards 160°E than in ERA-interim with a westward

shift of about 8.25° (see the location of maximum mass stream function of PWC in Table 4.4). The cooling center over the western Pacific in MERRA2 is also more robust than in ERA-interim. For CFSR, the ENSO-related deep heating center and the PWC are also located more westward than in ERA-interim. CFSR also has less robust heating than ERA-interim over the central to eastern Pacific in both the lower and mid to upper troposphere. The overturning strength of the ENSO-related PWC in CFSR is the largest among the three reanalyses (Table 4.4).

In regard to the CMIP5 models, as expected, both groups exhibit weaker ENSO-related deep heating and the related PWC anomalies than do the reanalyses. In group 1, since the lower level convergence center is located in the same longitudes as in the reanalyses while the upper divergence center is displaced more westward (Fig. 4.10), its ENSO-related PWC upper pole tilts toward the west more than in the other datasets, and so does its ENSO-related diabatic heating. This shows how the vertically-averaged ENSO-related diabatic heating in group 1 extends more westward (due to the heating residual from the upper westward-located heating). The maximum center of the mass stream function in the group 1 PWC is also found to be more westward (~10°-18°) than in the reanalyses. CMIP5 group 2, as discussed in the previous section, is expected to have the least robust ENSO-related PWC and diabatic heating anomalies. In fact, we see that group 2 exhibits in Fig. 4.11 a PWC-like local vertical circulation over the 120°E-160°E longitude range, with about 30° more westward displacement compared with the one in ERA-Interim. This circulation is far more narrow than in the other datasets. The diabatic heating anomalies are also accumulated to the west of 180° and can only be discharged to the west (in the

reanalyses and group 1, the heating can be discharged to both the west and the east) due to the far eastward-displaced upper level westerly anomalies. One might speculate that the large biases of group 2 compared to the reanalyses are related to both the weak lower-level convergence and lack of extensive upper westerly anomalies, making it difficult for the group 2 models to sustain the ENSO-related heating center/PWC that is strong enough to expand from western Pacific to the central or eastern Pacific.

4.5.4 Regional Hadley Circulations

Since the ENSO influence is the most robust over the tropical Pacific and Indo-Pacific regions, we choose two representative longitude sectors to show the sector-averaged ENSO-related Hadley cells and the related diabatic heating. One is the central Pacific (180° - 150°W), which includes the heating maxima of the reanalyses in Fig. 4.9; the other is the western Pacific (110°E - 130°E), the region of deep cooling and the descending branch of the ENSO-related PWC anomalies in the reanalyses. The mass stream function of the regional Hadley circulations is defined as $\psi = 2\pi R cos\phi \int_0^{p_s} v_{div} \frac{dp}{g}$ (Zhang et al. 2015). v_{div} is the divergent component of the meridional wind. The mass stream function of the regional Hadley cell is scaled by the coefficient of 2π in order to match the global one and is integrated from the top of the atmosphere to the surface. Unlike the zonally-averaged mass stream function of the Hadley circulation in section 4.3.d (Oort et al. 1996), the regional Hadley circulation mass stream function does not require ψ at the top and lower boundary to be zero in order to ensure mass conservation.

The vertical structures of ENSO-related diabatic heating anomalies and the related Hadley circulation in the central Pacific sector are shown in Fig. 4.12. In ERA-Interim, the ENSO-related diabatic heating/cooling anomalies are not symmetrically distributed in the two hemispheres. The heating anomalies over the equatorial region are more extended to the south (up to 10°S) than their counterparts in the north (0°-5°N). The heating maximum is also located in the Southern Hemisphere. The cooling anomalies in the Northern Hemisphere have a minimum center over about 7°N at the lower level of the troposphere (~800hPa), while those in the Southern Hemisphere exhibit a minimum center in the middle troposphere over ~18°N-20°N. Consistent with the asymmetrical heating/cooling, the center of the southern ENSO-related Hadley cell anomalies over the central Pacific is located more off the equator (Table 4.4). In MERRA-2, the deep heating anomalies are more expanded toward the higher latitudes in both hemispheres compared to those in ERA-Interim, especially in the middle to upper troposphere. However, the heating anomalies in MERRA-2 over 0°-5°S are slightly weaker than in ERA-Interim. The overturning strength of MERRA-2's ENSO-related Hadley cells anomalies is the strongest among the reanalyses, in both hemispheres. In CFSR, the heating anomaly pattern is also wider than in ERA-Interim, but only in the Northern Hemisphere. The heating anomalies in CFSR over 0°-5°S are generally less robust than in ERA-Interim, except for those at 750-650hPa. The overturning strength of the ENSO-related Hadley cell anomalies in CFSR is in between those of ERA-Interim and MERRA-2.

In CMIP5 group 1, although the vertical structures of the ENSO-related heating/cooling anomalies and Hadley cell anomalies are similar to those of the reanalyses, this group exhibits weaker ENSO-related heating/cooling anomalies in the central Pacific. This is partially due to the fact that the maximum heating anomaly center is further from the central Pacific (~15° more westward). The heating anomaly structure in group 1 is wider (more in the Northern Hemisphere) and lower than that in ERA-Interim. The cooling anomaly center over the Southern Hemisphere is also found to be lower than in the reanalyses. In group 2, since the maximum heating anomaly center is completely located in the western Pacific, the heating anomalies over 0°-5°S are very weak. Both of its northern and southern Hadley cell anomalies are also much weaker and more off the equator than in group 1 and the reanalyses.

In the western Pacific sector (Fig. 4.13) where the ENSO-related cooling anomalies are most robust, ERA-Interim exhibits two dominant cooling anomaly centers, one in each hemisphere, with the northern one much stronger than the southern one. In between these two centers, there is also a center at 5°S that is not as robust as the other two. Both MERRA-2 and CFSR only show the two major cooling anomaly centers without the one over the equator as shown in ERA-Interim. MERRA-2 continues to exhibit the most robust cooling and Hadley cell anomalies among the reanalyses. In CFSR, the cooling anomaly center in the Northern Hemisphere is located at 700hPa instead of 500-400hPa in ERA-Interim or MERRA-2, and the center is more northward-located than in the other reanalyses. The centers of the ENSO-related Hadley cell anomalies in CFSR are also more separated from each other than in ERA-Interim and MERRA-2.

Both CMIP5 groups exhibit the two cooling anomaly centers that are farther away from each other (in the poleward direction) than in reanalyses in the western Pacific, as are their two ENSO-related Hadley anomaly centers. The CMIP5 models also show less robust cooling anomalies over 0°-5°S. Group 1 shows stronger cooling both north and south of the equator compared to ERA-Interim. However, its cooling anomalies at middle to higher tropospheric levels are very weak, consistent with the dry/cooling equatorial anomaly band in the Indo-Pacific region in Fig. 4.9. The Hadley cell anomalies over the equatorial region are the strongest in group 1. Although group 2 has the weakest ENSO-related cooling anomalies and its two Hadley cell anomaly centers are the most distant from each other, the models in group 2 exhibit stronger upper-level cooling than those in group 1.

4.6 Discussion

We have dissected the 3D structure of the diabatic heating and atmospheric circulation in the reanalyses and CMIP5 models and have shown the intermodel diversity of these heating and circulation biases in the models. In the previous chapter, we demonstrated that the biases of ENSO-related precipitation (diabatic heating) could be related to those of the ENSO-related SST anomalies (Fig. 3.14, Chapter 3). Therefore, it is intriguing to see how positive Bjerknes feedback (Bjerknes 1969), a fundamental ocean-atmospheric mechanism for growth of El Niño or La Niña that links the SST, atmospheric diabatic heating, and surface wind stress altogether, can further contribute to our understanding of the intermodel diversity of ENSO.

In this section, we focus on the positive Bjerknes feedback from an atmospheric perspective, illustrated as follows (Zheng et al. 2014):

$$\frac{dSST}{dx} \rightarrow \frac{dQ}{dx} \rightarrow \frac{dSLP}{dx} \rightarrow \tau_x \rightarrow \frac{dSST}{dx}$$

Bjerknes hypothesized that initial positive SST anomalies in the equatorial eastern Pacific reduce the zonal SST gradient (dSST/dx) and hence the strength of the Walker circulation, resulting in weaker trade winds over the equator. The weaker trade winds/wind stress (τ_x) further weakens $dSST/dx$ (due to less upwelling) and reinforces the warm event. This applies vice versa to La Niña events. Inside of this positive Bjerknes feedback loop between $dSST/dx$ and τ_x, there exist three subprocesses: (1) changes of $dSST/dx$ cause the zonal gradient changes of the total diabatic heating (dQ/dx) through atmospheric convection and phase change of water vapor, leading to (2) reduction or intensification of the Walker circulation and the related change in zonal sea level pressure gradient ($dSLP/dx$), which in turn (3) influence the surface zonal wind stress (τ_x).

In order to numerically measure this positive Bjerknes feedback and its subprocesses in the reanalyses and the models, we use a method that is very similar to the one employed in Zheng et al. (2014). We calculate the cross-basin gradient dx for $dSST$ and $dSLP$ as the anomaly average (either SST or SLP) within an eastern to central Pacific box (160°-120°W, 5°S-5°N, which is included in the Niño 3.4 box) minus the average within a western Pacific one (120°-160°E). For the zonal gradient of diabatic heating (dQ/dx), the western Pacific box is the same as for $dSST/dx$ or $dSLP/dx$, while the central Pacific one is chosen as 170°E-150°W, 5°S-5°N,

representing the region with the maximum positive diabatic heating anomalies. All the variables above as well as τ_x anomalies have been DJF-averaged and regressed onto the ENSO time series in Section 4.5 before the following calculations. The Bjerknes feedback is estimated using linear regression of the ENSO-related τ_x along the Pacific equator (averaged from 5°S to 5°N) on the ENSO-related $dSST/dx$. The same calculation has been applied to subprocess 3 to find connections between anomalies of τ_x and $dSLP/dx$.

The Bjerknes feedback results (Fig. 4.14a) show that the maximum response of ENSO-related τ_x to ENSO-related $dSST/dx$ is located around 170°W in the reanalyses. Both CMIP5 groups exhibit weaker Bjerknes feedback than in the reanalyses. The feedback curve shape in group 1 is similar to that of the reanalyses but is slightly more westward shifted. Group 2 has a much flatter curve that is closer to the zero line than in group 1 and the reanalyses. This means that the Bjerknes feedback is weaker in group 2 across the Pacific basin, except the range of 135°-160°E in which the absolute regression values are higher than group 1 and the reanalyses. The group 2 also has larger intermodel diversity than group 1. With regard to the Bjerknes feedback subprocess 3 (Fig. 4.14b), ENSO-related τ_x and ENSO-related $dSLP/dx$ exhibit negative regression coefficients over the central Pacific, with the minimum value being located ~170°W. Group 1 shows weaker and slightly more westward-shifted response of ENSO-related τ_x anomalies to dSLP/dx than the reanalyses. The differences between the means of group 2 and group 1 are not very large across the Pacific besides in the western Pacific. The group 2 models

continue to exhibit larger intermodel diversity than group 1 in terms of this Bjerknes feedback subprocess.

In both of the other two subprocesses (Fig. 4.14 c & d), we can see in the scatter plot that the points representing group 1 (red asterisks) are closer to those of the reanalyses (black asterisks), while the group 2 cluster (blue asterisks) is almost perpendicular to the reanalyses cluster, especially in Fig. 4.14d. For subprocess 1 ($\mathrm{dQ/dx}$ versus $\mathrm{dSST/dx}$, Fig. 4.14c), the cluster of points representing group 2 are generally closer to a slope of zero, meaning that the ENSO-related $\mathrm{dQ/dx}$ in group 2 is less influenced by the change of ENSO-related zonal SST gradient. Fig. 4.14d shows that the Bjerknes feedback subprocess 2 in group 2 tend to have the opposite sign of the relation between $dSLP/dx$ and dQ/dx to that found in the reanalyses. These results suggest that differences of Bjerknes feedback between group 1 and 2 may be mostly due to the relationship between $\mathrm{dQ/dx}$ and the zonal gradient of SST anomalies and the response of zonal gradient of SLP anomalies to $\mathrm{dQ/dx}$.

As we have seen, the group 2 models tend to simulate weaker ENSO-related atmospheric features, such as precipitation anomalies and their seasonality (Chapter 3), total diabatic heating, convergence and divergence at the lower and upper levels, the Walker Circulation, the local Hadley cells, and the positive Bjerknes feedback. We have also examined near-surface variables including ENSO-related sea level pressure, zonal and meridional surface wind stress, surface wind stress curl, and both the du/dx and dv/dy components of surface divergence (Nigam et al. 1992). These near-surface ENSO-related features (not shown) are also simulated much less robustly in group 2 than in group 1 and the reanalyses. All of this evidence indicates

that the ENSO variability in the group 2 models is much weaker than in group 1 and the reanalyses, from the perspectives of mean states, seasonality, and development phase of ENSO (positive Bjerknes feedback).

4.7 Summary

Diabatic heating and the related circulation further reveal the model biases of mean and ENSO-related precipitation described in the previous chapter. In this chapter, we have intercompared and diagnosed the 3D tropical diabatic heating and the related atmospheric circulation in three state-of-the-art atmospheric reanalyses (ERA-Interim, MERRA-2 and CFSR) and two CMIP5 model groups from the perspectives of both climatology and ENSO.

In this study, we chose ERA-Interim as the basis when comparing to the other datasets and have validated the ERA-Interim diabatic heating with the latent heating from the Tropical Rainfall Measuring Mission (TRMM) estimates of the convective and stratiform components of precipitation. These two estimates of heating closely resemble each other in the heavy rainfall region over the tropical Pacific Ocean, suggesting that the tropical ERA-Interim diabatic heating can be credible.

Among the three reanalyses, we found the following results:

- Although the heating climatology and ENSO-related diabatic heating profiles of ERA-Interim, MERRA-2, and the CFSR are very similar, there exist fundamental diabatic heating differences among the three reanalyses.
- MERRA-2 tends to show less diabatic heating than ERA-Interim in those regions where ERA-Interim already exhibits smaller heating than the TRMM

CSH latent heating, e.g. the Pacific and Atlantic ITCZ in January and the SPCZ in July. CFSR exhibits seasonally consistent cooling departures over the equator relative to ERA-Interim. These differences indicate that the tropical diabatic heating and precipitation in ERA-Interim could be more reliable than in both MERRA-2 and CFSR.

- The ITCZ-related cooling departures in MERRA-2 from ERA-Interim in January are related to the weaker ascending motion of its Hadley cell at the northern edge of the deep heating region, and the MERRA2 SPCZ-related cooling departures in July are associated with the stronger descending motion of the associated Hadley cell. The Pacific Walker circulation (PWC) related diabatic heating (both of the mean climatology and during ENSO) in MERRA-2 are more westward than in ERA-Interim and CFSR both in climatology and ENSO. The diabatic heating profiles of MERRA-2 in the middle to upper troposphere tend to be larger than ERA-Interim and CFSR, especially over the deep convective regions.
- CFSR tends to have the most seasonally variable Hadley cells and PWC among the reanalyses. These variations lead to seasonally-consistent cooling departures over the equatorial Pacific in CFSR from ERA-Interim and MERRA-2. Similar cooling departures also show up in the CFSR ENSO-related diabatic heating anomaly results. The CFSR diabatic heating vertical profile over regions with different types precipitation are very close to those of ERA-Interim.

For the diabatic heating climatology and ENSO-related diabatic heating in the CMIP5 group 1 (the better performing one) and group 2 (the underperforming one), we have found that:

- In general, the CMIP5 group 1 models simulate diabatic heating and the related atmospheric circulation features much more similar to those in the reanalyses than do the group 2 models. Group 1 even exhibits diabatic heating vertical profiles of different types of precipitation similar to those of ERA-Interim and CFSR. Group 2, on the other hand, shows more biases in the climatology and the ENSO results, especially in the PWC-related features.
- For the diabatic heating climatology, the two groups exhibit larger biases over the tropical eastern Pacific and the tropical Atlantic Ocean (e.g. the double-ITCZ-like features). The group 2 shows a severe bias in the seasonally-consistent weaker heating over the equator, which is similar to the bias of a dry equator in its precipitation climatology in the previous chapter. These biases seem to be related to the stronger Hadley cells in the models than in the reanalyses. The maximum centers of the PWCs in both groups tend to be located 10° - 20° more eastward than in the reanalyses. Unlike the other datasets, the PWC in group 2 in April is very weak and broad with two maximum centers instead of the single center found in the others.
- With respect to the ENSO-related diabatic heating in CMIP5 models, both groups of models showed patterns of more westward-located heating/precipitation anomaly centers, consistent with the westward-located lower (upper) convergence (divergence) center. The group 2 diabatic

heating/precipitation anomaly maximum center is located far more westward over the equator than in every other dataset (30° more westward than the one in ERA-Interim), with a span only from the Maritime Continent to around the dateline.

- The group 2 models tend to simulate weaker ENSO variability in terms of mean states and seasonality as well as ENSO growth compared to the group 1 models, as indicated by features such as precipitation, total diabatic heating, the rotational and irrotational flows at the lower and upper levels, the Walker Circulation, the local Hadley cells, the positive Bjerknes feedback and the near-surface wind features. These weaker ENSO-related structures in group 2 result in a weak PWC-like vertical anomaly circulation located only in the western Pacific, consistent with the related diabatic heating anomalies. The weak heating can only be discharged to the west at the top of the troposphere due to the dislocation of the upper-level westerly anomalies, which further increase the difficulty to sustain broader ENSO-related PWC anomalies.
- The group 2 models also have a weaker and more westward-located maximum Bjerknes positive feedback than the group 1 models and the reanalyses during ENSO. These models also simulate unrealistic subprocesses in the ENSO-related Bjerknes positive feedback. For example, the zonal gradient of the total diabatic heating ($\mathrm{dQ/dx}$) is nearly unaffected by the change of zonal gradient of SST ($dSST/dx$). The relationship between the zonal sea level pressure gradient ($dSLP/dx$) and the change of dQ/dx in group 2 is opposite from the one in the reanalyses.

- Although group 1 exhibits much stronger resemblance to the reanalyses than group 2 in most of the heating and circulation features, these findings do not necessarily mean that the group 2 models provide less realistic simulations in every ENSO feature. For example, group 2 exhibits more robust ENSO-related cooling anomalies across the equatorial Maritime Continent than group 1, more closely resembling the reanalyses.

Concerning these large biases of the group 2 ENSO-related diabatic heating and the PWC anomaly cell, it is useful to see how these biases are connected with the background climatology biases. As we have seen in the previous chapter and the discussion above, the patterns of the climatology and the ENSO features/biases, especially those that are seasonally persistent, are closely related. For example, the group 2 dry bias of the ENSO-related precipitation anomalies over the equator is robustly related to the dry equator bias in the climatology (Chapter 3); the westward located ENSO-related heating anomaly center and the related PWC anomalies in MERRA-2 are consistent with the westward-located deep heating center in the heating climatology. One more thought is provided here on how the ENSO-related biases in group 2 are related to the climatology biases. The DJF-averaged PWC (not shown) in group 2 is very similar to the one in April (Fig. 4.6), with two weak centers, one of which is located ~35° more eastward than the maxima in the reanalyses. As this PWC bias and the related weaker diabatic heating in group 2 dominate in both the DJF and MAM seasons, the models may be more likely to

simulate weak ENSO-related PWCs and the associated heating/precipitation anomalies.

Table 4.1 Standard deviation of diabatic heating among ERAint, MERRA-2, CFSR and the two CMIP5 groups at certain latitudes.

Standard deviation	Equator (0°)	ITCZ	SPCZ
January	0.31	0.27 (3.5°N)	0.07 (8.5°S)
July	0.20	0.15 (8.5°N)	0.08 (5°S)

Table 4.2 Maximum or minimum value of zonally-averaged Hadley circulation mass stream function and its location. Unit: $\times 10^{10}$ Kg/s. The number of positive value, for example 21.82, means that there is an amount of 21.82×10^{10} Kg/s mass being transported northward above the level of this maximum value and an equal amount flowing southward below it. The Negative value represents motions in the reverse directions.

Mass Stream Function Maximum	ERA-Interim	MERRA-2	CFSR	CMIP5 Group 1	CMIP5 Group 2
January	21.82 (9°N, 700hPa)	22.70 (9°N, 750hPa)	20.44 (8.75°N, 700hPa)	23.81 (8.75°N, 700hPa)	21.84 (8.75°N, 700hPa)
July	-24.51 (3°S, 700hPa)	-24.93 (6°S, 700hPa)	-26.53 (1.25°N, 650hPa)	-24.74 (1.25°S, 700hPa)	-25.26 (1.25°N, 700hPa)

Table 4.3 Maximum value of the mass stream function and its location of the equatorial Walker circulation over the entire Pacific (averaged from 5°S to 5°N). Unit: $\times 10^{10}$ Kg/s. The number of value, for example 15.62, means that there is an amount of 15.62×10^{10} Kg/s mass being transported eastward above the level of this maximum value and an equal amount flowing westward below it.

Mass Stream Function Maximum	**ERA-Interim**	**MERRA-2**	**CFSR**	**CMIP5 Group 1**	**CMIP5 Group 2**
October	15.62 (164.25°W, 450hPa)	14.88 (180°, 450hPa)	13.64 (166.25°W, 550hPa)	13.25 (156.25°W, 500hPa)	14.10 (153.75°W, 500hPa)
April	15.16 (159.75°W, 550hPa)	14.49 (166.5°W, 600hPa)	16.09 (158.75°W, 550hPa)	10.05 (148.75°W, 600hPa)	10.05 (138.75°W, 600hPa)

Table 4.4 Maximum/minimum value and the location of mass stream function of ENSO-related Pacific Walker circulation (averaged over 5°S - 5°N) and local Hadley circulation cross-sections in the central Pacific sector (180° - 150°W) and the western Pacific sector (110°E - 130°E). Unit: $\times 10^{10}$ Kg/s. The positive (negative) value stands for clockwise (counterclockwise) circulation.

Mass Stream Function Maximum or Minimum	**ERA-Interim**	**MERRA-2**	**CFSR**	**CMIP5 Group 1**	**CMIP5 Group 2**
Pacific Walker Circulation	-8.50 (169.50°E, 400hPa)	-8.60 (161.25°E, 450hPa)	-8.68 (163.75°E, 450hPa)	-7.15 (151.25°E, 400hPa)	-7.08 (138.75°E, 400hPa)
Local Hadley Cell – central Pacific	8.58 (5.25°N, 800hPa)	9.62 (5.25°N, 800hPa)	9.41 (6.25°N, 800hPa)	7.17 (6.25°N, 700hPa)	2.53 (26.25°N, 400hPa)
	-8.87 (11.25°S, 400hPa)	-9.31 (13.5°S, 450hPa)	-9.31 (11.25°S, 450hPa)	-7.03 (11.25°S, 400hPa)	-3.24 (13.75°S, 500hPa)
Local Hadley Cell – western Pacific	-6.59 (16.5°N, 350hPa)	-7.33 (16.5°N, 400hPa)	-6.79 (18.75°N, 350hPa)	-4.86 (18.75°N, 500hPa)	-2.90 (26.25°N, 500hPa)
	3.96 (-16.5°S, 400hPa)	4.96 (17.25°S, 550hPa)	4.71 (18.75°S, 400hPa)	4.31 (21.25°S, 400hPa)	2.48 (18.75°S, 400hPa)

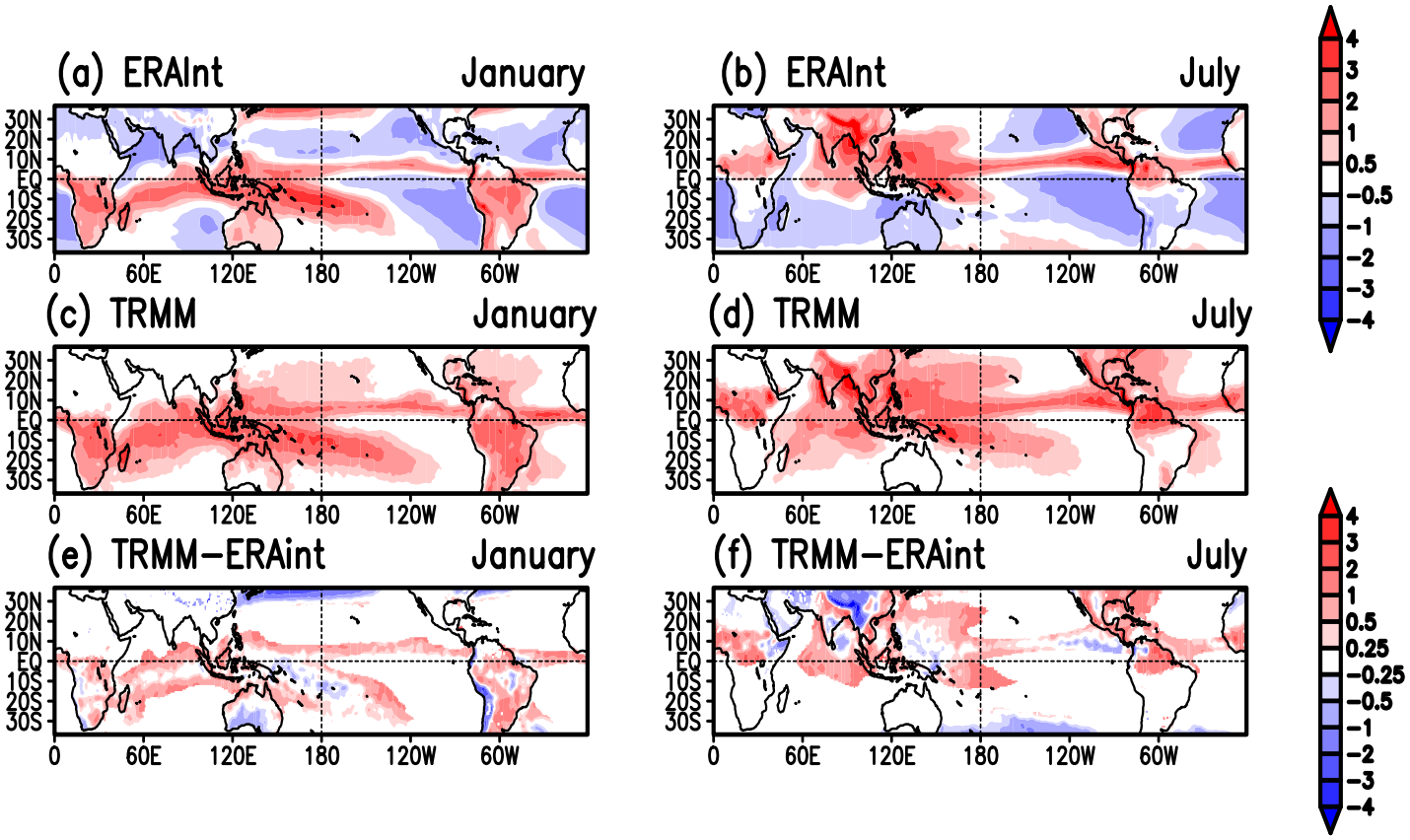

Figure 4.1 TRMM CSH latent heating and ERA-Interim mass-weighted vertically-averaged diabatic heating in January and July (a-d) and their differences (e-f) (averaged from 1000-150hPa, 01/1998-03/2015, unit of K/day). For each gridpoint in e-f, only the heating part of the ERA-Interim diabatic heating has been used for calculation and the cooling part was set to zero. The upper color bar is used for subplots (a)-(d), and the lower one is for (e) and (f).

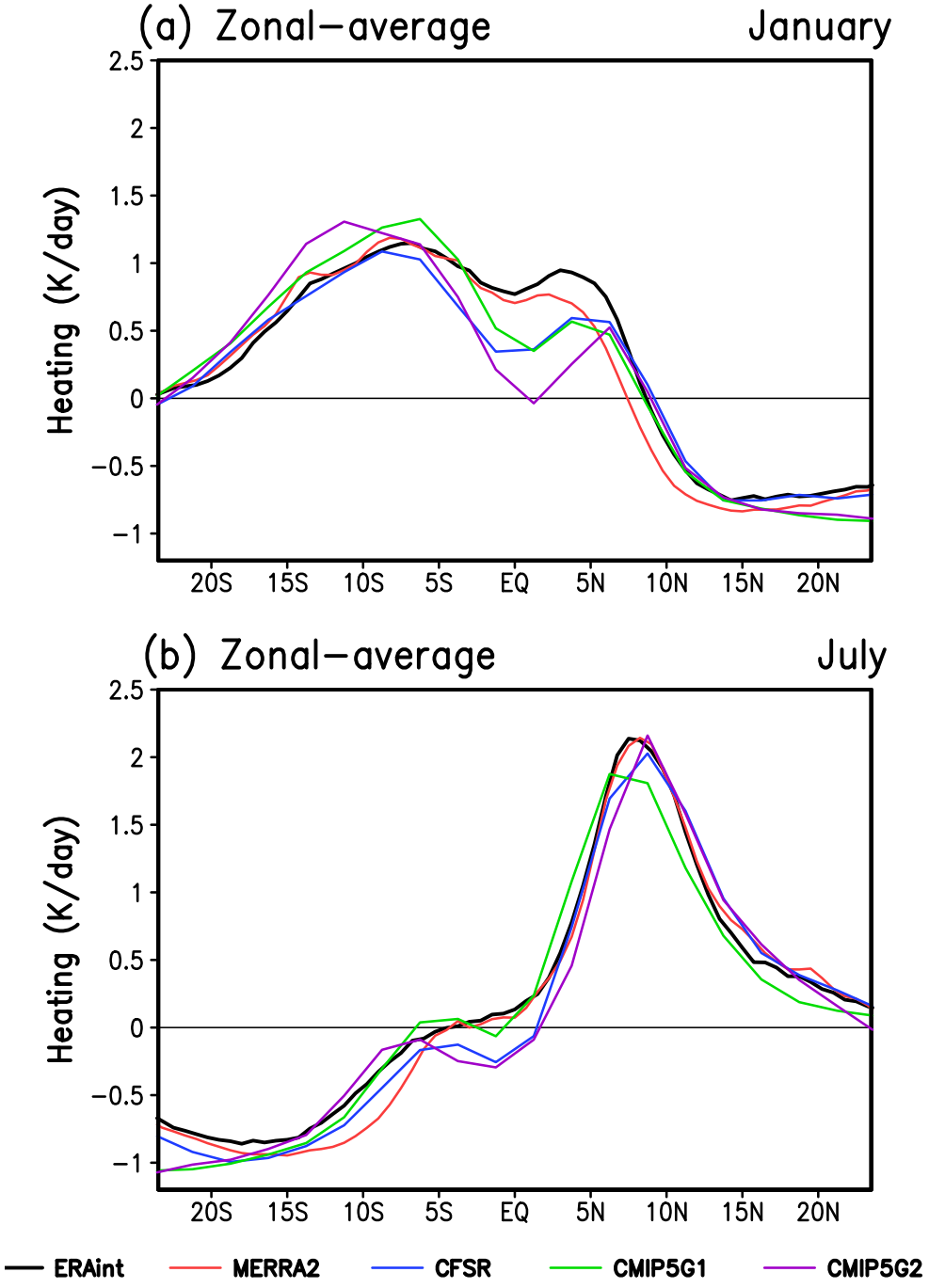

Figure 4.2 Zonal average of mass-weighted vertically-averaged diabatic heating for ERA-Interim, MERRA-2, CFSR and the two CMIP5 groups over the tropics (23.5S°-23.5°N) in January and July. The time period chosen is from 1980 to 2005.

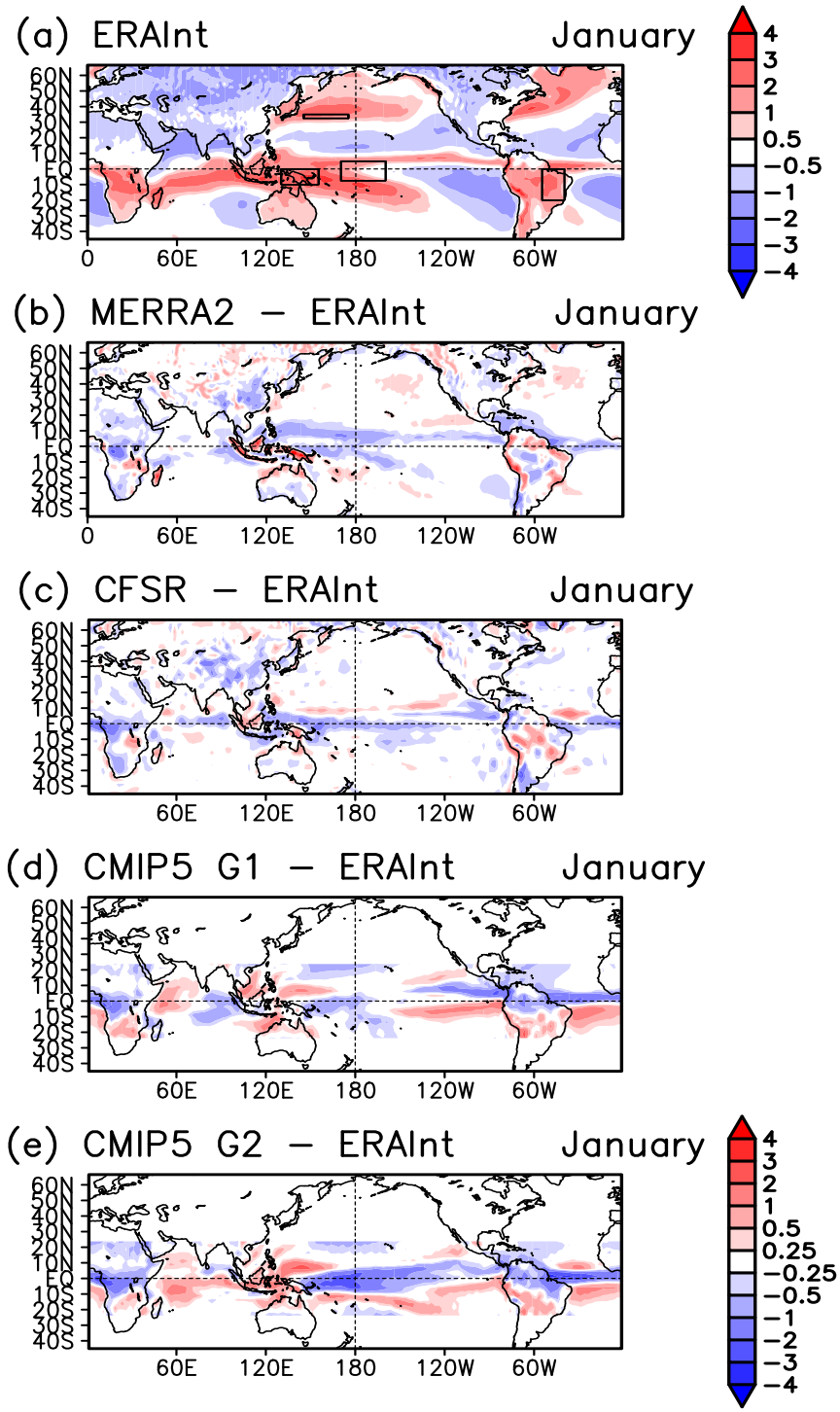

Figure 4.3 Mass-weighted vertically averaged diabatic heating (surface to 150mb) from ERA-Interim in January. The departures of MERRA-2, CFSR and the two CMIP5 groups from ERA-Interim are also shown. The time period for ERA-Interim, MERRA-2 and CFSR is from 1980 to 2016, and the period of 1980 - 2005 is used for the CMIP5 deviations. Unit is K/day for all datasets. The upper color bar is used for subplots (a)-(d), and the lower one is for (e) and (f).

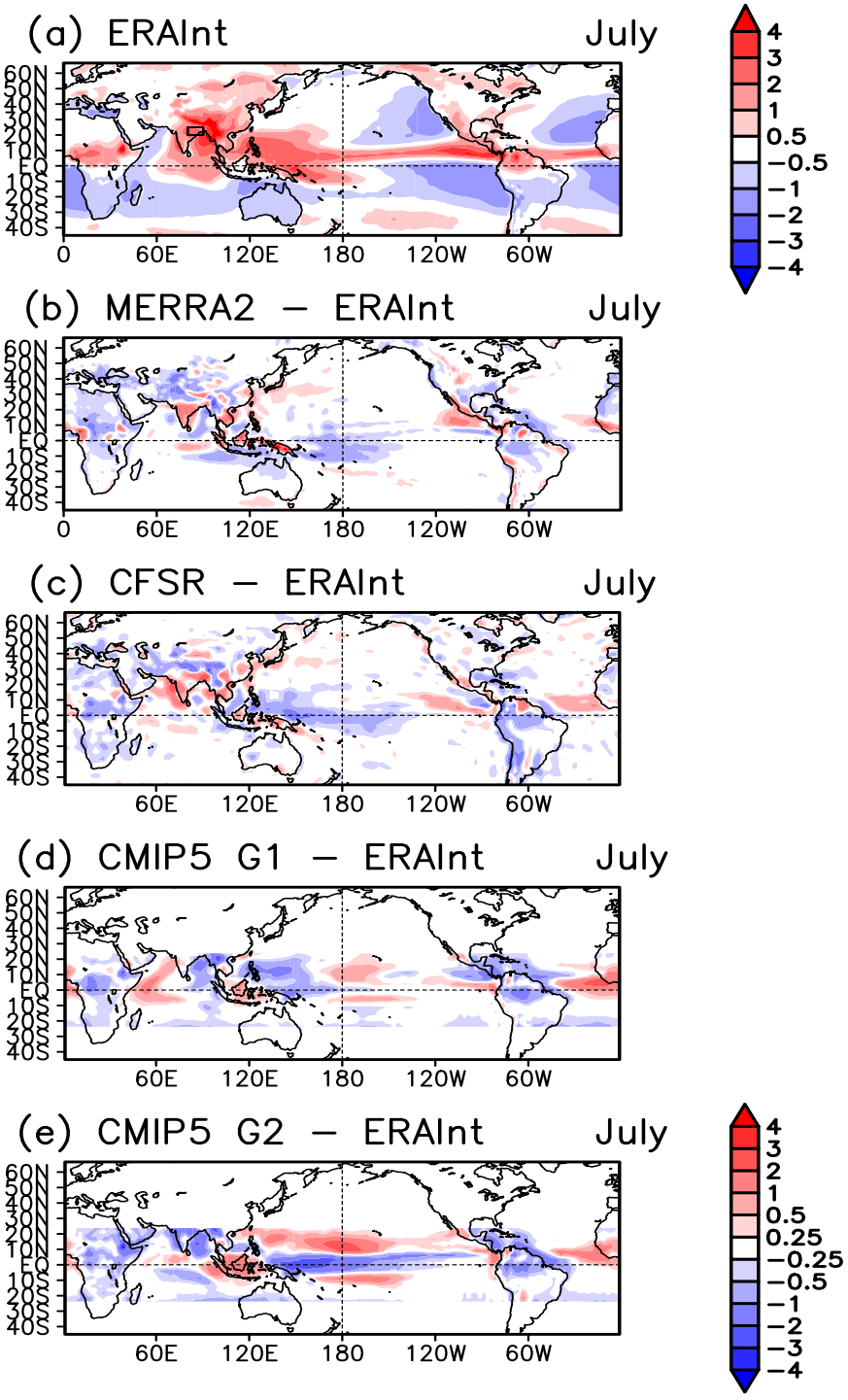

Figure 4.4 Mass-weighted vertically averaged diabatic heating (surface to 150mb) of ERA-Interim in July. The departures of MERRA-2, CFSR and the two CMIP5 groups from ERA-Interim are also shown. The time period for ERA-Interim, MERRA-2 and CFSR is 1980 – 2016, and the period of 1980 - 2005 is used for the CMIP5 deviations. Unit is K/day for all datasets. The upper color bar is used for subplots (a)-(d), and the lower one is for (e) and (f).

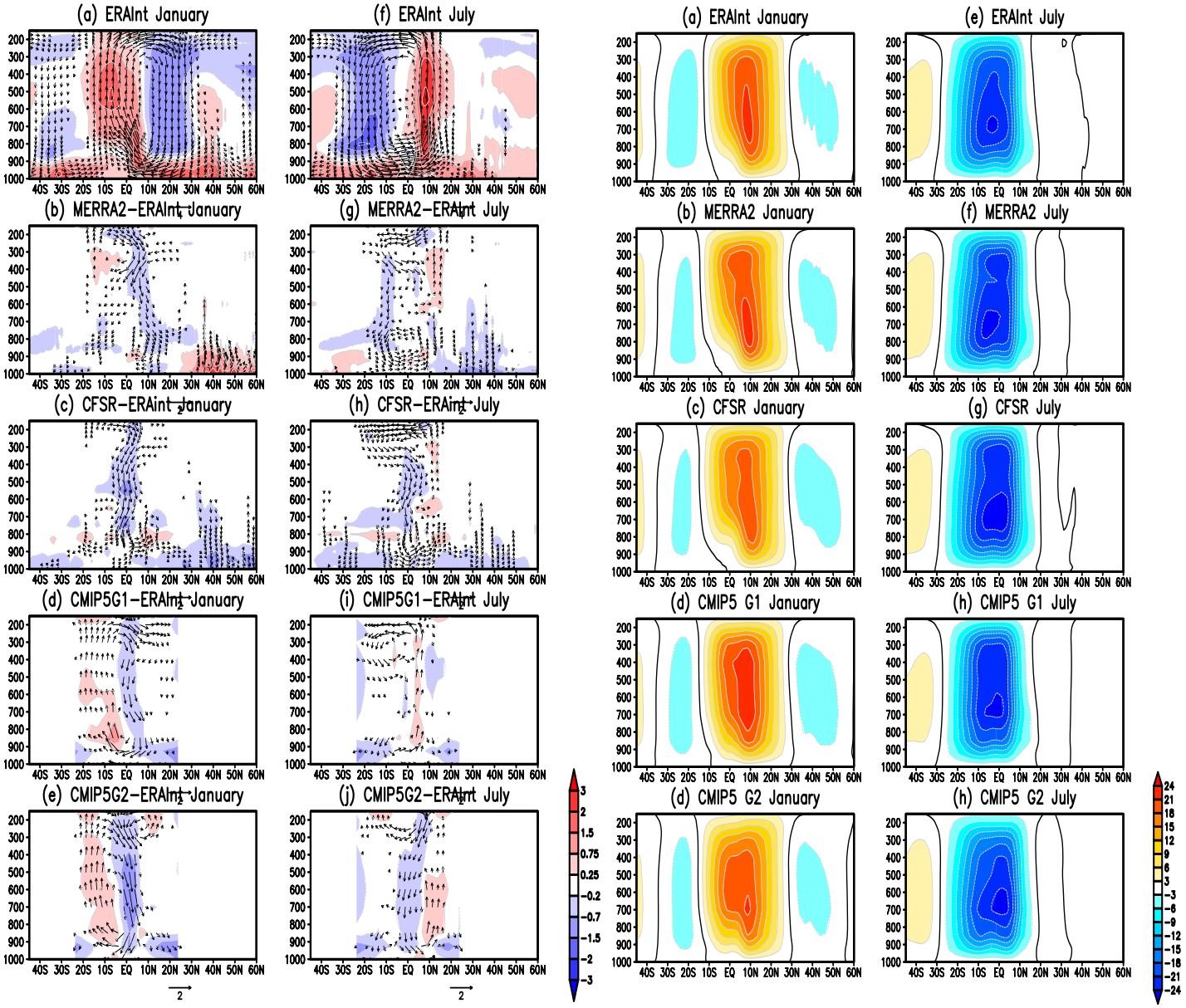

Figure 4.5 Left panel: mass-weighted zonally averaged diabatic heating (shown in colors and contours) and the Hadley circulation (shown as vectors) of ERA-Interim in January and July. The departures of MERRA-2, CFSR, and the two CMIP5 groups from ERA-Interim are also shown. The time period for ERA-Interim, MERRA-2 and CFSR is from 1980 to 2016, and the period of 1980 - 2005 is used for the CMIP5 deviations. Unit for diabatic heating is K/day. The vectors for the Hadley circulation are the sum of meridional wind v (m/s) and vertical pressure velocity $-\omega$ (Pa/min). Vectors smaller than 10% of the scales are not shown. **Right panel:** mass stream function of zonally averaged Hadley cells $\psi = 2\pi R cos\phi \int_0^{p_s} [\bar{v}] \frac{dp}{g}$. Unit: $\times 10^{10}$ Kg/s. Unit: $\times 10^{10}$ Kg/s. The thick black line represents zeros line. The positive values of the mass stream function correspond to clockwise rotation

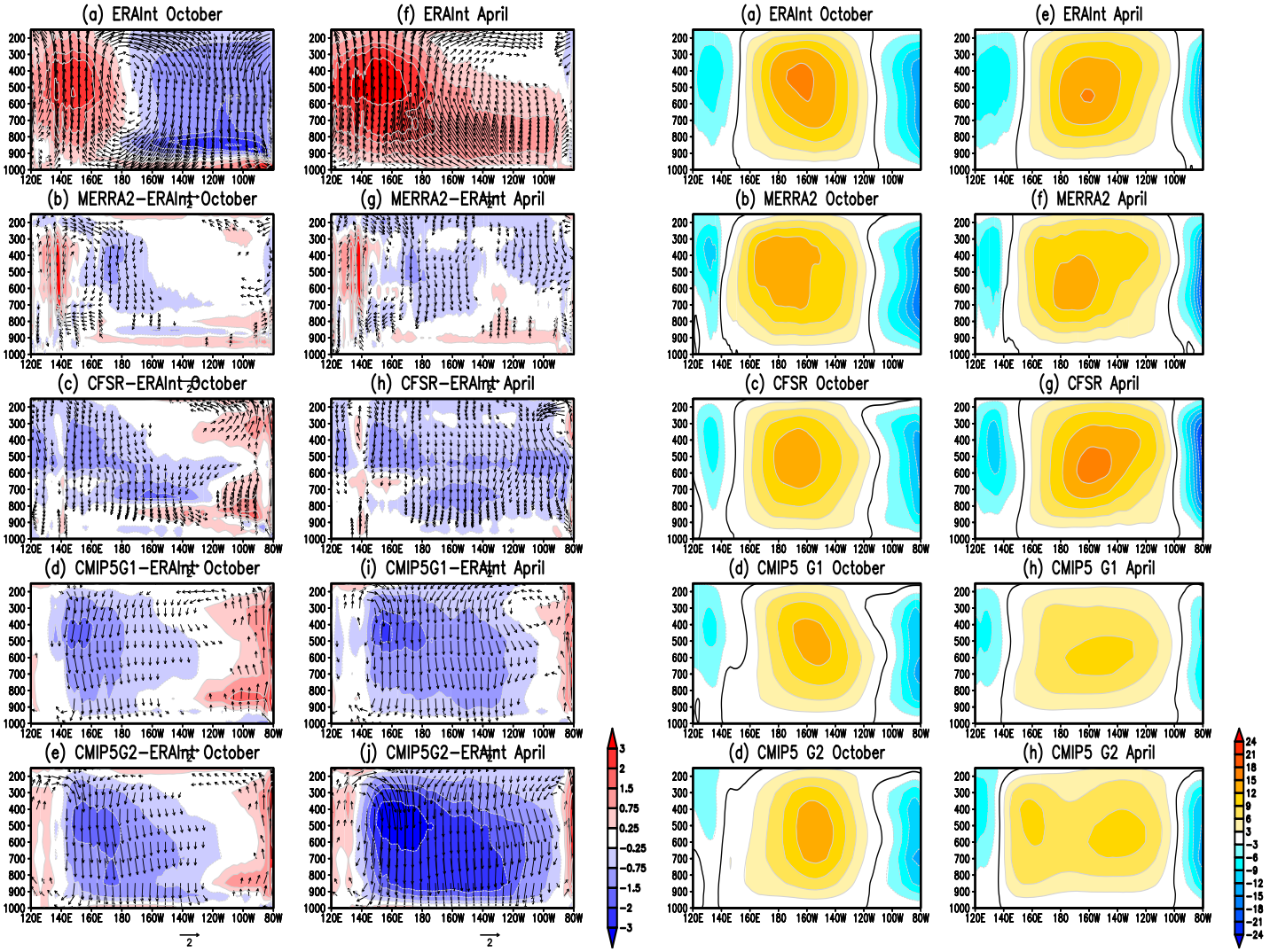

Figures 4.6 Left Panel: Mass-weighted meridionally-averaged (5°S - 5°N) diabatic heating (shown in colors and contours) and the Walker circulation (shown as vectors) of ERA-Interim in January, July and October. The departures of MERRA-2, CFSR and the two CMIP5 groups from ERA-Interim are also shown. The time period for ERA-Interim, MERRA-2 and CFSR is from 1980 to 2016, and the period of 1980 - 2005 is used for the CMIP5 deviations. Unit for diabatic heating is K/day. The vectors for the Walker circulation are the sum of divergent zonal wind (m/s) and vertical pressure velocity $-\omega$ (Pa/min). Vectors smaller than 20% of the scales are not shown. **Right Panel:** mass stream function ($\psi = 2\pi R \int_0^{p_s} u_{div} \frac{dp}{g}$) of Walker cell (average of 5°S - 5°N). Unit: $\times 10^{10}$ Kg/s. The thick black line represents zeros line. The positive values of the mass stream function correspond to the clockwise rotation.

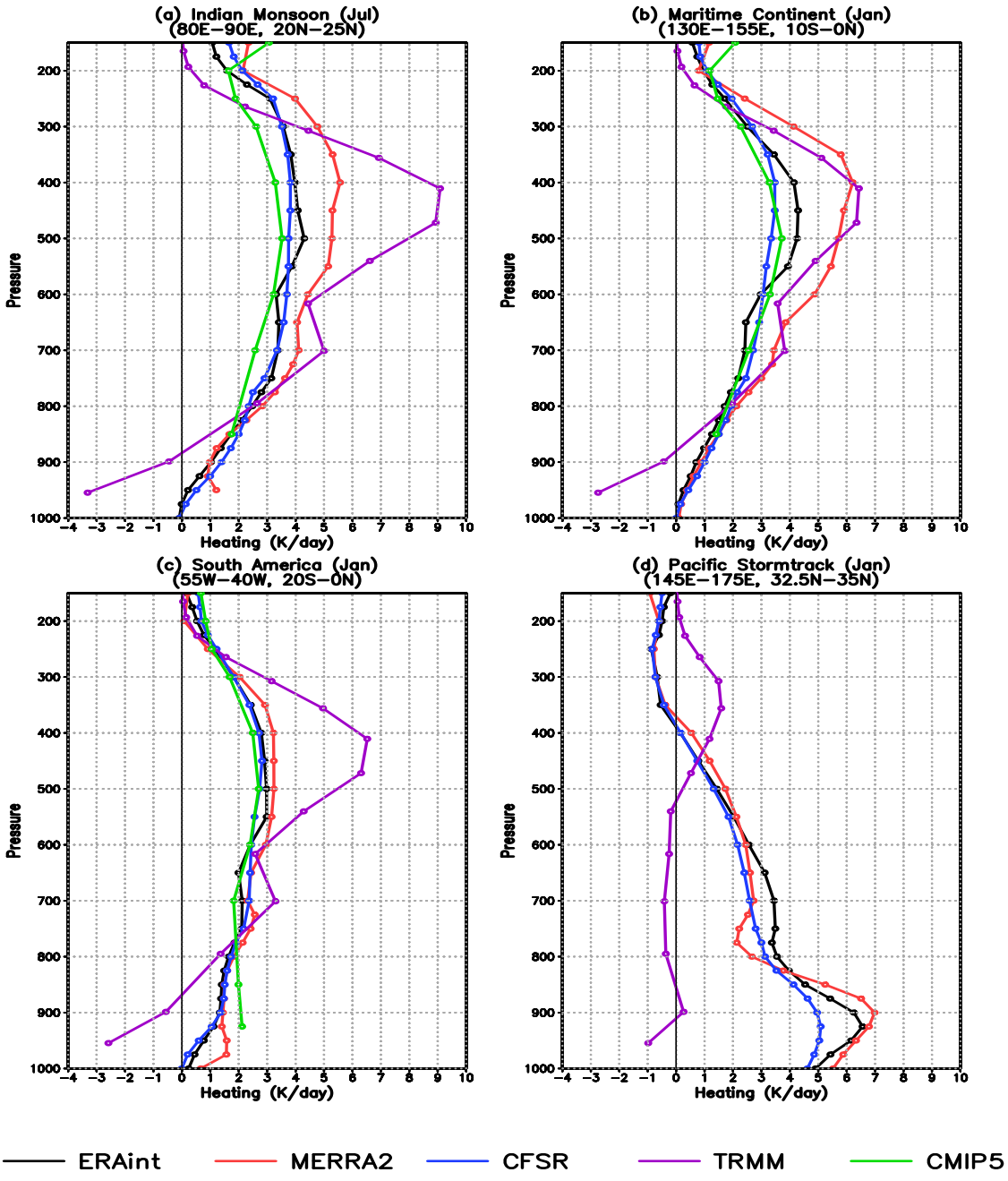

Figure 4.7 TRMM CSH latent heating profile (purple line) and diabatic heating profiles of ERA-Interim (black line), MERRA-2 (red line), CFSR (blue line) and CMIP5 group 1 (green line) in (a) Indian summer monsoon region (marked as the land box in Fig. 3); (b) Maritime Continent region (marked as the box over the Maritime Continent in Fig. 2); (c) South American region (mark as the box over South America in Fig. 2); and (d) Pacific Stormtrack region (mark as the oceanic box in Fig. 2). The period of 1998-2005 applies to all profiles.

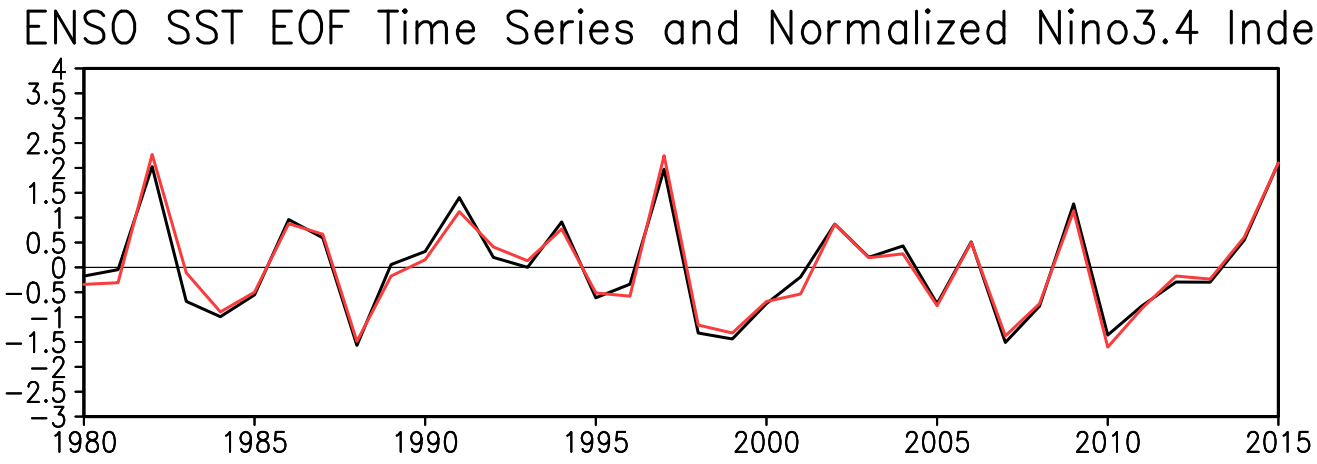

Figure 4.8 The normalized and detrended Nino-3.4 SST index (HadISST 1, shown as black line) and the ENSO-related SST time series from the first EOF time series of the detrended DJF-averaged HadISST 1.1 (shown as red line)

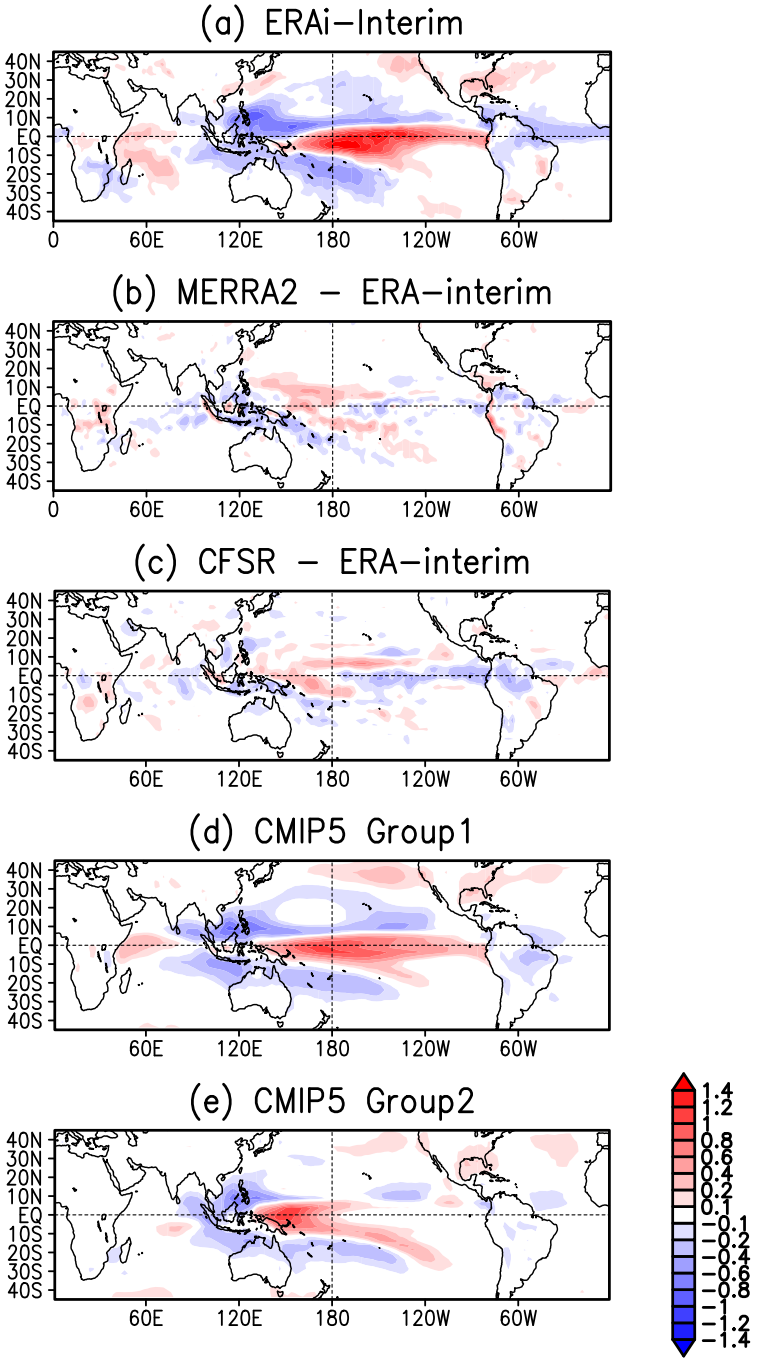

Figure 4.9 DJF-averaged ENSO covariant diabatic heating anomalies (area-weighted and vertically-averaged from surface to 150hPa, with unit of K/day) of ERA-Interim, CMIP5 group1 and group2 for the time period of 1980-2005. Since the heating anomaly patterns of MERRA-2 and CFSR are very similar to the one of ERA-Interim, only the departures of MERRA-2 and CFSR from ERA-Interim are shown. The ENSO-related diabatic heating anomalies were obtained from regression with the first EOF time series of the DJF-averaged HadISST or models' SST during the same period.

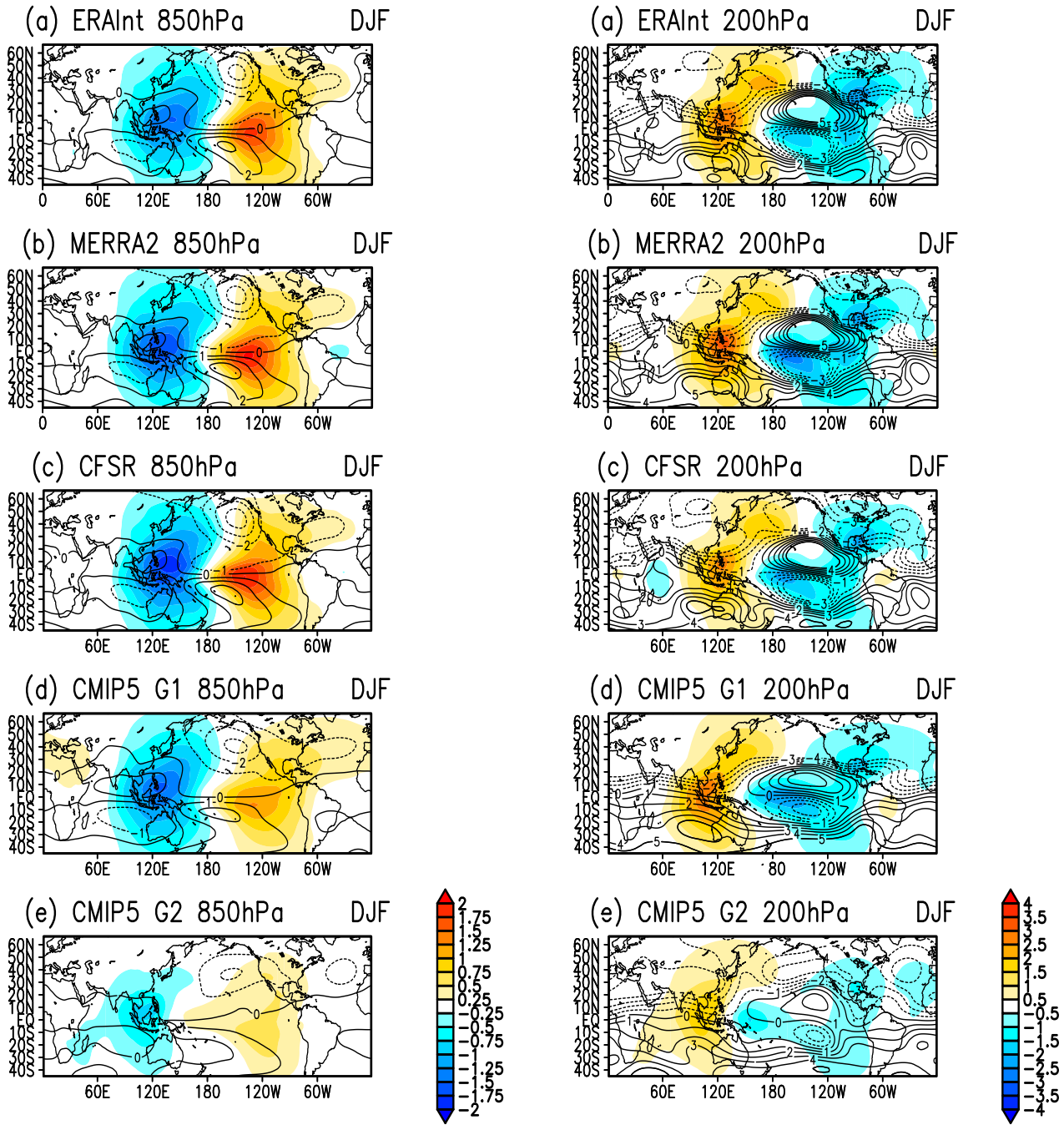

Figure 4.10 DJF-averaged ENSO covariant stream function and velocity potential anomalies (left panel: 850hPa; right panel: 200hPa) of ERA-Interim, MERRA-2, CFSR, CMIP5 group1 and group2 for the time period of 1980-2005. The colors represent the velocity potential and the contours stand for the stream function. For the velocity potential, positive (negative) values mean convergence (divergence). The positive (negative) values in the stream function stand for clockwise (counterclockwise) rotations.

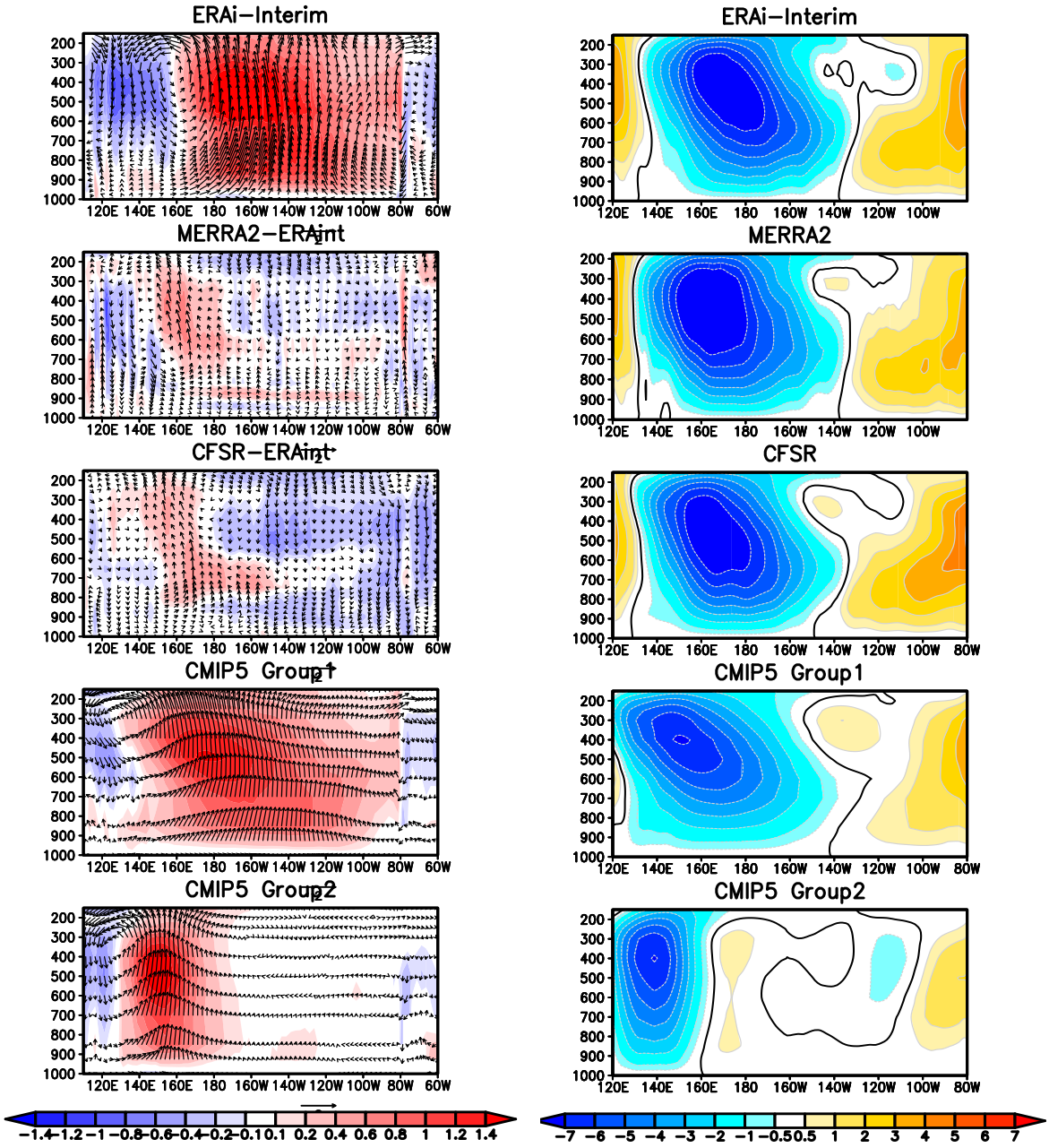

Figure 4.11 Left panel: DJF-averaged equatorial ENSO-related diabatic heating (meridionally averaged from 5°S to 5°N, shown in colors) and the related equatorial Walker circulation (shown as vectors) of ERA-Interim and the two CMIP5 groups. The departures from ERA-Interim are shown for MERRA-2 and CFSR. The time period used is 1980 - 2005. Unit for diabatic heating is K/day. The vectors for the Walker circulation are the sum of divergent zonal wind (m/s) and vertical pressure velocity $-\omega$ (Pa/min). Vectors smaller than 20% of the scales are not shown. **Right panel:** mass stream function ($\psi = 2\pi R \int_0^{p_s} u_{div} \frac{dp}{g}$) of Walker cell (mean of 5°S - 5°N). Unit: $\times 10^{10}$ Kg/s.

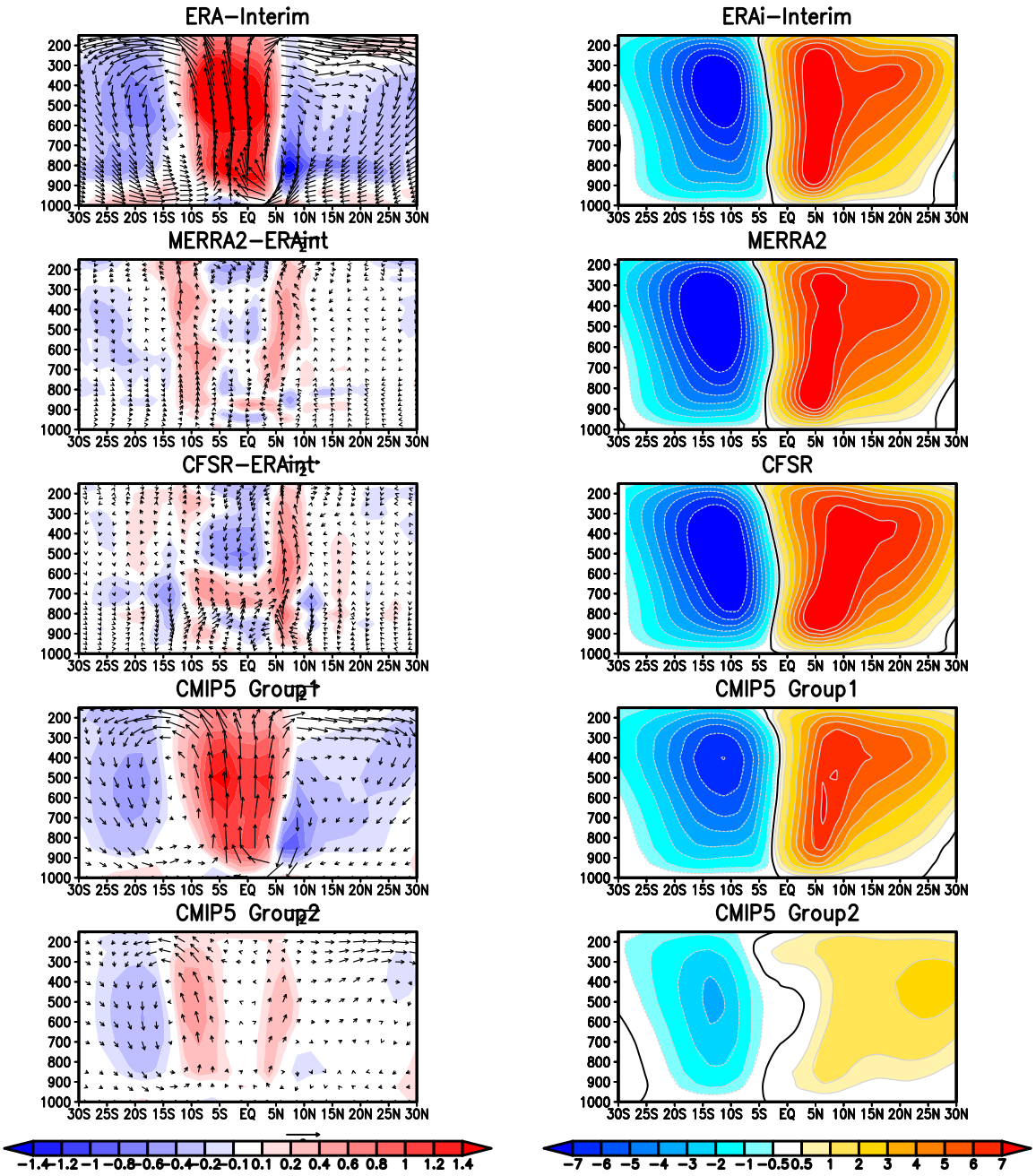

Figure 4.12 Left Panel: DJF-averaged ENSO-related heating cross-section in the central Pacific sector (averaged from 180° to 150°W, shown in colors) and the related local Hadley circulation (shown as vectors) of ERA-Interim and the two CMIP5 groups. The departures from ERA-Interim are shown for MERRA-2 and CFSR. The time period used is 1980 - 2005. Unit for diabatic heating is K/day. The vectors for the Hadley circulation are the sum of divergent zonal wind (m/s) and vertical pressure velocity $-\omega$ (Pa/min). Vectors smaller than 20% of the scales are not shown. **Right panel:** mass stream function ($\psi = 2\pi R cos\phi \int_0^{p_s} v_{div} \frac{dp}{g}$) of the local Hadley cell (average of 180° - 150°W). Unit: $\times 10^{10}$ Kg/s.

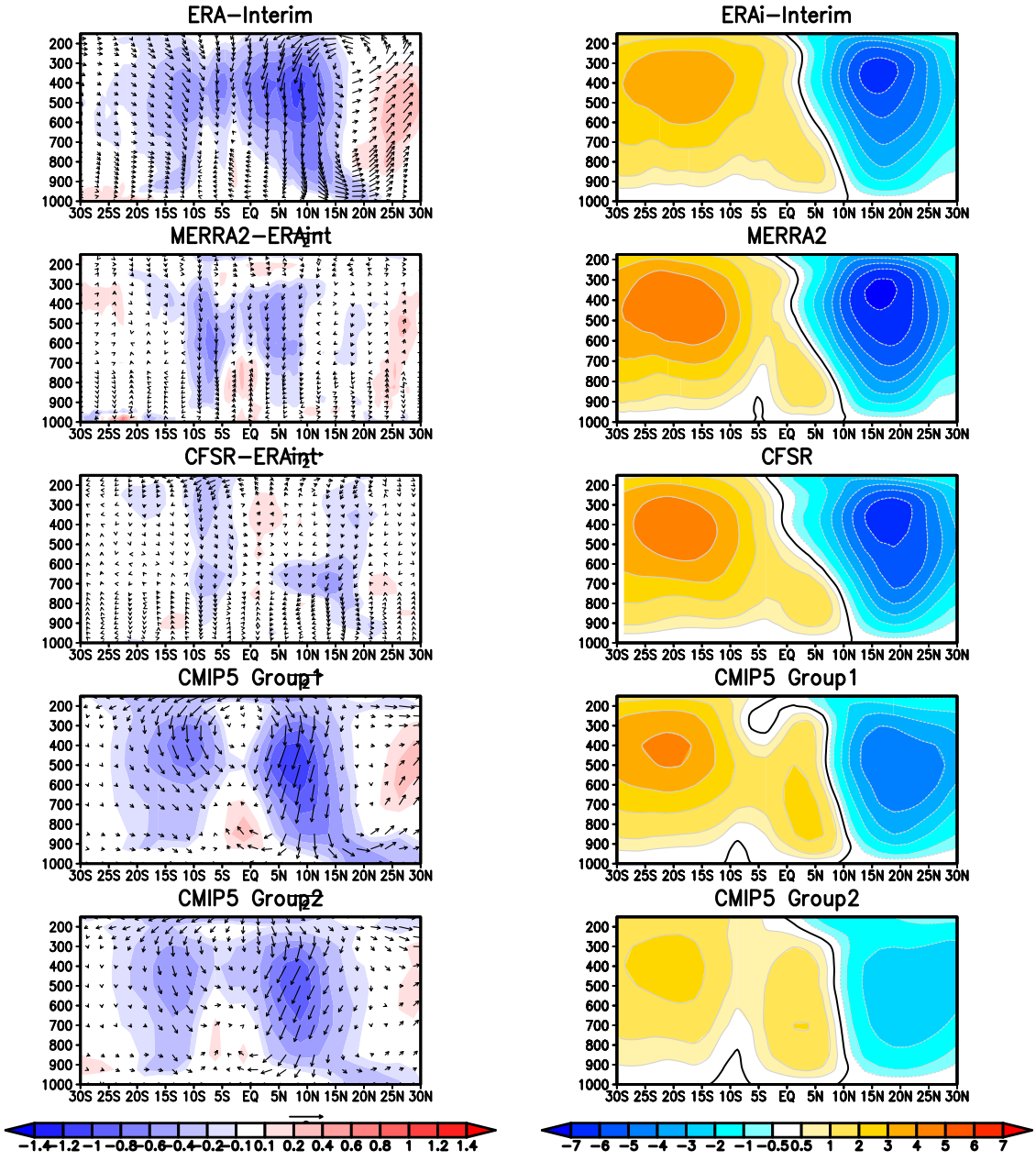

Figure 4.13 Left Panel: DJF-averaged ENSO-related heating cross-section in the western Pacific sector (averaged from 110°E to 130°E, shown in colors) and the related local Hadley circulation (shown as vectors) of ERA-Interim and the two CMIP5 groups. The departures from ERA-Interim are shown for MERRA-2 and CFSR. The time period used is 1980 - 2005. Unit for diabatic heating is K/day. The vectors for the Hadley circulation are the sum of divergent zonal wind (m/s) and vertical pressure velocity $-\omega$ (Pa/min). Vectors smaller than 20% of the scales are not shown. **Right panel:** mass stream function ($\psi = 2\pi R cos\phi \int_0^{p_s} v_{div} \frac{dp}{g}$) of the local Hadley cell (average of 110°E - 130°E). Unit: $\times 10^{10}$ Kg/s.

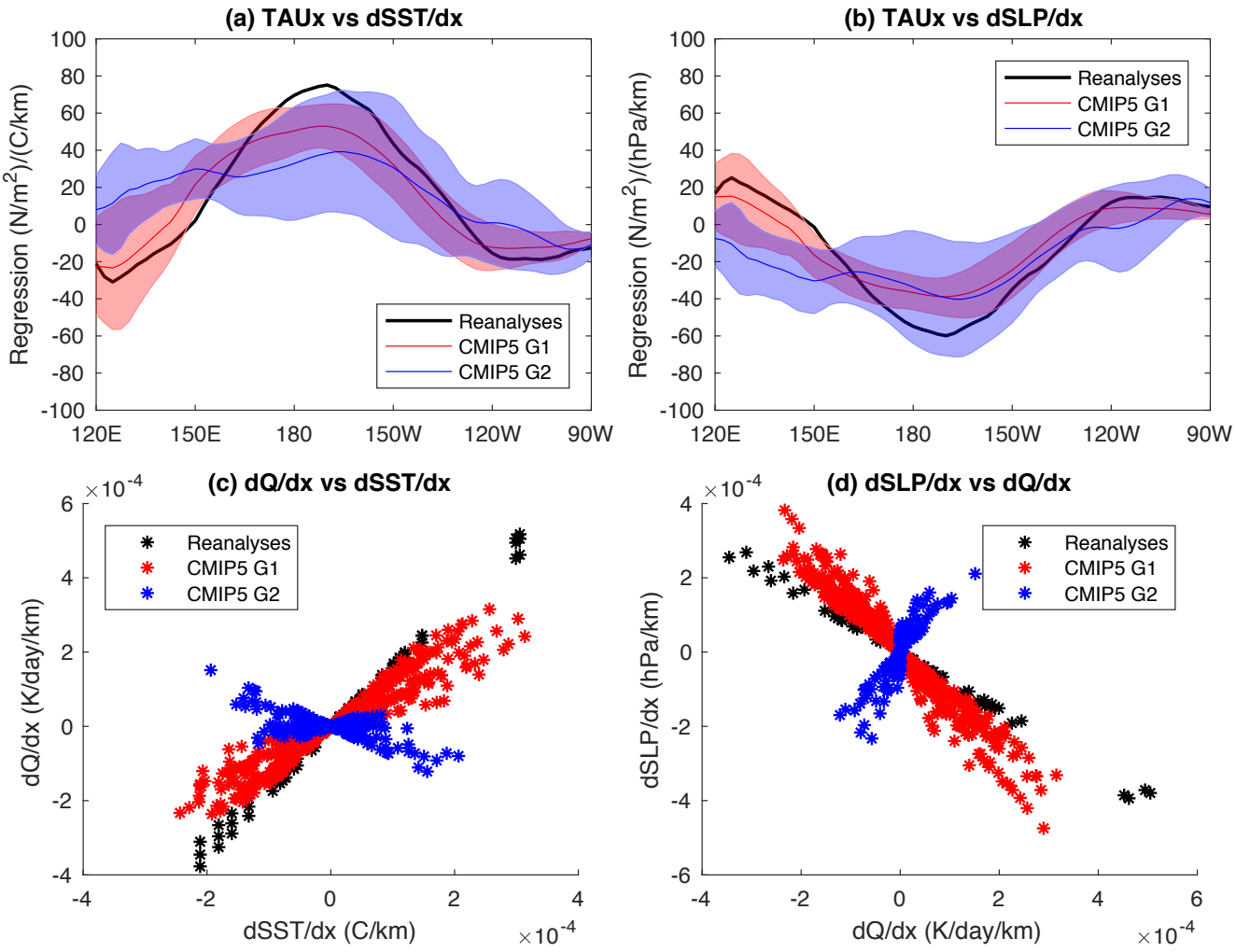

Figure 4.14 ENSO-related Bjerknes positive feedback and the three subprocesses in the reanalyses and the two CMIP5 groups. **(a)** Bjerknes feedback: linear regression coefficients between ENSO-related τ_x and ENSO-related $dSST/dx$; **(b)** Bjerknes feedback subprocess 3: linear regression coefficients between ENSO-related τ_x and ENSO-related $dSLP/dx$. The term "ENSO-related" means DJF-averaged anomaly field regressed onto the first EOF time series of DJF-averaged global SST anomalies. Black line represents the mean of the three reanalyses. Red (blue) line stands for the mean of CMIP5 group 1 (2), and the red (blue) shades are the standard deviation within group 1 (2). **(c)** Bjerknes feedback subprocess 1: scatter diagram between ENSO-related dQ/dx and ENSO-related $dSST/dx$; **(d)** Bjerknes feedback subprocess 1: scatter diagram between ENSO-related dQ/dx and ENSO-related $dSLP/dx$.

Chapter 5: Multi-decadal and Centennial Changes of ENSO and Related Precipitation During the 20th and 21st Centuries

5.1 Introduction

5.1.1 ENSO Impacts and Importance

Despite the fact that ENSO exerts its strongest influences around the equatorial Pacific through baroclinic equatorial wave dynamics (Wallace et al. 1998; Su and Neelin 2002), ENSO events can substantially affect variability in weather and climate in many parts of the world via teleconnections (Trenberth et al. 1998) from barotropic Rossby wave trains (Horel and Wallace 1981; Held and Kang 1987). Some of these severe changes in weather and climate (e.g. heavy rainfall, droughts and off-shore warming/reduced upwelling) during ENSO can have damaging consequences for agricultural production (Iizumi et al. 2014), fisheries (Niquen and Bouchon 2004), ecosystems (Valle et al. 1987, McGowan and Theobald 2017), health (Kovats 2000), economies (Cashin et al. 2015), and even cause or exacerbate civil conflicts involving the societies in the entire global tropics and the western coastline of the Americas (Hsiang et al. 2011). Also, the warmer ocean waters release excess heat into the atmosphere during extreme El Niño events, and further cause the global temperature to rise on the interannual time scale (Foster and Rahmstorf 2011). In retrospect, the recent three extreme El Niño events during 1982/83, 1997/98 and 2015/16 all brought worldwide disasters. The estimated costs for the 1982/83 event were 8-18 billion U.S. dollars (USD) and 35-45 billion USD for the 1997/98 event (Sponberg 1999). The 1997/98 event alone cost an estimated 23,000 human lives worldwide. The 2015/16

event affected the health and living conditions of more than 60 million people around the world (WHO 2016).

Inadequate preparation for these ENSO-related catastrophes is the major reason for such large costs and casualties, particularly in the developing tropical countries (Bermejo 2006). Although the overall seasonal climate forecast skill is highest during El Niño/La Niña events (Goddard and Dilley 2004), it is crucial to project future changes of ENSO events and plan for resilience and disaster prevention in those developing countries to avoid large socioeconomic consequences. One of the related and the most important issue to both the United Nations and climate scientists is how ENSO and the related precipitation variations will respond to greenhouse warming during the 21st century, as the growing global population could be increasingly vulnerable to natural disasters. Previous studies have demonstrated that an increase in frequency of extreme ENSO events may cause more severe droughts and floods in a warmer climate, with the largest precipitation changes in the tropical Pacific and polar regions (Christensen et al., 2013; Seager et al., 2010). However, for decades, there has been little consensus on how the amplitude and frequency of the ENSO variability may change (e.g. Yeh and Kirkman 2007, Collins et al. 2010, Watanabe et al. 2012). The recent advances of the CMIP5 models and improved long-term reanalyses provide a great opportunity to re-examine past and prospective ENSO changes, and scientists have been vigorously investigating this topic using the new datasets during the past five years.

5.1.2 ENSO Changes Under Global Warming

Several studies have quantitatively described the changes of ENSO frequency under global warming in the CMIP5 models. For a high greenhouse gas emission scenario (RCP 8.5, see Section 5.2) with projected global warming reaching about 4.5°C in year 2100, one study (Cai et al. 2014) concludes that the number of extreme El Niño events could double under global warming, with the frequency changing from about one event every 20 years to one every 10 years. Similar changes are seen for extreme La Niña events, with the frequency increasing from one in every 23 years to one in every 13 years (Cai et al. 2015). Under more moderate but also the most likely emission scenarios, e.g. representative concentration pathway (RCP) 2.6 or RCP 4.5 (see Section 5.2), with the global warming controlled to 1.5°C or 2°C before 2100, the frequency of extreme El Niño events is shown to increase linearly with rising global mean temperature (Wang et al. 2017), and even after the warming is controlled, the frequency could continue grow for another century. The frequency of extreme La Niña events seems to remain unchanged in the moderate scenarios.

Regarding the sign and amplitude of the projected ENSO changes, the CMIP5 models show diverse results as in the earlier versions of GCMs (Cai et al. 2015). Fewer than 60% of the models generate increased amplitude of the Niño 3 SST anomalies in the RCP8.5 scenario, and about 70% of the models produce an amplitude increase in the Niño 4 SST anomalies. Another study (Kim et al. 2014) finds that 9 CMIP5 models with a better representation of the various ENSO-related linear feedbacks (Jin et al. 2006) strongly agree on an increased amplitude of ENSO-related SST before the year 2040, but a decreasing one thereafter in the same scenario. The paper notes that such nonlinear change in ENSO variability is related to

the SST mean states, in which the SST warms faster in the eastern Pacific Ocean than the Maritime Continent before 2040 and then warms more rapidly in the latter region from 2040 to 2100.

ENSO asymmetry between El Niño and La Niña (so-called "ENSO nonlinearity") is another property of ENSO whose potential changes also interest climate scientists. In the tropics, a strong El Niño exhibits a warm maximum SST anomaly center in the eastern equatorial Pacific, while an extreme La Niña features an anomaly center in the central equatorial Pacific (Larkin and Harrison 2002). One study (Ham et al. 2017) has found that the asymmetry between El Niño and La Niña in the Niño 3 index tends to decrease by about 40% in the RCP 4.5 scenario compared to the historical simulation. This is largely due to the increased frequency of strong La Niña events, also illustrated by the increase (decrease) of precipitation sensitivity in the central Pacific during La Niña (El Niño). Kohyama et al. (2018) also point out that the ENSO nonlinearity is reduced in some CMIP5 models with stronger oceanic thermal stratification under global warming.

In addition, there exists diversity regarding different types of the ENSO events in the models (Capotondi et al. 2015). In past three decades, the type of El Niño with maximum SST warming in the central equatorial Pacific (CP El Niño) occurs much more often than the canonical eastern Pacific type (EP El Niño) (Kug et al. 2009). The CMIP3 models indicate that the CP-to-EP ENSO frequency ratio increases under global warming (Yeh et al. 2009). Studies (Kim and Yu 2012; Xu et al. 2017) have shown that the change of this frequency ratio is unclear in the CMIP5 models, but the

models suggest an increase of CP-to-EP ENSO intensity ratio in the RCP 4.5 scenario.

5.1.3 Relation to Mean State Changes

These aforementioned ENSO changes under global warming are closely associated with the changes in the mean state (Sadekov et al. 2013; Cai et al. 2015). Fig. 5.1 from Cai et al. (2015) summarized the projected model mean state changes of SST, thermocline, and Walker circulation due to global warming in previous studies. The warming leads to a weakened and more eastward-located Walker circulation (Bayr et al. 2014), which could be explained by a weaker zonal SST gradient and reduced total diabatic heating due to the fact that specific humidity increases more rapidly than tropical precipitation in the models (Held and Soden 2006; Chadwick et al. 2013). The SST increases more in the eastern Pacific and Maritime Continents, and less in the central Pacific. From a meridional perspective, as the easterlies weaken, less upwelling of cold waters will occur in the east, and the SST will warm faster at the equator than in the off-equatorial region. In addition, the westward upper ocean currents weaken, and the upper ocean warms more quickly than the deep ocean. Such changes result in stronger oceanic stratification and a flattened thermocline (east-west tilt is reduced). The thermocline also rises compared to that found in the historical simulation (Vecchi et al. 2006; DiNezio et al. 2009). This change in the mean state is favorable for occurrence of both extreme El Niño and La Niña events. In the case of El Niño, the projected weakened westward upper ocean currents can be easily reversed by a smaller eastward anomaly, therefore, the type of

the El Niño events that features this eastward propagation are more likely to occur (Kim and Cai 2014; Cai et al. 2015). Also, one previous study (Yeh et al. 2009) points out that a shallower thermocline in the central and western Pacific would strengthen the thermocline feedback in which the warm (cold) SST anomalies weaken (strengthen) equatorial easterlies and causes less (more) upwelling and thus change the slope of the thermocline. Such enhancement of the thermocline feedback further contributes to the development of larger SST anomalies around 180°. In the case of La Niña, both the shoaling thermocline and the warming in the Maritime Continent are favorable for extreme La Niña events (Cai et al. 2015).

Scientists have been trying to understand the inter-model diversity of ENSO changes for over a decade. Yeh and Kirkman (2007) discovered that the inter-model diversity of ENSO amplitude changes could be attributed to whether the ENSO regime in a model is more linear or nonlinear (symmetric or asymmetric between El Niño and La Niña). A model with a more linear (nonlinear) ENSO regime is less (more) sensitive to the mean state changes in global warming scenarios. Russell and Gnanadesikan (2014) used one of the models with a linear ENSO regime and found that the ocean's surface is less responsive to zonal wind stress perturbations during warming periods, which could be related to a stronger oceanic stratification. Recent studies have found that the inter-model diversity of ENSO changes are largely determined by two ENSO-related feedbacks, the aforementioned thermocline feedback and the zonal advective feedback. The zonal advective feedback describes how the warm (cold) SST anomalies weaken (strengthen) equatorial easterlies and reduce (enhance) transport of cold water from the eastern Pacific. Borlace et al.

(2013) used a 1000-year coupled global climate model and found that the stronger thermocline feedback in the central Pacific leads to an increase in ENSO amplitude. The variability of the thermocline feedback in the model is linked to the slowly varying mean states. Both Chen et al. (2015) and An et al. (2017) recognize that a narrower meridional width of SST and zonal wind stress anomalies in the CMIP5 models are related to stronger thermocline feedback and zonal advective feedback, which in turn increase the amplitude of ENSO under global warming.

5.1.4 ENSO-related Precipitation Changes Under Global Warming and Uncertainties

Changes of ENSO-related precipitation in a warning world are sensitive to two aspects: the change in the mean state of global precipitation, and the change in ENSO properties as mentioned above (Cai et al., 2015; Bonfils et al. 2015). Chadwick et al (2013) give a detailed description of the changes of CMIP5 precipitation mean states in the RCP 8.5 scenario and how these changes are related to background dynamics (atmospheric circulation) and thermodynamics (atmospheric moisture). They find that the largest changes in the precipitation are located over the central-eastern equatorial Pacific and are closely tied to spatial changes in the low-level convergence and convection as well as SST. The ITCZ and the SPCZ regions with heavy rainfall tend to show less impressive changes, which is due to the offset of a divergence feedback of convective mass flux against the Clausius-Clapeyron changes (humidity increases as temperature rises).

The tropical precipitation response to El Niño events is nonlinear in a warming world, as shown in Chung et al. 2014. They use several atmospheric GCMs (AGCM) under a SST forcing averaged from the CMIP3 models and find that ENSO-related precipitation and drought are likely to be enhanced as a response to global warming. The atmospheric mean circulation dynamics plays the biggest role in influencing the ENSO-related precipitation changes. In the CMIP5 models, Power et al (2013) reach a similar conclusion as Chung et al. (2014), finding that the nonlinear response of precipitation anomalies to surface global warming is the major cause of the robust El Niño-related precipitation changes, while the amplitude of the ENSO-driven surface temperature variability is secondary. Huang (2016) examined 32 CMIP5 models in the RCP 8.5 scenario and concluded that the increase of moisture enhances the ENSO-related precipitation anomalies and the El Niño SST changes gradually shift the ENSO-related precipitation more eastward.

However, most of these studies use a multi-model mean of the CMIP5 models that includes not only the models that are more skillful in simulating ENSO physics/thermodynamics but also those that under-perform (Chapter 3&4). As we have demonstrated before, these two groups of models simulate very differently the location and amplitude of ENSO-related features. Huang (2017) has shown that the largest uncertainties of the future projection of ENSO-related precipitation anomalies in the CMIP5 models exist over the tropical region from 150°E-150°W. This is also the longitude range in which the models disagree the most regarding the maximum ENSO-related precipitation/diabatic heating anomalies (e.g. Fig. 4.9). In addition, the studies mentioned above indicate that one of the most robust projected ENSO SST

changes will occur in the cold-tongue region. We have studied that the underperforming CMIP5 group tends to simulate a much cooler cold tongue than the better performing group and the reanalyses. If SST warms and the easterlies reduce enough in a larger emission scenario, it is likely that this underperforming group will develop robust but exaggerated changes in the location and amplitude of ENSO-related features, especially precipitation as it responds nonlinearly to the changes in SST amplitudes and patterns. Adding those models to the multi-model average will increase the uncertainty of the future changes in ENSO. Therefore, research is required to examine the projected changes of ENSO-related SST and precipitation based on different groups of the CMIP5 models in terms of their capability in simulating ENSO dynamics and thermodynamics.

Another motivation for this study is the availability of the first generation of century-length precipitation datasets, the 20th century precipitation reanalysis and the reconstructed precipitation (see Chapter 2). How the ENSO-related precipitation patterns and extremes vary during the entire 20th century is still unclear. These two precipitation datasets, as used in Chapter 3, are proving to be valuable assets for understanding the multi-decadal changes of ENSO-related precipitation in the 20th century. At the same time, the CMIP5 models together with these reanalysis datasets can form an arguably adequate size sample to investigate the ENSO-related precipitation multi-decadal variability during the 20th century.

This chapter is organized as follows. Section 2 will introduce the data and the methodology used. In section 3, we will compare ENSO-related precipitation between the 2nd half and the 1st half of 20th century in the reanalyses and the two CMIP5

groups. Section 4 will examine the multi-decadal changes of ENSO-related precipitation in the 21st century in the two CMIP5 groups in two different emission scenarios. Section 5 will further investigate the dynamical and thermodynamical differences between the 21st and 20th centuries in the two CMIP5 groups. Section 6 will summarize of the major findings in this study.

5.2 Data and Methodology

The long-term precipitation and sea surface temperature reanalyses used here are the same as in Chapter 3 (20CR/HadISST1.1, REC/ERSST V3b). The CMIP5 SST and precipitation outputs used to study the multi-decadal ENSO changes in the 20th century are from the 'historical' experiment as described in Chapter 2. For the 21st century projections of ENSO, the SST and precipitation from the two experiments 'RCP4.5' and 'RCP8.5' are employed (see Chapter 2). The period of 1901-2000 is selected to represent the 20th century. The period of 2006-2100 is used for the 21st century. The reason for the omission of the beginning five years during the 21st century is that about half of the CMIP5 models have a discontinuity in SST from the end month (12/2005) of the "historical experiment" to the starting month (01/2006) of either the "RCP4.5" or "RCP8.5" experiments. In this chapter, we continue to use two groups to characterize the better-performing and under-performing CMIP5 models with regard to ENSO and the related precipitation anomalies. The selection of the two groups here is still based on Table 1 and 2 in Chapter 3. In order to get more statistically meaningful results on multi-decadal changes of ENSO in all three experiments, we take more models into account for

each group in this chapter. Each group consists of 13 models with a total of 27 ensemble members. The models chosen for group 1 (better-performing) are CanESM2, CCSM4, CESM1-BGC, CESM1-CAM5, CMCC-CM, CMCC-CMS, CNRM-CM5, GFDL-ESM2M, GISS-E2-R, IPSL-CM5B-LR, MIROC5, NorESM1-ME and NorESM1-M, and for group 2 (under-performing) are ACCESS1-0, ACCESS1-3, CSIRO-Mk3-6-0, GFDL-CM3, GFDL-ESM2G, GISS-E2-H, GISS-E2-H-CC, HadGEM-AO, inmcm4, IPSL-CM5A-LR, IPSL-CM5A-MR, MPI-ESM-LR and MRI-CGCM3.

Since one of the goals in this chapter is to characterize the multi-decadal changes of ENSO-related SST and precipitation under global warming, it is important to cleanly separate ENSO, as an internal variation, from external global warming forcing and other internal variations on the longer scale such as PDO. In Chapters 3 and 4, we have used the first EOF mode of the annually- or seasonally-averaged high-pass-band-filtered SST anomaly field to represent the ENSO signal. Because the ENSO signal is strong in the leading EOF mode of SST anomalies, this method is convenient and sufficient for estimating and intercomparing the mean states of ENSO among the reanalyses and the CMIP5 models. However, the leading mode is responsible for the largest part of the variance, and therefore may also contain global warming as well as other major modes of variability in addition to ENSO (Deser, 2000). It is clearly not ideal to use only the first EOF results for ENSO variability in this study. Significant changes of SST (increases larger than 3°C) and precipitation (increases of at least 50%) may occur over the tropical Pacific region by 2100 under the scenario of higher concentration of greenhouse gases (e.g. RCP8.5, IPCC 2014),

which could potentially overshadow the ENSO-related SST and precipitation multi-decadal changes. Previous studies provide several more sophisticated methods to better separate or remove ENSO-related anomaly fields from the observed total SST anomaly. One method is rotated extended EOF analysis (REEOF, Guan and Nigam 2008), which disentangles global warming, ENSO and PDO variations by finding maximal variances through rotating the seven leading EOF modes of seasonally extended SST anomalies. Another method (called tropical dynamical ENSO patterns filter) devised by Compo et al. (2010) uses linear inverse modeling (LIM, e.g. Penland et al. 1993; Alexander et al. 2008) to help find four time-dependent eigenmodes that describe ENSO fluctuation-dissipation-relationships at different energetic phases. Although these methods can solve the issue of mode mixing within the canonical EOF method and can yield the different patterns showing waxing and waning of ENSO dynamics instead of a single ENSO mean state, they are not well suited for this study.

A simpler method to reduce EOF mode mixing and distinguish ENSO from global warming and PDO variability is used here following a method demonstrated in Wills et al. (2018) called low-frequency component analysis (LFCA). This LFCA is simply a method that combines the canonical EOF method with linear discriminant analysis (LDA, Ripley 1996, Chapter 3). LDA is a linear transformation technique that is similar to EOF analysis. It is commonly used as a dimensionality reduction technique to project a dataset onto a lower-dimensional space for good separability among classes. The basic difference between EOF and LDA is that EOF is an "unsupervised" algorithm that seeks a linear combination of variables by projecting

data in the direction of maximum variance, while LDA is a "supervised" one that projects data in the direction given by a linear discriminant function (a linear combination of independent variables) such that the class separation of the dependent variable within the data can be maximized.

Suppose the original SST anomaly data matrix is X, a size $m \times n$ matrix, with m number of grid points and n months. The LFCA method is based on projecting filtered data $\tilde{X}$ (filtered by a linear lowpass filter) onto a linear combination of the leading EOF modes of covariance matrix $C = \frac{1}{n-1} X^T X$, so that the ratio of the low-frequency components (e.g. global warming and PDO) to total variance of these EOF modes is maximized. From the canonical EOF method, we can get the leading N number of eigenvalue ${\lambda_i}^2$ $(i = 1 \dots N)$ of C and the associated eigenvector $\mathbf{v}_i$ (normalized). The ith principal component is, therefore, $\mathrm{PC}_i(t) = {\lambda_i}^{-1} X \mathbf{v}_i$. Since the filter is linear, the projection of the filtered data $\tilde{X}$ onto the ith EOF is equivalent to $\widetilde{\mathrm{PC}_i}(t) = {\lambda_i}^{-1} \tilde{X} \mathbf{v}_i$. A linear combinations of the unit variance of the leading eigenvector $\mathbf{v}_i (i = 1 \dots N)$ is built, $\boldsymbol{u}_i = \left[\frac{\mathbf{v}_1}{\lambda_1} \frac{\mathbf{v}_2}{\lambda_2} \dots \frac{\mathbf{v}_N}{\lambda_N}\right] \boldsymbol{e}_i$. When the filtered data is projected onto u , the ratio of the filtered low-frequency to total variance of the N leading EOFs, $\mathrm{r_i} = \frac{(\tilde{\mathrm{X}}\mathrm{u_i})^{\mathrm{T}} \tilde{\mathrm{X}}\mathrm{u_i}}{(\mathrm{X}\mathrm{u_i})^{\mathrm{T}} \mathrm{X}\mathrm{u_i}}$, should be maximized. The coefficient vectors $\boldsymbol{e}$ of the linear combination $\boldsymbol{u}$ are then the N eigenvectors of covariance matrix $cov(\widetilde{PC}, \widetilde{PC})$, which is sorted by r_i. The low-frequency component is $\mathrm{LFC}_i = X \boldsymbol{u}_i$ and the related spatial pattern of this component equals to $X^T \mathrm{LFC}_i$.

Wills et al (2018) used LFCA on the first three EOF modes of ERSST in the Pacific and successfully separate global warming, PDO and ENSO into three LFCA

modes. The time series (LFC) of each LFCA mode is uncorrelated with all of the others. In this study, we follow the LFCA method generally, but instead of a low-pass filter, we use a 10-year linear Butterworth high-pass filter to better characterize ENSO variability. This high-frequency component analysis (HFCA) method is applied to the seasonally averaged sequence (MAM, JJA, SON, DJF, MAM…) of SST anomalies with the seasonal cycle being removed by subtracting the long-term mean of each season. The region chosen for this study is the Pacific Ocean (100°E-70°W, 45°S-70°N). The HFCA results of HadISST 1.1 during the 20th century are presented in Fig. 5.2. The ENSO component (HFP1 and HFC1) is clearly separated from the PDO and the global warming components, as shown in the spatial pattern, time series and power spectrum. The ENSO time series from the first HFC is highly correlated with the Niño 3.4 index (r~0.85). In addition, this HFCA method works surprisingly well for the CMIP5 models. More than 97% of the ensemble members in 'Historical', 'RCP4.5' and 'RCP8.5' experiments clearly show the ENSO component in their first HFC mode, following by the PDO mode and the global warming one. This is a tremendous improvement over using the canonical EOF alone, in which the ENSO signals are sometimes mixed between the first two EOF modes.

The ENSO-related SST and precipitation anomalies presented in this study are the regression coefficients obtained by linearly regressing the seasonally averaged SST or precipitation anomalies (10-year high-pass filtered) onto this ENSO time series from the HFCA method. To test the significance of these ENSO-related regression coefficients, we employ the significance test for trends developed in Santer et al. (2000). They use the Student's t-test on the ratio r between the regression

coefficient and its standard error to test whether this coefficient (trend) is significant or not. A critical t value is determined by a specified significance level α and the number of degrees of freedom (the effect of temporal autocorrelation is considered). If the calculated r is larger than the critical t value, then the regression coefficient is significant. In the case of comparing the significance of differences between two regression coefficients (e.g. of the 20th century versus the 21st century), a z-test of the ratio between the differences of the two coefficients and the square root of the sum of the two coefficient variances (Paternoster et al. 1998) is used.

5.3 Multi-decadal Changes of ENSO-related SST and Precipitation During the 20th Century

In this section, we will investigate the multi-decadal ENSO-related precipitation and SST changes in four long-term reanalyses, REC, 20CR, ERSST v3b and HadISST 1.1, during the entire 20th Century. Chapter 3 and 4 also provide evidence for the capability of better performing CMIP5 models in simulating ENSO features that are very similar in the recent reanalyses, such as the patterns and structures of ENSO-related precipitation, diabatic heating and atmospheric circulations. We would like to see how these models simulate the multi-decadal ENSO changes during the past century, as well as whether the better performing models simulate the changes differently from the underperforming models. We use ENSO-related SST and precipitation anomalies of the second half of the 20th century minus those for the first half to represent multi-decadal ENSO change during the past century.

In the two SST reanalyses, ERSST and HadISST (Fig. 5.3a), positive ENSO-related SST anomalies in the eastern-central equatorial Pacific, especially those of the easternmost extreme, warmed the fastest in the second half of the 20th century in the global tropics. This region is where the maximum center of the ENSO-related SST anomalies is located. Meanwhile, the meridional width of the positive ENSO-related SST anomaly center in the eastern to central Pacific became narrower, as shown by cooling departures at the northern and southern edges of this positive center in Fig. 5.3a difference maps (third panel). Both of these changes appear to suggest an amplitude intensification of the ENSO events that happened in the later part of past century (e.g. Collins et al. 2010; Chen et al. 2015). The ENSO-related cooling anomalies in the western to central Pacific also warmed. Those anomalies in the Southern Hemisphere from the Maritime Continent to the east of Australia warmed faster than their northern counterparts. The positive SST anomalies in both tropical Atlantic and Indian Ocean intensified as well. ERSST exhibits these changes more robustly than HadISST, with significant changes (exceeding 95% confidence level) of the warming in the easternmost equatorial Pacific, Maritime Continent and the Arabian Sea.

Regarding the ENSO-related precipitation changes in the 20th century, 20CR results (Fig. 5.3b, left column) show an eastward shift of the ENSO-related precipitation in the central to eastern Pacific. The amplitude of precipitation anomalies in the eastern equatorial Pacific increased while the positive precipitation anomaly maximum center in the central Pacific became less robust. The dry anomalies in the western Pacific shifted westward. The dry anomaly maximum center

located around 160°E in the first half of the 20th century moved to the Maritime Continent in the second half. REC (Fig. 5.3b, right column), on the other hand, exhibits a strong intensification of both ENSO-related precipitation and droughts in the entire tropics in the second half. Such differences could be partially caused by a lack of precipitation observation over the ocean during the first 50 years. In addition, as the reconstruction of REC uses the leading EOF modes of ERSST (see Chapter 2), the more robust and significant changes in ENSO-related SST of ERSST could lead to a stronger nonlinear response of the ENSO-related precipitation changes in REC (e.g. Power et al. 2013; Yeh et al. 2018).

In CMIP5 models, both groups fail to show a significant change in their ENSO-related SST results (not shown). For precipitation, Table 5.1 indicates that the number of ensemble members simulating significant positive changes of ENSO-related precipitation (including both intensification and eastward/westward shift) over the tropical Pacific is double the number of ensemble members that display significant negative changes. In the group-averaged results (Fig. 5.4), group 1, the better performing group, exhibits some significant eastward shift of its ENSO-related precipitation in the equatorial Pacific. Group 2 is the model group that shows a more westward-located maximum center of precipitation anomalies and much drier anomalies in the equatorial Pacific. In this group, no significant increase or shift of ENSO-related precipitation occurs in the 20th century.

5.4 Multi-decadal Changes of ENSO-related Precipitation During the 21th Century

In this section, we present the projected multi-decadal changes of ENSO-related precipitation in two CMIP5 experiments, 'RCP4.5' and 'RCP8.5'. In the RCP4.5 scenario, most of the group 2 ensemble members tend to project significant positive changes in ENSO-related precipitation over the tropical Pacific, as shown in Table 5.1, while fewer ensemble members in group 1 have significant changes in the 21st century projections than in the historical simulation. In the group-averaged results (Fig. 5.5a), although group 1 exhibits stronger ENSO-related precipitation anomalies over the eastern to central equatorial Pacific, the change is not significant. In group 2, the ENSO-related precipitation anomaly center becomes more robust and shifts slightly to the east in the equatorial Pacific. These changes are significant in the central Pacific region. For the RCP8.5 scenario (Fig. 5.5b), the intensification of ENSO-related precipitation anomalies over the eastern to central equatorial Pacific in group 1 is much more robust and significant than in RCP 4.5, and the ENSO-related droughts over the western Pacific and Maritime Continent also intensify. In group 2, both the increase of ENSO-related precipitation and the eastward shift of the maximum precipitation anomaly center are more significant and more obvious as well in RCP8.5. Table 5.1 shows that 40 out of 54 ensemble members project significant positive changes of ENSO-related precipitation in the RCP8.5 scenario, instead of 31 (22) in the RCP4.5 scenario (historical simulation).

Fig. 5.5c presents the projected ENSO-related SST changes in these two scenarios. In group 2, the changes in ENSO-related SST in the western Pacific are clearly related to the changes of the precipitation anomalies in Fig. 5.5 a&b. The western edge of the positive ENSO-related SST anomalies in the western equatorial

Pacific moves to the east in the latter half of the 21st century and the maximum center of SST anomalies moves from the easternmost Pacific to the eastern-central Pacific (not shown). Such changes cause the negative anomaly departures in the westernmost Pacific in the second half of the 21st century (Fig. 5.5c right panel), which correspond to the drier anomalies in the ENSO-related precipitation in same region. The positive SST anomaly differences around 160°E are related to the increase in ENSO-related precipitation over the same longitude. In the ENSO-related diabatic heating of the Walker circulation results (Fig. 5.6 a&b, right panel), we can also see the eastward shift of the diabatic maximum center in group 2 in the two scenarios and the intensification of both the maximum center of heating anomaly (160°E to 180°, from near-surface to 150mb) and the cooling anomalies from 120°E to 140°E as well. Such consistency among the changes of ENSO-related precipitation, SST, and diabatic heating suggest that this ENSO-related air-sea coupling system of group 2 in the central to western Pacific could respond dynamically to the global warming. The warming in the SST anomalies around 180° can lead to more convection along with more water vapor in the atmosphere above, resulting in stronger diabatic heating anomalies that further increase the zonal gradient of diabatic heating in the western Pacific, which then intensifies the Walker circulation anomalies in the western Pacific. The increase in surface westerly anomalies can result in more warm water being transported to the east, which in turn strengthens the air-sea coupling in more eastern longitudes. All of these changes/differences are, again, more robust in the higher greenhouse gas emission scenario, RCP8.5, than in RCP4.5. For example, the diabatic heating anomaly center shifts are about 5° more eastward in RCP8.5 than in

RCP 4.5. The zonal gradient of the SST and diabatic heating anomalies in the western Pacific is also much larger in RCP8.5. In the eastern Pacific, group 2 exhibits an amplitude increase in the equatorial ENSO-related precipitation anomalies, but a decrease in the SST anomalies in the same region. In the Walker circulation-related diabatic heating anomaly results (Fig. 5.6 a&b, right panel), the precipitation-related diabatic heating increases in the middle to upper troposphere over the same region in the later 21st century, while the lower levels of the atmosphere get cooler. Also, the cooling anomalies above 80°W become stronger, which can cause stronger descending motion and may strengthen the local Walker circulation anomalies as well as the easterly anomalies and the related SST cooling anomalies.

In group 1, in contradiction to the increase and eastward shift of ENSO-related precipitation in the eastern Pacific, the ENSO-related SST anomalies tend to become weaker in most longitudes of the equatorial Pacific in the second half of the 21st century, indicating a reduction of the ENSO SST amplitude (Kim et al. 2014). The group 1 models' ENSO-related diabatic heating results over the equatorial Pacific (Fig. 5.6 a&b, left panel) show that the maximum diabatic heating anomaly center remains in the same location (around 180°) and the increase of diabatic heating anomalies mostly happens in the middle to upper troposphere zonally from 160°E to 100°W, instead of the eastward shift and vertical extension of the maximum diabatic heating anomaly center in group 2. The cooling anomalies in group 1 intensify in the lower to middle troposphere, especially from 110°E to 180°. Such different behaviors between the heating/cooling anomalies in upper and lower troposphere could be due to thermodynamical (heating from condensation of more water vapor) and/or

dynamical changes of the air-sea coupling systems, and understanding which of these dominate requires further research.

5.5 ENSO Differences Between the 20th and 21th Centuries

This section compares the centennial changes in ENSO-related SST, precipitation and diabatic heating between the 20th century and the 21st century under the RCP4.5 and RCP 8.5 scenarios. In group 1 models, ENSO-related SST anomalies (Fig. 5.7a, left panel) exhibit significant cooling departures in both RCP4.5 and RCP8.5 from the historical simulation in the easternmost Pacific. In the central Pacific, the SST anomalies become warmer in the 21st century, especially in the southern off-equatorial region. The ENSO-related precipitation change results (Fig. 5.7b, left panel) show that most of the precipitation anomaly intensification occurs over the eastern to central equatorial Pacific. As in Section 5.4, this precipitation increase is related to the increase of diabatic heating in the middle to upper troposphere (Fig. 5.7c, left panel) over the central-eastern Pacific, rather than the zonal shift of the maximum heating center, which is located above 180° in all three experiments. ENSO-related precipitation also increases in the southern off-equatorial region in the central Pacific, which corresponds to the amplitude increase of ENSO-related SST anomalies in the same region. In the ENSO-related diabatic heating in the cross section of the central Pacific (Fig. 5.7d left panel), the intensification of ENSO-related precipitation in this region is shown as an increase of heating from low level convection above 15°S -10°S. Over the western Pacific especially in the SPCZ region, both the amplitudes of the ENSO-related SST and precipitation anomalies

decrease in the 21st century. These changes are also shown in the diabatic heating anomalies (Fig. 5.7c & 5.7e, left panel) as cooling departures over 120°E -180° and 20°S to the equator.

The ENSO-related SST, precipitation, and diabatic heating centennial changes between the 20th and the 21st centuries are generally more robust in group 2 than in group 1. In its ENSO-related SST anomaly results (Fig. 5.7a, right panel), the positive SST anomalies warm most in the central equatorial Pacific in the 21st century. The negative anomalies in the western Pacific also become cooler. These changes suggest that the amplitude of ENSO increases in the 21st century in group 2. As a result, the ENSO-related precipitation anomalies (Fig. 5.7b, right panel) as well as the related diabatic heating and cooling in the western to central equatorial Pacific (Fig. 5.7c, right panel) are more robust in the 21st century. The maximum center of ENSO-related precipitation and diabatic heating anomalies also shift 5° -10° further eastward (not shown). Therefore, the bias of the ENSO-related drier equatorial anomalies, which is associated with the dry equator bias, is greatly reduced in the 21st century (especially in the RCP8.5 scenario), compared to in the 20th century. In the ENSO-related diabatic heating cross-section in the central Pacific (Fig. 5.7d, right panel), both the deep heating anomalies between 10°S -5°N and the cooling anomalies in the northern and southern off-equatorial regions increase in the 21st century, indicating that the ENSO-related Hadley circulation anomalies over the central Pacific are enhanced. An increase is also seen in the diabatic cooling anomalies over the western Pacific (Fig. 5.7e, right panel). Unlike group 1, group 2 exhibits more robust changes

in the cooling anomalies above the northern off-equatorial region in the western Pacific.

All of these aforementioned centennial changes between the 20th and the 21st centuries regarding either the intensification or zonal shift are similar but more intense in the RCP 8.5 scenario, compared to in RCP4.5. Table 5.2 shows that more ensemble members tend to project significant positive changes in ENSO-related precipitation under RCP8.5 than RCP4.5, particularly within group 1. This suggests that, although the ENSO-related features of each ensemble member respond differently to global warming, an increase in such response in a higher greenhouse gas emission scenario from a lower emission scenario can be anticipated in the majority of the ensemble members.

To study whether the centennial changes of air-sea interaction in the equatorial Pacific are different in the two groups, we use the same positive Bjerknes feedback method described in Section 4.5. The Bjerknes feedback is measured by linear regression of the ENSO-related τ_x along the equator in the Pacific (averaged from 5°S to 5°N) on the ENSO-related $\mathrm{dSST}/\mathrm{dx}$ (Zheng et al. 2014). The cross-basin gradient dx for $dSST$ is the SST anomaly average within an eastern to central Pacific box (160°-120°W, 5°S-5°N minus the average within a western Pacific one (120°-160°E). Similar feedback results as in Fig. 4.14a are found in the 20th century results (Fig. 5.8a), in that group 1 tends to better simulate the curve of the Bjerknes feedback in the equatorial Pacific than group 2 with generally smaller standard deviation among the ensemble members. In this historical simulation, group 1 and 2 both simulate the location of maximum regression coefficient between the ENSO-related

dSST/dx and the ENSO-related τ_x more eastward than 20CR. In the RCP4.5 experiment, the maximum regression coefficients of both group 1 and 2 become larger. The location of maximum coefficients in group 1 remains the same, while in group 2 the location is shifted to the west, almost to the same position as where the 20CR maximum in the historical simulation is located. The standard deviation among the ensemble members in group 2 also shrinks. With regard to the RCP8.5 scenario, the maximum Bjerknes feedback in group 2 moves further to the east and is closer to the location in group 1, which also shifts slightly to the east. The maximum coefficients in group 1 become larger in RCP8.5 than in RCP4.5, while those in group 2 become smaller in RCP8.5. The standard deviation of both groups increases, with that of group 1 larger than in group 2. These results indicate that global warming leads to a more realistic location of the maximum Bjerknes feedback (ENSO-related air-sea interaction) in group 2. The location of the maximum Bjerknes feedback in group 1 is less sensitive to global warming, but the amplitude of this feedback increases as global temperature rises. In group 2, the response of the Bjerknes feedback amplitude to global warming is less linear than in group 1. The uncertainty of the actual amplitude of the Bjerknes feedback increases among the ensemble members in a higher greenhouse gas emission scenario.

Based on these ENSO-related SST, precipitation, diabatic heating and air-sea interaction results, we see a stronger ENSO response to global warming in group 2 than in group 1. Since the group 2 models generally have weaker ENSO variability and more unrealistic ENSO-related SST and precipitation patterns (e.g. more westward-located maximum precipitation anomaly center), as demonstrated in

Chapter 3 and 4, it is very likely that these multi-decadal or centennial ENSO-related changes are exaggerated in group 2. Therefore, the ENSO-related projections in group 2 should be used with caution.

5.6 Summary

This study uses a new method (HFCA) that is similar to the one developed in Wills et al. (2018) to cleanly separate the ENSO variability from longer term sources of variability such as global warming and the PDO. This method can reduce the effect of those phenomena with longer periods on ENSO as much as possible and is convenient to use with both reanalyses and CMIP5 models. We examined the multi-decadal and centennial changes of ENSO-related SST, precipitation, diabatic heating, and air-sea interaction during the 20th century, as obtained from the HFCA-derived ENSO time series, in the long-term precipitation and SST reanalyses (20CR, REC, HadISST and ERSST). In addition, 26 CMIP5 models are separated into two groups based on their performance in precipitation and ENSO-related precipitation (Chapter 3 and 4), in order to study how the two groups respond differently during the 20th and 21st centuries.

In the 20th century, the ERSST and HadISST results suggest an amplitude intensification of ENSO during the last 50 years of the past century. The ENSO-related precipitation changes are different between 20CR and REC. 20CR exhibits an eastward shift of the ENSO-related precipitation in the central to eastern Pacific and a westward shift of the ENSO-related drought in the western Pacific during the 20th century. The ENSO-related changes in REC do not show any location shift but do

exhibit an intensification of both ENSO-related precipitation and droughts. Since precipitation responds nonlinearly to global warming (Power et al. 2013), more long-term precipitation observation and reanalyses are needed to further understand how ENSO-related precipitation changed in the past century. In CMIP5, although twice the number of ensemble members simulate positive ENSO-related precipitation changes than negative changes in the tropical Pacific, the group-averaged results do not show significant changes in ENSO-related precipitation and SST.

During the 21st century, under two different greenhouse gas emission scenarios, RCP4.5 and RCP8.5, although group 1 projects weaker ENSO-related SST in the latter half of the 21st century, its ENSO-related precipitation responds nonlinearly and shows an increase in the eastern equatorial Pacific. The group 2 models show more unanimous results of intensification and eastward shifts in ENSO-related SST, precipitation and diabatic heating/cooling in the western Pacific.

Comparing the ENSO-related features in the 21st century to those in the 20th century, more ensemble members tend to project significant positive changes in ENSO-related precipitation in the 21st century, especially in the higher greenhouse gas emission scenario (RCP8.5). In general, the models tend to project similar but more robust ENSO-related changes in the RCP 8.5 scenario than in RCP4.5. However, the differences of ENSO-related changes between CMIP5 group 1 and group 2 are very large. In general, the group 1 models exhibit significant ENSO-related precipitation changes that are related to the intensification of equatorial diabatic heating anomalies in the middle to upper troposphere. The group 2 models, on the other hand, exhibit increased amplitudes of ENSO-related precipitation and

SST in the western-central Pacific with an eastward shift. The diabatic heating anomalies over the western-central Pacific also move to the east and intensify vertically, which can result in stronger ENSO-related Walker and Hadley circulations in the tropical Pacific in group 2. This eastward shift is also shown in the location of maximum Bjerknes feedback in group 2. In addition, these multi-decadal or centennial changes of ENSO-related features in group 2 are much more robust and more unanimous among the models than in group 1. Based on the weaker ENSO variability and more unrealistic ENSO-related precipitation patterns and diabatic heating structures in group 2 as demonstrated in Chapter 3 and 4, we suspect that these ENSO-related changes of group 2 could be exaggerated and less reliable than the results of group 1.

Although we have investigated the ENSO-related precipitation changes in the CMIP5 models from a thermodynamical (diabatic heating) perspective, we still do not know what proportion of the changes in ENSO-related precipitation is from the thermodynamical (water phase changes) and dynamical (circulation changes) mechanisms. Future research, such as using the moisture budget (Trenberth and Guillemot 1995), is needed to further understand the ENSO-related precipitation in the better ENSO performing CMIP5 models.

Table 5.1 List of number of ensemble members in simulating or projecting significant (passing 95% confidence level) positive "+" or negative "-" changes of ENSO-related precipitation over tropical Pacific within the 20th or 21st century in all three experiments. The changes here include both intensification and zonal shift of large precipitation system (> 30° longitudes), but not the meridional shift. Each group has total of 27 ensemble members.

	Historical	**RCP4.5**	**RCP8.5**
Group1 "+"	12	11	19
Group1 "-"	6	4	0
Group2 "+"	10	21	21
Group2 "-"	5	0	2

Table 5.2 List of number of ensemble members in simulating or projecting significant (passing 95% confidence level) positive "+" or negative "-" changes of ENSO-related precipitation over tropical Pacific in the 21st century from the 20th century. The changes here include both intensification and zonal shift of large precipitation system (> 30° longitudes), but not the meridional shift. Each group has total of 27 ensemble members.

	RCP4.5	**RCP8.5**
Group1 "+"	17	21
Group1 "-"	6	4
Group2 "+"	22	22
Group2 "-"	0	1

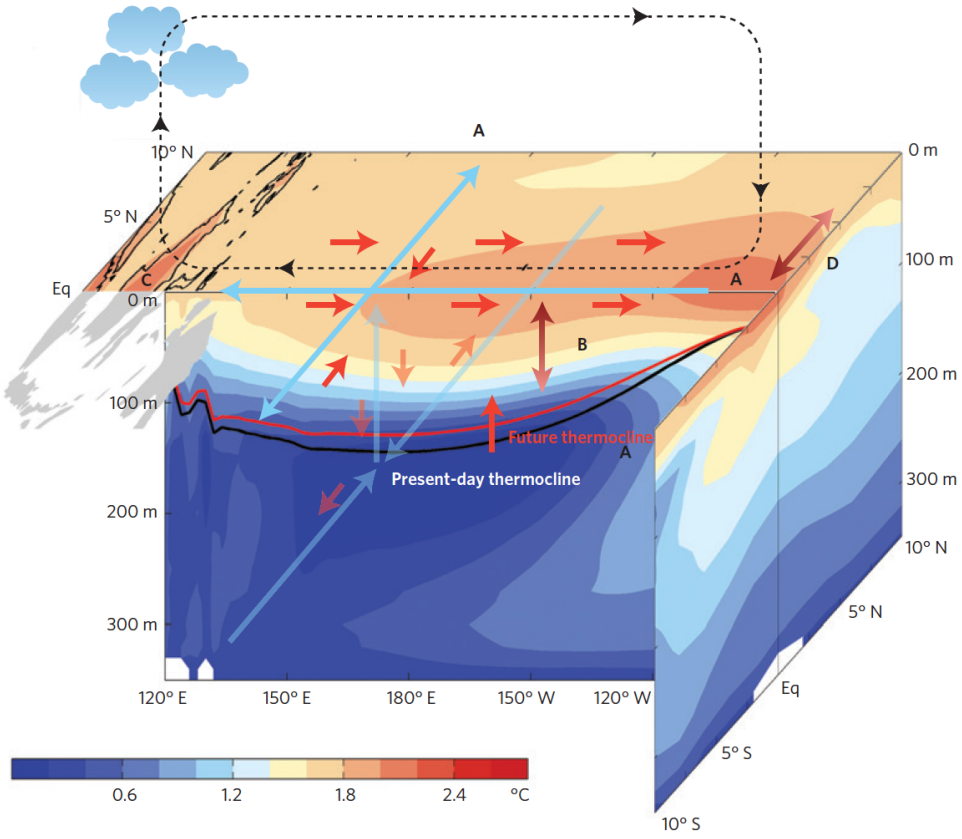

Figure 5.1 global warming induced changes at the surface and in the upper ocean (shown in zonal and meridional cross-sections) (From Cai et al. 2015, Figure 1)

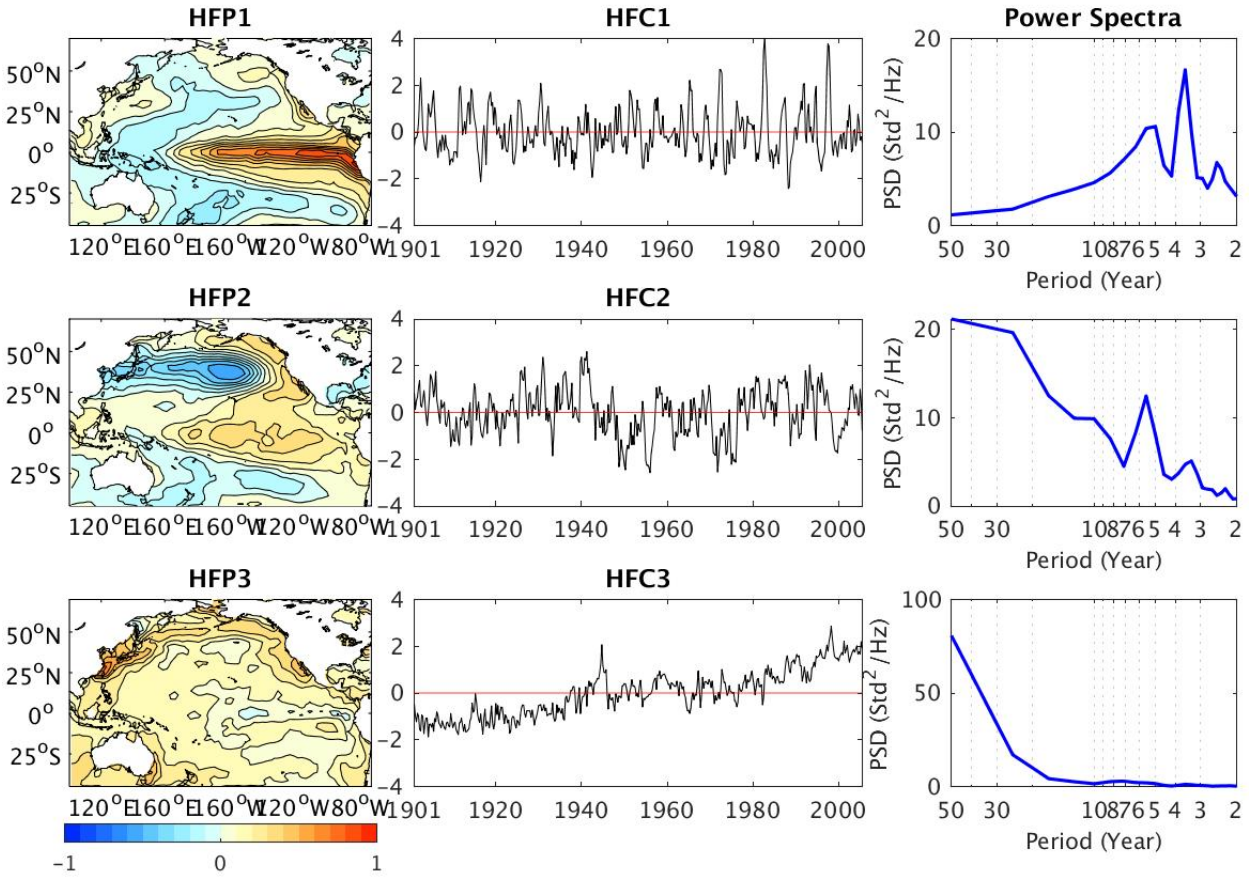

Figure 5.2 High-frequency components (HFC) of Pacific SST during the 20th century. **Left column:** High-frequency spatial patterns (HFP, unit: °C/standard deviation). HPC1 is the ENSO variability; HPC2 is the PDO variability and HPC3 is the global warming. **Middle column:** the corresponding high-frequency components (HFC). **Right column:** corresponding power spectra.

(a) ENSO-related SST Changes (left panel: HadISST; right panel: ERSST)

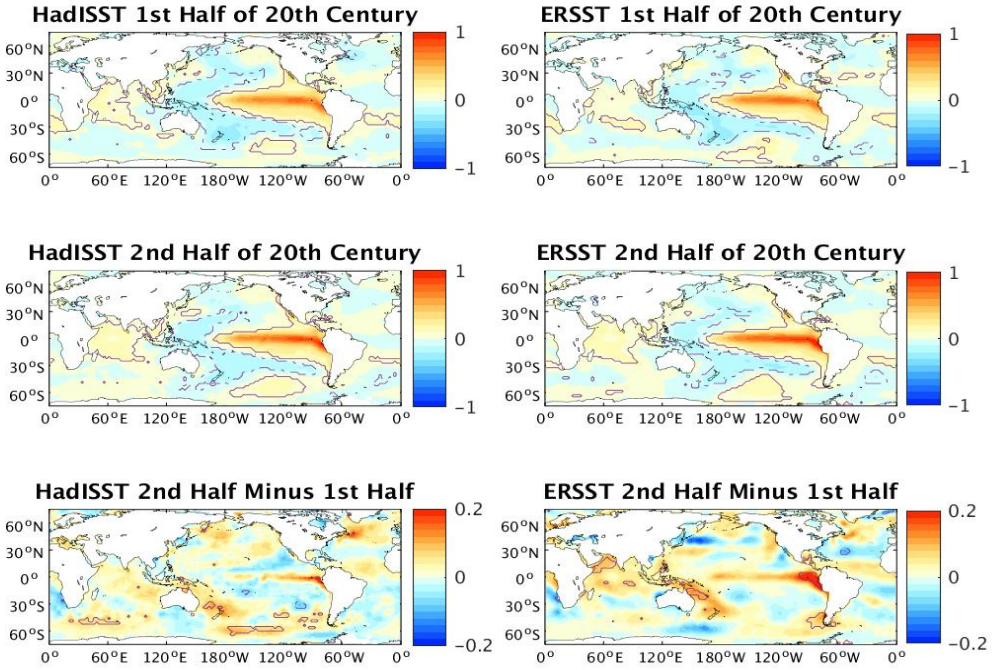

(b) ENSO-related Precipitation Changes (left panel: 20CR; right panel: REC)

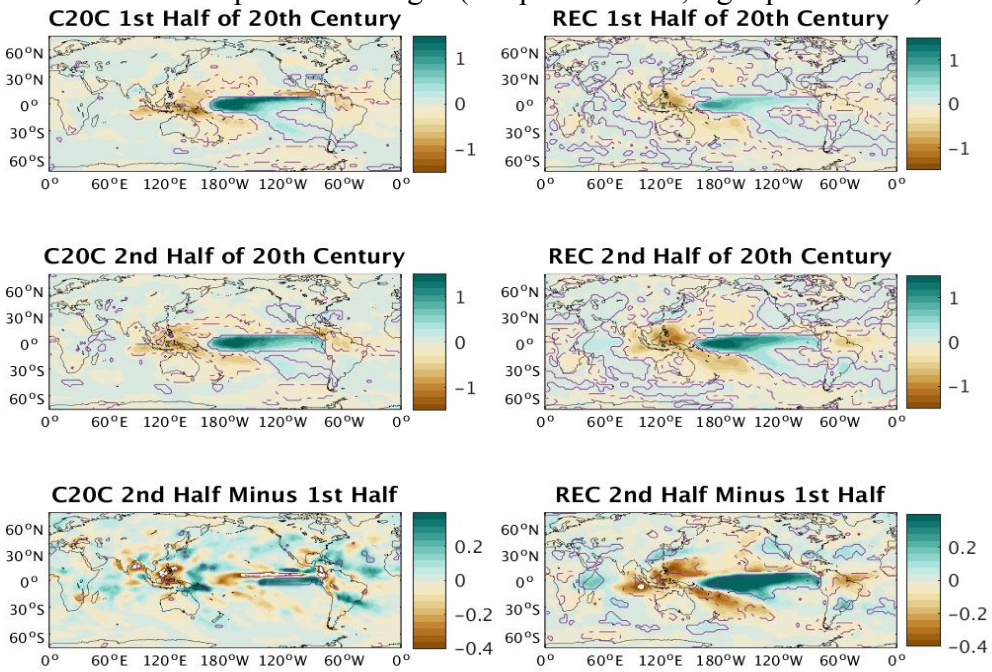

Figure 5.3 ENSO-related **(a)** SST (unit: K) and **(b)** precipitation (unit: mm/day) regression coefficient results of **the reanalyses** during the first half (1901-1950) and second half (1951-2000) of the 20th century and the differences between the two halves. Contours in magenta color stand for significance levels. 99% significance level is used for each half-century result with a Student T-test (Santer et al. 2000), and 95% is for the difference result using a Z-test (Paternoster et al. 1998).

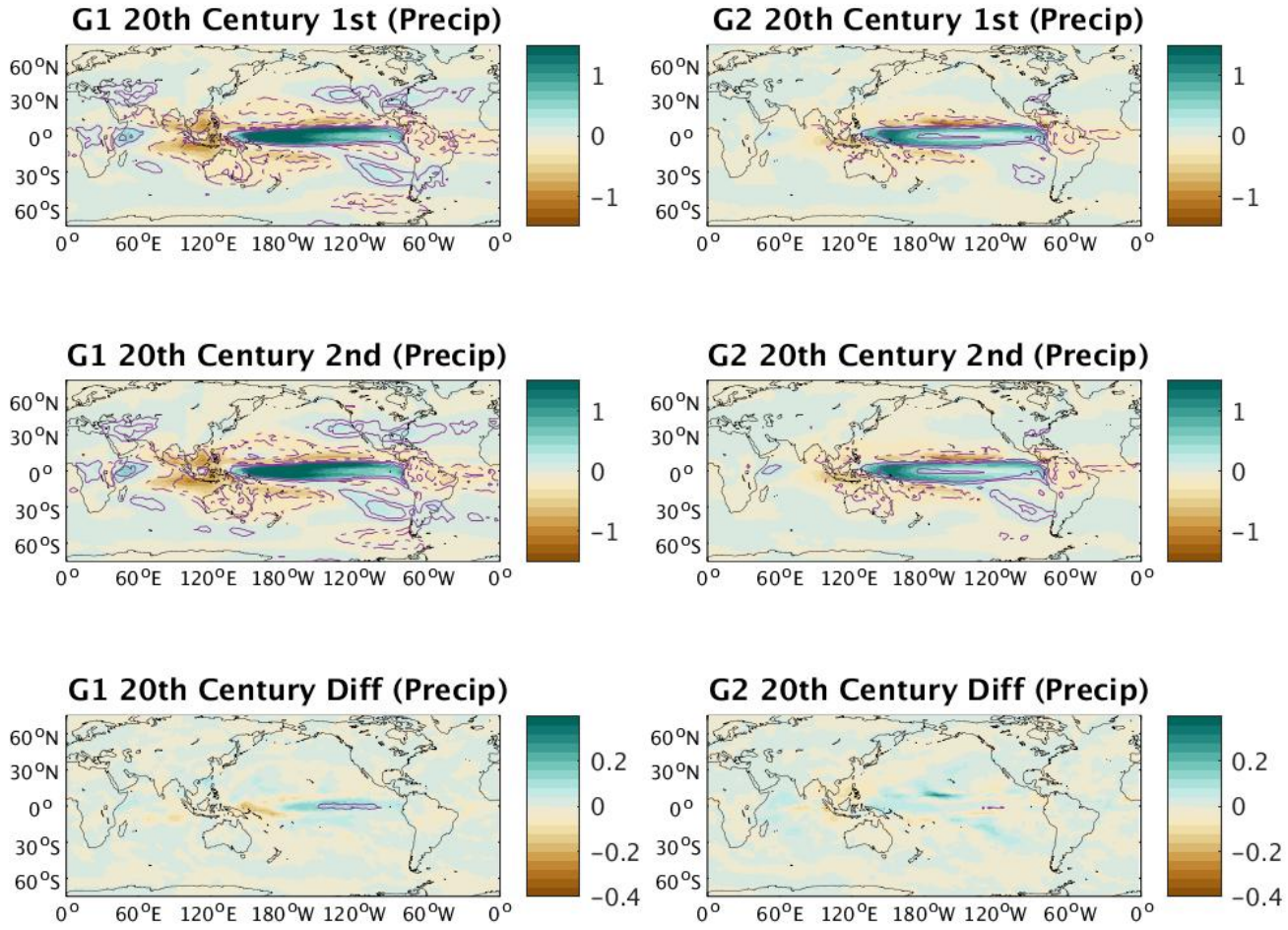

Figure 5.4 ENSO-related precipitation (unit: mm/day) regression coefficient results of the first half (1901-1950) and second half (1951-2000) of the 20th century and the differences between them in **the two CMIP5 groups**. Contours in magenta color stand for significance levels. 99% significance level is used for each half century result, and is contoured for 1/3 and 2/3 of the total number of ensemble members within each group passing a 99% confidence level of a Student T-test. 95% significance level is for the difference result (bottom panel), with contour of 5, 10, 15 and 20 ensemble members passing a 95% confidence level of a Z-test.

(a) ENSO-related precipitation changes in RCP 4.5 scenario

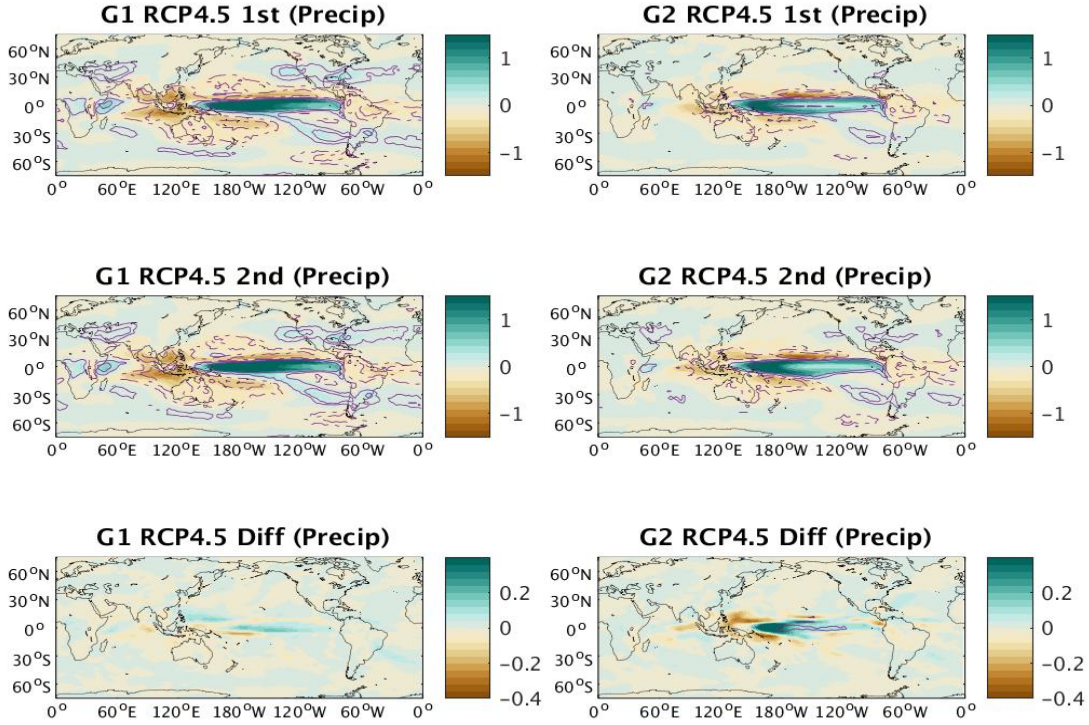

(b) ENSO-related precipitation changes in RCP 8.5 scenario

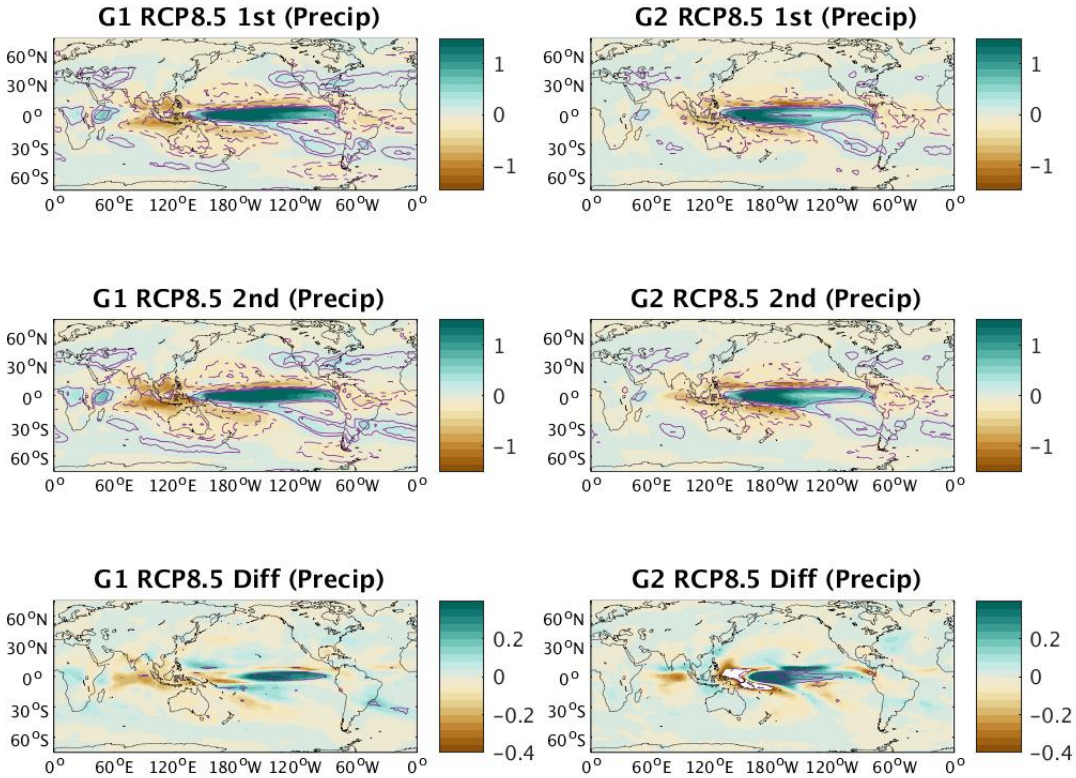

(c) ENSO-related SST changes in RCP4.5 and RCP 8.5 scenarios

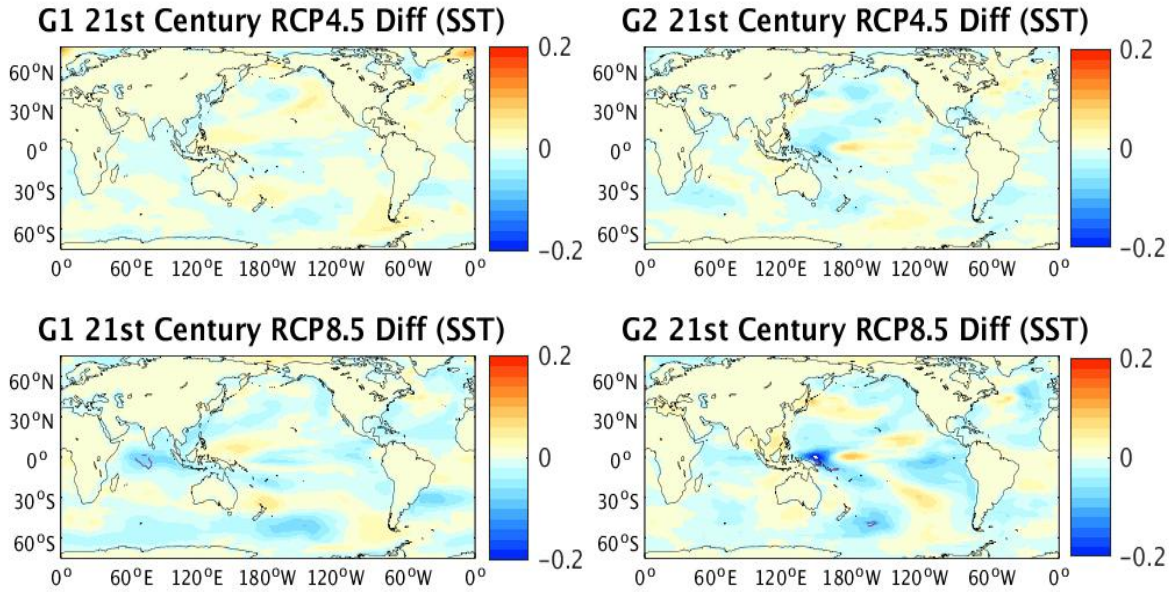

Figure 5.5 (a) ENSO-related precipitation (unit: mm/day) regression coefficient results of the first half (2006-2050) and second half (2051-2100) of the 21st century and the differences between them in **the two CMIP5 groups** under the RCP4.5 scenario. **(b)** Same as a, but under the RCP 8.5 scenario. Contours in magenta color stand for significance levels (99% for each half century result, and 95% for the difference result, using same methods as Figure 5.4). **(c)** ENSO-related SST (unit: K/day) regression coefficient results of the differences between the first half (2006-2050) and second half (2051-2100) of the 21st century in **the two CMIP5 groups** under the **RCP4.5** (upper panel) and **RCP8.5** (lower panel) scenarios.

(a) Diabatic heating of Walker circulation during ENSO in RCP4.5

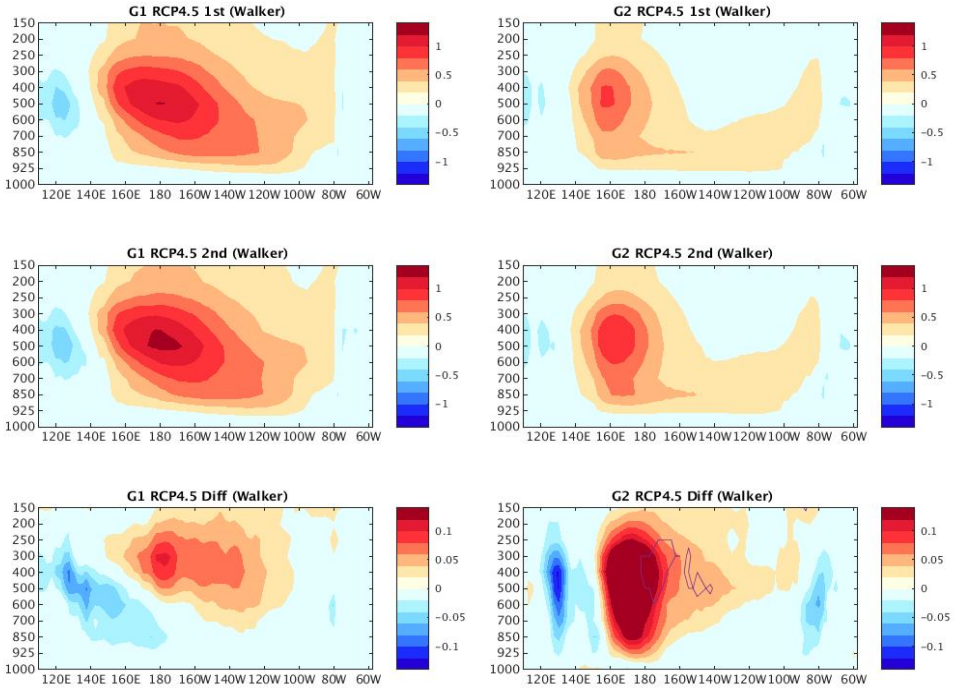

(b) Diabatic heating of Walker circulation during ENSO in RCP8.5

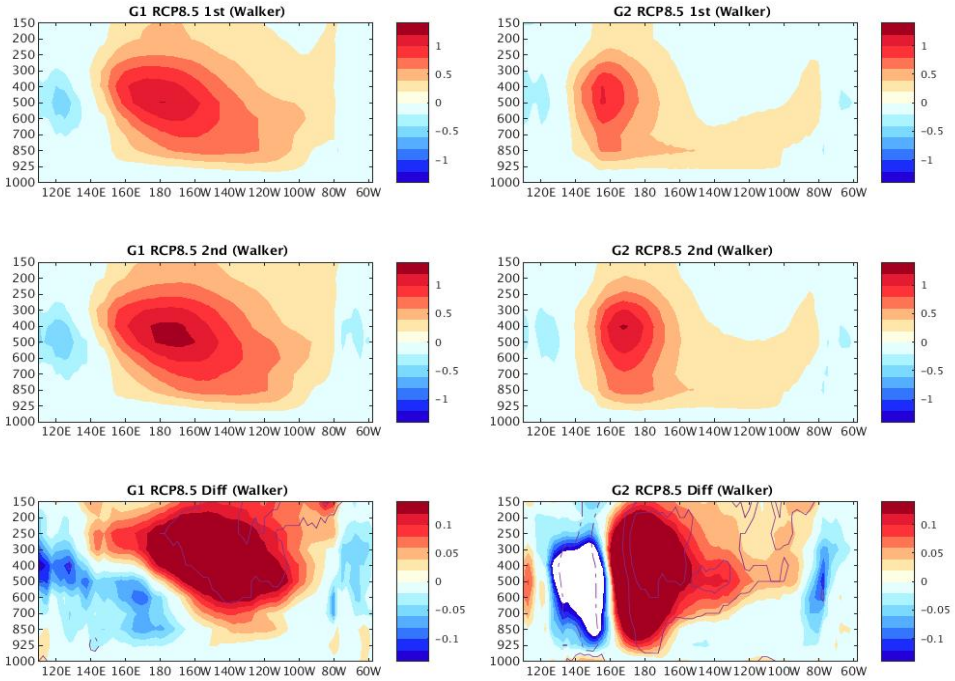

Figure 5.6 (a) ENSO-related diabatic heating (unit: K/day) regression coefficients of Walker circulation (averaged 5°S - 5°N) during the first half (2006-2050) and second half (2051-2100) of the 21st century and the differences between them in **the two CMIP5 groups** under the RCP4.5 scenario. **(b)** Same as a, but under the RCP 8.5 scenario. Contours are defined same as in previous figures.

(a) ENSO-related SST changes

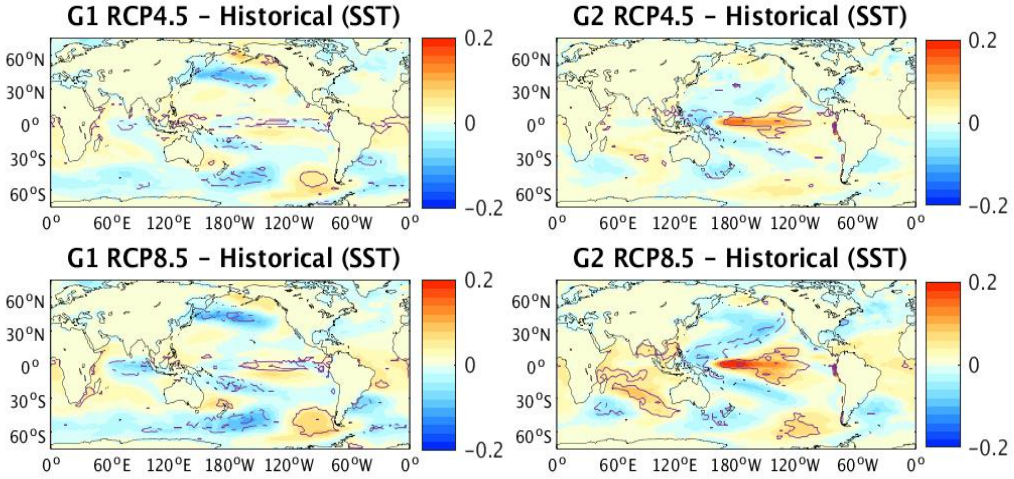

(b) ENSO-related precipitation changes

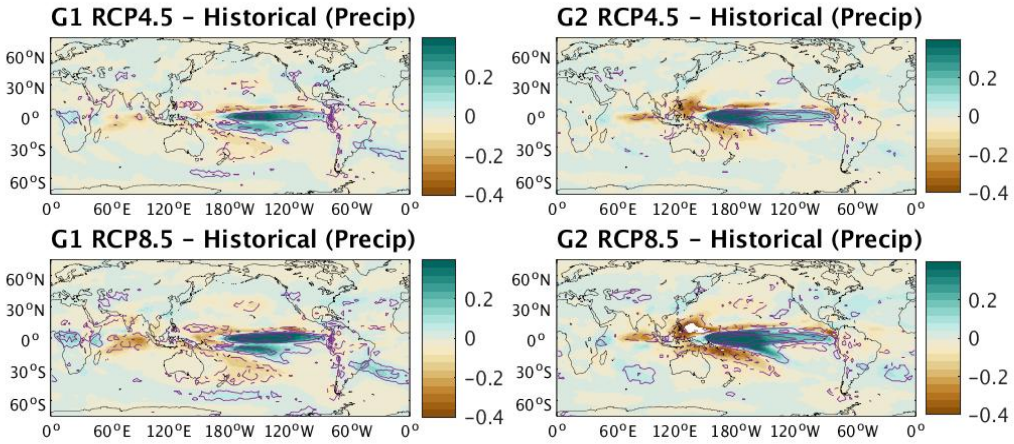

(c) ENSO-related diabatic heating changes (Walker circulation)

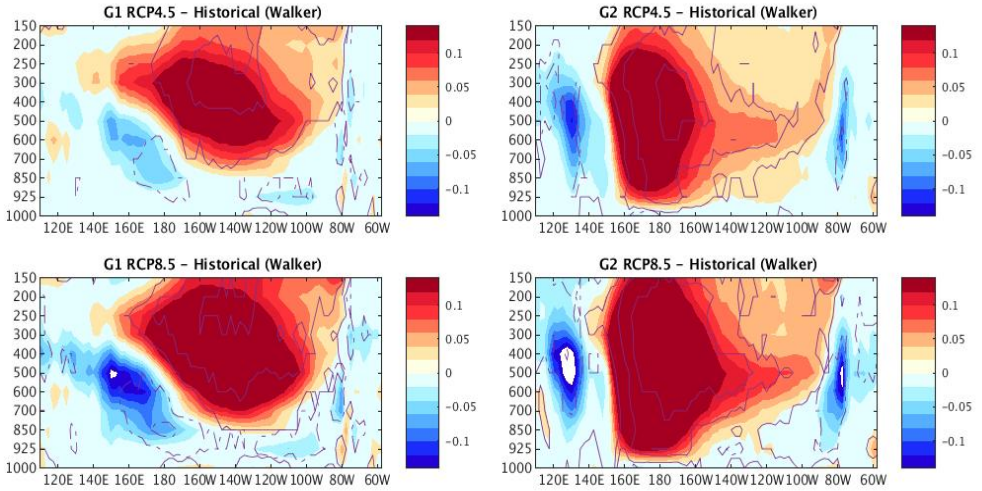

(d) ENSO-related diabatic heating changes (Hadley circulation cross-section at maximum ENSO-related precipitation/diabatic heating region, averaged from 180° to 150°W)

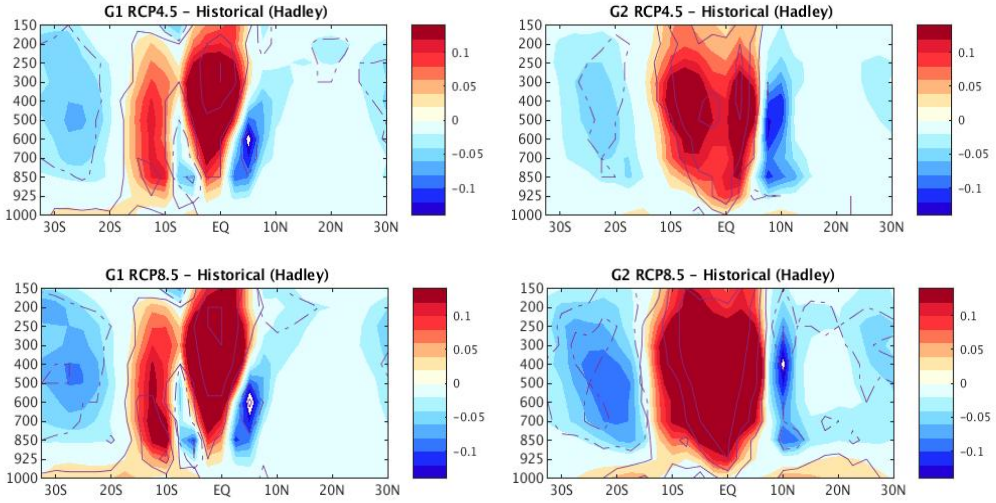

(e) ENSO-related diabatic heating changes (Hadley circulation cross-section at western Pacific, averaged from 110°W to 130°W)

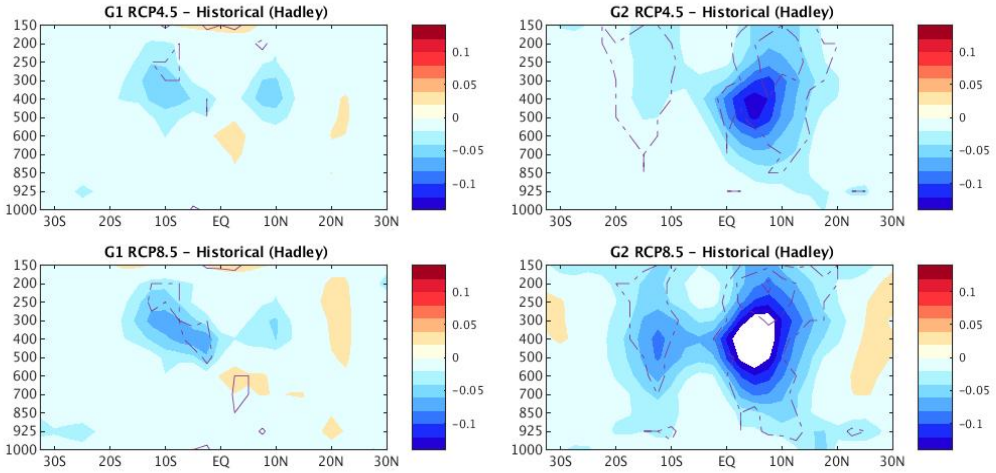

Figure 5.7 ENSO-related SST (K), precipitation (mm/day), diabatic heating (K/day) changes between the 21st century projection (2006-2100) and the 20th century historical simulation (1901-2005) in the **RCP4.5 and RCP 8.5** scenarios. Contours are defined same as in previous figures.

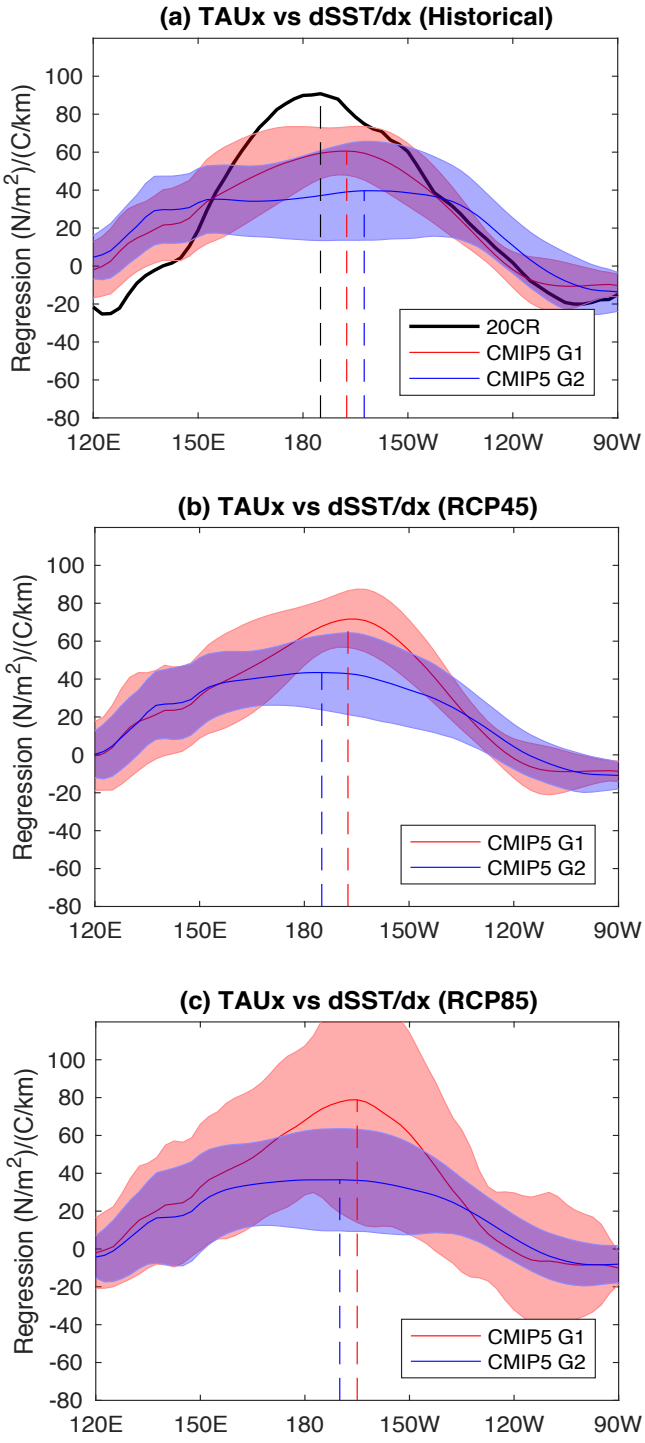

Figure 5.8 Bjerknes positive feedback represented by linear regression coefficients between ENSO-related τ_x and ENSO-related $dSST/dx$ in 20CR and the two CMIP5 groups. Red (blue) lines stand for the mean of CMIP5 group 1 (2), and the red (blue) shades are the standard deviation within group 1 (2).

Chapter 6: Summary and Future Research

6.1 Outline and Main Issues

ENSO, as the most significant interannual variability in the atmosphere-ocean coupling system, remains a challenge for GCMs to simulate realistically. Considering the great socioeconomic consequences brought by extreme ENSO events, it is important to 1) evaluate the ENSO simulations of the state-of-the-art coupled GCMs in the CMIP5 project for the modelers to further improve the next generation of coupled GCMs and 2) study the ENSO projection of the future for United Nations and local governments to make preparation for the potential ENSO-related changes under global warming. In this dissertation, precipitation is used to represent ENSO and its impact. We have evaluated the 20^{th} century mean states of precipitation and ENSO-related precipitation anomalies in the CMIP5 models with two recent long-term precipitation datasets (20CR and REC) (Chapter 3), and have developed a method to classify the models into two groups based on their performances. The related group biases are identified and the possible connections between the biases of precipitation climatology and the ENSO-related precipitation biases have been discussed.

In order to further understand these ENSO-related precipitation biases in the CMIP5 models, the tropical-precipitation-related atmospheric dynamics and thermodynamics during ENSO have been dissected and diagnosed, including the 3D structures of the ENSO-related diabatic heating and atmospheric circulations as well as the ENSO-related air-sea interaction (Chapter 4). Comparing these ENSO features in the two CMIP5 groups to those of the recent high-resolution atmospheric

reanalyses (ERA-Interim, MERRA-2 and CFSR) can reveal the intermodel diversity of the atmospheric components of ENSO. Additionally, as diabatic heating is a fundamental characteristic of the large scale atmospheric circulation but cannot be observed directly, it is essential to intercompare the diabatic heating among the three state-of-the-art reanalyses, and determine the best one by validating them with other independent heating observations (e.g. TRMM CSH latent heating).

How ENSO and the related precipitation anomalies will respond to greenhouse warming is an issue that concerns both scientists and the United Nations. Despite a growing body of research on the behavior of ENSO under global warming, the changes of ENSO-related precipitation in a warming world are less studied. Also, the multi-decadal changes of ENSO-related precipitation in the 20th century are poorly known due to the previous unavailability of long-term precipitation datasets. Chapter 5 characterizes these changes in the 20th century in 20CR and REC, and studies the multi-decadal and centennial changes of the ENSO-related precipitation during the 20th and 21st centuries in the CMIP5 models based on intermodel diversity of ENSO-related precipitation biases.

The main topics of this dissertation are summarized as follows:

- The capability of 20CR, REC and the CMIP5 models to represent observed precipitation climatology and ENSO-related precipitation anomalies in the 20th century (Chapter 3)
- The CMIP5 model biases in precipitation climatology and ENSO-related precipitation anomalies as well as the classification of the models according to these biases (Chapter 3)

- The possible connections between the model biases of ENSO-related precipitation and biases of precipitation climatology/ ENSO-related SST anomalies (Chapter 3)
- The best atmospheric reanalysis among ERA-Interim, MERRA-2, and CFSR for representing 3D structures of tropical diabatic heating and the related atmospheric circulations (Chapter 4)
- The CMIP5 model biases of the ENSO-related atmospheric features, such as the diabatic heating, the upper and lower tropospheric stream function and velocity potential, the Pacific Walker circulation, and local Hadley circulations as well as the air-sea interaction (Chapter 4)
- The differences between the better performing CMIP5 group and the underperforming one in the perspectives of these aforementioned ENSO-related features (Chapter 4)
- The multi-decadal changes of ENSO-related precipitation in the 20th century in 20CR, REC and the CMIP5 models, and whether these changes are statistically significant (Chapter 5)
- The multi-decadal and centennial changes of ENSO-related precipitation during the 20th and 21st centuries under different greenhouse gas emission scenarios, based on different groups of the CMIP5 models in simulating ENSO dynamics and thermodynamics (Chapter 5)

6.2 Summary

In Chapter 3, both REC and 20CR are similar to the TRMM, ERA-Interim, MERRA-2, and CFSR precipitation from the perspective of annually-averaged precipitation climatology during 1998-2005. REC resembles the other precipitation datasets (TRMM, ERA-Interim, MERRA-2 and CFSR) more than 20CR. 20CR is wetter than REC by an average of 0.50mm/day over the ocean. The differences between the two datasets are the largest in the tropics, especially in the SPCZ. Compared with REC and 20CR, the 30 CMIP5 models used in this dissertation exhibit the common coupled GCM precipitation biases of a dry equator, DITCZ in the eastern Pacific, and an overly zonal SPCZ, despite the fact that the models generally have good spatial correlations with the observations.

The spatial fields of the ENSO-related precipitation in REC and 20CR are very similar to each other. The CMIP5 models have diverse spatial correlations with these two datasets. Those models that exhibit lower pattern correlations with REC and 20CR in ENSO-related precipitation are the ones with a more severe dry equator bias, and they tend to have rainfall reduction over the equatorial Pacific in the ENSO-related precipitation as well. Two groups of the CMIP5 models are classified based on their higher (lower) correlations with the observations from the perspective of precipitation climatology and ENSO-related precipitation anomalies. The better performing group (group 1) simulates more realistic spatial patterns, amplitude, and seasonal variability of ENSO-related precipitation anomalies compared to the underperforming group (group 2). In general, the model ENSO-related precipitation anomalies over the tropical Pacific Ocean extend too far west and are meridionally

narrower than the observations, exhibiting more "Hadley-like" than "Walker-like" patterns.

The spatial structure of the ENSO-related precipitation anomalies in the models, especially the meridional width and zonal length, are associated with the corresponding ENSO positive SST anomaly pattern. The deficiency of ENSO-related precipitation over the equatorial Pacific is strongly related to the underestimated precipitation climatology in the same region, and is less sensitive to the ENSO SST variability. The DITCZ-like bias in the ENSO-related precipitation is positively correlated with the ENSO-related SST biases, but is less connected to the DITCZ itself.

Chapter 4 finds that ERA-Interim better represents the tropical diabatic heating and atmospheric circulation climatology compared to MERRA-2 and CFSR, as MERRA-2 and CFSR have smaller diabatic heating than ERA-Interim in those regions where ERA-Interim already exhibits less robust heating than the TRMM CSH latent heating. MERRA-2 shows weaker ITCZ-related diabatic heating than ERA-Interim in January, which is related to the weaker ascending motion of its Hadley cell at the northern edge of the deep heating region, as well as the weaker SPCZ-related heating in MERRA-2 in July that is associated with the stronger descending motion of its Hadley cell. The Pacific Walker circulation (PWC) related diabatic heating in MERRA-2 is located more westward than in ERA-Interim and CFSR. CFSR tends to have seasonally-consistent less robust heating over the equatorial Pacific than ERA-Interim and MERRA-2. In the ENSO-related diabatic heating, MERRA-2 exhibits a more westward-located heating anomaly center than in ERA-Interim and CFSR.

CFSR continues to show a cooler equatorial Pacific than is found in ERA-Interim and MERRA-2 in its ENSO-related diabatic heating.

The CMIP5 group 1 models simulate better 3D structures of diabatic heating and the related atmospheric circulation climatology than do the group 2 models. The aforementioned biases of DITCZ and dry equator might be related to the stronger Hadley cells in the models. The ENSO-related diabatic heating anomalies in CMIP5 models are more westward-located, along with the westward-located lower (upper) convergence (divergence) center in the central Pacific, especially in group 2.

The group 2 models tend to simulate weaker ENSO variability in terms of mean states and seasonality as well as ENSO growth than the group 1 models, as indicated by the results of ENSO-related precipitation anomalies and their seasonality, total diabatic heating, convergence and divergence at the lower and upper levels, the Walker circulation, the local Hadley cells, the positive Bjerknes feedback, and near-surface wind features. Although group 1 models simulate these ENSO-related features much better than do those in group 2, they exhibits stronger "Hadley-like" ENSO-related diabetic heating and atmospheric circulations in the western Pacific.

Chapter 5 examines the multi-decadal and centennial ENSO changes in precipitation, SST, and diabatic heating with a new method modified from Wills et al. (2018) that can cleanly separate the ENSO variability from global warming and the Pacific Decadal Oscillation (PDO). In the 20th century, the ENSO-related SST features strengthened in the later 50 years, indicated by two long-term SST reanalyses, HadISST and ERSST. The ENSO-related precipitation changes are

different in 20CR and REC. The changes in 20CR include an eastward shift of the ENSO-related precipitation anomaly features in the central-eastern Pacific and a westward shift of the ENSO-related drought in the western Pacific. REC shows an intensification of both ENSO-related precipitation and droughts instead of zonal shifts. During the 21st century under both RCP4.5 and RCP8.5 scenarios, the two CMIP5 groups behave differently in the ENSO-related precipitation/SST. Group 1 projects weaker ENSO-related SST but stronger ENSO-related precipitation in the eastern equatorial Pacific in the latter half of the 21st century. The group 2 models, on the other hand, show intensification and eastward shifts of both ENSO-related SST and the related precipitation in the western Pacific.

Most models' ensemble members project significant positive changes in ENSO-related precipitation anomalies between the 21st and 20th centuries, especially in the RCP 8.5 scenario. Group 1 ensemble members show significant ENSO-related precipitation increases in the central-eastern Pacific, which are related to the intensification of diabatic heating anomalies in the middle to upper troposphere. Group 2 models project stronger intensification of ENSO-related precipitation and SST with an obvious eastward shift during the 21st century in the western-central Pacific. Such changes are associated with the stronger ENSO-related diabatic heating of the Walker and Hadley circulation anomalies in the models. The Bjerknes feedback in group 2 during the 21st century also occurs in a more realistic location than in the 20th century. These multi-decadal and centennial ENSO-related changes in group 2 could be exaggerated, considering that group 2 simulates weaker historical ENSO variability but they are much more robust than in group 1.

6.3 Future Work

The current work addresses the atmospheric components of ENSO-related biases in the current coupled GCMs and the atmospheric response of ENSO variability under global warming. Additional research will be needed to examine the oceanic features, as many previous studies have pointed out that the thermocline feedback might play a major role in determining the inter-model diversity of ENSO in the CMIP5 models (e.g. Chen et al. 2014; An et al. 2017). In particular, it is very important to study the potential causes of diverse performances of the CMIP5 CGCMs that uses the same atmosphere model but different ocean models, e.g. GFDL-ESM2M and GFDL-ESM2G. In addition, the response of ENSO-related precipitation to global warming must be further diagnosed from the thermodynamical and dynamical components in the moisture budget.

Much remains unknown also about the PDO variability in the reanalyses and the CMIP5 models. The PDO is a complex phenomenon characterized by multi-decadal variability in the northern Pacific and is probably due to a combination of several physical processes (e.g. Newman et al. 2016). One is that the changing surface ocean heat fluxes and the Ekman transport in the Aleutian low region associated with PDO are affected by local weather noise and tropical forcings such as ENSO (especially the eastern-Pacific type) through atmospheric teleconnections. In this dissertation, we have demonstrated a method that successfully separates ENSO, PDO and global warming signals in the reanalyses and the CMIP5 models. This method could be employed to study the PDO variability in these datasets. Our

preliminary results show that most of the CMIP5 models can simulate PDO-like variability, however, the intermodel diversity of the PDO-related spatial patterns is very large in both of the northern and tropical Pacific. Since both ENSO and PDO can exert influences on each other (Newman et al. 2016), realistic simulations of ENSO and PDO variability are necessary to project more accurate changes of ENSO in a warming world.

Currently, more advanced long-term reanalyses such as ERA-5 from ECMWF and the CMIP Phase 6 (Eyring et al., 2016) are under development and will be released soon. The new generation of global datasets can further spur the advancement in understanding ENSO and its teleconnections in both of the past and the future.

Bibliography

Adler, R. F., & Coauthors (2003). The version-2 Global Precipitation Climatology Project (GPCP) monthly precipitation analysis (1979–present). J. Hydrometeor., 4, 1147–1167

Allan, R., Linsday, J., & Parker, D., (1996). El Niño Southern Oscillation and Climatic Variability (Collingwood, Australia: CSIRO).

Allan, R. and T. Ansell (2006). A New Globally Complete Monthly Historical Gridded Mean Sea Level Pressure Dataset (HadSLP2): 1850–2004. J. Climate, 19, 5816–5842,https://doi.org/10.1175/JCLI3937.1

An, Soon-Il & Jin, F.-F. (2000). An eigen analysis of the interdecadal changes in the structure and frequency of ENSO mode. Geophysical Research Letters. 27. 2573-2576. https://doi.org/10.1029/1999GL011090

An, S. Il, Heo, E. S., & Kim, S. T. (2017). Feedback process responsible for intermodel diversity of ENSO variability. Geophysical Research Letters, 44(9), 4272–4279. http://doi.org/10.1002/2017GL073203

Barnett, T. LP., M. Latif, N. Graham, M. Flugel, S. Pazan, and W. White (1993). ENSO and ENSO-related predictability. Part I: Prediction of equatorial Pacific sea surface temperature with a hybrid coupled ocean-atmosphere model. J. Climate, 6, 1545-1566.

Barnston, A. G., & C. F. Ropelewski (1992). Prediction of ENSO episodes using canonical correlation analysis. J. Climate, 5, 1315-1345.

Bayr, T., D. Dommenget, T. Martin, and S. B. Power (2014), The eastward shift of the Walker circulation in response to global warming and its relationship to ENSO variability, Clim. Dyn., 43, 2747–2763, doi:10.1007/s00382-014-2091-y.

Bellenger, H., Guilyardi, E., Leloup, J., Lengaigne, M., & Vialard, J. (2014). ENSO representation in climate models: From CMIP3 to CMIP5. Climate Dynamics, 42, 1999–2018. doi:10.1007/s00382-013-1783-z

Bellucci, a., Gualdi, S., & Navarra, a. (2010). The double-ITCZ syndrome in coupled general circulation models: The role of large-scale vertical circulation regimes. Journal of Climate, 23, 1127–1145. doi:10.1175/2009JCLI3002.1

Bengtsson, L., Hagemann, S., & Hodges, K. I. (2004). Can climate trends be calculated from reanalysis data? Journal of Geophysical Research D: Atmospheres, 109(11), 1–8. http://doi.org/10.1029/2004JD004536

Bermejo, P. (2006). Preparation and Response in Case of Natural Disasters: Cuban Programs and Experience. Journal of public health policy. 27. 13-21. 10.1057/palgrave.jphp.3200056.

Berrisford, P., Kållberg, P., Kobayashi, S., Dee, D., Uppala, S., Simmons, A. J., … Sato, H. (2011). Atmospheric conservation properties in ERA-Interim. Quarterly Journal of the Royal Meteorological Society, 137(659), 1381–1399. http://doi.org/10.1002/qj.864

Bjerknes, J. (1966). A possible response of the atmospheric Hadley circulation to equatorial anomalies of ocean temperature. Tellus, 18(4), 820–829. http://doi.org/10.3402/tellusa.v18i4.9712

Bjerknes, J. (1969). Atmospheric teleconnections from the equatorial Pacific. Monthly Weather Review, 97(3), 163–172. http://doi.org/10.1175/1520-0493(1969)097<0163:ATFTEP>2.3.CO;2

Bollasina, M. A., Y. Ming, and V. Ramaswamy (2011), Anthropogenic aerosols and the weakening of the South Asian summer monsoon, Science, 334(6055), 502–505, doi:10.1126/science.1204994.

Bonfils, C. J. W., Santer, B. D., Phillips, T. J., Marvel, K., Ruby Leung, L., Doutriaux, C., & Capotondi, A. (2015). Relative contributions of mean-state shifts and ENSO-driven variability to precipitation changes in a warming climate. Journal of Climate, 28(24), 9997–10013. http://doi.org/10.1175/JCLI-D-15-0341.1

Borlace, S., Cai, W., & Santoso, A. (2013). Multidecadal ENSO amplitude variability in a 1000-yr simulation of a coupled global climate model: Implications for observed ENSO variability. Journal of Climate, 26(23), 9399–9407. http://doi.org/10.1175/JCLI-D-13-00281.1

Brown, J. N., Sen Gupta, A., Brown, J. R., Muir, L. C., Risbey, J. S., Whetton, P., … Wijffels, S. E. (2013). Implications of CMIP3 model biases and uncertainties for climate projections in the western tropical Pacific. Climatic Change, 119, 147–161. doi:10.1007/s10584-012-0603-5

Brown, J. N., Langlais, C., & Maes, C. (2014). Zonal structure and variability of the Western Pacific dynamic warm pool edge in CMIP5. Climate Dynamics, 42, 3061–3076. doi:10.1007/s00382-013-1931-5

Brown, J. R., Moise, A. F., & Colman, R. a. (2013). The South Pacific Convergence Zone in CMIP5 simulations of historical and future climate. Climate Dynamics, 41, 2179–2197. doi:10.1007/s00382-012-1591-x

Burke, M., Hsiang, S. M., & Miguel, E. (2013). Climate and Conflict. Journal of Chemical Information and Modeling, 53(9), 1689–1699. http://doi.org/10.1017/CBO9781107415324.004

Cai, W., Borlace, S., Lengaigne, M., van Rensch, P., Collins, M., Vecchi, G., … Jin, F. F. (2014). Increasing frequency of extreme El Niño events due to greenhouse warming. Nature Climate Change, 4, 111. Retrieved from http://dx.doi.org/10.1038/nclimate2100

Cai, W., Santoso, A., Wang, G., Yeh, S. W., An, S. Il, Cobb, K. M., … Wu, L. (2015). ENSO and greenhouse warming. Nature Climate Change, 5(9), 849–859. http://doi.org/10.1038/nclimate2743

Cai, W., Wang, G., Santoso, A., Mcphaden, M. J., Wu, L., Jin, F. F., … Guilyardi, E. (2015). Increased frequency of extreme La Niña events under greenhouse warming. Nature Climate Change, 5(2), 132–137. http://doi.org/10.1038/nclimate2492

Cane, M. A. The evolution of El Niño, past and future. Earth Planet. Sci. Lett. 230, 227–240 (2005).

Capotondi, A., Wittenberg, A. T., Newman, M., Di Lorenzo, E., Yu, J. Y., Braconnot, P., … Yeh, S. W. (2015). Understanding enso diversity. Bulletin of the American Meteorological Society, 96(6), 921–938. http://doi.org/10.1175/BAMS-D-13-00117.1

Cashin, P. (2015). Fair Weather or Foul? The Macroeconomic Effects of El Niño - Institute Working Papers 0239 - Dallas Fed, (239). Retrieved from https://www.imf.org/external/pubs/ft/wp/2015/wp1589.pdf

Chadwick, R., Boutle, I., & Martin, G. (2013). Spatial patterns of precipitation change in CMIP5: Why the rich do not get richer in the tropics. Journal of Climate, 26(11), 3803–3822. http://doi.org/10.1175/JCLI-D-12-00543.1

Chan, S. C., & Nigam, S. (2009). Residual diagnosis of diabatic heating from ERA-40 and NCEP reanalyses: Intercomparisons with TRMM. Journal of Climate, 22(2), 414–428. http://doi.org/10.1175/2008JCLI2417.1

Chen, Dake & Cane, Mark. (2008). El Niño prediction and predictability. Journal of Computational Physics. 227. 3625-3640. 10.1016/j.jcp.2007.05.014.

Chen, L., Li, T., & Yu, Y. (2015). Causes of strengthening and weakening of ENSO amplitude under global warming in four CMIP5 models. Journal of Climate, 28(8), 3250–3274. http://doi.org/10.1175/JCLI-D-14-00439.1

Chikira, M., & Sugiyama, M. (2010). A Cumulus Parameterization with State-Dependent Entrainment Rate. Part I: Description and Sensitivity to Temperature and Humidity Profiles. Journal of the Atmospheric Sciences, 67, 2171–2193. doi:10.1175/2010JAS3316.1

Christensen, J. H., and Coauthors, 2013: Climate phenomena and their relevance for future regional climate change. Climate Change 2013: The Physical Science Basis, T. F. Stocker et al., Eds., Cambridge University Press, 1217–1308.

Chung, C. T. Y., Power, S. B., Arblaster, J. M., Rashid, H. A., & Roff, G. L. (2014). Nonlinear precipitation response to El Niño and global warming in the Indo-Pacific. Climate Dynamics, 42(7-8), 1837–1856. http://doi.org/10.1007/s00382-013-1892-8

Clarke, A. (2008). An introduction to the dynamics of El Niño and the Southern Oscillation. Academic Press, Waltham, Massachusetts, USA, p. 324.

Clarke L, Edmonds J, Jacoby H, Pitcher H, Reilly J, Richels R (2007) CCSP Synthesis and Assessment Product 2.1, Part A: Scenarios of Greenhouse Gas Emissions and Atmospheric Concentrations. U.S. Government Printing Office. Washington, DC.

Collins, M., An, S.-I., Cai, W., Ganachaud, A., Guilyardi, E., Jin, F.-F., … Wittenberg, A. (2010). The impact of global warming on the tropical Pacific Ocean and El Niño. Nature Geoscience, 3(6), 391–397. http://doi.org/10.1038/ngeo868

Compo, G. P., Whitaker, J. S., Sardeshmukh, P. D., Matsui, N., Allan, R. J., Yin, X., … Worley, S. J. (2011). The Twentieth Century Reanalysis Project. Quarterly Journal of the Royal Meteorological Society, 137(January), 1–28. doi:10.1002/qj.776

Curtis, S., & Adler, R. (2000). ENSO indices based on patterns of satellite-derived precipitation. Journal of Climate, 13, 2786–2793. doi:10.1175/1520-0442(2000)013<2786:EIBOPO>2.0.CO;2

Dai, A., Fung, I. Y., Del Genio, A. D., Dai, A., Fung, I. Y., & Genio, A. D. Del. (1997). Surface Observed Global Land Precipitation Variations during 1900–88. Journal of Climate, 10(11), 2943–2962. http://doi.org/10.1175/1520-0442(1997)010<2943:SOGLPV>2.0.CO;2

Dai, A., & Wigley, T. M. L. (2000). Global patterns of ENSO-induced precipitation. Geophysical Research Letters, 27(9), 1283–1286. doi:10.1029/1999GL011140

Dai, A. (2006). Precipitation Characteristics in Eighteen Coupled Climate Models. J. Climate, 19, 4605–4630, https://doi.org/10.1175/JCLI3884.1

Dai, N., & Arkin, P. A. (2017). Twentieth century ENSO-related precipitation mean states in twentieth century reanalysis, reconstructed precipitation and CMIP5 models. Climate Dynamics, 48(9-10), 3061–3083. http://doi.org/10.1007/s00382-016-3251-z

De Szoeke, S. P., & Xie, S. P. (2008). The tropical eastern pacific seasonal cycle: Assessment of errors and mechanisms in IPCC AR4 coupled ocean-atmosphere general circulation models. Journal of Climate, 21, 2573–2590. doi:10.1175/2007JCLI1975.1

Deser, C. and M.L. Blackmon (1995). On the Relationship between Tropical and North Pacific Sea Surface Temperature Variations. J. Climate, 8, 1677–1680,https://doi.org/10.1175/1520-0442(1995)008<1677:OTRBTA>2.0.CO;2

Deser, C., Alexander, M. a, Xie, S.-P., & Phillips, A. S. (2010). Sea surface temperature variability: patterns and mechanisms. Annual review of marine science (Vol. 2, pp. 115–143). doi:10.1146/annurev-marine-120408-151453

Dijkstra, H. A. (2006). The ENSO phenomenon : theory and mechanisms To cite this version : Advances in Geosciences The ENSO phenomenon : theory and mechanisms. Advances in Geosciences, (6), 3–15.

DiNezio, P. N., Clement, A. C., Vecchi, G. A., Soden, B. J., Kirtman, B. P., & Lee, S. K. (2009). Climate response of the equatorial pacific to global warming. Journal of Climate, 22(18), 4873–4892. http://doi.org/10.1175/2009JCLI2982.1

Dong, B. W., Sutton, R. T., & Scaife, a a. (2006). Multidecadal modulation of El Nino-Southern Oscillation (ENSO) variance by Atlantic Ocean sea surface temperatures. Geophysical Research Letters, 33, L08705–L08705. doi:10.1029/2006GL025766

Eyring, V., Bony, S., Meehl, G. A., Senior, C. A., Stevens, B., Stouffer, R. J., and Taylor, K. E. (2016). Overview of the Coupled Model Intercomparison Project Phase 6 (CMIP6) experimental design and organization, Geosci. Model Dev., 9, 1937-1958, https://doi.org/10.5194/gmd-9-1937-2016

Flato, G. M. (2011). Earth system models: An overview. Wiley Interdisciplinary Reviews: Climate Change, 2(December), 783–800. doi:10.1002/wcc.148

Foster, G., & Rahmstorf, S. (2011). Global temperature evolution 1979–2010. Environmental Research Letters, 6(4), 044022. http://doi.org/10.1088/1748-9326/6/4/044022

Fueglistaler, S., Dessler, a E., Dunkerton, T. J., Folkins, I., Fu, Q., & Ote, P. W. (2009). Tropical tropopause layer, Rev. Geophys., 47, RG1004, doi(2008), 101029/. http://doi.org/10.1029/2008RG000267.1.

Gao, S., & Li, X. (2008). Cloud-Resolving Modeling of Convective Processes. doi: 10.1007/978-1-4020-8276-4

Gelaro, R., W. McCarty, M.J. Suárez, R. Todling, A. Molod, L. Takacs, C.A. Randles, A. Darmenov, M.G. Bosilovich, R. Reichle, K. Wargan, L. Coy, R. Cullather, C. Draper, S. Akella, V. Buchard, A. Conaty, A.M. da Silva, W. Gu, G. Kim, R. Koster, R. Lucchesi, D. Merkova, J.E. Nielsen, G. Partyka, S. Pawson, W. Putman, M. Rienecker, S.D. Schubert, M. Sienkiewicz, and B. Zhao (2017). The Modern-Era Retrospective Analysis for Research and Applications, Version 2 (MERRA-2). J. Climate, 30, 5419–5454, https://doi.org/10.1175/JCLI-D-16-0758.1

Goddard, L. and M. Dilley (2005). El Niño: Catastrophe or Opportunity. J. Climate, 18, 651–665, https://doi.org/10.1175/JCLI-3277.1

Grose, M. R., Brown, J. N., Narsey, S., Brown, J. R., Murphy, B. F., Langlais, C., … Irving, D. B. (2014). Assessment of the CMIP5 global climate model simulations of the western tropical Pacific climate system and comparison to CMIP3. International Journal of Climatology, 3399, 3382–3399. doi:10.1002/joc.3916

Guan, B., & Nigam, S. (2008). Pacific sea surface temperatures in the twentieth century: An evolution-centric analysis of variability and trend. Journal of Climate, 21(12), 2790–2809. http://doi.org/10.1175/2007JCLI2076.1

Guilyardi, E., Wittenberg, A., Fedorov, A., Collins, M., Wang, C., Capotondi, A., … Stockdale, T. (2009). Understanding El Niño in ocean-atmosphere general circulation models: Progress and challenges. Bulletin of the American Meteorological Society, 90(March), 325–340. doi:10.1175/2008BAMS2387.1

Guilyardi, E., Bellenger, H., Collins, M., Ferrett, S., Cai, W., & Wittenberg, A. (2012). A first look at ENSO in CMIP5. Clivar Exchanges, 17(58), 29–32. Retrieved from http://www.uib.no/People/ngfhd/EarthClim/Publications/Papers/Guilyardi_etal_2012.pdf

Hagos, S., Zhang, C., Tao, W. K., Lang, S., Takayabu, Y. N., Shige, S., … L'ecuyer, T. (2010). Estimates of tropical diabatic heating profiles: Commonalities and uncertainties. Journal of Climate, 23(3), 542–558. http://doi.org/10.1175/2009JCLI3025.1

Ham, Y. G., and Kug J. S. (2014). ENSO phase-locking to the boreal winter in CMIP3 and CMIP5 models. Climate Dyn., 43, 305–318, doi:10.1007/s00382-014-2064-1.

Ham, Y. G., & Kug, J. S. (2015). Improvement of ENSO Simulation Based on Intermodel Diversity. Journal of Climate, 28, 998–1015. doi:10.1175/JCLI-D-14-00376.1

Ham, Y. G., & Kug, J. S. (2016). ENSO amplitude changes due to greenhouse warming in CMIP5: Role of mean tropical precipitation in the twentieth century. Geophysical Research Letters, 43(1), 422–430. http://doi.org/10.1002/2015GL066864

Ham, Y. G. (2017). A reduction in the asymmetry of ENSO amplitude due to global warming: The role of atmospheric feedback. Geophysical Research Letters, 44(16), 8576–8584. http://doi.org/10.1002/2017GL074842

Hartmann, D. L., H. H. Hendon, and R. A. Houze Jr. (1984). Some implications of the mesoscale circulations in tropical cloud clusters for large-scale dynamics and climate. J. Atmos. Sci., 41, 113–121.

Held, I., & Kang, I.-S. (1987). Barotropic Models of the Extratropical Response to El Niño. Journal of The Atmospheric Sciences - J ATMOS SCI. 44. 3576-3586. 10.1175/1520-0469(1987)044<3576:BMOTER>2.0.CO;2.

Held, I. M., & Soden, B. J. (2006). Robust responses of the hydrologic cycle to global warming. J. Clim., 19, 5686–5699. http://doi.org/10.1175/JCLI3990.1

Hirota, N., Y. N. Takayabu, M. Watanabe, and M. Kimoto (2011). Precipitation reproducibility over tropical oceans and its relationship to the double ITCZ problem in CMIP3 and MIROC5 climate models. J. Climate, 24, 4859–4873.

Hirota, N., & Takayabu, Y. N. (2013). Reproducibility of precipitation distribution over the tropical oceans in CMIP5 multi-climate models compared to CMIP3. Climate Dynamics, 41, 2909–2920. doi:10.1007/s00382-013-1839-0

Horel, John & M. Wallace, John. (1981). Planetary-scale atmospheric phenomena associated with the Southern Oscillation. Monthly Weather Review. 109. 813-829. 10.1175/1520-0493(1981)109<0813:PSAPAW>2.0.CO;2.

Hoskins, B. J., and D. J. Karoly (1981). The steady linear response of a spherical atmosphere to thermal and orographic forcing. J. Atmos. Sci., 38, 1179-1196.

Hou, A. Y., Kakar, R. K., Neeck, S., Azarbarzin, A. A., Kummerow, C. D., Kojima, M., … Iguchi, T. (2014). The global precipitation measurement mission. Bulletin of the American Meteorological Society, 95(5), 701–722. http://doi.org/10.1175/BAMS-D-13-00164.1

Houze Jr., R. a. (1997). Stratiform precipitation in the tropics: A meteorological paradox? Bull. Amer. Meterol. Soc., 78(10), 2179–2196. http://doi.org/10.1175/1520-0477(1997)078<2179:SPIROC>2.0.CO;2

Hsiang, S. M., Meng, K. C., & Cane, M. A. (2011). Civil conflicts are associated with the global climate. Nature, 476(7361), 438–441. http://doi.org/10.1038/nature10311

Huang, P. (2016). Time-Varying Response of ENSO-Induced Tropical Pacific Rainfall to Global Warming in CMIP5 Models. Part I: Multimodel Ensemble Results. J. Climate,29, 5763–5778, https://doi.org/10.1175/JCLI-D-16-0058.1

Huang, P. (2017). Time-varying response of ENSO-induced tropical pacific rainfall to global warming in CMIP5 models. Part II: Intermodel uncertainty. Journal of Climate, 30(2), 595–608. http://doi.org/10.1175/JCLI-D-16-0373.1

Huffman, G.J., R.F. Adler, D.T. Bolvin, G. Gu, E.J. Nelkin, K.P. Bowman, Y. Hong, E.F. Stocker, D.B. Wolff (2007). The TRMM Multi-satellite Precipitation Analysis: Quasi-Global, Multi-Year, Combined-Sensor Precipitation Estimates at Fine Scale. J. Hydrometeor., 8:38-55

Huffman, G.J., D. T. Bolvin, and G. Gu (2009). Improving the global precipitation record: GPCP version 2.1. Geophys. Res. Lett., 36, L17808, doi:10.1029/2009GL040000.

Hwang, Y. T., Frierson, D. M. W., & Kang, S. M. (2013). Anthropogenic sulfate aerosol and the southward shift of tropical precipitation in the late 20th century. Geophysical Research Letters, 40(April), 2845–2850. doi:10.1002/grl.50502

IPCC (2013). Climate Change 2013: The Physical Science Basis. Contribution of Working Group I to the Fifth Assessment Report of the Intergovernmental Panel on Climate Change [Stocker, T.F., D. Qin, G.-K. Plattner, M. Tignor, S.K. Allen, J. Boschung, A. Nauels, Y. Xia, V. Bex and P.M. Midgley (eds.)]. Cambridge University Press, Cambridge, United Kingdom and New York, NY, USA, 1535 pp, doi:10.1017/CBO9781107415324.

Ji, M., A. Kumar, and A. Leetmaa (1994). An experimental coupled forecast system at the National Meteorological Center: Some early results. Tellus, 46A, 398-418

Jiang, J. H., et al. (2012), Evaluation of cloud and water vapor simulations in CMIP5 climate models using NASA "A-Train" satellite observations, J. Geophys. Res., 117, D14105, doi: 10.1029/2011JD017237.

Jin, F.-F. & Kim, S. & Bejarano, L. (2006). A coupled-stability index of ENSO. Geophysical Research Letters. doi: 332. 10.1029/2006GL027221.

Joseph, R., Smith, T. M., Sapiano, M. R. P., & Ferraro, R. R. (2009). A New High-Resolution Satellite-Derived Precipitation Dataset for Climate Studies. Journal of Hydrometeorology, 10(4), 935–952. http://doi.org/10.1175/2009JHM1096.1

Kang, I., H. No, and F. Kucharski (2014). ENSO Amplitude Modulation Associated with the Mean SST Changes in the Tropical Central Pacific Induced by Atlantic Multidecadal Oscillation. J. Climate, 27, 7911–7920, https://doi.org/10.1175/JCLI-D-14-00018.1

Kestin, T.S., D.J. Karoly, J. Yano, and N.A. Rayner (1998). Time–Frequency Variability of ENSO and Stochastic Simulations. J. Climate, 11, 2258–2272,https://doi.org/10.1175/1520-0442(1998)011<2258:TFVOEA>2.0.CO;2

Khandekar, M. L. (1982). Comments on "Planetary-Scale Atmospheric Phenomena Associated with the Southern Oscillation." Monthly Weather Review. http://doi.org/10.1175/1520-0493(1982)110<1495:COSAPA>2.0.CO;2

Kim, S. T., and Yu J.-Y. (2012). The two types of ENSO in CMIP5 models, Geophys. Res. Lett., 39, L11704, doi: 10.1029/2012GL052006.

Kim, S. T., Cai, W., Jin, F. F., & Yu, J. Y. (2014). ENSO stability in coupled climate models and its association with mean state. Climate Dynamics, 42, 3313–3321. doi:10.1007/s00382-013-1833-6

Kim, S. T., Cai, W., Jin, F.-F., Santoso, A., Wu, L., Guilyardi, E., & An, S.-I. (2014). Response of El Niño sea surface temperature variability to greenhouse warming. Nature Climate Change, 4(9), 786–790. http://doi.org/10.1038/nclimate2326

Kim, W. M., & Cai, W. (2014). The importance of the eastward zonal current for generating extreme El Niño. Climate Dynamics, 42(11-12), 3005–3014. http://doi.org/10.1007/s00382-013-1792-y

Kirtman,B. P.,Y. Fan, & E.K. Schneider (2002). The COLAglobal coupled and anomaly coupled ocean–atmosphere GCM.J. Climate, 15, 2301–2320, doi:10.1175/1520-0442(2002)015,2301:TCGCAA.2.0.CO;2.

Knapp, K.R., M.C. Kruk, D.H. Levinson, H.J. Diamond, and C.J. Neumann (2010). The International Best Track Archive for Climate Stewardship (IBTrACS). Bull. Amer. Meteor. Soc., 91, 363–376, https://doi.org/10.1175/2009BAMS2755.1

Kohyama, T., Hartmann, D. L., & Battisti, D. S. (2012). Weakening of nonlinear ENSO under global warming.

Kovats, R. S. (2000). El Niño and human health. WHO, 78(9), 1127–1135. http://doi.org/10.1590/S0042-96862000000900008

Kravtsov, S. (2012). An empirical model of decadal ENSO variability. Climate Dyn., 39, 2377–2391, doi:10.1007/s00382-012-1424-y.

Kug, J. S., Jin, F. F., & An, S. Il. (2009). Two types of El Niño events: Cold tongue El Niño and warm pool El Niño. Journal of Climate, 22(6), 1499–1515. http://doi.org/10.1175/2008JCLI2624.1

Kummerow, C., Barnes, W., Kozu, T., Shiue, J., & Simpson, J. (1998). The Tropical Rainfall Measuring Mission (TRMM) sensor package. Journal of Atmospheric and Oceanic Technology, 15(3), 809–817. http://doi.org/10.1175/1520-0426(1998)015<0809:TTRMMT>2.0.CO;2

L'Heureux, M. L., Lee, S., & Lyon, B. (2013). Recent multidecadal strengthening of the Walker circulation across the tropical Pacific. Nature Climate Change, 3(6), 571–576. http://doi.org/10.1038/nclimate1840

Larkin, N. K., & Harrison, D. E. (2002). ENSO warm (El Niño) and cold (La Niña) event life cycles: Ocean surface anomaly patterns, their symmetries, asymmetries, and implications. Journal of Climate, 15(10), 1118–1140. http://doi.org/10.1175/1520-0442(2002)015<1118:EWENOA>2.0.CO;2

Larkin, N. K., and D. E. Harrison (2005). Global seasonal temperature and precipitation anomalies during El Niño autumn and winter. Geophys. Res. Lett., 32, L16705, doi:10.1029/2005GL022860.

Latif, M., & Keenlyside, N. S. (2009). El Nino/Southern Oscillation response to global warming. Proceedings of the National Academy of Sciences, 106(49), 20578–20583. http://doi.org/10.1073/pnas.0710860105

Li, J., Xie, S. P., Cook, E. R., Morales, M. S., Christie, D. A., Johnson, N. C., … Fang, K. (2013). El Niño modulations over the past seven centuries. Nature Climate Change, 3(9), 822–826. http://doi.org/10.1038/nclimate1936

Lin, J. L. (2007). The double-ITCZ problem in IPCC AR4 coupled GCMs: Ocean-atmosphere feedback analysis. Journal of Climate, 20, 4497–4525. doi:10.1175/JCLI4272.1

Lindzen, R. S., & Nigam, S. (1987). On the role of sea surface temperature gradients in forcing low-level winds and convergence in the tropics. doi:10.1175/1520-0469(1987)044<2418:OTROSS>2.0.CO;2

Iizumi, T., Luo, J.-J., Challinor, A. J., Sakurai, G., Yokozawa, M., Sakuma, H., … Yamagata, T. (2014). Impacts of El Niño Southern Oscillation on the global yields of major crops. Nature Communications, 5, 3712. Retrieved from http://dx.doi.org/10.1038/ncomms4712

Mansbach, D. K., & Norris, J. R. (2007). Low-level cloud variability over the equatorial cold tongue in observations and models. Journal of Climate, 20(8), 1555–1570. http://doi.org/10.1175/JCLI4073.1

McGowan, H., & Theobald, A. (2017). ENSO weather and coral bleaching on the Great Barrier Reef, Australia. Geophysical Research Letters, 44, 10,601–10,607. https://doi.org/10.1002/2017GL074877

McPhaden, M. J., A. J. Busalacchi, R. Cheney, J. R. Donguy, K. S. Gage, D. Halpern, M. Ji, P. Julian, G. Meyers, G. T. Mitchum, and others (1998) The Tropical Ocean-Global Atmosphere (TOGA) observing system: A decade of progress. J. Geophys. Res., 103, 14,169–14,240.

McPhaden, M. J., Zebiak, S. E., & Glantz, M. H. (2006). ENSO as an integrating concept in earth science. Science (New York, N.Y.), 314(December), 1740–1745. doi:10.1126/science.1132588

Mcphaden, M. J., Zebiak, S. E., Glantz, M. H., & Mcphaden, M. (2014). ENSO as an Concept Integrating in Earth Science, 314(5806), 1740–1745.

Mechoso, C. R., Robertson, a. W., Barth, N., Davey, M. K., Delecluse, P., Gent, P. R., … Tribbia, J. J. (1995). The Seasonal Cycle over the Tropical Pacific in Coupled Ocean–Atmosphere General Circulation Models. Monthly Weather Review. doi:10.1175/1520-0493(1995)123<2825:TSCOTT>2.0.CO;2

Meehl, G. a. (1987). The Annual Cycle and Interannual Variability in the Tropical Pacific and Indian Ocean Regions. Monthly Weather Review. http://doi.org/10.1175/1520-0493(1987)115<0027:TACAIV>2.0.CO;2

Molod, A., Takacs, L., Suarez, M., & Bacmeister, J. (2015). Development of the GEOS-5 atmospheric general circulation model: Evolution from MERRA to MERRA2. Geoscientific Model Development, 8(5), 1339–1356. http://doi.org/10.5194/gmd-8-1339-2015

Moss, R. H., Edmonds, J. A., Hibbard, K. A., Manning, M. R., Rose, S. K., Van Vuuren, D. P., … Wilbanks, T. J. (2010). The next generation of scenarios for climate change research and assessment. Nature, 463(7282), 747–756. http://doi.org/10.1038/nature08823

Murphy B. F. , Scott B. Power, and Simon McGree (2014). The varied impacts of el niño–southern oscillation on pacific island climates. J. Climate, 27, 4015–4036. doi: http://dx.doi.org/10.1175/JCLI-D-13-00130.1

Newman, M., Alexander, M. A., Ault, T. R., Cobb, K. M., Deser, C., Di Lorenzo, E., … Smith, C. A. (2016). The Pacific decadal oscillation, revisited. Journal of Climate, 29(12), 4399–4427. http://doi.org/10.1175/JCLI-D-15-0508.1

Nigam, S. (1994). On the dynamical basis for the Asian summer monsoon rainfall—El Nin˜o relationship. J. Climate, 7, 1750– 1771.

Nigam S, Chung C, DeWeaver E. (2000). ENSO diabatic heating in ECMWF and NCEP–NCAR reanalyses, and NCAR CCM3 simulation. J. Climate 13: 3152–3171.

Niquen, M. & Bouchon, M. (2004). Impact of El Niño events on pelagic fisheries in Peruvian waters. Deep-sea Research Part Ii-topical Studies in Oceanography - DEEP-SEA RES PT II-TOP ST OCE. 51. 563-574. 10.1016/S0967-0645(04)00052-9.

Norris, J.R. and C.B. Leovy (1994). interannual Variability in Stratiform Cloudiness and Sea Surface Temperature. J. Climate, 7, 1915–1925, https://doi.org/10.1175/1520-0442(1994)007<1915:IVISCA>2.0.CO;2

Oort, A.H. and J.J. Yienger, 1996: Observed Interannual Variability in the Hadley Circulation and Its Connection to ENSO. J. Climate, 9, 2751–2767,https://doi.org/10.1175/1520-0442(1996)009<2751:OIVITH>2.0.CO;2

Paternoster, R., Brame, R., Mazerolle, P., & Piquero A. (1998). Using the Correct Statistical Test for the Equality of Regression Coefficients. Criminology, 36(4), 859–866. http://doi.org/10.1111/j.1745-9125.1998.tb01268.x

Peterson, T. C., & Vose, R. S. (1997). An Overview of the Global Historical Climatology Network Temperature Database. Bulletin of the American Meteorological Society, 78(12), 2837–2849. http://doi.org/10.1175/1520-0477(1997)078<2837:AOOTGH>2.0.CO;2

Philander, S. G. (1985). El Niño and La Niña. Journal of Atmospheric Sciences. http://doi.org/10.1175/1520-0469(1985)042<2652:ENALN>2.0.CO;2

Philander S. G. (1990) El Nino, La Nina and the Southern Oscillation. Academic Press, Science

Power, S., Delage, F., Chung, C., Kociuba, G., & Keay, K. (2013). Robust twenty-first-century projections of El Niño and related precipitation variability. Nature, 502(7472), 541–545. http://doi.org/10.1038/nature12580

Räisänen, J. (2007). How reliable are climate models? Tellus, Series A: Dynamic Meteorology and Oceanography, 59, 2–29. doi:10.1111/j.1600-0870.2006.00211.x

Rasmussen, E. M., and T. H. Carpenter (1982). Variations in tropical sea surface temperature and surface wind fields associated with the Southern Oscillation/El Niño. Mon. Wea. Rev., 110, 354-384.

Raymond, W.H., W.S. Olson, and G. Callan (1995). Diabatic Forcing and Initialization with Assimilation of Cloud Water and Rainwater in a Forecast Model. Mon. Wea. Rev., 123, 366–382, https://doi.org/10.1175/1520-0493(1995)123<0366:DFAIWA>2.0.CO;2

Rayner, N. A., Parker, D. E., Horton, E. B., Folland, C. K., Alexander, L. V., Rowell, D. P., … Kaplan, a. (2003). Global analyses of sea surface temperature, sea ice, and night marine air temperature since the late Nineteenth Century, 108. doi:10.1029/2002JD002670

Reichler, T., & Kim, J. (2008). How well do coupled models simulate today's climate? Bulletin of the American Meteorological Society, 89, 303–311. doi:10.1175/BAMS-89-3-303

Riahi, K., Rao, S., Krey, V., Cho, C., Chirkov, V., Fischer, G., … Rafaj, P. (2011). RCP 8.5---A scenario of comparatively high greenhouse gas emissions. Climatic Change, 109(1), 33. http://doi.org/10.1007/s10584-011-0149-y

Ropelewski C. F. and Halpert M. S. (1987). Global and Regional Scale Precipitation Patterns Associated with the El Niño/Southern Oscillation. Mon. Wea. Rev., 115, 1606-1626. doi: 10.1175/15200493(1987)115<1606:GARSPP>2.0.CO;2

Rudolf, B., & Schneider, U. (2005). Caculation of gridded precipitation data for the global land-surface using in-situ gauge observation. 2nd Workshop of the Internation Precipitation Working Group IPWG, 231–247.

Russell, A. M., & Gnanadesikan, A. (2014). Understanding multidecadal variability in ENSO amplitude. Journal of Climate, 27(11), 4037–4051. http://doi.org/10.1175/JCLI-D-13-00147.1

Quan, X.-W., et al. (2004), Change of the tropical Hadley cell since 1950, in The Hadley Circulation: Past, Present, and Future, edited by H. F. Diaz and R. S. Bradley, pp. 85 – 120, Cambridge Univ. Press, New York.

Sabeerali C. T., & Rao, Suryachandra & Dhakate, Ashish & Salunke, Kiran & Goswami, B. N.. (2014). Why ensemble mean projection of South Asian monsoon rainfall by CMIP5 models is not reliable? Climate Dynamics. 10.1007/s00382-014-2269-3.

Sadekov, A. Y., Ganeshram, R., Pichevin, L., Berdin, R., McClymont, E., Elderfield, H., & Tudhope, A. W. (2013). Palaeoclimate reconstructions reveal a strong link between El Niño-Southern Oscillation and Tropical Pacific mean state. Nature Communications, 4, 2692. Retrieved from http://dx.doi.org/10.1038/ncomms3692

Saha, S., Moorthi, S., Pan, H. L., Wu, X., Wang, J., Nadiga, S., … Goldberg, M. (2010). The NCEP climate forecast system reanalysis. Bulletin of the American Meteorological Society, 91(8), 1015–1057. http://doi.org/10.1175/2010BAMS3001.1

Santer, B. D., Wigley, T. M. L., Boyle, J. S., Gaffen, D. J., Hnilo, J. J., Nychka, D., … Taylor, K. E. (2000). Statistical significance of trends and trend differences in layer-average atmospheric temperature time series. Journal of Geophysical Research, 105(D6), 7337–7356. http://doi.org/10.1029/1999JD901105

Seager, R., N. Naik, and G.A. Vecchi (2010). Thermodynamic and Dynamic Mechanisms for Large-Scale Changes in the Hydrological Cycle in Response to Global Warming. J. Climate, 23, 4651–4668, https://doi.org/10.1175/2010JCLI3655.1

Schumacher, C., & Houze, R. A. (2003). Stratiform rain in the tropics as seen by the TRMM precipitation radar. Journal of Climate, 16(11), 1739–1756. http://doi.org/10.1175/1520-0442(2003)016<1739:SRITTA>2.0.CO;2

Schumacher, C., Houze, R. A., & Kraucunas, I. (2004). The Tropical Dynamical Response to Latent Heating Estimates Derived from the TRMM Precipitation Radar. Journal of the Atmospheric Sciences, 61(12), 1341–1358. http://doi.org/10.1175/1520-0469(2004)061<1341:TTDRTL>2.0.CO;2

Schumacher, C., M.H. Zhang, and P.E. Ciesielski (2007). Heating Structures of the TRMM Field Campaigns. J. Atmos. Sci., 64, 2593–2610,https://doi.org/10.1175/JAS3938.1

Smith, T.M. and R.W. Reynolds. (2003). Extended Reconstruction of Global Sea Surface Temperatures Based on COADS Data (1854–1997). J. Climate, 16, 1495–1510,https://doi.org/10.1175/1520-0442(2003)016<1495:EROGSS>2.0.CO;2

Smith, T. M., Reynolds, R. W., Peterson, T. C., & Lawrimore, J. (2008). Improvements to NOAA's historical merged land-ocean surface temperature analysis (1880-2006). Journal of Climate, 21, 2283–2296. doi:10.1175/2007JCLI2100.1

Smith, T. M., Arkin, P. A. and Sapiano M. R. P. (2009), Reconstruction of near-global annual precipitation using correlations with sea surface temperature and sea level pressure, J. Geophys. Res., 114, D12107, doi: 10.1029/2008JD011580.

Smith, T. M., Arkin, P. A., Ren, L., & Shen, S. S. P. (2012). Improved reconstruction of global precipitation since 1900. Journal of Atmospheric and Oceanic Technology, 29, 1505–1517. doi:10.1175/JTECH-D-12-00001.1

Sponberg, K. (1999). Navigating the numbers of climatological impact. Compendium of Climatological Impacts, University Corporation for Atmospheric Research, Vol. 1, National Oceanic and Atmospheric Administration, Office of Global Programs, 13 pp. Available online at http://www.cip.noaa. gov/docs/navimpact.pdf.

Stockdale, T. N., and coauthors (2011). ECMWF seasonal forecast system 3 and its prediction of sea surface temperature. Clim. Dyn., 37, 455-471.

Su, H. and J.D. Neelin (2002). Teleconnection Mechanisms for Tropical Pacific Descent Anomalies during El Niño. *J. Atmos. Sci.,* 59, 2694–2712,https://doi.org/10.1175/1520-0469(2002)059<2694:TMFTPD>2.0.CO;2

Suarez, M. J., & Schopf, P. S. (1988). A Delayed Action Oscillator for ENSO. Journal of the Atmospheric Sciences. http://doi.org/10.1175/1520-0469(1988)045<3283:ADAOFE>2.0.CO;2

Sun, D.-Z., T. Zhang, Y. Sun, and Y. Yu (2014). Rectification of El Nino-Southern Oscillation into Climate Anomalies of Decadal and Longer Time-scales: Results from Forced Ocean GCM Experiments. J. Climate, 27, 2545-2561.

Symons GJ. (1866). On the rainfall of the British Isles. In Report on 35th Meeting of the Brit. Ass. for the Adv. of Sci., Birmingham, 1865, pp 192–242.

Tao, W.-K., Lang, S., Simpson, J., & Adler, R. (1993). Retrieval algorithms for estimating the vertical profiles of latent heat release: Their applications for TRMM. Meteorological Society Japan, 71(December), 685–700. http://doi.org/10.2151/jmsj1965.71.6_685

Tao, W. K., Smith, E. A., Adler, R. F., Haddad, Z. S., Hou, A. Y., Iguchi, T., … Yang, S. (2006). Retrieval of latent heating from TRMM measurements. Bulletin of the American Meteorological Society, 87(11), 1555–1572. http://doi.org/10.1175/BAMS-87-11-1555

Tao, W. K., Lang, S., Zeng, X., Shige, S., & Takayabu, Y. (2010). Relating convective and stratiform rain to latent heating. Journal of Climate, 23(7), 1874–1893. http://doi.org/10.1175/2009JCLI3278.1

Tao, W.-K., Takayabu, Y. N., Lang, S., Shige, S., Olson, W., Hou, A., … Bhardwaj, A. (2016). TRMM Latent Heating Retrieval: Applications and Comparisons with Field Campaigns and Large-Scale Analyses. Meteorological Monographs, 56(Code 612), 2.1–2.34. http://doi.org/10.1175/AMSMONOGRAPHS-D-15-0013.1

Taylor, K. E., Stouffer, R. J., & Meehl, G. a. (2012). An overview of CMIP5 and the experiment design. Bulletin of the American Meteorological Society, 93(april), 485–498. doi:10.1175/BAMS-D-11-00094.1

Trenberth, K. E. (1976), Spatial and temporal variations of the Southern Oscillation. Q.J.R. Meteorol. Soc.,102: 639–653. doi: 10.1002/qj.49710243310

Trenberth, K. E., & Guillemot, C. J. (1995). Evaluation of the global atmospheric moisture budget as seen from analyses. Journal of Climate. http://doi.org/10.1175/1520-0442(1995)008<2255:EOTGAM>2.0.CO;2

Trenberth, K. E., & Hoar, T. J. (1997). El Niño and climate change. Geophysical Research Letters, 24(23), 3057–3060. http://doi.org/10.1029/97GL03092

Trenberth, K. E., Branstator, G. W., Karoly, D., Kumar, A., Lau, N.-C., & Ropelewski, C. (1998). Progress during TOGA in understanding and modeling global teleconnections associated with tropical sea surface temperatures. Journal of Geophysical Research: Oceans, 103(C7), 14291–14324. http://doi.org/10.1029/97JC01444

Valle, C. A., F. Cruz, J. B. Cruz, G. Merlen & M. Coulter (1987). The impact of the 1982-1983, El Niño-Southern Oscillation on seabirds in the Galapagos Islands Ecuador. Journal of Geophysical Research. doi: 92:14437-14444.

Vecchi, G. A., & Wittenberg, A. T. (2010). El Niño and our future climate: Where do we stand? Wiley Interdisciplinary Reviews: Climate Change, 1(2), 260–270. http://doi.org/10.1002/wcc.33

Verdon, D. C., and S. W. Franks (2006), Long-term behaviour of ENSO: Interactions with the PDO over the past 400 years inferred from paleoclimate records, Geophys. Res. Lett., 33, L06712, doi:10.1029/2005GL025052.

Vincent, D. G. (1994). The South Pacific convergence zone (SPCZ): A review. doi:10.1175/1520-0493(1994)122<1949:TSPCZA>2.0.CO;2

Vincent, E. M., Lengaigne, M., Menkes, C. E., Jourdain, N. C., Marchesiello, P., & Madec, G. (2011). Interannual variability of the South Pacific Convergence Zone and implications for tropical cyclone genesis. Climate Dynamics, 36, 1881–1896. doi:10.1007/s00382-009-0716-3

Wallace, J. M., E. M. Rasmusson, T. P. Mitchell, V. E. Kousky, E. S. Sarachik, and H. vonStorch (1998), On the structure and evolution of ENSO-related climate variability in the tropical Pacific: Lessons from TOGA, J. Geophys. Res., 103(C7), 14241–14259, doi: 10.1029/97JC02905.

Wang, C., Xie, S. P., & Carton, J. a. (2004). A global survey of ocean – atmosphere interaction and climate variability. Earth Climate: The Ocean-Atmosphere Interaction, 147, 1–19. doi:10.1029/147GM01

Wang, G., Cai, W., Gan, B., Wu, L., Santoso, A., Lin, X., … McPhaden, M. J. (2017). Continued increase of extreme El Ninõ frequency long after 1.5 C warming stabilization. Nature Climate Change, 7(8), 568–572. http://doi.org/10.1038/NCLIMATE3351

Wang, Julian & F. Ropelewski, C. (1995). An assessment of ENSO-Scale secular variability. Journal of Climate - J CLIMATE. 8. 1584-1599. 10.1175/1520-0442(1995)008<1584:AAOESS>2.0.CO;2.

Watanabe, M., and Coauthors (2010). Improved climate simulation by MIROC5: Mean states, variability, and climate sensitivity. J. Climate, 23, 6312–6335, doi:10.1175/2010JCLI3679.1.

Weaver, C. P. (2003). Efficiency of storm tracks an important climate parameter? The role of cloud radiative forcing in poleward heat transport, J. Geophys. Res., 108(D1), 4018, doi: 10.1029/2002JD002756.

Whitaker, J.S. and T. Hamill (2002). Ensemble data assimilation without perturbed observations. Mon. Wea. Rev., 130, 1913-1924. http://dx.doi.org/10.1175/1520-0493(2002)130<1913:EDAWPO>2.0.CO;2

WHO. (2016). EL NINO AND HEALTH : Global Overview - January 2016, (October 2015). Retrieved from http://www.who.int/hac/crises/el-nino/who_el_nino_and_health_global_report_21jan2016.pdf

Widlansky, M. J., Timmermann, A., Stein, K., McGregor, S., Schneider, N., England, M. H., … Cai, W. (2012). Changes in South Pacific rainfall bands in a warming climate. Nature Climate Change, 3(4), 417–423. doi:10.1038/nclimate1726

Wills, R. C., Schneider, T., Wallace, J. M., Battisti, D. S., & Hartmann, D. L. (2018). Disentangling Global Warming, Multidecadal Variability, and El Niño in Pacific Temperatures. Geophysical Research Letters, 45(5), 2487–2496. http://doi.org/10.1002/2017GL076327

Wittenberg, A. T., Rosati, A., Lau, N. C., & Ploshay, J. J. (2006). GFDL's CM2 global coupled climate models. Part III: Tropical Pacific climate and ENSO. Journal of Climate, 19, 698–722. doi:10.1175/JCLI3631.1

Wolter, K., and M. S. Timlin (1998). Measuring the strength of ENSO events - how does 1997/98 rank? Weather, 53, 315-324.

Worley, S. J., Woodruff, S. D., Reynolds, R. W., Lubker, S. J. and Lott, N. (2005), ICOADS release 2.1 data and products. Int. J. Climatol., 25: 823-842. doi:10.1002/joc.1166

Wright, J. S. and Fueglistaler, S. (2013). Large differences in reanalyses of diabatic heating in the tropical upper troposphere and lower stratosphere, Atmos. Chem. Phys., 13, 9565-9576, https://doi.org/10.5194/acp-13-9565-2013.

Wyrtki, K. (1975). El Niño—the dynamic response of the equatorial Pacific Ocean to atmospheric forcing. J. Phys. Oceanogr., 5, 572-584.

Wyrtki, K. (1981). An Estimate of Equatorial Upwelling in the Pacific. Journal of Physical Oceanography. http://doi.org/10.1175/1520-0485(1981)011<1205:AEOEUI>2.0.CO;2

Xie, P. P., & Arkin, P. A. (1997). Global precipitation: a 17-year monthly analysis based on gauge observations, satellite estimates, and numerical model outputs. Bull. Am. Meteorol. Soc., 78(June), 2539–2558. http://doi.org/10.1175/1520-0477(1997)078<2539:GPAYMA>2.0.CO;2

Xie, P (2010): CPC unified gauge-based analysis of global daily precipitation. https://ams.confex.com/ams/90annual/techprogram/paper_163676.htm

Xu, K., C. Tam, C. Zhu, B. Liu, and W. Wang (2017). CMIP5 Projections of Two Types of El Niño and Their Related Tropical Precipitation in the Twenty-First Century. J. Climate, 30, 849–864, https://doi.org/10.1175/JCLI-D-16-0413.1

Yanai M, Esbensen S, Chu J-H. (1973). Determination of bulk properties of tropical cloud clusters from large-scale heat and moisture budgets. J. Atmos. Sci. 30: 611–627.

Yeh, S. W., & Kirtman, B. P. (2007). ENSO amplitude changes due to climate change projections in different coupled models. Journal of Climate, 20(2), 203–217. http://doi.org/10.1175/JCLI4001.1

Yeh, S.-W., Kug, J.-S., Dewitte, B., Kwon, M.-H., Kirtman, B. P., & Jin, F.-F. (2009). El Niño in a changing climate. Nature, 461, 511. Retrieved from http://dx.doi.org/10.1038/nature08316

Yin X, Gleason B. E., Compo G. P., Matsui N., Vose R. S. (2008). The International Surface Pressure Databank (ISPD) land component version 2.2. National Climatic Data Center, Asheville, NC. Available from ftp://ftp.ncdc.noaa.gov/pub/data/ispd/doc/ISPD2_2.pdf

Yu B., & Zwiers F. W. (2010). Changes in equatorial atmospheric zonal circulations in recent decades. Geophys Res Lett. doi: 37:L05701

Zebiak, S. E. (1982). A Simple Atmospheric Model of Relevance to El Niño. Journal of the Atmospheric Sciences. http://doi.org/10.1175/1520-0469(1982)039<2017:ASAMOR>2.0.CO;2

Zebiak, S. E., & Cane, M. A. (1987). A model El Nino-Southern Oscillation. Monthly Weather Review. http://doi.org/10.1175/1520-0493(1987)115<2262:AMENO>2.0.CO;2

Zhang, C. (2001), Double ITCZs, J. Geophys. Res., 106(D11), 11785–11792, doi: 10.1029/2001JD900046.

Zhang, C. and S.M. Hagos (2009). Bi-modal Structure and Variability of Large-Scale Diabatic Heating in the Tropics. J. Atmos. Sci., 66, 3621–3640, https://doi.org/10.1175/2009JAS3089.1

Zhang, G., and Z. Wang (2015), Interannual variability of tropical cyclone activity and regional Hadley circulation over the Northeastern Pacific. Geophys. Res. Lett., 42, 2473–2481. doi:10.1002/2015GL063318.

Zhang, W., Jin, F. F., Zhao, J. X., & Li, J. (2013). On the bias in simulated ENSO SSTA meridional widths of CMIP3 models. Journal of Climate, 26(10), 3173–3186. http://doi.org/10.1175/JCLI-D-12-00347.1

Zheng, F., X.-H. Fang, J.-Y. Yu, and J. Zhu (2014), Asymmetry of the Bjerknes positive feedback between the two types of El Niño, Geophys. Res. Lett., 41, 7651–7657, doi: 10.1002/2014GL062125.